

NEW LIGHT ON OPTICAL ACTIVITY:  
INTERACTION OF ELECTROMAGNETIC WAVES  
WITH CHIRAL PHOTONIC METAMATERIALS

Zur Erlangung des akademischen Grades eines  
DOKTORS DER NATURWISSENSCHAFTEN  
der Fakultät für Physik des Karlsruher Instituts für Technologie

genehmigte

DISSERTATION

von

Diplom-Physiker Manuel Decker  
aus Karlsruhe

Tag der mündlichen Prüfung: 2. Juli 2010  
Referent: Prof. Dr. Martin Wegener  
Korreferent: Prof. Dr. Kurt Busch







# Publications

## Parts of this work have already been published.

### In scientific journals:

- D. Diessel, M. Decker, S. Linden, and M. Wegener, *Near-field optical experiments on low-symmetry split-ring-resonator arrays*, Opt. Lett., submitted (2010).
- M. Decker, R. Zhao, C. M. Soukoulis, S. Linden, and M. Wegener, *Twisted split-ring-resonator photonic metamaterial with huge optical activity*, Opt. Lett. **35**, 1593 (2010).
- M. Decker, S. Burger, S. Linden, and M. Wegener, *Magnetization waves in split-ring-resonator arrays: Evidence for retardation effects*, Phys. Rev. B **80**, 193102 (2009).
- J. K. Gansel, M. Thiel, M. S. Rill, M. Decker, K. Bade, V. Saile, G. von Freymann, S. Linden, and M. Wegener, *Gold Helix Photonic Metamaterial as Broadband Circular Polarizer*, Science **325**, 1513 (2009).
- M. Decker, S. Linden, and M. Wegener, *Coupling effects in low-symmetry planar split-ring-resonator arrays*, Opt. Lett. **34**, 1579 (2009).
- M. Decker, M. Ruther, C. E. Kriegler, J. Zhou, C. M. Soukoulis, S. Linden, and M. Wegener, *Strong optical activity from twisted-cross photonic metamaterials*, Opt. Lett. **34**, 2501 (2009).
- M. Decker, M. W. Klein, M. Wegener, and S. Linden, *Circular dichroism of planar chiral magnetic metamaterials*, Opt. Lett. **32**, 856 (2007).
- S. Linden, M. Decker, and M. Wegener, *Model System for a One-Dimensional Magnetic Photonic Crystal*, Phys. Rev. Lett. **97**, 083902 (2006).

### At conferences:

- M. Decker, R. Zhao, C. M. Soukoulis, S. Linden, and M. Wegener, *Strong Circular Dichroism from Twisted Split-Ring Resonators*, Conference on Lasers and Electro-Optics/Quantum Electronics and Laser Science Conference CLEO/QUELS (2010).

- M. Decker, M. W. Klein, M. Wegener, and S. Linden, *Circular Dichroism in Double-Layer Chiral Metamaterials*, Conference on Lasers and Electro-Optics/Quantum Electronics and Laser Science Conference and Photonic Applications Systems Technologies CLEO/QUELS & PhAST (2007).
- S. Linden, M. Decker, and M. Wegener, *Photonic Crystals made from “Magnetic Atoms”*, Conference on Lasers and Electro-Optics/Quantum Electronics and Laser Science Conference and Photonic Applications Systems Technologies CLEO/QUELS & PhAST (2006).

### **Additional work has been published.**

#### **In scientific journals:**

- N. Feth, S. Linden, M. W. Klein, M. Decker, F. B. P. Niesler, Y. Zeng, W. Hoyer, J. Liu, S. W. Koch, J. V. Moloney, and M. Wegener, *Second-harmonic generation from complementary split-ring resonators*, *Opt. Lett.* **33**, 1975 (2008).
- M. Thiel, M. Decker, M. Deubel, M. Wegener, S. Linden, and G. von Freymann, *Polarization Stop Bands in Chiral Polymeric Three-Dimensional Photonic Crystals*, *Adv. Mater.* **19**, 207 (2007).

#### **At conferences:**

- N. Feth, M. Decker, G. Dolling, M. W. Klein, S. Linden, and M. Wegener, *Photonic metamaterials - new opportunities for nanoimprint*, 2007 Digest of the LEOS Summer Topical Meetings, 76 (2007).
- S. Linden, C. M. Soukoulis, G. Dolling, M. Decker, and M. Wegener, *Metamaterials see the light*, 2007 Pacific RIM Conference on Lasers and Electro-Optics, Vols 1-4, 363 (2007).

# Contents

<b>1</b>	<b>Introduction</b>	<b>1</b>
<b>2</b>	<b>Fundamentals of Metamaterials</b>	<b>5</b>
2.1	Maxwell's Equations for Isotropic Media . . . . .	6
2.2	The Metamaterial Concept . . . . .	12
2.2.1	Negative-Index Metamaterials . . . . .	13
2.2.2	Effective-Parameter Retrieval . . . . .	14
2.2.3	Negative Refraction . . . . .	17
2.2.4	Perfect Lens . . . . .	18
2.3	Maxwell's Equations for Biisotropic and Bianisotropic Media . . . . .	19
<b>3</b>	<b>Optics of Metal Nanoparticles</b>	<b>23</b>
3.1	Drude Model . . . . .	24
3.2	Mie Theory . . . . .	26
3.3	Optical Response of Metallic Nanoparticles . . . . .	26
3.4	Magnetic Response of Split-Ring Resonators . . . . .	28
3.5	Magnetic Response of Cut-Wire Pairs . . . . .	33
<b>4</b>	<b>Methods</b>	<b>35</b>
4.1	Fabrication . . . . .	36
4.1.1	Sample Preparation . . . . .	37
4.1.2	Single-Exposure Electron-Beam Lithography . . . . .	37
4.1.3	Fabrication of Multi-Layer Metamaterials . . . . .	38
4.2	Optical Characterisation . . . . .	41
4.2.1	Transmittance Measurements in the Visible/Near-Infrared . . . . .	41
4.2.2	Transmittance Measurements in the Infrared . . . . .	43
4.3	Numerical Calculation and Postprocessing . . . . .	44
<b>5</b>	<b>Interaction of Dipoles in Metamaterials</b>	<b>45</b>
5.1	Lorentz-Oscillator Model . . . . .	46
5.1.1	Near-Field Dipole-Dipole Coupling . . . . .	46
5.2	In-Plane Interactions of Magnetic Dipoles . . . . .	49
5.2.1	Magnetic Coupling via Dielectric Waveguides . . . . .	49

5.2.2	Magnetic Coupling in Low-Symmetry Split-Ring-Resonator Supercells . . . . .	54
5.2.3	Far-Field Retarded Magnetic-Dipole Interactions . . . . .	58
5.3	3D-Coupling of Magnetic Dipoles . . . . .	65
<b>6</b>	<b>An Introduction to Chirality</b>	<b>69</b>
6.1	A Geometrical View on Chirality . . . . .	70
6.2	Effective Chiral Media . . . . .	71
6.2.1	Symmetry Constraints . . . . .	72
6.2.2	Bianisotropy vs. Chirality . . . . .	75
6.3	Wave Propagation in Chiral Media . . . . .	77
6.4	Reflection and Transmission of Chiral Media . . . . .	79
6.4.1	Normal Incidence on a Chiral slab . . . . .	80
6.4.2	Oblique Incidence on Chiral Interfaces . . . . .	82
6.5	Polarisation Spectroscopy . . . . .	85
6.5.1	Calculation of the Polarisation State of Light . . . . .	85
6.5.2	Circular Polarisation . . . . .	88
6.5.3	Jones Calculus . . . . .	90
6.5.4	Generation of Circular Polarisation . . . . .	93
6.6	Optical Activity and Circular Dichroism . . . . .	96
6.6.1	Derivation of the Polarisation State of Light from Experiments . . . . .	98
<b>7</b>	<b>“Planar” Chiral Photonic Metamaterials</b>	<b>101</b>
7.1	Chiral Symmetry in Two Dimensions . . . . .	102
7.2	Chiral Double-Layer Gammadions . . . . .	102
7.3	Influence of Symmetry Breaking . . . . .	107
7.4	Forward and Backward Propagation . . . . .	107
<b>8</b>	<b>3D-Chiral Photonic Metamaterials</b>	<b>111</b>
8.1	Twisted-Crosses Photonic Metamaterial . . . . .	112
8.2	Chiral Twisted-Split-Ring-Resonator Metamaterial . . . . .	116
8.3	Three-Dimensional Metallic Helices . . . . .	119
<b>9</b>	<b>Conclusions</b>	<b>123</b>
<b>A</b>	<b>Plane Wave Properties in Chiral Media</b>	<b>129</b>
A.1	Wave Propagation in Chiral Media . . . . .	129
A.2	Chiral Retrieval Procedure . . . . .	132
A.3	Polarisation State of Complex-Valued Fields . . . . .	135
	<b>Bibliography</b>	<b>138</b>
	<b>Acknowledgements</b>	<b>149</b>

# Chapter 1

## Introduction

Polarisation is considered as one of the fundamental properties of light. In daily life, however, this remarkable property is not perceivable at first sight as the polarisation sensitivity of the human eye is rather poor. Additionally, the polarisation state of light is subject to a constant change in nature owing to scattering, reflections and refraction at interfaces. Nevertheless, the polarisation properties of light are commonly made use of in various everyday applications such as polarising sunglasses which minimise the glare due to the reflected light from the environment or polarisation filters in cameras which are used to enhance the contrast of the photographs. Furthermore, polarisation filters for circularly polarised light are used in 3D-movies to code the different images for the spectators' eyes in order to generate a three-dimensional experience.

Actually, polarisation manipulation is not only performed in 3D-cinemas but also in daily life. Normally, you will never think of polarisation rotation, for instance, when observing light passing through a glass of red wine. However, if you built a transmittance setup to detect the emerging polarisation state of linearly polarised incident light that is transmitted through the wine, you would be astonished to find that the polarisation plane of light is rotated by about  $6^\circ$  in clockwise direction. This optical activity stems from the dextrorotatory tartaric acid in the wine and the rotatory power originates from the molecular structure of the tartaric acid. This fascinating effect was already investigated in the early 18th century by Louis Pasteur who managed to explain why a solution of natural tartaric acid, obtained from wine indeed, exhibits optical activity while for tartaric acid derived from chemical synthesis optical activity is completely absent. He therefore separated the sodium-ammonium-tartrate crystals from the synthesised solution and found that there were equal amounts of two mirror symmetric forms (enantiomers) of the tartrate crystals. After tediously sorting the crystals with a magnifying glass and a pair of tweezers, Pasteur demonstrated that the solutions of the two enantiomers rotated the polarisation plane of light into opposite directions while the (racemic) mixture of the two solutions of tartrate showed no polarisation change at all. He was therefore the first to demonstrate that optical activity depends on the handedness or “chirality” of the molecules in solution [1].

The term “chirality” stems from the greek word “ $\chi\epsilon\iota\rho$ ” meaning “*hand*” and describes geometrical structures that cannot be mapped onto their mirror image by any kind of rotation,

translation or combinations thereof. As a consequence a chiral structure does not exhibit inversion and/or mirror symmetry. Following this recipe, J. C. Bose demonstrated optical activity in artificial composite chiral materials in 1898. Bose literally twisted a bundle of parallel 10-cm-long jute fibres in order to measure the optical rotation power of this chiral composite material at radio-frequencies [2].

Only shortly afterwards Paul Drude developed a concept to describe optical activity in helical-shaped conducting materials. The basic idea behind his concept is that coupling of the electric and the magnetic field components of light provided by circulating ring currents in the conducting helix leads to a rotation of the polarisation plane of the incident linearly polarised light [3]. Karl F. Lindman verified Drude's model of optical activity in 1920 [4] by measuring the optical rotatory power of  $2 \times 500$  manually bent copper helices at 13-cm-wavelength (1-MHz to 3-MHz-frequency). His measurement revealed that the optical rotatory power of the metal helical composite structure reaches that of natural materials just like tartaric acid, for instance. This magnetoelectric coupling can also be found in chiral molecules where electric/magnetic moments in the different functional groups within the molecule give rise to optical activity. Hence, in order to fabricate an optically active medium, one needs to have control over both the geometry and the magnetoelectric coupling of the material system.

Recent progress in nanofabrication techniques, in particular electron-beam lithography, has opened new paths to bring optically active materials to optical operation frequencies. As a consequence, many groups are interested in fabricating artificial chiral materials that even outperform optical activity and circular dichroism of natural materials in the optical spectral range. However, obtaining a magnetic response from natural materials, which is essential for magnetoelectric coupling, is challenging as the magnetic permeability of all natural materials is nearly unity for THz-frequencies. The electric permittivity on the other hand can normally be found to vary to a certain extent particularly at high frequencies above  $\omega_0 = 10$  THz. Thus, we need to gain control over the electric and magnetic response at optical frequencies with the use of artificial materials which can be designed to fulfil our requirements. These manmade materials are named "metamaterials" as they provide functionalities going "beyond" those of natural materials (from the greek prefix " $\mu\epsilon\tau\acute{\alpha}$ " meaning "beyond"). The principle idea behind this concept is that a periodic arrangement of metal nanostructures with a lattice constant much smaller than the wavelength of light can be regarded as an effective material since the incident light is not able to resolve the periodic substructure of the metamaterial. We can then tune the effective response of the metamaterial by choosing the design of the underlying artificial building blocks. If we make use of this degree of freedom, many interesting effects that cannot be found in nature can result: a magnetic response at optical frequencies [5, 6] or even a negative refractive index [7, 8], just to mention two examples which gained much attention in the past years. The most prominent artificial building block is the so-called split-ring resonator (SRR), a U-shaped metal nanoparticle that can be seen as plasmonic analogue of an LC-circuit providing a magnetic response even at optical frequencies [5]. The SRR enables us to couple electric and magnetic dipoles with the magnetic and electric component of the incident light field [9], one prerequisite of obtaining optical activity.

---

The second main ingredient for optical activity is chiral symmetry. Since electron-beam lithography as standard nanofabrication technique sets certain limits to possible metamaterial designs, most chiral metamaterials at optical frequencies are based on arrays of planar nanostructures [10, 11] which, strictly speaking, cannot exhibit a chiral optical response as “planar chirality” does not exist in a three-dimensional world. Hence, structural asymmetries in propagation direction of light have to be introduced in order to provide three-dimensional chirality [11]. This requirement implies a construction scheme for three-dimensional chiral metamaterials specifically designed for electron-beam lithography: we start with an achiral planar structure and introduce a certain “twist” into the axial-direction in order to achieve structural chirality of such a composite structure (instead of “molecular” chirality). Using this method we obtain three-dimensional chiral metamaterials exhibiting large optical activity and circular dichroism that can even exceed that in tartaric acid ( $\approx 13^\circ/\text{dm}$ ) or in a solution of sugar molecules ( $\approx 66^\circ/\text{dm}$ ), for example.

## Outline of this Thesis

Chapter 2 gives an introduction into the basic concepts of optics in general and to the concept of metamaterials in particular. We describe what effects can be expected when we vary the permittivity  $\epsilon$  and the permeability  $\mu$  of an isotropic effective medium. We then include magnetoelectric coupling into our reasoning and classify effective materials with respect to their effective material parameters. Thereby, particular emphasis is laid on chiral materials. In Chapter 3 we review the optical response of metal nanoparticles and introduce the splitting resonator (SRR) and the cut-wire pairs as fundamental plasmonic building blocks for magnetic metamaterials. In Chapter 4 we then describe the nanofabrication tools used for fabrication of the planar and bi-layer metamaterial structures and introduce our experimental setups for optical characterisation before we present our results on coupling of effective magnetic moments in nanostructured arrays in Chapter 5. We demonstrate that strong magnetic coupling between metallic nanostructures can be achieved and even retardation effects play a major role on the scale of common metamaterial designs.

In the following chapter (Chapter 6) we review the basic properties of chiral structures and of light propagation in chiral media on the one hand. On the other hand we will have closer look at the methods how circular polarised transmittance spectra are obtained and how the polarisation state of the emerging light is analysed. We will then present our results on optical activity and circular dichroism in double-layer gammadion-shaped metamaterials in Chapter 7. We demonstrate that optical activity in our double-layer gammadion structures is based on the structural asymmetry in the axial direction and that the optical response is compatible with reciprocity. In Chapter 8 we present our results on three-dimensional chiral metamaterials consisting of chiral dimers of two functional layers which are rotated with respect to each other. These structures exhibit pure, large optical activity in combination with circular dichroism that outperforms values of natural materials by orders of magnitudes.

Finally, in the last chapter of this Thesis we summarise our results on magnetic coupling and chiral metamaterials and conclude with a brief outlook.



# Chapter 2

## Fundamentals of Metamaterials

Maxwell's equations are the fundamental equations describing all electromagnetic phenomena. When an electromagnetic wave propagates in a natural material, which is characterised by a lattice constant much smaller than the wavelength of light, the light field effectively averages over the fine atomic substructure and only "sees" an effective homogeneous medium. In this case, wave propagation can be described by the macroscopic Maxwell's equations. Normally it is sufficient to introduce two effective quantities in order to account for the medium involved – the relative permittivity  $\bar{\epsilon}$  describing the material's electric response to an electromagnetic wave and the relative permeability  $\bar{\mu}$  describing the corresponding magnetic response. The refractive index of an isotropic medium,  $\epsilon$  and  $\mu$

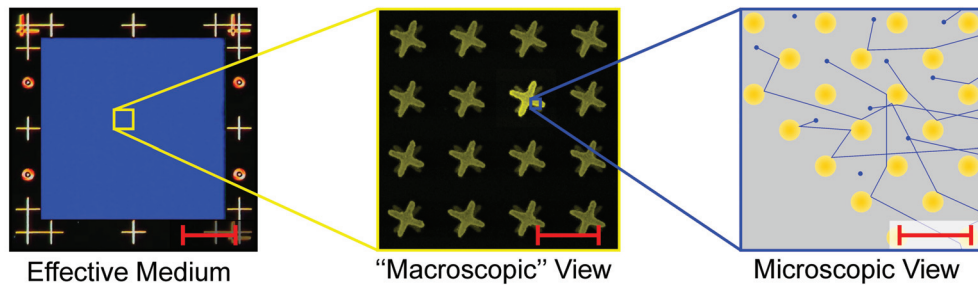


Figure 2.1: Illustration of a (gold) twisted-crosses chiral metamaterial from three different point of views. The left-hand side illustrates the effective-medium view on an  $80 \times 80 \mu\text{m}^2$  field of the metamaterial observed *via* an optical microscope (scalebar is  $25 \mu\text{m}$ ). The incident light field only "sees" the effective metamaterials response. A coloured SEM image of a  $4 \times 4$  array of twisted crosses is shown in the middle (scalebar is  $500 \text{nm}$ ) representing the "macroscopic" point of view. The metamaterial's response is given by the response of the pairs of coupled gold crosses. The artist's view on the microscopic "kinetic gas theory" proposed by Paul Drude to describe the optical response of metals [3] is shown on the right-hand side (scalebar is  $5 \text{\AA}$ ). The electrons (in blue) are "scattered" by the (yellow) gold atoms.

being scalars, follows from the well known relation  $n^2 = \epsilon\mu$ . In nature, any magnetic response from conventional materials vanishes ( $\mu = 1$ ) at infrared and higher frequencies, as magnetic polarisation in natural materials follows from orbital currents or unpaired electron spins which are resonant in the GHz-region. In contrast to that, significant electric polarisation can only be obtained for THz-frequencies owing to the resonant behaviour of

electric excitation modes. This is why in most textbooks only the permittivity  $\epsilon$  is used as a characteristic material parameter whereas the permeability  $\mu$  is very often set to unity at optical frequencies.

In order to tune the electric and magnetic response ( $\epsilon$  and  $\mu$ ) of a material we have to go down to the atomic scale and replace the atoms in the crystal lattice by “artificial atoms” which exhibit the required optical response. If this artificial material or metamaterial, which surely cannot be fabricated on an atomic scale, meets the requirement that the lattice constant is much smaller than the wavelength of the incident light, it can still be regarded as an effective medium with a specific effective permittivity and permeability based on the design of the “artificial atom”. For  $\epsilon$  and  $\mu$  being open to discussion, plenty of additional intriguing effects besides the well-known world of optics result. Probably the most prominent feature is the negative index of refraction [12–14] that can be achieved when  $\epsilon$  and  $\mu$  both are negative in the same spectral region. In this case,  $n = -\sqrt{|\epsilon||\mu|}$  according to Equation (2.32).

Going one step further, we can also imagine materials in which a magnetic polarisation can be excited by an incident electric field and an electric polarisation by an incident magnetic field. Now we have to account for an additional material parameter  $\xi$  characteristic of a whole new class of materials, so-called bianisotropic materials. A very interesting subclass of bianisotropic materials are biisotropic or chiral materials, being able to rotate the polarisation plane of incident linearly polarised light.

In the following, we start with the macroscopic Maxwell’s equations and motivate the use of effective material parameters to describe the effective response of isotropic media. After an introduction to the concept of metamaterials we will motivate the use of the effective-medium theory formulated by Maxwell-Garnett [15] for metamaterial structures and present some popular aspects and possible applications of isotropic metamaterial designs. Finally, the metamaterial term is expanded to include the class of bianisotropic and biisotropic or chiral materials and we will discuss how (meta-) materials are classified with respect to the properties of the effective material parameters.

## 2.1 Maxwell’s Equations for Isotropic Media

The propagation of electromagnetic waves is characterised by the macroscopic Maxwell’s equations (in SI units) [16]

$$\nabla \mathbf{D} = \rho \quad (2.1)$$

$$\nabla \mathbf{B} = 0 \quad (2.2)$$

$$\nabla \times \mathbf{E} = -\frac{\partial \mathbf{B}}{\partial t} \quad (2.3)$$

$$\nabla \times \mathbf{H} = \mathbf{J} + \frac{\partial \mathbf{D}}{\partial t} \quad (2.4)$$

with the following notations and units:

- $\mathbf{E}$  electric field,  $[\mathbf{E}] = \text{Vm}^{-1}$

- $\mathbf{D}$  electric displacement,  $[\mathbf{D}] = \text{Asm}^{-1}$
- $\mathbf{H}$  magnetic induction,  $[\mathbf{H}] = \text{Am}^{-1}$
- $\mathbf{B}$  magnetic field,  $[\mathbf{B}] = \text{Vs}^{-1}\text{m}^{-1}$
- $\rho$  free electric charge density,  $[\rho] = \text{Asm}^{-3}$
- $\mathbf{J}$  free electric current density,  $[\mathbf{J}] = \text{Am}^{-2}$
- $\epsilon_0$  electric permittivity of vacuum:  $\epsilon_0 = 8.8542 \cdot 10^{-12} \text{AsV}^{-1}\text{m}^{-1}$
- $\mu_0$  magnetic permeability of vacuum:  $\mu_0 = 4\pi \cdot 10^{-7} \text{VsA}^{-1}\text{m}^{-1}$

Strictly speaking, we would have to start with the microscopic Maxwell's equations taking microscopic currents and charge distributions into account. Since experimentally we rather detect the temporal and spatial mean value of the microscopic fields than the actual microscopic fields of, *e.g.*, electrons and atoms on the atomic scale, we can describe the optical response of any (macroscopic) object by the macroscopic<sup>1</sup> Maxwell's equations given by Equations (2.1)-(2.4). Now the effects resulting from the atomic substructure of the material are described by an effective electric and magnetic polarisation  $\mathbf{P}(\mathbf{E}, \mathbf{H})$  and  $\mathbf{M}(\mathbf{E}, \mathbf{H})$ , respectively. The resulting constitutive material relations between the electric field and the electric displacement and between the magnetic field and the magnetic induction are given by:

$$\mathbf{D} = \epsilon_0 \mathbf{E} + \mathbf{P}(\mathbf{E}, \mathbf{H}) \quad (2.5)$$

$$\mathbf{B} = \mu_0 (\mathbf{H} + \mathbf{M}(\mathbf{E}, \mathbf{H})) \quad (2.6)$$

As we want to limit ourselves to linear optics, *i.e.*, we want to deal with weak electric fields only, we can expand  $\mathbf{P}$  in a power series and neglect all terms of higher order than the linear term. If we further neglect coupling of the electric field component to the magnetic field component  $\mathbf{M}(\mathbf{E}, \mathbf{H}) \approx \mathbf{M}(\mathbf{H})$  and *vice versa*  $\mathbf{P}(\mathbf{E}, \mathbf{H}) \approx \mathbf{P}(\mathbf{E})$ , we exclude bianisotropic and chiral media (see Section 2.3) at this point. The linear response function of the electric polarisation is then given by:

$$\mathbf{P}(\mathbf{r}, t) = \int_{-\infty}^{\infty} \int_{-\infty}^{\infty} \bar{\chi}_e(\mathbf{r}, \mathbf{r}', t, t') \mathbf{E}(\mathbf{r}', t') dt' d\mathbf{r}' \quad (2.7)$$

Here,  $\bar{\chi}_e$  is a second-rank tensor. In isotropic, uniaxial and biaxial crystals we can find a diagonal representation of  $\bar{\chi}_e$  where the field components  $E_i$  ( $i \in x, y, z$ ) decouple. This results in linearly polarised eigenstates of the wave equation (2.14), (2.15). In this chapter, we restrict ourselves to effective materials fulfilling the following simplifications:

<sup>1</sup>The material parameters of the "macroscopic" Maxwell's equations must not be confused with the effective material parameters of metamaterial structures obtained by the effective-medium theory. The "macroscopic" Maxwell's equations rather relate to systems between the microscopic world and the effective-medium theory used for the description of metamaterials (see Fig. 2.1)

- isotropic medium, *i.e.*,  $\mathbf{P}(\mathbf{r}, t) \parallel \mathbf{E}(\mathbf{r}, t) \Rightarrow \bar{\chi}_e(\mathbf{r}, \mathbf{r}', t, t') \rightarrow \chi_e(\mathbf{r}, \mathbf{r}', t, t')$
- homogeneous medium with local response:  $\Rightarrow \chi_e(\mathbf{r}, \mathbf{r}', t, t') \rightarrow \chi_e(t, t')$
- no explicit time dependence:  $\Rightarrow \bar{\chi}_e(t, t') \rightarrow \chi_e(t - t')$
- causality, *i.e.*,  $\chi_e(t - t') \equiv 0$  for  $t < t'$

We now obtain

$$\mathbf{P}(\mathbf{r}, t) = \epsilon_0 \int_{-\infty}^t \chi_e(t - t') \mathbf{E}(\mathbf{r}, t') dt. \quad (2.8)$$

Fourier transformation from the time domain into the frequency domain

$$f(\omega) = \mathcal{F} \{f(t)\} = \frac{1}{\sqrt{2\pi}} \int_{-\infty}^{\infty} f(t) e^{i\omega t} dt \quad (2.9)$$

finally results in

$$\mathbf{P}(\omega) = \epsilon_0 \chi_e(\omega) \mathbf{E}(\omega). \quad (2.10)$$

Following the same reasoning we deduce for the magnetisation

$$\mathbf{M}(\omega) = \chi_m(\omega) \mathbf{H}(\omega) \quad (2.11)$$

$\chi_e(\omega)$  and  $\chi_m(\omega)$  are the electric and magnetic susceptibilities, which characterise the linear response of the material to an external field. We therefore obtain the macroscopic material equations in the following form:

$$\begin{aligned} \mathbf{D} &= \epsilon_0 (1 + \chi_e(\omega)) \mathbf{E} \\ &= \epsilon_0 \epsilon(\omega) \mathbf{E} \end{aligned} \quad (2.12)$$

$$\begin{aligned} \mathbf{B} &= \mu_0 (1 + \chi_m(\omega)) \mathbf{H} \\ &= \mu_0 \mu(\omega) \mathbf{H} \end{aligned} \quad (2.13)$$

with the (relative) electric permittivity  $\epsilon(\omega)$  and the (relative) magnetic permeability  $\mu(\omega)$ .

### Wave Propagation in Isotropic Materials

The wave equation for an electromagnetic wave in an isotropic linear medium can easily be obtained from Maxwell's equations (2.1)-(2.4):

$$\left( \Delta - \mu_0 \epsilon_0 \frac{\partial^2}{\partial t^2} \mu \epsilon \right) \mathbf{E} = 0 \quad (2.14)$$

$$\left( \Delta - \mu_0 \epsilon_0 \frac{\partial^2}{\partial t^2} \mu \epsilon \right) \mathbf{B} = 0 \quad (2.15)$$

The wave equations can be solved using a plane wave *ansatz*, *i.e.*,

$$\mathbf{E}(\mathbf{r}, t) = \mathbf{E}_0 e^{i(\mathbf{k}\mathbf{r} - \omega t)} \quad (2.16)$$

and

$$\mathbf{B}(\mathbf{r}, t) = \mathbf{B}_0 e^{i(\mathbf{k}\mathbf{r} - \omega t)}, \quad (2.17)$$

respectively. We obtain

$$\mathbf{k}^2 - \mu(\omega)\epsilon(\omega)\mu_0\epsilon_0\omega^2 = 0 \quad (2.18)$$

and consequently

$$\mathbf{k}^2 = n^2(\omega)\mathbf{k}_0^2. \quad (2.19)$$

Here,  $c_0 = \sqrt{1/\mu_0\epsilon_0}$  is the vacuum speed of light,  $\mathbf{k}_0$  is the wave vector *in vacuo* and

$$n^2(\omega) = \mu(\omega)\epsilon(\omega) \quad (2.20)$$

is the material's refractive index. We can also identify the dispersion relation for an electromagnetic wave in an isotropic medium:

$$k = n(\omega) \frac{\omega}{c_0} \quad (2.21)$$

For real-valued refractive indices the phase velocity  $v_p$  and group velocity  $v_g$  are given by

$$v_p = \frac{\omega}{k} = \frac{c_0}{n(\omega)} = c \quad (2.22)$$

$$v_g = \frac{\partial\omega}{\partial k} = \frac{c_0}{n(\omega) + \omega \frac{\partial n(\omega)}{\partial \omega}} \quad (2.23)$$

Hence, for natural materials the phase velocity normally is parallel to the wavevector (see

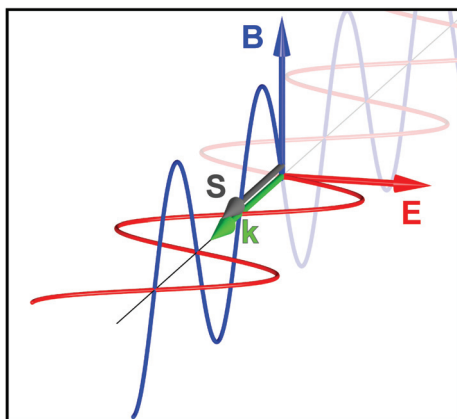


Figure 2.2: Electromagnetic wave propagating in vacuum. Wavevector  $k$  and Poynting vector  $S$  are in the same direction perpendicular to  $\mathbf{E}$  and  $\mathbf{B}$ .

Fig.2.2) while in the case of anomalous dispersion ( $\frac{\partial n(\omega)}{\partial \omega} < 0$ ) the group velocity may become antiparallel with respect to the wavevector  $\mathbf{k}$  in a specific spectral region. Since for

dielectric materials the group velocity and the energy flow, *i.e.*, the average energy flow per unit time and unit area

$$\langle \mathbf{S}(\mathbf{r}, t) \rangle = \frac{1}{2} \text{Re} [\mathbf{E}(\mathbf{r}, t) \times \mathbf{H}^*(\mathbf{r}, t)] \quad (2.24)$$

are oriented parallel to each other, this results in so-called backward waves.

Finally we can determine the angle of refraction  $\theta_t$  of a plane wave passing through an interface of two effective media at an arbitrary angle  $\theta_i$  using Snell's law

$$\frac{\sin \theta_i}{\sin \theta_t} = \frac{n_t}{n_i}. \quad (2.25)$$

We can additionally determine the complex reflection and transmission coefficients of a plane wave at an interface making use of Fresnel's equations [17]

$$r_s = \left( \frac{E_{0r}}{E_{0i}} \right)_s = \frac{\frac{n_i}{\mu_i} \cos \theta_i - \frac{n_t}{\mu_t} \cos \theta_t}{\frac{n_i}{\mu_i} \cos \theta_i + \frac{n_t}{\mu_t} \cos \theta_t} = \frac{Z_i^{-1} \cos \theta_i - Z_t^{-1} \cos \theta_t}{Z_i^{-1} \cos \theta_i + Z_t^{-1} \cos \theta_t} \quad (2.26)$$

$$t_s = \left( \frac{E_{0t}}{E_{0i}} \right)_s = \frac{2 \frac{n_i}{\mu_i} \cos \theta_i}{\frac{n_i}{\mu_i} \cos \theta_i + \frac{n_t}{\mu_t} \cos \theta_t} = \frac{2 Z_i^{-1} \cos \theta_i}{Z_i^{-1} \cos \theta_i + Z_t^{-1} \cos \theta_t} \quad (2.27)$$

$$r_p = \left( \frac{E_{0r}}{E_{0i}} \right)_p = \frac{\frac{n_t}{\mu_t} \cos \theta_i - \frac{n_i}{\mu_i} \cos \theta_t}{\frac{n_i}{\mu_i} \cos \theta_i + \frac{n_t}{\mu_t} \cos \theta_t} = \frac{Z_t^{-1} \cos \theta_i - Z_i^{-1} \cos \theta_t}{Z_i^{-1} \cos \theta_i + Z_t^{-1} \cos \theta_t} \quad (2.28)$$

$$t_p = \left( \frac{E_{0t}}{E_{0i}} \right)_p = \frac{2 \frac{n_i}{\mu_i} \cos \theta_i}{\frac{n_i}{\mu_i} \cos \theta_t + \frac{n_t}{\mu_t} \cos \theta_i} = \frac{2 Z_i^{-1} \cos \theta_i}{Z_i^{-1} \cos \theta_t + Z_t^{-1} \cos \theta_i} \quad (2.29)$$

The impedance of the medium is defined by

$$Z = \sqrt{\frac{\mu \mu_0}{\epsilon \epsilon_0}} = Z_0 \sqrt{\frac{\mu}{\epsilon}} \quad (2.30)$$

where  $Z_0$  is the vacuum impedance. Note that in many optics textbooks (see, *e.g.*, Ref. [17]) the permeability  $\mu$  is set to unity at optical frequencies. In the case of magnetic (meta-)materials, however,  $\mu$  is an essential parameter and must not be neglected.

### Negative Refractive Index

Although the refractive index for common materials is always positive, it is possible to obtain negative values of  $n$  under certain conditions. In particular, when calculating the square root

$$n = \pm \sqrt{\mu \epsilon} \quad (2.31)$$

for complex values for  $\epsilon$  and  $\mu$  one obtains [18]

$$n = \sqrt{|\epsilon| |\mu|} \exp \left[ \frac{i}{2} \left( \text{arccot} \frac{\epsilon'}{\epsilon''} + \text{arccot} \frac{\mu'}{\mu''} \right) \right] \quad (2.32)$$

where

$$\epsilon = \epsilon' + i\epsilon'', \text{ and } \mu = \mu' + i\mu''.$$

In order to obtain a negative refractive index, a negative real part of both the permittivity and the permeability is not necessarily required as the imaginary parts have to be considered as well. However, the best performance of negative-index materials is achieved when  $Re[\epsilon]$  and  $Re[\mu]$  both are negative. In either case, the material parameters  $\epsilon$ ,  $\mu$  and  $n$  have to fulfill several physical conditions:

### 1. Passive Medium:

Since we want to limit our discussion to passive media, we have to ensure that the imaginary part of the refractive index is always positive as otherwise a propagating wave will grow exponentially. Equation (2.32) already implies that this conditions is always fulfilled as

$$0 < \frac{1}{2} \left( \operatorname{arccot} \frac{\epsilon'}{\epsilon''} + \operatorname{arccot} \frac{\mu'}{\mu''} \right) < \pi. \quad (2.33)$$

### 2. Energy Conservation:

The energy density  $w$  of the electromagnetic field, which in the case of transparent dispersive media is given by

$$w = \operatorname{Re} \left[ \frac{\partial (\epsilon(\omega)\omega)}{\partial \omega} \right] |\mathbf{E}|^2 + \operatorname{Re} \left[ \frac{\partial (\mu(\omega)\omega)}{\partial \omega} \right] |\mathbf{H}|^2 \geq 0 \quad (2.34)$$

has to be positive. If both  $\epsilon$  and  $\mu$  were frequency independent and negative, the energy density would be negative as well. Due to energy conservation this is not feasible, hence, for negative values of  $\epsilon$  and  $\mu$  dispersion is absolutely essential.

### 3. Causality:

The real- and imaginary parts of the material parameters are connected *via* the Kramers-Kronig relations [16] as otherwise the material's response to the electromagnetic field would be preceding the exciting fields, hence, violating causality. As a consequence, any dispersive medium is always more or less absorbing as well. For the permittivity  $\epsilon(\omega)$  the Kramers-Kronig relations read:

$$\operatorname{Re} [\epsilon(\omega)] = 1 + \frac{2}{\pi} PV \int_0^\infty \frac{\operatorname{Im} [\epsilon(\omega')]}{\omega'^2 - \omega^2} d\omega' \quad (2.35)$$

$$\operatorname{Im} [\epsilon(\omega)] = -\frac{2\omega}{\pi} PV \int_0^\infty \frac{\operatorname{Re} [\epsilon(\omega')] - 1}{\omega'^2 - \omega^2} d\omega' \quad (2.36)$$

$PV$  being the principle value of the integral

$$PV \int_{-\infty}^{\infty} f(x) dx = \int_{-\infty}^{\infty} PV [f(x)] dx = \lim_{\epsilon \rightarrow 0} \left[ \int_{-\infty}^{x_0 - \epsilon} f(x) dx + \int_{x_0 + \epsilon}^{\infty} f(x) dx \right].$$

However, tuning  $\epsilon$  and  $\mu$  alone is not the only route to achieve a negative index of refraction. An alternative material class presented by Pendry [19] is provided by chiral materials, where negative values for  $n$  can be obtained for circularly polarised light. This class of materials additionally requires coupling of the electric field to the magnetic field which we explicitly excluded before as it is subject to Chapter 6.

## 2.2 The Metamaterial Concept

In the preceding section we have dealt with wave propagation in a conventional medium. As we are now interested in engineering the material parameters in order to manipulate the dispersion and the polarisation properties of an electromagnetic wave in this medium, we have to find the appropriate materials that fit our requirements. Unfortunately, there is only a limited choice provided by nature. While the electric permittivity can normally be found to vary to a certain extent particularly at high frequencies ( $\omega_0 > 10$  THz), the magnetic permeability of all natural materials is nearly unity [20] for THz-frequencies. Thus, we need to fabricate artificial materials to tune the electric and magnetic response at optical frequencies. These manmade materials are named “metamaterials” as they provide functionalities going “beyond” those of natural materials (from the greek prefix “ $\mu\epsilon\tau\acute{\alpha}$ ” meaning “beyond”). The principle idea behind this concept is to design a fundamental building block which interacts with the incident light in a fashion that provides the desired optical response. If the incident light in turn can only “see” an effective response of many of these artificial building blocks, the metamaterial can be described by effective material parameters (see Fig. 2.1).

An arrangement of “artificial atoms” whose interparticle spacing is much smaller than the wavelength of the incident light fulfills this requirement and can thus be seen as an effective medium. Although a periodic arrangement of the “atoms” in a metamaterial is generally not necessary, it is often chosen in order to ease the fabrication process. In this sense metamaterials are often referred to as artificial periodic structures with lattice constants  $a$  well below the wavelength of light

$$\lambda \gg a. \quad (2.37)$$

Due to the strong coupling of electromagnetic waves to metal particles *via* plasmonic modes (see Chapter 3), the functional building blocks of metamaterials are usually made of metallic nanostructures. By properly designing the shape of those metallic particles we are capable of manipulating the dispersion and polarisation of an incident plane wave:

- Firstly, we are able to excite not only electric dipoles *via* small (spherical) metal inclusions (see Chapter 3.3) but also magnetic dipoles can be excited by properly designing the shape of the nanoparticles. The most prominent representative is the so-called split-ring resonator (SRR) introduced in Chapter 3.4. The resulting magnetic permeability  $\mu \neq 1$  is a prerequisite for tailoring the magnetic properties of the metamaterial. In combination with thin metallic wires which provide a negative permittivity  $\epsilon$  we obtain a negative refractive index metamaterial, for example (see Section 2.2.1).
- To gain control over the polarisation state of light we have to couple the magnetic and electric field components to induce optical activity and circular dichroism. This can be achieved by, *e.g.*, the chiral structure designs introduced in Chapter 7 and 8.

The first theory to deal with the linear optical properties of such composite materials was developed by Maxwell-Garnett in 1920 [15]. In his work, Maxwell-Garnett derived

an effective-medium theory for materials composed of (non-periodic) small spherical metal particles embedded in a dielectric host material (so-called metal glasses or stained glasses). Assuming that the wavelength of the incident light is much larger than the characteristic interparticle separation (or lattice constant)  $a$ , *i.e.*,  $\lambda/a \gg 1$ , he deduced an expression for the effective electric response in the “macroscopic” Maxwell’s equations and therefore formulated an effective-medium theory. Today, the ratio  $\lambda/a$  is the principle measure for a structure design to be classified as a metamaterial, a photonic crystal or an ordinary diffracting material. For natural crystals and visible light the typical ratio of  $\lambda/a$  is about

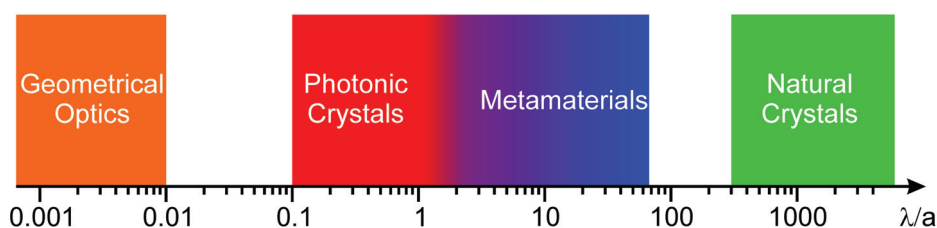


Figure 2.3: The ratio between incident wavelength  $\lambda$  and lattice constant  $a$  classifies the view on the interaction of light with matter. Starting from geometrical optics, where light is considered as rays undergoing reflection and refraction processes, we pass the scattering or diffraction regime where the wave aspect of light is crucial. Entering the effective-medium limit for  $\lambda/a > 1$ , interaction processes of light with matter can be described by effective material parameters. Almost all natural materials lie in this regime for optical frequencies.

1000, hence visible light cannot resolve the individual atoms. In metamaterials this ratio is usually lower (commonly  $\lambda/a \approx 3 - 10$ ) but still the incident light cannot resolve the fundamental building blocks. If the ratio is reduced to two or less, Wood anomalies [21, 22] and Bragg scattering occur and the effective-medium approximation becomes highly questionable. When  $\lambda/a$  is on the order of unity, the spatial dependence of the permittivity becomes relevant and results in a photonic band structure of a so-called photonic crystal (see Fig. 2.3).

In this Thesis we use the term metamaterial only for materials which do not exhibit Bragg scattering in the relevant spectral region as this would clearly contradict the effective-medium view. Thus, the ratio of resonance wavelength over lattice constant for the fabricated metamaterial structures is chosen to be  $\lambda/a > 2$ .

### 2.2.1 Negative-Index Metamaterials

The most prominent metamaterial designs that have been fabricated in the early years of metamaterials are the negative-index metamaterials. We therefore want to give a short introduction to this topic.

Typically, a negative-index metamaterial is a metal-dielectric composite that exhibits a negative refractive index  $n < 0$  within a particular spectral range. This can be achieved by fulfilling the sufficient condition that  $Re[\epsilon] < 0$  and  $Re[\mu] < 0$ , or by fulfilling the more general condition that  $Re[\epsilon]Im[\mu] + Re[\mu]Im[\epsilon] < 0$ . Remarkably, the negative-index metamaterials with both negative permittivity and negative permeability show the best performance (lower losses), *i.e.*, the ratio  $-Re[n]/Im[n]$  is higher than for metamaterials

which “only” fulfill  $Re[\epsilon]Im[\mu] + Re[\mu]Im[\epsilon] < 0$ . Hence, it is desirable to achieve negative permittivity and negative permeability in the same spectral region. We therefore need to tailor both the electric and the magnetic response of the metamaterial unit cell. While the desired electric response can simply be obtained by the use of thin metal wires acting as a “diluted metal” [23], a magnetic response can be achieved by resonantly exciting a ring current in a U-shaped metallic nanoparticle, for instance. Thus, the first negative-index metamaterial design is a combination of the split-ring resonator (SRR) which was introduced as “magnetic atom” by Pendry [5] in 1999 and thin metallic wires as diluted metal with a plasma frequency at GHz-frequencies [23]. The experimental realisation was performed by Smith *et al* [12] in 2000 for wavelengths of about 6 cm (5-GHz-frequency). In the frequency range where the constituents alone, the SRR or the diluted metal, have a purely imaginary refractive index  $n = i\sqrt{|\epsilon||\mu|}$  ( $\epsilon < 0, \mu > 0$  or  $\epsilon > 0, \mu < 0$ ) no wave propagation is possible. The transmittance in this region is nearly zero (see Fig. 2.4(c) red and blue curves). In contrast to that, for the composite structure ( $\epsilon < 0, \mu < 0$ ) wave propagation is allowed and we find non-zero values for the transmittance (see Fig. 2.4(c) black curve). This is the spectral region where according to Equation (2.32) the refractive index is negative. A model calculation following the results of [12] for the transmittance spectra of the composite structure consisting of a resonant magnetic metamaterial and a diluted metal is presented in Fig. 2.4.

As the structure dimensions of the combined negative-index metamaterial are on the order of  $\lambda/10$  it can be described by effective-medium theory and therefore by the commonly known textbook material equations

$$\mathbf{D} = \epsilon_0\epsilon(\omega)\mathbf{E} \quad (2.38)$$

$$\mathbf{B} = \mu_0\mu(\omega)\mathbf{H} \quad (2.39)$$

$$n = \pm\sqrt{\epsilon\mu}. \quad (2.40)$$

Now the question arises how one can obtain the actual effective material parameters of a fabricated metamaterial structure. Since the material parameters cannot be measured directly, a negative index of refraction was first indirectly demonstrated from the occurrence of the above mentioned pass bands [7, 12, 24] in the transmittance spectra and deduced from numerical calculations. Later, a negative refractive index was experimentally verified [8, 25] by measuring the (negative) angle of refraction. However, it is also possible to do it the other way around.

## 2.2.2 Effective-Parameter Retrieval

As the effective material parameters are directly connected with the complex-valued reflection and transmission coefficients *via* the Fresnel equations (2.26)-(2.29), it is also possible to retrieve the effective parameters from the normal-incidence reflection and transmission data of an effective-medium slab [26, 27]. The basic assumption is that if an inhomogeneous structure of the thickness  $d$  can be replaced conceptually by a continuous effective material of the same thickness, then the scattering characteristics should be identical as well (see

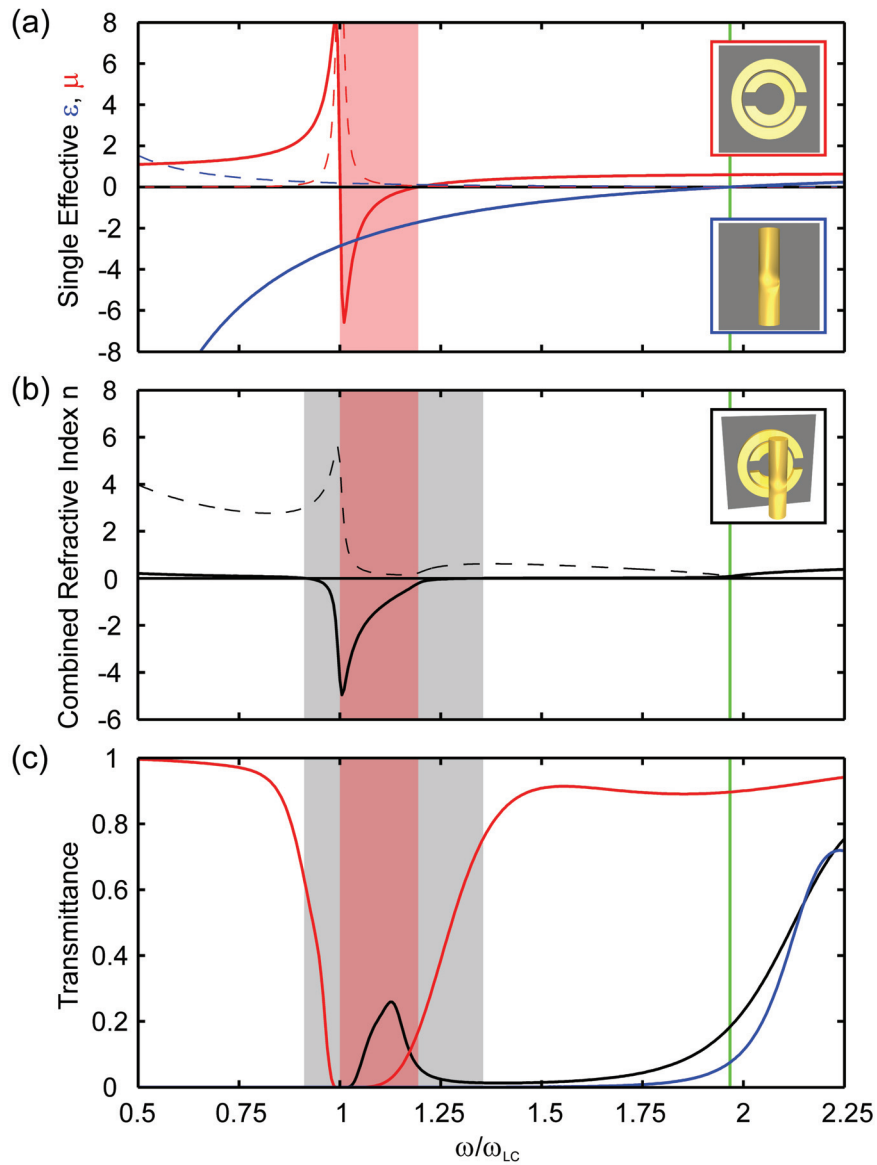


Figure 2.4: Model calculation for the effective magnetic response of a split-ring resonator array (red curves) and the effective electric response of an array of metal wires (blue curves). (a) shows the real (solid) and imaginary (dashed) parts of the modelled effective material parameters  $\epsilon$  and  $\mu$ . The light red area indicates the region where  $Re[\mu] < 0$ , the green line marks the relative frequency where  $Re[\epsilon] = 0$ . The calculated real/imaginary part of the refractive index is shown in (b) (black solid/dashed). The gray shaded area indicates the region of negative  $Re[n]$ . (c) shows the calculated transmittance spectra for the split-ring resonators (red) and metal wires (blue) alone. The transmittance of a 780-nm-slab of the composite negative-index structure with a pronounced pass band, where  $Re[\epsilon]$  and  $Re[\mu]$  are negative, is plotted in black. The (angular) frequency is normalised with respect to the resonance frequency of the split-ring resonators.

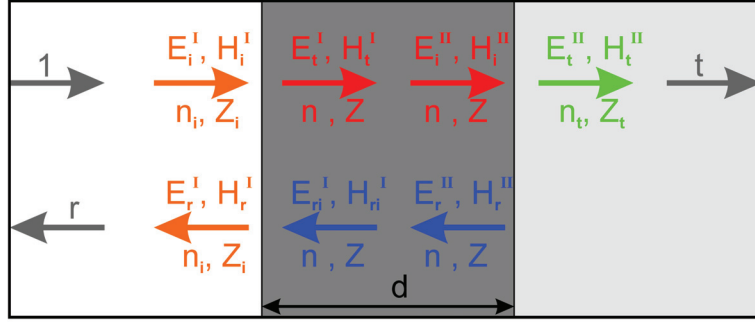


Figure 2.5: Schematic illustration of the field components for the Fresnel equations for the retrieval of the effective refractive index  $n$ , impedance  $Z$ , permeability  $\mu$  and permittivity  $\epsilon$  of an isotropic metamaterial slab of thickness  $d$  from the complex reflection and transmission coefficients.

Fig. 2.5). In this case analytical expressions for the refractive index  $n$  and the impedance  $Z$  can be found based on the complex-valued amplitude transmission coefficient ( $t$ ) and the complex-valued amplitude reflection coefficient ( $r$ ) [27]

$$Z = \pm Z_i \cdot \sqrt{\frac{\left(\frac{1+r}{t} - \cos(nk_0d)\right)^2}{-(Z_i/Z_t)^2(1 - \cos^2(nk_0d))}} \quad (2.41)$$

with

$$\cos(nk_0d) = \left( \frac{1 - r^2 + Z_i/Z_t t^2}{t(1 + Z_i/Z_t + r(Z_i/Z_t - 1))} \right). \quad (2.42)$$

For the refractive index  $n$  we obtain

$$Re[n] = \pm Re \left[ \frac{1}{k_0d} \arccos \left( \frac{1 - r^2 + Z_i/Z_t t^2}{t(1 + Z_i/Z_t + r(Z_i/Z_t - 1))} \right) \right] + \frac{2\pi m}{k_0d}, \quad m \in \mathbb{Z} \quad (2.43)$$

$$Im[n] = \pm Im \left[ \frac{1}{k_0d} \arccos \left( \frac{1 - r^2 + Z_i/Z_t t^2}{t(1 + Z_i/Z_t + r(Z_i/Z_t - 1))} \right) \right] \quad (2.44)$$

$Z_i$  and  $Z_t$  are the impedances of the media in front of and behind the metamaterial layer, respectively. The signs in Equations (2.41)-(2.44) have to be chosen in order to fulfill energy conservation, meaning  $Re[Z] \geq 0$  and  $Im[n] > 0$ . This results in unambiguous values for  $Re[Z]$ ,  $Im[Z]$  and  $Im[n]$ .  $Re[n]$  has to be determined by requiring  $n$  to be an analytical, physically reasonable function. Starting with  $m = 0$  for  $\omega \rightarrow 0$  and a positive value for  $Re[n]$  as starting point, this gives us a continuous function for the refractive index. From these values the effective permittivity  $\epsilon = n/Z$  and the effective permeability  $\mu = nZ$  are derived [27]. We note that we choose a “physically reasonable” range for  $Re[n]$ . Strictly speaking, the choice of the arcus-cosine function still is ambiguous and the effective parameter retrieval has to be taken with caution.

### Validity of the Retrieved Parameters

The interpretation of the effective parameters in the optical regime is difficult especially for two-dimensional metamaterials consisting of a single functional layer. Since the derived

values for the material parameters are intrinsic properties of the material, they should not vary with sample thickness  $d$ , *i.e.*, with the number of periods in the  $z$ -direction, otherwise the effective parameters cannot be viewed as effective “bulk” material parameters and the optical response is rather based on (surface) coupling effects than on wave propagation effects in the effective medium. Indeed in the optical regime, there is a strong influence of the number of layers in  $z$ -direction on the effective parameters in experiments owing to strong coupling effects [28, 29]. Therefore it is favourable to fabricate multi-layer metamaterials with a large number of functional layers in propagation direction in order to minimise surface effects [25, 28–30].

Furthermore, effective material parameters exhibiting pronounced resonance behaviour have to be taken with great caution. Large fluctuations in the refractive index may result in an effective wavelength within the material that is on the order of or even smaller than the lattice constant in the  $x$ -,  $y$ - or  $z$ -direction. In this case, strictly speaking, the effective-medium theory is not valid anymore.

### 2.2.3 Negative Refraction

A second possibility to determine the refractive index of isotropic negative-index metamaterials is to evaluate the angle of refraction. For oblique incidence with an angle  $\theta_i$  we can measure the angle of refraction  $\theta_t$  of the emerging light beam and obtain the refractive index of the effective medium using Snell’s law (see Ref. [8]). In contrast to positive-index materials, however, the angle of refraction for a negative-index metamaterial will be negative ( $\theta_t < 0$ ) – hence, the light is refracted to the “wrong” side of the surface normal. To understand this behaviour, we will have a closer look on the field configurations at an interface of a negative-index medium in comparison to a positive-index medium (see Fig. 2.6).

For given effective material parameters we can calculate the complex reflection and transmission coefficients of an electromagnetic wave passing the interface using Fresnel’s equations (2.26)-(2.29).

Figure 2.6 illustrates s-polarised and p-polarised incidence of light onto a positive-index and a negative-index medium, respectively. We clearly observe a negative angle of refraction  $\theta_t$  for light impinging onto a surface to a negative-index medium. Applying the boundary conditions for the E- and the B-fields at the interface of a positive-index material to a negative-index material and taking Maxwell’s equations into account we can derive the orientation of the E- and B-fields as well as the direction of the wavevector and the Poynting vector inside the negative-index material. From

$$n(\mathbf{k}_0 \times \mathbf{E}) = \omega\mu\mu_0\mathbf{H} \quad \text{and} \quad \mathbf{S} = \mathbf{E} \times \mathbf{H}$$

we obtain that the wavevector inside a negative-index medium is antiparallel to the Poynting vector, hence antiparallel to the direction of energy propagation. Taking the material equations into account, we obtain the field configuration plotted in Fig. 2.6. Remarkably, the energy in both vacuum and medium propagates from left to right, while in the negative-index medium the phase velocity is opposite to the propagation direction. Waves showing

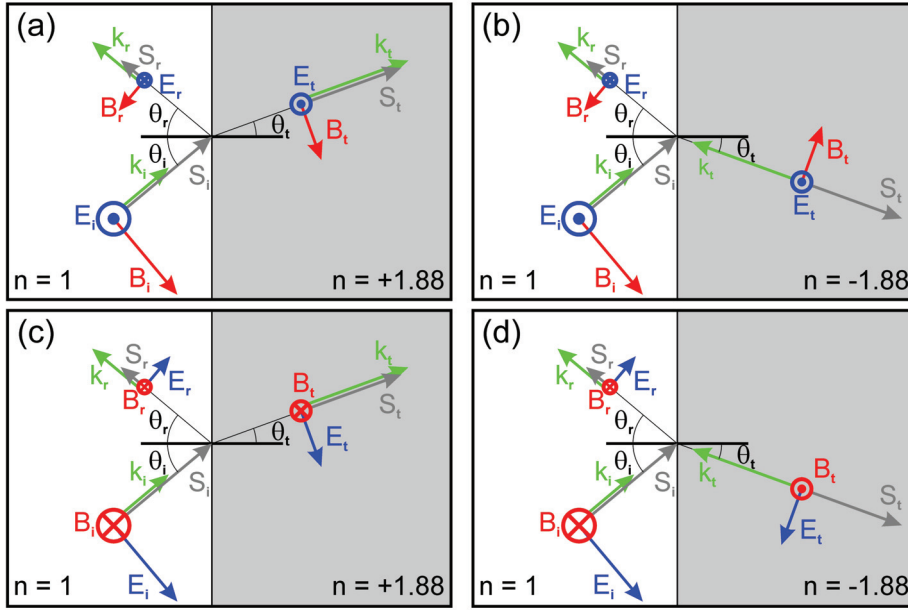


Figure 2.6: Illustration of the propagation characteristics of an electromagnetic wave impinging from vacuum onto a halfspace with refractive index  $n = +1.88$  [(a)+(c)] and  $n = -1.88$  [(b)+(d)] for s-polarised incidence [(a)+(b)] and p-polarised incidence [(c)+(d)], respectively. Remarkably, for the case of a negative refractive index the light beam is refracted to the “wrong side”. Furthermore, the wavevector  $k_t$  is antiparallel to the Poynting vector  $S$  as the tripod of  $k$ ,  $E$  and  $B$  is left-handed.

this behaviour are also referred to as backward waves. Due to the phase-matching condition for the parallel component of the wavevector on both sides of the interface, the wave is refracted to the same side of the surface normal as the incident wave. Thus, a negative angle of refraction  $\theta_t < 0$  with respect to the surface normal results.

Although negative refraction is a consequence of a negative refractive index, it is no sufficient condition. In particular, negative refraction can also be observed [27]

- In anisotropic materials for specific angles of incidence [31–33]
- In photonic crystals due to anomalous dispersion [34, 35]
- In thin metallic films as a negative beam displacement [36, 37]
- In thin dielectric films as a negative beam displacement due to interference effects [27].

Thus, negative refraction must not be mistaken as equivalent to a negative refractive index.

## 2.2.4 Perfect Lens

One very popular candidate for a future application of negative-index metamaterials is the so-called perfect lens, introduced by J. B. Pendry in 2000 [19]. He calculated that a slab of a negative-index material ( $\epsilon = \mu = n = -1$ ) is capable of focussing light emitted from

a point source  $S$  in front of the slab onto an image point  $I$  behind the negative-index slab due to negative refraction (see Fig. 2.7(a)). Pendry also deduced that the evanescent modes of the source are amplified inside the negative-index slab compensating for the exponential decay outside. As a consequence the image at the back side of the negative index slab is a perfect reconstruction of the source at the front. Such a perfect lens allows for subwavelength or even perfect imaging for the ideal case (see Fig. 2.7(b)). In practice, the restoration of

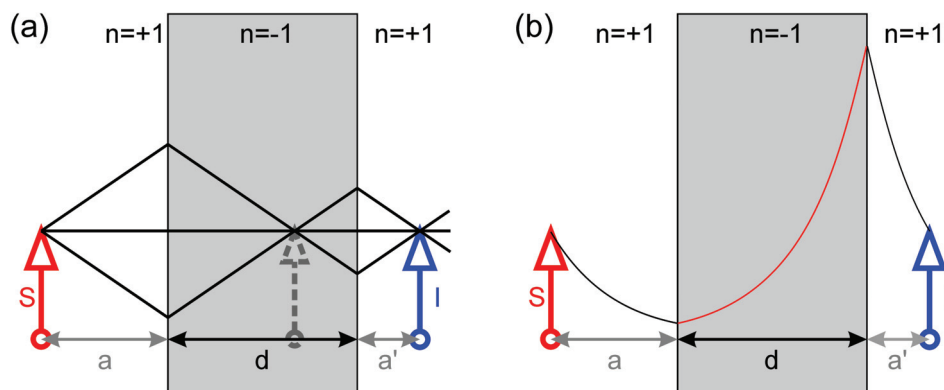


Figure 2.7: (a) Due to negative refraction, light from a source  $S$  in front of a planar negative-index slab ( $n = -1$ ) can be mapped to its image  $I$  behind the slab. Inside the slab an intermediate image is formed. As  $d = a + a'$  has to be fulfilled the optical path  $s = (+1)k_0a + (-1)k_0d + (+1)k_0a'$  is zero. (b) For a perfect lens the large evanescent Fourier components from the source are amplified inside the negative-index slab. This results in a perfect reconstruction of all Fourier components in the image plane, hence a perfect image of the source is obtained [19].

the evanescent fields is unfortunately extremely sensitive to deviations from the ideal case discussed above. Even small losses result in an image resolution that is comparable to normal lenses in the near-field [38]. In order to save at least the idea of a superlens, *i.e.*, a lens with subwavelength resolution in the far-field, Liu *et al* [39] introduced a grating at the back side of the slab in order to transform the evanescent waves emerging from a negative-index slab into propagating modes. An alternative way of breaking the diffraction limit is a magnifying cylindrical hyperlens which makes use of plasmon coupling between close metallic layers to transport the high-frequency Fourier modes of an image to produce a magnified image of a subwavelength object [40, 41].

## 2.3 Maxwell's Equations for Biisotropic and Bianisotropic Media

So far we have limited ourselves to isotropic materials where the electric field components do not couple to the magnetic field components and *vice versa*. The resulting metamaterial designs allow for manipulation of the dispersive behaviour of electromagnetic waves. In particular, negative refraction and perfect lenses result from this approach. If we explicitly account for magnetoelectric cross-coupling in our structure designs, we have to revise the material equations (2.12) and (2.13) and take the polarisation state of light

into consideration. We therefore modify the expressions for the polarisation and the magnetisation in Equation (2.5) and (2.6) in the following way:

$$\mathbf{P}(\mathbf{E}, \mathbf{H}) = \epsilon_0 \bar{\chi}_e \mathbf{E} + \bar{\boldsymbol{\xi}} \mathbf{H} \quad (2.45)$$

$$\mathbf{M}(\mathbf{E}, \mathbf{H}) = \frac{1}{\mu_0} \bar{\boldsymbol{\zeta}} \mathbf{E} + \bar{\chi}_m \mathbf{H} \quad (2.46)$$

and obtain for the constitutive material equations [42]:

$$\mathbf{D} = \epsilon_0 \bar{\boldsymbol{\epsilon}}(\omega) \mathbf{E} + \bar{\boldsymbol{\xi}}(\omega) \mathbf{H} \quad (2.47)$$

$$\mathbf{B} = \bar{\boldsymbol{\zeta}} \mathbf{E} + \mu_0 \bar{\boldsymbol{\mu}}(\omega) \mathbf{H}. \quad (2.48)$$

As Maxwell's equation in general are reciprocal, the coupling coefficient of the electric field component to the magnetic field component  $\bar{\boldsymbol{\xi}}$  and the coupling coefficient for the magnetic field component to the electric field component  $\bar{\boldsymbol{\zeta}}$  have to be directly connected with each other *via* the relation  $\bar{\boldsymbol{\zeta}} = -\bar{\boldsymbol{\xi}}^t$ . The material equations (2.47) and (2.48) consequently read [42]:

$$\mathbf{D} = \epsilon_0 \bar{\boldsymbol{\epsilon}}(\omega) \mathbf{E} + \bar{\boldsymbol{\xi}}(\omega) \mathbf{H} \quad (2.49)$$

$$\mathbf{B} = -\bar{\boldsymbol{\xi}}^t \mathbf{E} + \mu_0 \bar{\boldsymbol{\mu}}(\omega) \mathbf{H}. \quad (2.50)$$

In the most general case a metamaterial is described by the second-rank tensors  $\bar{\boldsymbol{\epsilon}}$ ,  $\bar{\boldsymbol{\mu}}$  and  $\bar{\boldsymbol{\xi}}$ . Depending on the structure of these tensors we can classify the metamaterial with respect to

- Anisotropy:

Only  $\bar{\boldsymbol{\epsilon}}$  and  $\bar{\boldsymbol{\mu}}$  are tensors connecting  $\mathbf{D}$  and  $\mathbf{E}$  fields and  $\mathbf{B}$  and  $\mathbf{H}$  fields, respectively. No magnetoelectric coupling of  $\mathbf{E}$  and  $\mathbf{H}$  fields is present ( $\bar{\boldsymbol{\xi}} = 0$ ). In uni- or biaxial crystals, we can find a diagonal representation of  $\bar{\boldsymbol{\epsilon}}$  and  $\bar{\boldsymbol{\mu}}$ . We therefore obtain, *e.g.*, birefringent materials.

$$\bar{\boldsymbol{\epsilon}} = \begin{pmatrix} \epsilon_{xx} & 0 & 0 \\ 0 & \epsilon_{yy} & 0 \\ 0 & 0 & \epsilon_{zz} \end{pmatrix}, \quad \bar{\boldsymbol{\mu}} = \begin{pmatrix} \mu_{xx} & 0 & 0 \\ 0 & \mu_{yy} & 0 \\ 0 & 0 & \mu_{zz} \end{pmatrix}, \quad \bar{\boldsymbol{\xi}} = \begin{pmatrix} 0 & 0 & 0 \\ 0 & 0 & 0 \\ 0 & 0 & 0 \end{pmatrix} \quad (2.51)$$

- Isotropy:

Isotropic materials are a subclass of anisotropic materials where  $\epsilon$  and  $\mu$  are scalars. The response of the material in any direction of 3D-space is identical.

$$\bar{\boldsymbol{\epsilon}} = \epsilon \begin{pmatrix} 1 & 0 & 0 \\ 0 & 1 & 0 \\ 0 & 0 & 1 \end{pmatrix}, \quad \bar{\boldsymbol{\mu}} = \mu \begin{pmatrix} 1 & 0 & 0 \\ 0 & 1 & 0 \\ 0 & 0 & 1 \end{pmatrix}, \quad \bar{\boldsymbol{\xi}} = \begin{pmatrix} 0 & 0 & 0 \\ 0 & 0 & 0 \\ 0 & 0 & 0 \end{pmatrix} \quad (2.52)$$

- Bianisotropy:

Bianisotropy is the most general case including magnetoelectric coupling. All material

parameters are tensors. For simplicity  $\epsilon$  and  $\mu$  are often assumed to be scalars as the essence of bianisotropic media lies in the parameter  $\bar{\xi}$ .

$$\bar{\epsilon} = \epsilon \begin{pmatrix} 1 & 0 & 0 \\ 0 & 1 & 0 \\ 0 & 0 & 1 \end{pmatrix}, \quad \bar{\mu} = \mu \begin{pmatrix} 1 & 0 & 0 \\ 0 & 1 & 0 \\ 0 & 0 & 1 \end{pmatrix}, \quad \bar{\xi} = \begin{pmatrix} \xi_{xx} & \xi_{yx} & \xi_{zx} \\ \xi_{xy} & \xi_{yy} & \xi_{zy} \\ \xi_{xz} & \xi_{yz} & \xi_{zz} \end{pmatrix} \quad (2.53)$$

- **Biisotropy:**

Biisotropic (reciprocal) media are a subclass of bianisotropic materials. They are also referred to as Pasteur media or chiral media as they are capable of rotating the polarisation plane of incident light. Here, all material parameters  $\epsilon$ ,  $\mu$  and  $\xi$  are scalars for 3D-biisotropy.

$$\bar{\epsilon} = \epsilon \begin{pmatrix} 1 & 0 & 0 \\ 0 & 1 & 0 \\ 0 & 0 & 1 \end{pmatrix}, \quad \bar{\mu} = \mu \begin{pmatrix} 1 & 0 & 0 \\ 0 & 1 & 0 \\ 0 & 0 & 1 \end{pmatrix}, \quad \bar{\xi} = \xi \begin{pmatrix} 1 & 0 & 0 \\ 0 & 1 & 0 \\ 0 & 0 & 1 \end{pmatrix} \quad (2.54)$$

To determine the propagation behaviour of a plane wave in a specific medium given by the material parameters above, we insert the corresponding equations into Maxwell's equations (2.1)-(2.4) and calculate the corresponding wave equation. For isotropic, uniaxial and biaxial (anisotropic) natural crystals the corresponding wave equation is characterised by linear polarisation eigenstates oriented parallel to the crystal axes. In general, however, the polarisation eigenstates are elliptical.

In this Thesis we will discuss biisotropic or chiral metamaterials like, for example, an array of chiral twisted-crosses [43] or twisted split-ring resonators [44]. Following the aforementioned reasoning we want to determine the wave equation, the polarisation eigenstates and the effective material parameters of the chiral medium. For chiral materials we consequently have to include magnetoelectric coupling, which we intentionally neglected so far. Coupling of the electric and magnetic field components can be achieved by coupling of plasmonic modes in metal nanoparticles. The next chapter therefore focusses on the optical response of metal nanoparticles – the main ingredient of (chiral) metamaterial structures.



## Chapter 3

# Optics of Metal Nanoparticles

Up to now the raw material for nearly every scientist working in the field of metamaterials is either gold or silver. Especially gold, being a noble metal standing out by its good conductivity and general resistance to oxidation and corrosion is a widespread material not only used for electrical contacts or jewelry. In the vast field of plasmonics gold is used to a great extent to investigate plasmonic properties of structures like nanospheres, -holes, -wires, -gratings, perforated thin films, grooves or waveguides, for instance.

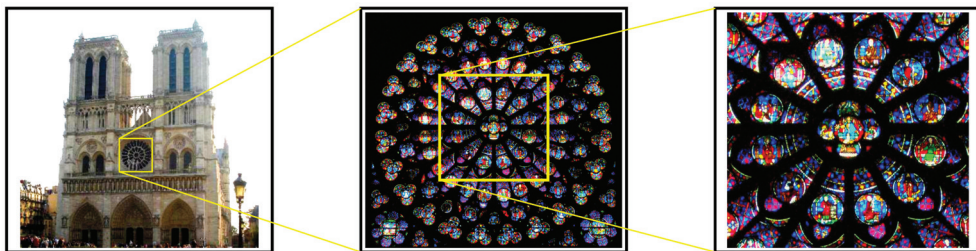


Figure 3.1: Picture of the cathedral “Notre Dame de Paris” (left) and its 12-m rose window (middle) fabricated with stained glasses. The picture on the right-hand side shows a close up of the center of the rose window. The large variety of colours of stained glasses can be attributed to the different sizes of the metal nanoparticles and the density of the particles in the glass.

It is therefore of particular interest to understand the optical response of gold films and of simple gold nanoparticles. This chapter is meant to give a short introduction to plasmonics with a focus on the optical response of arrays of gold nanoparticles in analogy to arrays of “artificial atoms” in metamaterials. We start from the analytical modelling of gold as a Drude metal and go on to the description of the optical response of gold nanoparticles in the scope of Mie theory, where spherical gold nanoparticles can have several plasmonic excitation modes. Due to the lack of analytical solutions for more complex particle shapes we will introduce the electrostatic approximation to derive the (dipole) response of ellipsoidal particles. Finally, we want to introduce the so-called split-ring resonator (SRR) and the cut-wire pairs, two basic structure designs for metamaterials exhibiting a resonant behaviour of the magnetic susceptibility.

### 3.1 Drude Model

The desire to tailor the optical response of manmade materials (see Fig.3.1) requires effective coupling of the electromagnetic field to the underlying structures. This goal can be achieved by the use of highly conductive materials like metals. In typical metals the high electric conductivity can be attributed to small numbers of electrons located in the outermost atomic s-orbital. Due to their very low ionisation energy ( $< 10$  eV) the wavefunctions of these (conduction-band) electrons are extended over the whole (ion) lattice and form a plasma of delocalised electrons also known as free electron gas.

This concept was first introduced by Paul Drude at the end of the 19th century. The so-called Drude model is based on his view on metals as a classical gas of electrons performing a diffusive motion [3]. In this sense, the optical response, *i.e.*, the dielectric function of a Drude metal can be described as a collective motion of the free electron gas against a fixed background of positive ion cores.

In the following simple *ansatz* we assume negligible electron-electron interaction (independent-electron approximation) and electron-ion interactions (free-electron approximation). The basic equation of motion for one electron driven by an external electric field is then given by:

$$m\ddot{\mathbf{x}} + m\gamma\dot{\mathbf{x}} = -e\mathbf{E} \quad (3.1)$$

where  $m$  is the electron's effective mass and  $\gamma$  is the damping of the system. Here, the damping owing to the radiation reaction force given by the Abraham-Lorentz formula is assumed to be small [45]. An oscillating incident light field  $\mathbf{E}(t) = \mathbf{E}_0 e^{-i\omega t}$  then causes an oscillation of the conduction-band electrons  $\mathbf{x}(t) = \mathbf{x}_0 e^{-i\omega t}$  and consequently results in a complex amplitude and a complex macroscopic polarisation given by

$$\mathbf{P} = -ne\mathbf{x} = -\frac{ne^2}{m(\omega^2 + i\gamma\omega)}\mathbf{E}. \quad (3.2)$$

We insert this result into

$$\mathbf{D} = \epsilon_0\mathbf{E} + \mathbf{P} = \epsilon_0 \left( 1 - \frac{ne^2}{m\epsilon_0(\omega^2 + i\gamma\omega)} \right) \mathbf{E} \quad (3.3)$$

and identify the linear macroscopic permeability of a Drude metal

$$\epsilon(\omega) = \left( 1 - \frac{\omega_{pl}^2}{\omega^2 + i\gamma\omega} \right), \quad (3.4)$$

where  $\omega_{pl}^2 = ne^2/\epsilon_0 m$  is the plasma frequency. In realistic metals, however, we also have to take account for the interband transitions of bound electrons which additionally contribute to the dielectric function. They result in an increase of the imaginary part of the metal's dielectric function at the corresponding resonance wavelengths on the one hand. On the other hand, the real part of the dielectric function is influenced even for wavelengths above the interband transitions [46]. Hence, for visible or near-infrared light above the interband resonances, an additional background dielectric constant is used.

$$\epsilon(\omega) = \left( \epsilon_\infty - \frac{\omega_{pl}^2}{\omega^2 + i\gamma\omega} \right) \quad (3.5)$$

In 1972 J. B. Johnson and R. W. Christy [47] measured the optical constants for selective noble metals, namely gold, silver and copper, from transmittance and reflectance measurements of thin films of 18.5 – 50 nm thickness. They also stated that only for film thicknesses above 25 nm the values for the refractive indices is independent of the film thickness. The left-hand side of Fig. 3.2 shows a Drude fit to the experimental data from

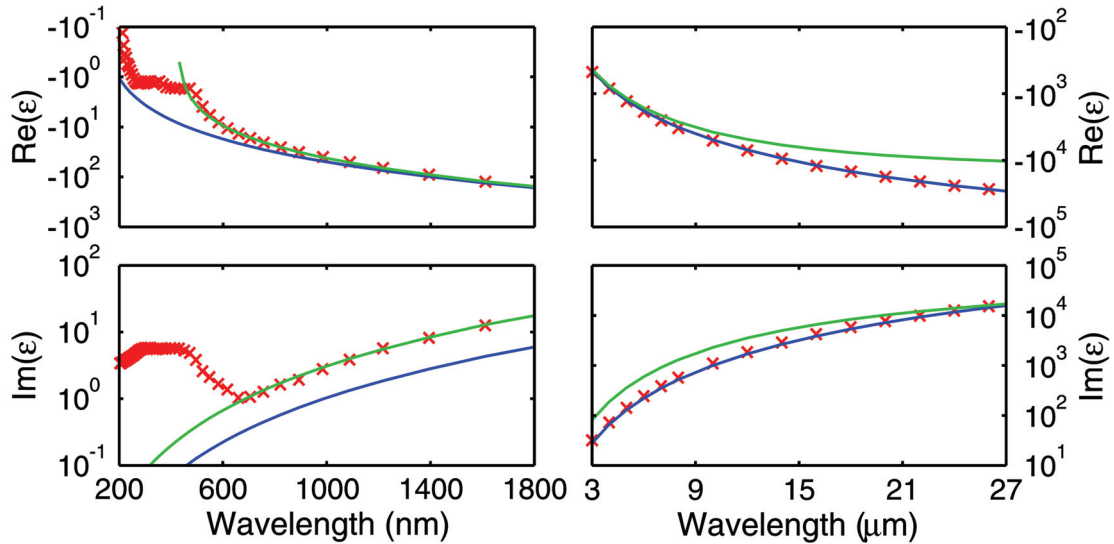


Figure 3.2: Experimental data (red crosses) for the dielectric function of gold measured by Johnson and Christy [47] on the left-hand side and by Bennett and Bennet [48] on the right-hand side. Two exemplary Drude fits are plotted in green (fit to the Johnson Christy data) and blue (fit to the Bennett data). The Drude parameters for the VIS/NIR-fit (green) are  $\epsilon_\infty = 9.0685$ ,  $\omega_p = 2\pi \cdot 2163$  THz,  $\gamma = 2\pi \cdot 19$  THz and for the far-IR (blue)  $\epsilon_\infty = 1$ ,  $\omega_p = 2\pi \cdot 2176$  THz,  $\gamma = 2\pi \cdot 6$  THz.

the visible (VIS) to near-infrared (NIR) spectral range for gold at  $\lambda = 200 - 1800$  nm [47]. For comparison, far-infrared data ( $\lambda = 3 - 32$   $\mu\text{m}$ ) [48] of the permittivity of gold are plotted on the right-hand side. The data for the VIS/NIR spectral range from Ref. [47] and the above Drude fit to these data are taken as initial values for the gold's dielectric function used in the numerical calculations to the experiments. Nevertheless, this initial parameter set is a first approximation and may change to some extent as surface roughness and impurities change the gold quality and influence the damping and the plasma frequency of the Drude metal. Furthermore, the spectral position of the metamaterial structures has to be taken into account when modelling the Drude parameters, as for higher frequencies lying closer to the interband transitions of gold at about 600-nm-wavelength, the experimental data differ from the far-infrared Drude behaviour. In particular, we have to introduce a background dielectric constant  $\epsilon_\infty$  and adapt the plasma frequency to take account for the interband transitions (see Equation (3.5)). The actual Drude parameters in the numerical calculations of the metamaterial structures fabricated in this Thesis are chosen to get the best agreement between numerical and experimental data.

Despite the great problem of oxidation, the most prominent alternative to gold is silver because of its lower losses and higher conductivity. However, we use gold to avoid the problem of oxidation in order to preserve the quality of the optical spectra.

## 3.2 Mie Theory

When we now go on from closed metal films to arrays or solutions of metal particles, we enter a colourful world, fascinating the people for ages – starting in the Roman era in the 4th century *AD* when the famous Lycurgus cup was fabricated and culminating in the Middle Ages where stained glass was used for gothic church windows like in the famous 12-m rose window of the cathedral “Notre Dame de Paris” (built from 1163 to 1345, see Fig.3.1). To fabricate such an astonishing piece of work, the craftsmen added different metallic salts during fabrication of the small coloured glass elements. Though, up to the beginning of the 20th century a sound explanation for the occurrence of the large variety of colours proved to be very difficult despite the fact that the fabrication process has been quite well understood [15]:

*“...on the manufacture of gold and copper ruby glasses and of silver glass, the gold or copper or silver is mixed with the other ingredients of the glass before the first firing. If, when the glass is formed in a furnace, the whole be quickly cooled, the glass with the metal in it is colourless and exactly resembles real glass. ... when the glass is re-heated the metal ‘crystallises out of solution’ ... and appears in the small particles ... These particles of metal ... account for the colour of the glass.”*

The rich variety of coloured stained glasses actually has its foundations in plasmonic excitations. For a consistent description of this phenomenon, however, it is not sufficient to account for electric-dipole interactions amongst the metal nanoparticles alone, as Maxwell-Garnett assumed [15]. The actual dimensions of the metal particles have to be taken into consideration as well. Hence, one has to solve Maxwell’s equations for the interaction of a single spherical nanoparticle with an incident electromagnetic field without any approximation as a first step. This was done by Gustav Mie in 1908 for spherical metal particles in strongly diluted colloidal metal solutions [49]. The essence of his approach is that the collective excitation of the electrons at the surface of a particle owing to an electromagnetic field cannot be assumed to be a mere dipole oscillation for particles larger than 20 nm anymore. The optical response of a spherical metal nanoparticle is more accurately described by a multipole expansion including higher-order excitation modes. For larger particles, the higher-order multipole moments rapidly gain in importance (see Ref. [20]) and result in a resonance shift with the size of the gold particles. The collective excitations of the conduction-band electrons (see Fig. 3.3) are named localised surface plasmons, particle plasmons or Mie resonances.

Combining the two ideas of Maxwell-Garnett and Mie, a great part of the colourful world of metal glasses could finally be demystified at the beginning of the 20th century.

## 3.3 Optical Response of Metallic Nanoparticles

In practice, however, especially when talking about metamaterials a spherical metal particle is rather the exception to the rule. Consequently, the expansion of Mie theory to ellipsoidal particles would be the next ingredient for the design of metamaterials. Unfortunately, there

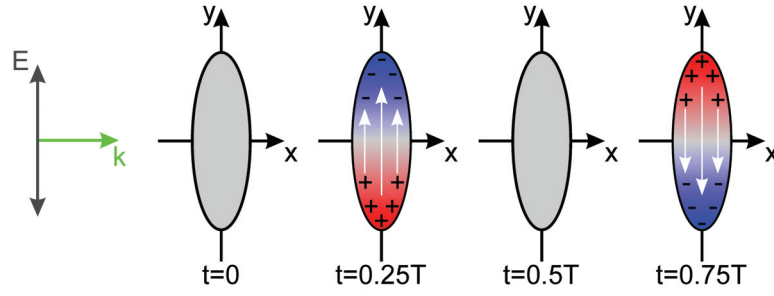


Figure 3.3: The collective displacement of the free electrons against the positive background due to the incident light field is sketched for an ellipsoid particle at times  $t = 0, 0.25T, 0.5T, 0.75T$ . The restoring force of the depolarisation field points in the opposite direction to the applied field. This results in an oscillation of the free electrons with respect to the fixed positive background charge.

is no rigorous analytical solution to the problem of an ellipsoidal metal particle interacting with an electromagnetic field. We therefore have to go one step back again and calculate the resonance behaviour of a metal ellipsoid neglecting higher excitation modes than the electric-dipole resonance (see Fig. 3.4). If the particle's dimensions are much smaller than the wavelength of light, we can solve the problem of an ellipsoidal metallic particle exposed to a homogeneous electric field [50]. We consequently discard retardation effects and assume that the response of the particle to an applied electric field is that of an electric dipole described by

$$\mathbf{p} = \epsilon_m \bar{\alpha} \mathbf{E} \quad , \quad \bar{\alpha} = \begin{pmatrix} \alpha_x & 0 & 0 \\ 0 & \alpha_y & 0 \\ 0 & 0 & \alpha_z \end{pmatrix}. \quad (3.6)$$

This approach is also known as the electrostatic approximation. The surface of the ellipsoid shown in Fig. 3.4 is given by:

$$\frac{x^2}{r_x^2} + \frac{y^2}{r_y^2} + \frac{z^2}{r_z^2} = 1, \quad (3.7)$$

where  $r_x$ ,  $r_y$  and  $r_z$  are the principal axes of the ellipsoid. If an electric field is applied parallel to one of its principal axes, the polarisability in this direction is given by:

$$\alpha_i = \frac{4}{3} \pi r_x r_y r_z \frac{\epsilon(\omega) - \epsilon_m}{\epsilon_m + L_i (\epsilon(\omega) - \epsilon_m)} \quad (3.8)$$

with

$$L_i = \frac{r_x r_y r_z}{2} \int_0^\infty \frac{1}{(r_i^2 + q) \sqrt{(r_x^2 + q)(r_y^2 + q)(r_z^2 + q)}} dq \quad (3.9)$$

where  $\epsilon_m$  is the dielectric constant of the surrounding environment,  $\epsilon(\omega)$  is the permittivity of the metal and  $L_i$  are geometrical factors describing the proportion of one axis with respect to the other two. Therefore only two axes are independent and

$$\sum_i L_i = 1. \quad (3.10)$$

In order to make predictions about the spectral positions of the resonances one has to

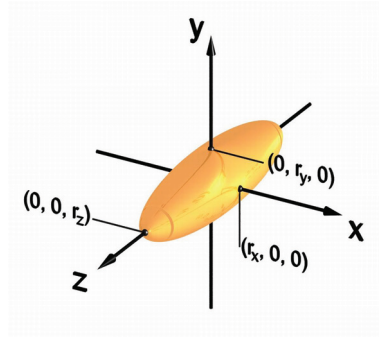


Figure 3.4: Illustration of an ellipsoidal gold particle with its minor and major axes in the  $x$ -,  $y$ - and  $z$ -direction, respectively.

maximise the polarisability, *i.e.*,  $|\epsilon_m + L_i(\epsilon(\omega) - \epsilon_m)|$  has to be minimised. For small imaginary parts of  $\epsilon(\omega)$  and  $\epsilon_m$  this results in the following condition for  $\epsilon(\omega)$  for each of the axes:

$$\epsilon(\omega) = \epsilon_m \left( 1 - \frac{1}{L_i} \right) \quad (3.11)$$

Since  $L_i < 1$ , Equation (3.11) can only be fulfilled for metals below the plasma frequency. Finally, the resonance frequency can be derived with the help of the dispersion relation of gold, for instance (see Fig. 3.2). Furthermore we can deduce a set of very simple “rules of thumb” for designing and interpreting the optical spectra of metal nanostructures (see Ref. [20]):

1. An increase of  $\epsilon_m$ , *i.e.*, of the refractive index of the surrounding medium, leads to a decrease of the resonance frequency and *vice versa*.
2. If the particle is elongated along the axis parallel to the incident polarisation the particle’s resonance is red-shifted.
3. If the particle is elongated along the axis perpendicular to the incident polarisation the resonance is blue-shifted.

This description of the optical response of an ellipsoidal metal nanoparticle can serve as starting point for qualitative statements on the resonance behaviour of even more complex metallic nanostructures. Nevertheless, we have to keep in mind that according to Mie theory [49] the use of the electrostatic approximation for particles larger than about 20 nm has to be taken with caution. In Chapter 5.2.3 we will see that retardation effects indeed play a crucial role in metamaterial designs.

### 3.4 Magnetic Response of Split-Ring Resonators

A solution of small spherical gold nanoparticles that can be described by effective-medium theory [15] is, in principle, a very simple kind of metamaterial as we are able to influence the (resonant) absorption and scattering behaviour by varying the particle size and the density of

the particles, for example. Thus, if we can define the actual shape of a metal nanoparticle, we will have the tools for manipulating both the dispersive and the polarisation behaviour on a higher level than “only” absorption and scattering.

Pendry’s design proposal of a cylindrical coil with a single slit [5] was the successful attempt to influence the effective magnetic response of a metallic structure. The functionality of this split-ring-resonator (SRR) design is based on the simple idea of a circulating ring current generating a magnetic-dipole moment perpendicular to the SRR. Provided we have a closed ring in which the current can flow we are only able to couple to the magnetic-dipole moment *via* the magnetic field. In order to efficiently couple to the ring current *via*

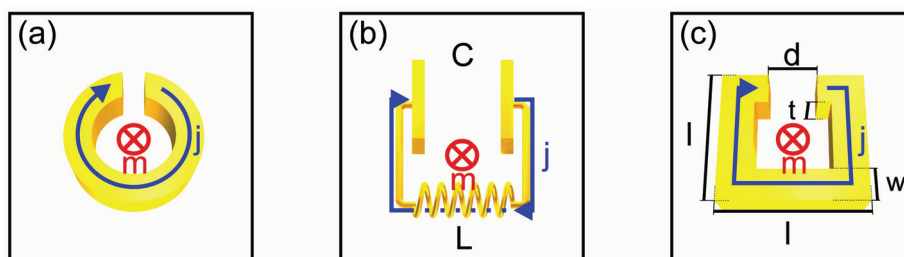


Figure 3.5: The split-ring resonator designs in (a) [12] and (c) [51, 52] can be viewed as a resonant LC-circuit (b) with a capacitance  $C$ , an inductance  $L$  and damping  $R$ . From this model the magnetic response of a split-ring resonator (c) can be calculated from Equation (3.15) with the parameters given in (c).

the electric field [53] one has to introduce a capacitance into the structure design. This is done by the small slit in the cylinder (see Fig. 3.5(a)). According to Ref. [53] this results in two possibilities to induce a circulating current – one *via* the incident magnetic field perpendicular to the SRR (Fig. 3.6(a),(b)) and the other one *via* an incident electric field parallel to the gap-bearing side of the SRR (Fig. 3.6(b)+(c)). For both cases, the SRR can be seen as a small LC-circuit, where the ring represents the inductance and the ends of the ring form the capacitance (see Fig. 3.5(b)). For an LC-circuit one expects a resonant behaviour of the underlying currents and consequently an enhanced magnetic moment at the resonance frequency  $\omega_{LC}$ . If we use a simplified version of the SRR as shown in Fig. 3.5(c), the standard formula for the capacitance of a plate capacitor

$$C = \epsilon_0 \epsilon \frac{wt}{d} \quad (3.12)$$

and for the inductance of a long coil with only one winding

$$L = \mu_0 \frac{l^2}{t} \quad (3.13)$$

can be used to estimate the resonance frequency of the SRR

$$\omega_{LC} = \frac{1}{\sqrt{LC}} = \frac{1}{l} \frac{c_0}{\sqrt{\epsilon}} \sqrt{\frac{d}{w}}. \quad (3.14)$$

Equation (3.14) implies that any resonance wavelength can be obtained by scaling down

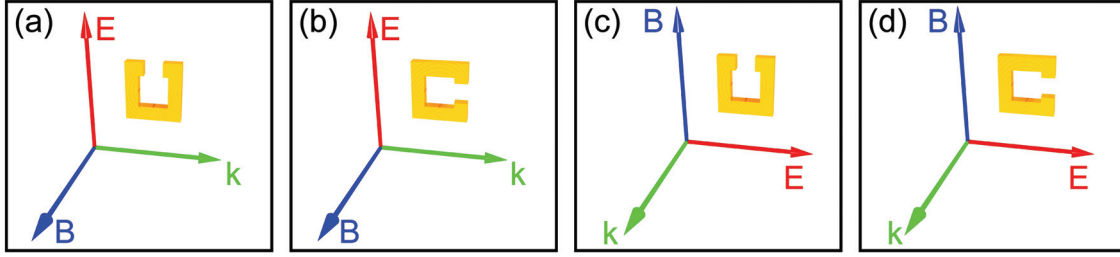


Figure 3.6: Depending on the orientation of the split-ring resonator with respect to the incident fields the electromagnetic wave couples to the magnetic oscillation mode *via* the B- (a) and the E-field (c) only or both field components can couple to the magnetic mode (b). In (d) only the higher-order electric modes can be excited.

the structure dimensions. Indeed, the experimental values of the resonance wavelengths of the SRR have steadily decreased from 30 mm [8], *via* 300  $\mu\text{m}$  [54], 50  $\mu\text{m}$  [55], 3.2  $\mu\text{m}$  [51], 1.5  $\mu\text{m}$  [56, 57], 900 nm [52] down to 500 nm [58]. However, there is a limit to size scaling when the finite kinetic energy of the electrons, the ohmic losses and the radiative losses in the metal gain in importance [52, 59, 60]. As a consequence, further feature-size reduction will hardly reduce the resonance frequency.

The LC-circuit model of an SRR provides a very good estimate for the resonance frequency condition, as long as the ohmic currents dominate over the displacement currents. This is fulfilled if the slit width is small. Finally, the magnetic response from the coupled capacitance and inductance of the SRR can be derived and we get a Lorentz-like behaviour for the magnetic permeability  $\mu$  [61]

$$\mu(\omega) = 1 + \frac{F\omega^2}{\omega_{LC}^2 - \omega^2 - i\gamma\omega}, \quad (3.15)$$

where  $F$  is the filling fraction of the unit cell ( $0 < F \leq 1$ ) and  $\gamma$  is the damping due to ohmic and radiative losses. Due to the presence of the slit in the SRR, an applied electric field excites an electric polarisation as well, resulting in an effective permittivity which can be written as [60]

$$\epsilon(\omega) = 1 + \left(\frac{dc_0}{l^2}\right)^2 \frac{F}{\omega_{LC}^2 - \omega^2 - i\gamma\omega}. \quad (3.16)$$

The ability to excite a magnetic-dipole moment by an incident electric field is the manifestation of magnetoelectric coupling in the SRR (see Fig. 3.7). Consequently, the SRR is, strictly speaking, a bianisotropic design [62, 63] although this aspect is often assumed to play a minor role [26] or even not accounted for (see [5, 12, 24], for example). If one accounts for bianisotropy, the material equations (see Chapter 2.3) are given by Equation (2.49) and Equation (2.50) and the bianisotropy parameter can be calculated to [61]

$$\bar{\xi}(\omega) = - \left(\frac{dc_0}{l^2}\right) \frac{F\omega}{\omega_{LC}^2 - \omega^2 - i\gamma\omega} \cdot \begin{pmatrix} 0 & 1 \\ -1 & 0 \end{pmatrix}. \quad (3.17)$$

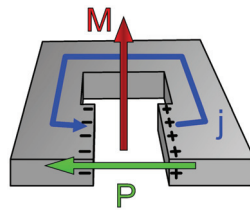


Figure 3.7: Coupling of an electromagnetic wave to the magnetic mode of a split-ring resonator. The induced current ( $j$ ) always results in a polarisation ( $P$ ) and a magnetisation ( $M$ ) due to the presence of the slit. Hence, the electric and magnetic field components are coupled *via* the split-ring resonator.

### Plasmonic View on the Split-Ring Resonator

So far we had a look at an analytical model for the excitation of a magnetic resonance in terms of the LC-circuit model. Actually, when investigating the response of an SRR, there are additional excitation modes that can only be explained in the plasmonic picture [64].

In the previous section we have investigated the plasmonic properties of ellipsoidal metal nanoparticles [50]. An incident electromagnetic wave excites a plasmonic mode (particle plasmon) with a resonance frequency depending on the shape of the particle. If we now simply bend the two ends of a very long ellipsoidal particle by  $90^\circ$ , for example, we end up with the SRR design depicted in Fig. 3.5(c). Indeed, the SRR's higher modes are similar to the modes of a straight antenna (see Fig. 3.8):

- The fundamental “magnetic” mode for which half the wavelength fits the length of the antenna (Fig. 3.8(a)), can be identified as the magnetic mode exhibiting a circulating current distribution in the SRR.
- The second “vertical electric” mode is obtained when one wavelength fits the length of the antenna. In the SRR, the currents in the two arms are parallel to each other (Fig. 3.8(b)).
- The third “horizontal electric” plasmon mode is obtained when three half-wavelengths of the incident light match the length of the antenna. Here, the currents in the arms of the SRR are antiparallel (Fig. 3.8(c)) giving rise to a weak magnetic response as well [57]. In this case, however, no circulating ring current is formed in contrast to the fundamental mode.

The current patterns for the three modes can all be related to electric-dipole moments, while only the fundamental mode gives rise to a significant magnetic-dipole moment perpendicular to the current distribution. The third mode also shows a weak magnetic response, that can be excited for oblique incidence [57]. Exemplary calculations of the transmittance and reflectance spectra of an array of split-ring resonators according to Ref. [51] are shown in Fig. 3.9.

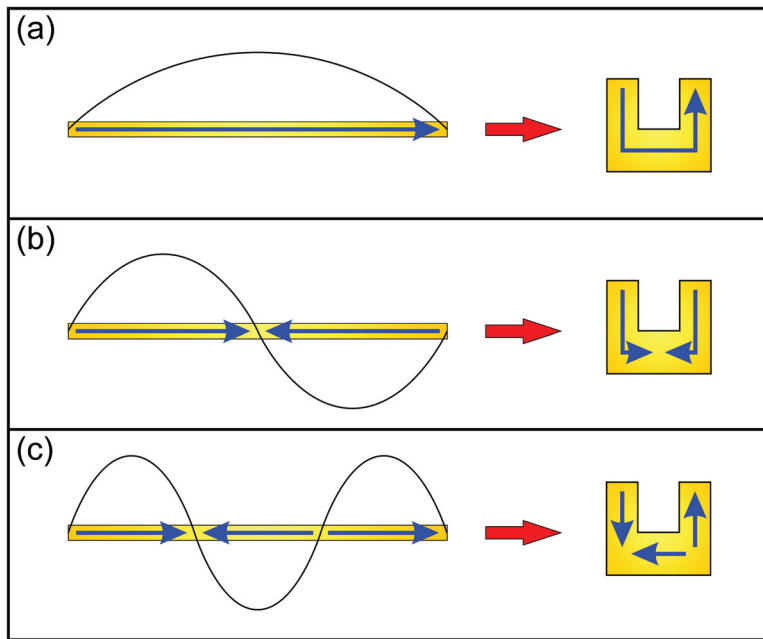


Figure 3.8: Comparison of the first three excitation modes (a)-(c) of a straight plasmonic antenna (left-hand side) and of a metallic split-ring resonator (right-hand side). The thin black lines visualise the excitation modes in the antenna giving rise to the (blue) current distributions (on the left). The equivalent current distributions of the split-ring resonator are plotted (in blue) on the right. The first excitation mode is the so-called fundamental “magnetic” mode, the second is the “vertical electric” and the third is the “horizontal electric” mode.

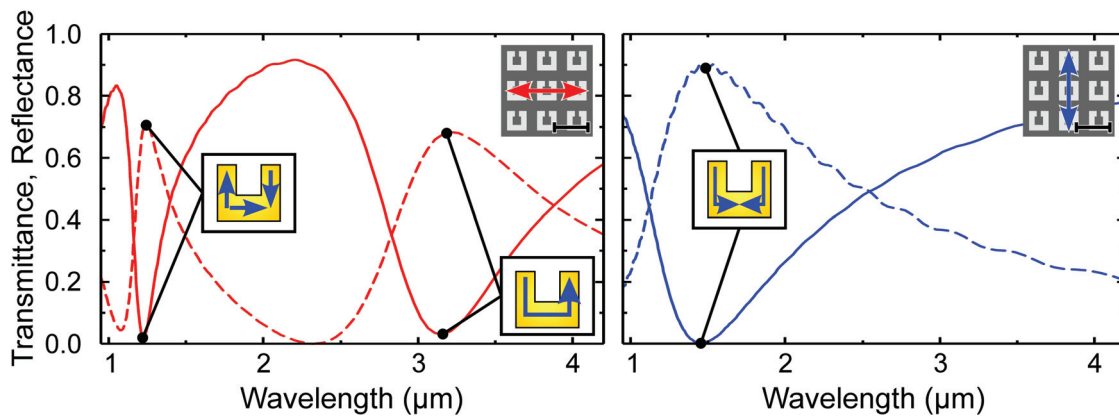


Figure 3.9: Exemplary transmittance (solid) and reflectance (dashed) spectra for an array of split-ring resonators. Normal-incidence view on the structure is shown in the insets. The scalebar is 500 nm, the incident E-field vector is indicated as red/blue arrow. The underlying current distributions of the different resonant plasmon modes is visualised in the spectra. Only for horizontal incidence (lhs in red) the fundamental (magnetic) resonance of the split-ring resonators can be excited.

### 3.5 Magnetic Response of Cut-Wire Pairs

For physical reasons the SRR can hardly be operated at visible frequencies [52, 59]. In particular, the displacement currents gain more and more importance for the magnetic properties at high (visible) frequencies [65]. An alternative to the SRR as a “magnetic atom” is the so called cut-wire pair, proposed Lagarkov *et al.* [66] and Podolskiy *et al.* [6, 67]. In the cut-wire pairs, the displacement currents play a major role for the formation of a ring current. This makes them a more favourable design for operation at visible frequencies. Furthermore, from the fabrication point of view, smaller feature sizes of the cut-wire pair design are possible and consequently higher operation frequencies as well.

#### Coupled Plasmon Resonances

The cut-wire pair can be considered as a coupled system of two electric dipoles, in particular of the two fundamental particle plasmons of the two wires (see Fig. 3.10). As a result there are two eigenmodes – a symmetric (high-frequency) mode, where the two particle plasmons oscillate in phase and an antisymmetric (low-frequency) mode, where both plasmons oscillate with opposite phase. Owing to the displacement current in the space between the two wire ends, the antisymmetric mode exhibits a circular current distribution and therefore produces a magnetic response. It is important to notice that in the case of the cut-wire

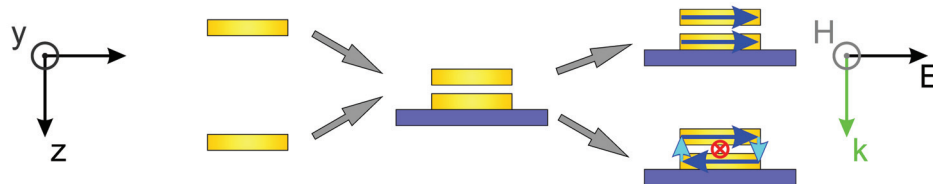


Figure 3.10: When combining two single metallic wires (left) to form a cut-wire pair (middle) the particle plasmons of the individual wires couple and two modes arise – a symmetric electric mode (upper right) and an antisymmetric magnetic mode (lower right, magnetic moment is plotted in red). Including the displacement currents between the end of the wires (light blue), the antisymmetric mode shows a ring current (dark and light blue arrows). The incident plane wave is indicated on the right-hand side of the figure.

pair, retardation effects are of major importance, as for a purely symmetric case (symmetric geometry in the electrostatic approximation) only the symmetric mode can be excited by an incident electromagnetic field. In Chapter 5.2.3 we will further investigate the influence of retardation effects on metamaterials. Exemplary calculations of the transmittance and reflectance spectra of an array of cut-wire pairs following Ref. [68] are shown in Fig. 3.11.

The ability to excite a magnetisation by an incident electric field and a polarisation by an incident magnetic field *via* coupling of particle plasmons makes the SRR and the cut-wire pairs very interesting and versatile structure designs for metamaterial unit cells. Indeed the fundamental aspects of the two designs can be identified in all chiral and non-chiral metamaterials presented in this Thesis.

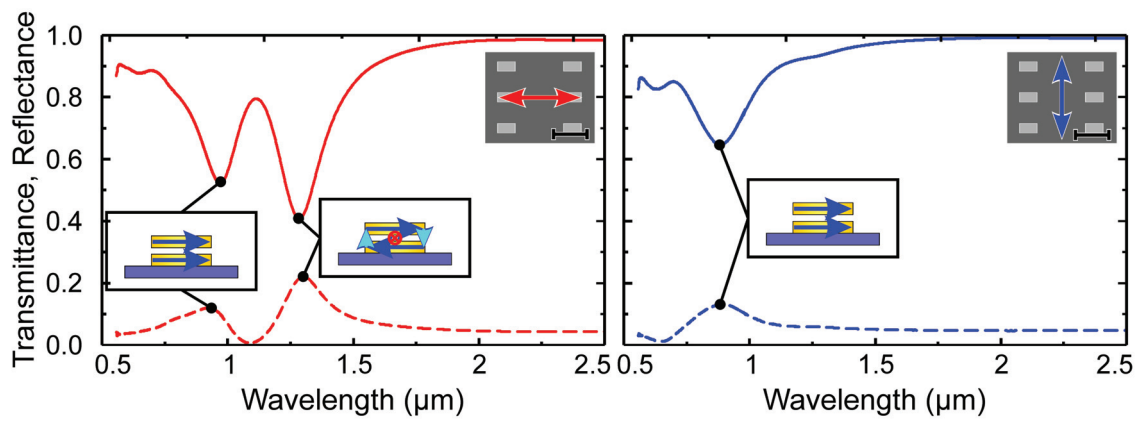


Figure 3.11: Exemplary transmittance (solid) and reflectance (dashed) spectra for an array of cut-wire pairs. Normal-incidence view on the structure is shown in the insets. The scalebar is 500 nm, the incident E-field vector is indicated as red/blue arrow. The underlying current distributions of the different resonant plasmon modes is visualised in the spectra.

# Chapter 4

## Methods

In the following sections we will present the fabrication techniques as well as the optical characterisation methods for a typical metamaterial sample. In general, there are various ways for obtaining metamaterial structures. A brief overview can be found in Ref. [69]. The metamaterials presented in this Thesis, have all been fabricated by electron-beam lithography (EBL) – a technique that provides the possibility to fabricate nanoscale 2D-mask patterns in a (positive) photoresist using a scanning-electron microscope (SEM) whose electron-beam is deflected according to a predefined design pattern. After metallisation by electron-beam evaporation and a subsequent lift-off process the 2D-photoresist mask is converted into the desired metallic metamaterial structure (see Section 4.1). The SEM then gives us the

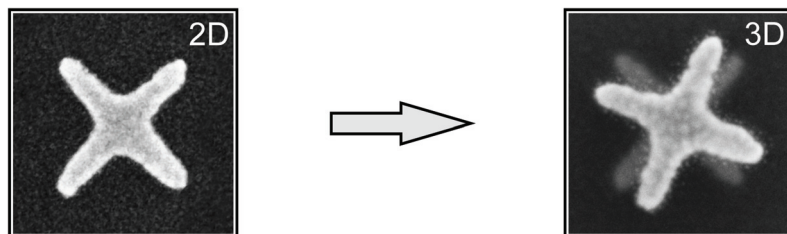


Figure 4.1: SEM images of a planar single-layer cross (left-hand side) fabricated by a standard electron-beam lithography technique. For the bi-layer twisted crosses shown on the right-hand side a specific two-step lithography procedure with an intermediate planarisation step was developed (see Section 4.1.3).

opportunity to characterise the geometry of the final metamaterial structures with respect to structure quality and structure dimensions down to an accuracy of several nanometers. Electron-beam lithography, however, inherently limits our possibilities to two-dimensional metamaterial designs like the single-layer cross shown on the left-hand side in Fig. 4.1. In order to obtain multi-layer chiral metamaterials (right-hand side of Fig. 4.1) a two-step EBL process with an intermediate planarisation step has to be developed. This procedure is presented in Section 4.1.3.

For the optical characterisation of our metamaterial samples we use two setups. The home-built transmittance setup presented in Section 4.2.1 is used to measure the circular- and linear-transmittance spectra in the spectral range from 500-nm to 2.2- $\mu\text{m}$ -wavelength (VIS-setup). In addition, this setup offers the possibility to perform angle-resolved

transmittance measurements for angles of up to  $\pm 45^\circ$  with respect to the surface normal. For circular transmittance measurements in the infrared (2.5- $\mu\text{m}$  to 7- $\mu\text{m}$ -wavelength) we use the commercial Fourier-transform microscope spectrometer (FTIR-setup) described in Section 4.2.2.

## 4.1 Fabrication

Electron-beam lithography requires a scanning-electron microscope (SEM) in combination with a computer-controlled beam-deflection unit to be able to expose a photoresist with predefined patterns. In the SEM, the electrons emitted from an electron source are accelerated and focussed onto an image plane by electric and magnetic lenses. With the help of a beam blanker, inserted at the first image plane, we can switch the electron beam on and off. Behind the image plane the beam size can be adjusted by several apertures, which determine the maximum resolution of the image. Then, the beam is focussed onto the specimen where both the (back) scattered high-energy electrons and the lower-energy secondary electrons can be detected. An additional beam-deflection unit scans the electron beam over the sample and provides a grayscale image of the scanned sample area (see, *e.g.*, Fig. 4.1).

Making use of the SEM's functionality, we can also expose a photoresist which is sensitive to high-energy electrons in order to literally write arbitrary two-dimensional shapes with a maximum resolution of several nanometers. For this purpose, the beam deflection unit and the beam blanker are attached to a high-speed pattern generator controlled by a CAD software.

Unfortunately, the maximum writing resolution is not simply given by the smallest achievable spot size of the electron beam. Owing to the generation of secondary electrons the resist on the substrate is also exposed in the proximity of the scanned pattern and fine features cannot be resolved anymore. This proximity effect results in a decrease of the maximum writing resolution to values of approximately 10 – 20 nm. Additionally, aberrations occur when the beam is focussed and deflected from the optical axis. In particular, the electron beam becomes astigmatic: the focal spot becomes oval and the exposed areas exhibit an asymmetry following the shape of the spot. This astigmatism has to be corrected by an additional lens system which has to be adjusted carefully to achieve optimum structure quality.

In this Thesis we use two different EBL systems:

- A Zeiss “Supra 55 VP” SEM in combination with an external “ELPHI Plus 6 MHz high-speed pattern generation hardware” by Raith GmbH which is provided by the DFG-Center for Functional Nanostructures (CFN), Karlsruhe Institute of Technology (KIT).
- A Raith “e\_LiNE” ultra-high-resolution electron-beam-lithography system with interferometric stage. This system is provided by the Institute for Nanotechnology, Karlsruhe Institute of Technology (KIT).

In principle, both systems are capable of precise alignment of a second functional layer above the first one since the positioning of the electron beam alone can be realised with an accuracy of below 5 nm for both systems. In practice, however, only the e\_LiNE-system can be used for the alignment process, as only the interferometric stage allows for driving to the exact position of the alignment markers with an accuracy of tens of nanometers. This is essential for the alignment procedure presented in Section 4.1.3.

### 4.1.1 Sample Preparation

The starting point of the fabrication process is the preparation of the substrates for EBL. We use  $10 \times 10 \times 1 \text{ mm}^3$  Suprasil substrates<sup>1</sup> covered with a 5-nm-thin film of conductive indium-tin-oxide (ITO), processed by electron-beam evaporation in an oxygen environment at pressures of  $1.2 \cdot 10^{-5}$  mbar. Afterwards the substrate is post-baked for 5 h at 450°C. The ITO layer prevents local charging of the substrate during EBL and additionally serves as adhesion promoter for gold on the Suprasil substrate. Since thin ITO films are nearly transparent for ultraviolet to infrared wavelengths, it is a suitable conductive material for our experiments. Finally a (4%) solution of the standard positive resist polymethyl-methacrylate (PMMA) in anisole<sup>2</sup> is spin-coated onto the ITO-covered Suprasil substrate at 5000 rpm for 90 seconds and post-baked at 165°C for 30 minutes in a convection oven. The resulting ITO-Suprasil substrate is covered with an approximately 200-nm-thick film of PMMA, which can now be structured by EBL.

### 4.1.2 Single-Exposure Electron-Beam Lithography

For the fabrication of single-layer planar metamaterials only one EBL step is necessary. During exposure of the substrate with high-energy (30 keV) electrons, the chemical bonds of the long PMMA chains are broken up where the deposited local charge dose exceeds values of  $175 \mu\text{C}/\text{cm}^2$ . As a consequence all areas exposed to a charge dose above this threshold can be removed by a developer consisting of one part methyl-isobutyl-ketone (MIBK) mixed with three parts of isopropanol. After 20 seconds of development the 2D-negative mask of the metamaterial structure design is metallised with a 25-nm to 60-nm-thin gold film by electron-beam evaporation<sup>3</sup> at pressures below  $10^{-6}$  mbar. As a last step, the gold-covered negative mask is removed during a lift-off procedure performed in hot acetone in an ultrasonic bath. The low-symmetry metamaterial structure presented in Chapter 5.2.2 and 5.2.3 and the single-layer gammadion metamaterial in Chapter 7.2 are fabricated in this manner. An illustration of the standard fabrication process of a single-layer planar metamaterial is presented in Fig. 4.2.

<sup>1</sup>Suprasil 1 by B. Halle Nachfl. GmbH, Germany

<sup>2</sup>NANO™ PMMA 950K A4 by MicroChem. Corp., USA

<sup>3</sup>Evaporation source e-vap 4000-UHV, MDC Vacuum Products Corp., USA; Deposition controller STC-200/SQ, Sycon Instruments, USA

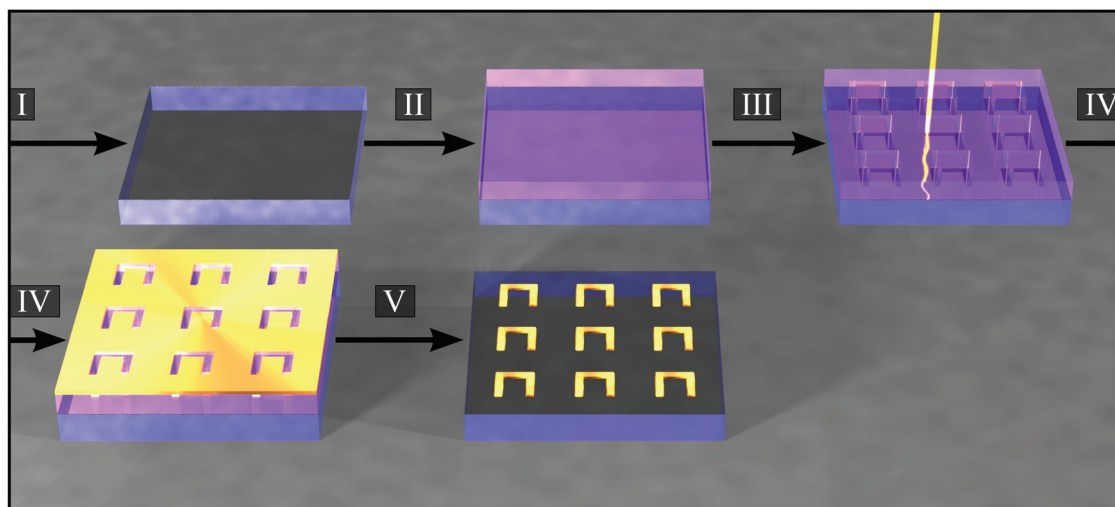


Figure 4.2: Illustration of the typical fabrication steps to produce a single-layer metamaterial. After evaporation (I) of a conductive ITO layer (dark gray) onto the bare glass substrate (blue), the photoresist (light red) is processed by spin-coating (II). The photoresist is then patterned by EBL (III) and the exposed areas are removed in a developer. In the next step a 25-nm to 60-nm-thin layer of gold is deposited on the structured sample by e-beam evaporation (IV). Finally, the photoresist and the excessive gold is removed in a lift-off procedure (V).

### 4.1.3 Fabrication of Multi-Layer Metamaterials

Simple multi-layered structures composed of two identical layers on top of each other separated by a dielectric spacer can easily be fabricated by multiple electron-beam evaporation after the single-layer-EBL process, for instance. Such structures like the double-layer gammadion metamaterial (Chapter 7.2) or the double-wire pairs (Chapter 5.2.1) consist of a three-layer-sandwich: one layer of gold, one layer of  $\text{MgF}_2$  and another layer of gold which are subsequently evaporated. This method has already been extended to structures consisting of up to seven layers [30]. The width of each layer, however, decreases with the number of deposited layers and poses the limit to the maximum number of layers when the width of the topmost layer approaches zero [30]. In order to obtain “truly” three-dimensional metamaterials a single EBL step, however, is not sufficient anymore. Particularly, chiral metamaterials (see Chapter 8) require at least two functional layers rotated relative to each other. We have therefore developed a two-step EBL process with intermediate planarisation following the method of Ref. [70]. The crucial part of the two-step EBL procedure is an accurate alignment of a second functional metamaterial layer with respect to the first one. We use alignment markers, *i.e.*,  $10\ \mu\text{m}$  large gold crosses centered at fixed coordinate positions with respect to the internal coordinate system ( $u/v$ -coordinate-system) of the so-called writefield<sup>4</sup> (see Fig. 4.4). Those markers and the metamaterial structure have to be written in the first lithography step as illustrated in Fig. 4.3(a).

In order to minimise alignment errors caused by the drift of the electron beam in the course of the exposure of the first and, particularly, later, when writing the second functional

<sup>4</sup>The writefield is the maximum scanning range of the electron beam without moving the sample stage of the SEM

layer, we have to minimise the overall exposure time of the metamaterial field. This can be achieved by using single-line exposures in combination with high dose-factors instead of low-dose area-mode exposures. Additionally, the high-dose line mode reduces asymmetries of the single nanostructures arising from stigmation aberrations of the electron beam. The CAD-design file of the first functional layer of the twisted-crosses metamaterial discussed in Chapter 8.1 is illustrated in Fig. 4.3(a). We use a magnification<sup>5</sup> of  $1800\times$ , resulting in a maximum writefield size of  $100 \times 100 \mu\text{m}^2$  and a maximum scanning resolution of 1.6 nm.

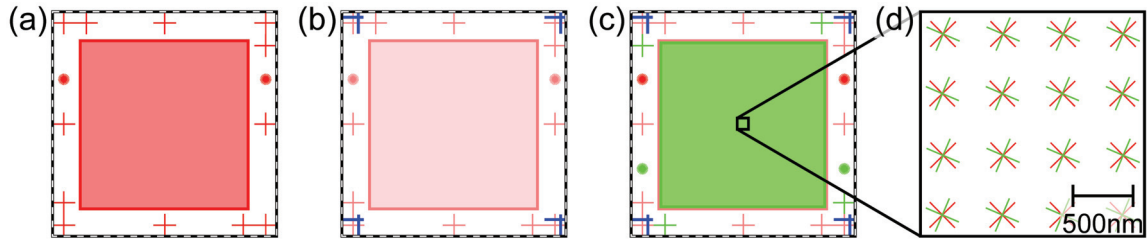


Figure 4.3: (a) The first layer (red) of the CAD file contains the alignment markers (red crosses) and the metamaterial’s first functional layer (red square). The maximum writefield size of  $100 \times 100 \mu\text{m}^2$  is indicated as black-dashed line. (b) During alignment the outermost marker positions are scanned *via* line-scans (blue lines). The deviation of the scanned marker positions to the expected positions is translated into writefield correction values. (c) As a final step the second functional metamaterial layer (green) is exposed. (d) A zoom into the two functional layers shows the twisted-crosses metamaterial design investigated in Chapter 8.1.

## Planarisation

After processing the first functional metamaterial layer on the substrate the sample is planarised by a 500-nm to 700-nm-thick layer of commercially available spin-on dielectric<sup>6</sup> (SOD). This dielectric spacer layer is processed by three cycles of spin-coating at 3000 rpm for 60 seconds and a subsequent post-bake on a hotplate at  $120^\circ\text{C}$  for one minute. After three cycles, the sample is post-baked for 30 minutes in a convection oven at  $120^\circ\text{C}$ . Then the 500-nm to 700-nm-thick spacer layer is gradually etched down to the desired thickness by reactive-ion etching<sup>7</sup>. The film thickness is measured by a thin-film reflectometer<sup>8</sup>. Depending on the final thickness of the spacer layer a second conducting ITO layer has to be deposited since, during EBL, charging effects of the non-conductive spin-on dielectric increase with the thickness of the spacer layer. This can result in a substantial beam drift. Owing to the short exposure times for the metamaterial structures investigated in Chapter 8 (spacer thicknesses of  $s \approx 50 - 150 \text{ nm}$ ) an additional ITO layer has not been required.

Finally we have to provide the photoresist for the second exposure. We therefore spin-coat an additional layer of PMMA onto the planarised substrate.

<sup>5</sup>The magnification of the SEM determines both the maximum scanning resolution and the maximum writefield size.

<sup>6</sup>IC1-200, Futurrex Inc., USA

<sup>7</sup>RIE Plasmalab80Plus, Oxford Instruments Plasma Technology, UK, gas flows are: 40 sccm of  $\text{SF}_6$  and 10 sccm of Ar; Process parameters are: forward power of 80 W and chamber pressure of 100 mTorr. This results in an etching rate of about 1 – 1.5 nm/s.

<sup>8</sup>NanoCalc 2000, Mikropack GmbH, Germany

## Alignment and Second Exposure

In order to position the second functional metamaterial layer right above the first one in the second EBL step we have to find the positions of the alignment markers written in the first EBL step without exposing the photoresist in the areas relevant to the second layer. It is therefore of fundamental importance that the positioning accuracy of the SEM stage is well below 100 nm even for travel distances of several millimeters. This basic requirement is fulfilled for the e.LiNE system's interferometric stage.

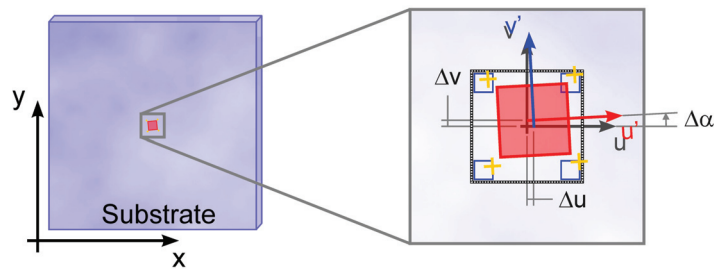


Figure 4.4: Simplified illustration of the alignment procedure. The global SEM coordinate system ( $x/y$ -axes) is chosen to have its origin at the lower left corner of the substrate (blue). The absolute position of the metamaterial field has to be found with an accuracy of few tens of nanometers. The zoom in on the right-hand side shows the markers (yellow crosses) written in the first lithography step which are tilted with respect to the expected positions (blue squares). The first metamaterial layer is indicated in red. The original writefield (black/white-dashed line) of the original internal  $u/v$  coordinate system (in gray) has to be shifted by  $\Delta u$  and  $\Delta v$  and rotated by  $\Delta\alpha$  after the alignment scans of the markers on the substrate. The corrected new  $u'/v'$  coordinate system (in red/blue) is used for the exposure of the second metamaterial layer.

Once the approximate position of a specific field is found the exact orientation of the internal  $u/v$ -coordinate system of the electron beam is determined by scanning the (three) expected positions of the alignment markers of the first layer (see Fig. 4.3(b)) and calculating the correction values for the scaling, the rotation and the  $u/v$ -shifts of the new  $u'/v'$ -axes from the actual positions of the markers (see Fig. 4.4). Normally the corrected position of the new  $u'/v'$ -coordinate system, hence, the size of the area to be written in the second EBL step still lies within the maximum scanning range of the original  $u/v$ -coordinate system. Then the stage is not moved and the second EBL-step can be started using the corrected  $u'/v'$ -coordinate system. Otherwise the stage position has to be corrected and a new alignment is necessary until the second layer lies within the maximum writefield. The exposure patterns of the two layers, the alignment markers and the scan marks for the alignment procedure are programmed with the CAD software of the e.LiNE system (see Fig. 4.3(c) and (d)). Owing to the underlying first metallic metamaterial layer and the additional spacer layer, backscattering of the electrons increases. As a consequence, new relative exposure doses for the second functional layer of the metamaterial have to be chosen.

The alignment procedure presented here can be fully automated. In practice, however, the best results are achieved by a semi-automated procedure: one has to manually check the values for the scaling,  $u/v$ -shift and -rotation and repeat the alignment procedure if necessary before starting the exposure. In this way a misalignment between the two functional layers

of below 10 nm over the entire sample footprint of  $100 \times 100 \mu\text{m}^2$  has been achieved. An overview of the whole fabrication process is presented in Fig. 4.2 and Fig. 4.5.

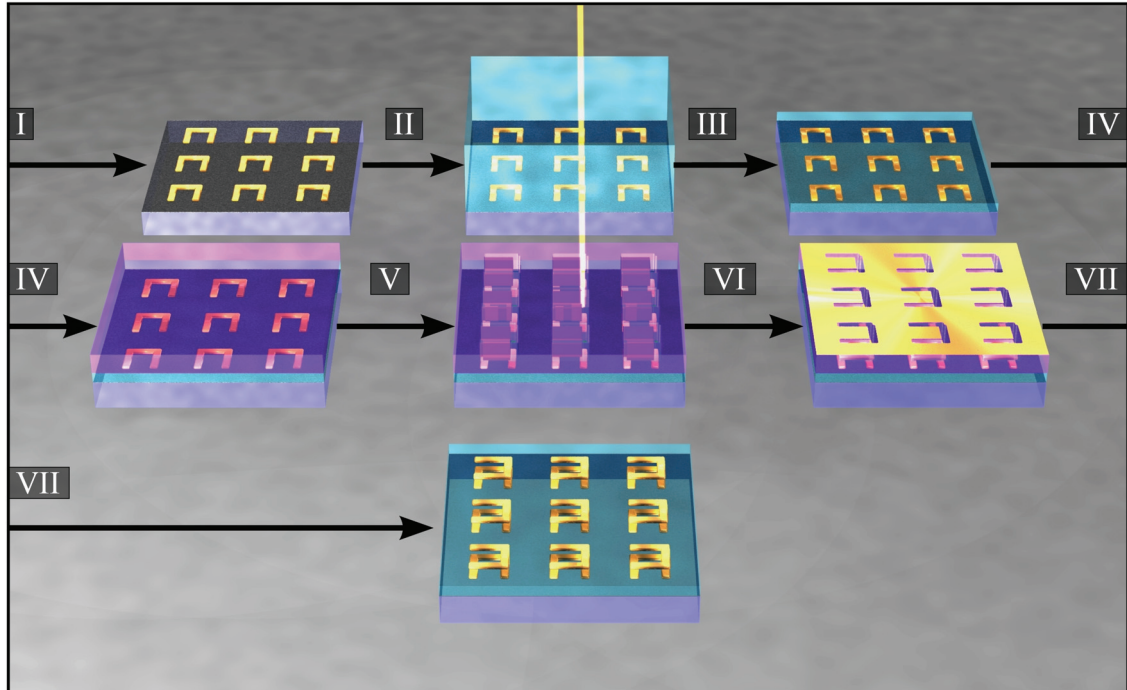


Figure 4.5: The fabrication steps of a two-layer metamaterial structure are illustrated in this figure. Starting with the planar metamaterial structure (I) obtained by the standard EBL-process depicted in Fig. 4.2 the sample is planarised by spin-coating of an about 500-nm-thick layer of spin-on dielectric (II). After etching this spacer layer (in light green) down to several tens of nanometers (III) the photoresist (light red) is deposited on the planarised sample by spin-coating (IV). The second functional layer of the metamaterial is then written by EBL (V). After evaporation of the final gold layer (VI) and the lift-off procedure (VII) the final two-layer metamaterial is obtained.

## 4.2 Optical Characterisation

For linear optical characterisation of the metamaterial structures presented in Chapter 5, 7 and 8 we use two dedicated setups, a home-built spectroscopy setup for visible and near-infrared wavelengths from  $0.5 - 2.2 \mu\text{m}$  and a commercially available FTIR-spectrometer for the infrared from  $2.2\text{-}\mu\text{m}$  to  $7\text{-}\mu\text{m}$ -wavelength. Both setups are equipped with polarising optical components to perform polarisation spectroscopy.

### 4.2.1 Transmittance Measurements in the Visible/Near-Infrared

The home-built transmittance setup for visible and near-infrared wavelengths (VIS-setup) is schematically shown in Fig. 4.6. Light from a 100-W-tungsten-halogen lamp is focussed into a multimode optical fibre and sent into the optical setup where the collimated beam passes

through a Glan-Thompson polariser<sup>9</sup> followed by a superachromatic quarter-wave plate<sup>10</sup> (SQWP). The collimated beam passes an aperture and a microscope objective<sup>11</sup> focussing the light onto the substrate with an effective half-opening angle of  $5^\circ$  corresponding to a numerical aperture of  $NA = 0.088$ . The substrate is mounted onto a 3D-micrometer stage in combination with a  $360^\circ$  rotation stage and two goniometers ( $\Delta\alpha = \pm 25^\circ$ ) which enables us to perform angle-resolved measurements. The emerging light passes a second microscope objective producing a collimated beam which is sent through a second combination of a SQWP and a Glan-Thompson polariser. Then the light is imaged onto a rectangular knife-edge aperture where only the relevant part of the sample is selected for detection. Finally, the light transmitted through the selected area of the sample can be sent into a CCD-camera or it can be coupled into a second optical fibre attached to either an optical spectrum analyser<sup>12</sup> (0.5- $\mu\text{m}$  to 1.7- $\mu\text{m}$ -wavelength) or a home-built FTIR spectrometer (a piezo-controlled Michelson interferometer with a liquid-nitrogen-cooled indium-antimonide detector from 0.5- $\mu\text{m}$  to 2.2- $\mu\text{m}$ -wavelength). Owing to the polarisation devices behind the

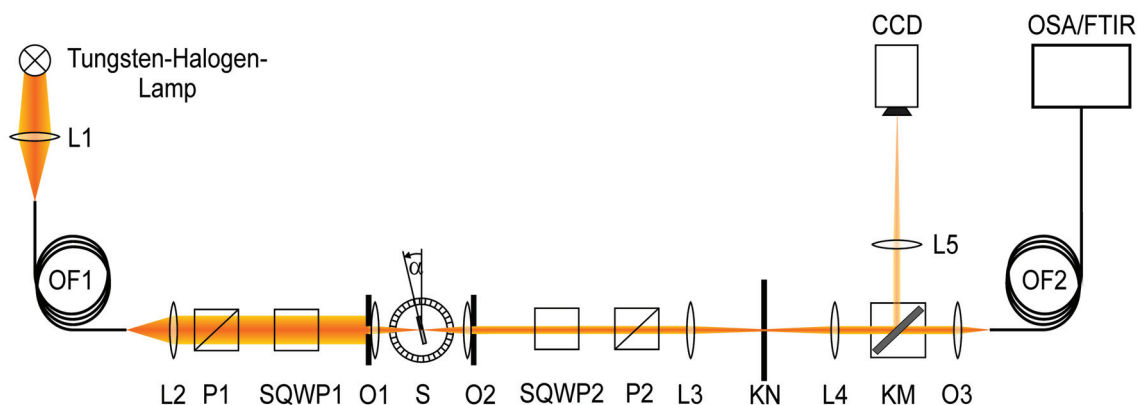


Figure 4.6: Illustration of the VIS-setup for the visible/near-infrared. Light from a tungsten-halogen lamp is sent through an optical fibre (OF1) into the optical setup. After the collimating lens (L2) a polariser (P1) in combination with a SQWP generates circular polarisation. The circularly polarised light then is focussed by a microscope objective (O1) onto the sample (S). A second microscope objective (O2) collimates the emerging light that passes the analysing SQWP and polariser (P2) afterwards. A focussing lens (L3) produces an intermediate image on a knife-edge aperture (KN), by which the detectable area of the sample can be selected. The emerging light is collimated once again (L3) and a kinetic mirror (KM) is used to select one of the detection devices. Hence, the light is focussed by either L5 onto a CCD-camera or by the microscope objective O3 onto a second optical multimode fibre (OF2) which feeds an optical spectrum analyser or a home-built Fourier transform spectrometer, respectively.

sample, this setup not only allows for choosing the incident polarisation but also enables us to analyse the polarisation state of the emerging light. It is therefore also possible to measure the intensity conversion of circular- as well as of linear-incident polarisation into the corresponding orthogonal polarisation state. A detailed description of how circularly-polarised light is generated and analysed is provided in Chapter 6.5. All transmittance spectra

<sup>9</sup>Glan-Thompson Polariser 3PTO001, Melles Griot, USA

<sup>10</sup>Superachromatic  $\lambda/4$  Plate RSU 2.4.15, 600-nm to 2700-nm-wavelength, B. Halle Nachfl., Germany

<sup>11</sup>Zeiss Achroplan LD 20x KO,  $NA = 0.4$ .

<sup>12</sup>ANDO AQ-6315B Optical Spectrum Analyzer

are normalised with respect to the transmittance right beside the metamaterial field, *i.e.*, with respect to the transmittance of the bare glass substrate with the ITO layer. For linearly polarised transmittance measurements, the SQWPs are removed from the optical system.

## 4.2.2 Transmittance Measurements in the Infrared

For experiments in the infrared spectral range (2.5- $\mu\text{m}$  to 7- $\mu\text{m}$ -wavelength), we use a commercial Fourier-transform spectrometer<sup>13</sup> with an attached optical microscope (FTIR-setup). The light is focussed and collected with  $\times 36$  reflective Cassegrain lenses (NA = 0.5). Hence, the sample is illuminated at oblique incidence at angles from between  $15^\circ - 30^\circ$  with respect to the substrate's surface normal. In order to achieve normal incidence with small angles of incidence, we have modified the Cassegrain optics by introducing a small circular aperture such that the full opening angle of the light incident onto the sample is reduced to about  $5^\circ$ . By tilting the sample by  $22.5^\circ$  we achieve normal incidence of the emerging light beam onto the sample (see Fig. 4.7). The detection is realised by a liquid- $N_2$ -cooled InSb-detector. A linear  $\text{CaF}_2$  "High Extinction Ratio" holographic polariser<sup>14</sup> and a custom-made  $\text{MgF}_2$ -based superachromatic quarter-wave plate<sup>15</sup> are mounted in a compact holder and provide circularly polarised incident light (for details concerning the orientation of the SQWP and the polariser we refer to Chapter 6.5.4). Unfortunately, our experimental setup does not allow for analysing the emerging polarisation of light. Again, all transmittance spectra are referenced to the transmittance of the glass substrate and the ITO layer.

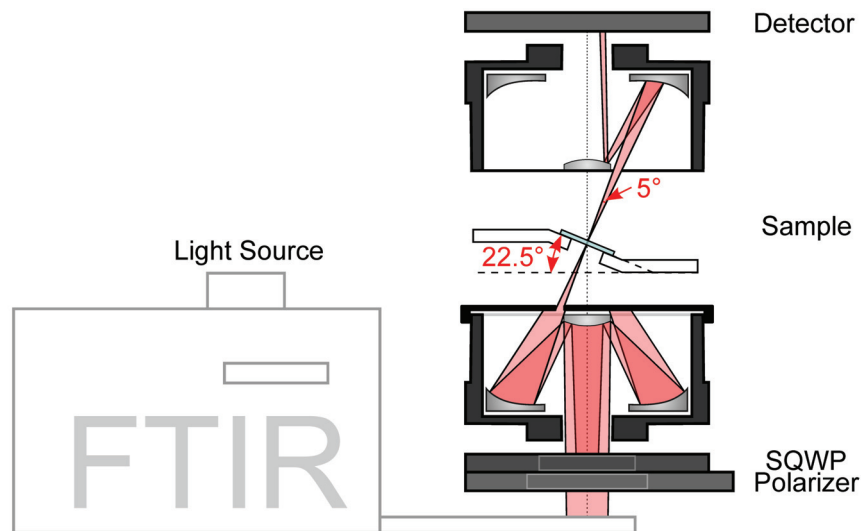


Figure 4.7: Illustration of the FTIR-setup for infrared transmittance measurements. The combination of a polariser and the SQWP generate circular polarisation. The RCP/LCP light is then focussed onto the sample by a reflective Cassegrain lens. A small aperture in the Cassegrain objective realises small opening angles of  $5^\circ$ . The sample is rotated by  $22.5^\circ$  to achieve normal incidence.

<sup>13</sup>Bruker Tensor 27 with Bruker Hyperion 1000, Bruker Optik, Germany

<sup>14</sup>Bruker Optik GmbH, Germany

<sup>15</sup>B. Halle Nachfl., Germany

### 4.3 Numerical Calculation and Postprocessing

In order to support and interpret our experimental data, we perform numerical calculations with the commercial finite-element software package COMSOL Multiphysics<sup>16</sup>. We use predefined library functions (MKFEM, version 2.0 by M. W. Klein [71]) as a simplified interface to the COMSOL software package in a MATLAB<sup>17</sup> environment. Numerical calculations are performed with an iterative solver and a multigrid mesh hierarchy, *i.e.*, a coarse mesh is generated in a first step and in the second step the problem is solved for a refined mesh containing all edges of the coarse mesh. Alternatively, the coarse mesh can be issued with vector elements of higher orders instead of the mesh refinement in the second step. Owing to the lower memory consumption of this method compared to a direct solver this allows us to calculate larger models. Numerical convergence of the calculated results, however, has to be checked. We therefore vary the mesh discretisation and check that the calculated results do not vary systematically by more than 2% for finer meshes than the original one. We use periodic boundary conditions in the  $x$ - and the  $y$ -direction (propagation in negative  $z$ -direction) to account for the periodic arrangement of the metamaterial's unit cells. We therefore have to restrict ourselves to rectangular metamaterial unit cells in a rectangular lattice. Nevertheless, this is often only a minor restriction. The functionality of periodic unit cells in the calculations includes interaction *via* higher-order multipole moments as well as interaction beyond the nearest neighbours and retardation effects.

The numerical solution of Maxwell's equations for the given experimental conditions provides us with the complex normal-incidence transmission and reflection spectra *via* the electric fields at the lower (upper) surface of the simulation volume. We have expanded the model library of Ref. [71] by a post-evaluation method in order to obtain information about the polarisation state of the emerging light. We can therefore calculate the linear- $x$  and the linear- $y$  polarised complex-valued transmission for an arbitrarily polarised incident plane wave. The actual calculations are performed using linear- $x$  and linear- $y$  polarised incident light. It is then straightforward to translate the results into the transmittances for, *e.g.*, diagonal ( $\pm 45^\circ$ ) polarisations and circular (RCP and LCP) polarisations of the incident light.

From these results, the Jones matrix of a metamaterial slab and consequently the polarisation state of the emerging light, the polarisation eigenstates and the optical rotatory power of the metamaterial design can be deduced (see Chapter 6.5).

---

<sup>16</sup>COMSOL Multiphysics GmbH, Germany

<sup>17</sup>MATLAB, The MathWorks Inc., USA

# Chapter 5

## Interaction of Dipoles in Metamaterials

The main task for achieving a desired metamaterial response is a proper design of the shape and the arrangement of metal nanoparticles within one unit cell. A single ellipsoidal metal nanoparticle or nanoantenna already provides an electric-dipole response in a first approximation (see Chapter 3.3). We can also create a magnetic-dipole response by simply bending the antenna to form an SRR (see Chapter 3.4) or by coupling two antennae to form a cut-wire pair (see Chapter 3.5). If we neglect higher order (multipole-) coupling, the optical response of simple configurations of metal nanoparticles can be modelled by an arrangement of effective electric or magnetic dipoles. This motivates the introduction of a Lorentz-oscillator model to describe both the response of a single dipole driven by an incident (electric) field and the response of two coupled dipoles.

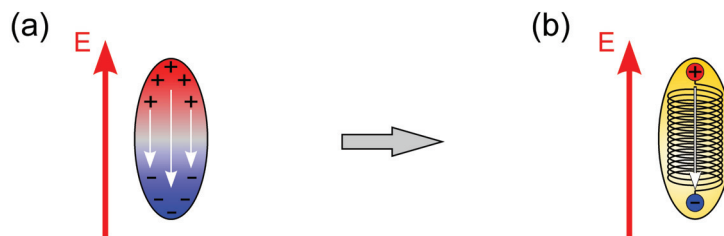


Figure 5.1: (a) Illustration of the charge distribution of an ellipsoidal metal nanoparticle driven by an electric field indicated as red arrow. (b) depicts the simplified view on the collective excitation mode (particle plasmon) as electric-dipole oscillation, described by the Lorentz-oscillator model.

We will present first experimental results on magnetic coupling of double-wire pairs *via* a dielectric waveguide [72] and demonstrate direct coupling of the magnetic dipoles within one unit cell of a particular low-symmetry metamaterial [73]. Furthermore, we provide experimental evidence that dipole-dipole coupling cannot be treated as a pure near-field effect anymore, even on the scale of typical photonic metamaterials. We show that far-field effects, particularly retardation of the dipoles' response, are of fundamental importance [74]. Finally, we will extend this concept from two to three dimensions and show that multi-layered three-dimensional metamaterials exhibit longitudinal coupling of magnetic dipoles.

## 5.1 Lorentz-Oscillator Model

In this section we want to introduce the use of a simple electric Lorentz-oscillator model (in close analogy to the optical response of dielectrics) to describe the dipole-like response of metal nanoparticles to a driving electromagnetic field (see Fig. 5.1). In this model an electron is displaced with respect to a fixed positive background charge by an oscillating electric field. The displacement of the charged particles results in an electric-dipole moment given by

$$p = e \cdot X_0.$$

where  $e$  is the elementary charge and  $X_0$  is the displacement amplitude. The one-dimensional equation of motion for the oscillating dipole is that of a driven harmonic oscillator:

$$\ddot{x} + 2\gamma\dot{x} + \tilde{\omega}_0^2 x = -\frac{e}{m_e} E_0 e^{-i\omega t} \quad (5.1)$$

Here,  $m_e$  is the electron mass,  $\gamma$  is the (ohmic) damping of the system,  $\tilde{\omega}_0$  is the resonance frequency of the undamped system and  $E = E_0 e^{-i\omega t}$  is the exciting field. The resonance frequency of the undriven damped system is given by  $Re[\omega_0] = \sqrt{\tilde{\omega}_0^2 - \gamma^2}$ . For simplicity, we neglect radiation damping which typically results in a broadening of the plasmon resonance and is small for small particle dimensions [45]. Solving Equation (5.1) using the *ansatz*  $x = X_0 \exp(-i\omega t)$  provides the time-dependent displacement and, hence, the amplitude and relative phase of the displacement with respect to the excitation

$$X_0 = \frac{eE_0}{m_e (\tilde{\omega}_0^2 - \omega^2 - 2i\gamma\omega)}.$$

We can finally calculate the effective electric response of a metamaterial consisting of an array of non-interacting electric dipoles, which is given by the macroscopic electric polarisation  $P = n_0 \cdot p$ . Here,  $n_0$  is the dipole density. The effective permittivity then is

$$\epsilon(\omega) = 1 + \frac{\omega_{pl}^2}{(\tilde{\omega}_0^2 - \omega^2 - 2i\gamma\omega)}$$

with the plasma frequency  $\omega_{pl}^2 = (n_0 e^2)/(m_e \epsilon_0)$ . The dielectric function of this electric Lorentz-oscillator metamaterial is sketched in Fig. 5.2.

### 5.1.1 Near-Field Dipole-Dipole Coupling

Now, we want to use this simple Lorentz-oscillator model to calculate the near-field response of two coupled dipoles. We therefore have to solve the two coupled equations of motion given by

$$\ddot{x}_1 + 2\gamma\dot{x}_1 + \tilde{\omega}_0^2 x_1 + W(x_1 - x_2) = 0 \quad (5.2)$$

$$\ddot{x}_2 + 2\gamma\dot{x}_2 + \tilde{\omega}_0^2 x_2 - W(x_1 - x_2) = 0. \quad (5.3)$$

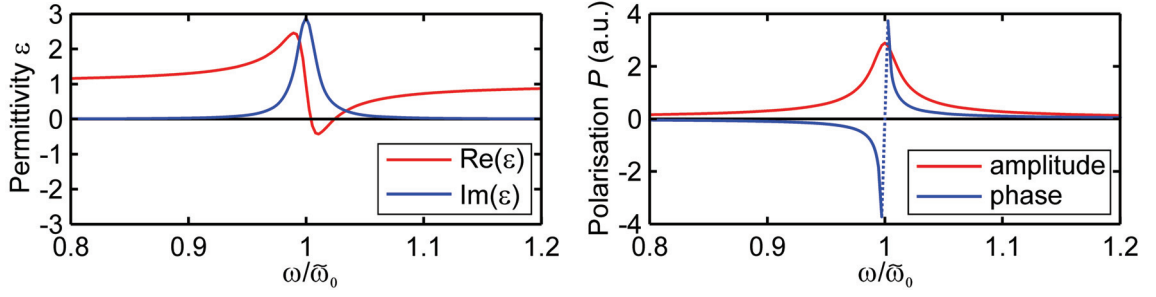


Figure 5.2: The real part (red) and the imaginary part (blue) of the dielectric function of an ensemble of non-interacting Lorentz oscillators is plotted on the left-hand side. The  $x$ -axis is normalised with respect to the resonance frequency  $\tilde{\omega}_0$ . Owing to its resonant behaviour the real part of the permittivity exhibits negative values above the resonance frequency. The corresponding amplitude (red) and the phase (blue) of the electric polarisation  $P$  are depicted on the right-hand side.

For simplicity, we assume identical dipoles which are coupled *via* the positive coupling constant  $W$ . This results in the homogeneous equation system

$$\begin{pmatrix} -\omega^2 - 2i\gamma\omega + \tilde{\omega}_0 + W & -W \\ -W & -\omega^2 - 2i\gamma\omega + \tilde{\omega}_0 + W \end{pmatrix} \begin{pmatrix} X_1 \\ X_2 \end{pmatrix} = \begin{pmatrix} 0 \\ 0 \end{pmatrix}$$

which provides two eigenfrequencies

$$\begin{aligned} \omega_L &= \sqrt{\tilde{\omega}_0^2 - \gamma^2} - i\gamma \\ \omega_H &= \sqrt{\tilde{\omega}_0^2 + 2|W|} - \gamma^2 - i\gamma. \end{aligned}$$

The ratio of the dipole amplitudes is then given by

$$\begin{aligned} \omega_L : \frac{X_2}{X_1} &= +1 \\ \omega_H : \frac{X_2}{X_1} &= -1. \end{aligned}$$

As a result we obtain a low-frequency symmetric mode  $\omega_L$  and a high-frequency antisymmetric mode  $\omega_H$  in the case of positive coupling of the two dipoles ( $W = +|W|$ ). We note that the total dipole moment of the antisymmetric mode vanishes and, consequently, coupling to the antisymmetric mode *via* an electromagnetic field is only possible if we account for (far-field) retardation effects.

For negative coupling ( $W = -|W|$ ) we obtain

$$\begin{aligned} \omega_H &= \sqrt{\tilde{\omega}_0^2 - \gamma^2} - i\gamma \\ \omega_L &= \sqrt{\tilde{\omega}_0^2 - 2|W|} - \gamma^2 - i\gamma \end{aligned}$$

with a ratio of the amplitudes

$$\begin{aligned} \omega_H : \frac{X_2}{X_1} &= +1 \\ \omega_L : \frac{X_2}{X_1} &= -1. \end{aligned}$$

For negative coupling, the antisymmetric mode becomes the low-frequency mode and the symmetric mode becomes the high-frequency mode.

If we now translate the results above to specific arrangements of dipoles, we can distinguish two situations:

- If two coupled dipoles with their dipole axis in  $x$ -direction are displaced in  $x$ -direction (longitudinal coupling) the restoring force of the symmetric configuration is at its minimum. Hence, the symmetric mode is the low-energy mode and the coupling constant  $W$  is positive (see Fig. 5.3(a)).
- If the dipoles are displaced in  $y$ -direction (transverse coupling) the restoring force of the symmetric configuration is at its maximum and the symmetric mode is the high-energy mode with a negative coupling constant  $W$  (see Fig. 5.3(b)).

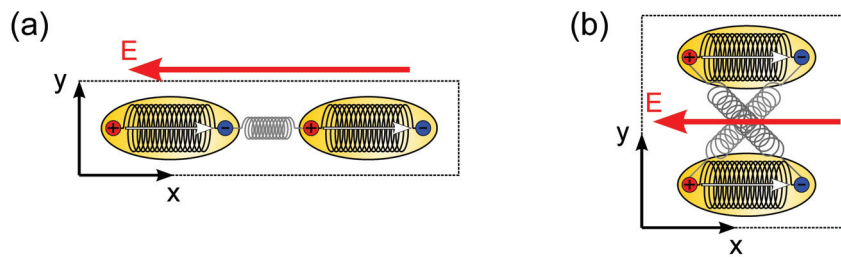


Figure 5.3: Coupling of two plasmons gives rise to a splitting or hybridisation of the plasmon resonance. For longitudinal coupling (a) the symmetric mode is the low-energy mode while for transversal coupling (b) the symmetric mode is the high-energy mode. The orientation of the E-field vector is indicated as red arrow. This figure is adapted from Ref. [75].

### Magnetic Plasmonic Dipoles

So far, we have described the optical response of individual and coupled metal antennae in the simple model of (coupled) electric Lorentz oscillators. In Chapter 3.4, however, we already learned that both the optical response of a bent antenna, *i.e.*, an SRR, and of two coupled antennae, *i.e.*, a cut-wire pair, exhibits a magnetic-dipole moment. These two designs therefore act as “isolated magnetic dipoles” and can be regarded as magnetic counterparts of the electric Lorentz oscillator. As a result, the same reasoning as for electric Lorentz oscillators can be applied to the magnetic-dipole oscillators as well, including magnetic dipole-dipole coupling. Actually, the coupling strength of magnetic and electric dipoles in SRR metamaterials (see, *e.g.*, Refs. [76, 77]) and in negative-index metamaterials presented in Ref. [78] are of the same order of magnitude, hence, the actual arrangement of plasmonic nanostructures is crucial for the characteristics of the optical response of the coupled system.

## 5.2 In-Plane Interactions of Magnetic Dipoles

We will now investigate arrays of planar metal nanostructures before introducing multi-layered metamaterial structures in Section 5.3 and more detailed in Chapter 7 and 8. The coupling of simple spherical gold nanoparticles arranged on a plane substrate has been investigated by several groups in the near-field regime so far [75, 79–82]. By positioning the nanoparticles closely together (with interparticle distances of few tens of nanometers) in long chains, coherent propagation of energy along the chains can be achieved *via* electric near-field coupling. In this fashion, even plasmonic switches and plasmonic splitters are obtained by designing appropriate particle arrangements [80]. These findings imply that coupling effects in arrays of metamaterial unit cells should be taken into consideration as well. Since metamaterials exhibiting a magnetic-dipole moment ( $\mu \neq 1$ ) [5] at optical frequencies have become available only recently [51, 57, 68, 83–85] it is of particular interest to investigate magnetic coupling effects in nanostructured arrays composed of those “artificial magnetic building blocks”. In the following sections we present several experiments demonstrating coupling of “magnetic atoms” in periodic nanostructures.

### 5.2.1 Magnetic Coupling via Dielectric Waveguides

We use pairs of long gold wires which are separated by a 50-nm-thick spacer layer of  $\text{MgF}_2$  (see Fig.5.4(a)) in order to investigate magnetic coupling of a periodic array of these “magnetic atoms” *via* a dielectric slab waveguide [72]. The coupling of the resonant magnetic dipoles to the Bragg resonance in the underlying dielectric waveguide is expected to result in a mode splitting, *i.e.*, an anticrossing behaviour of the coupled dipole/waveguide mode. This effect is similar to the mode splitting of two coupled harmonic oscillators which was introduced in Section 5.1.1.

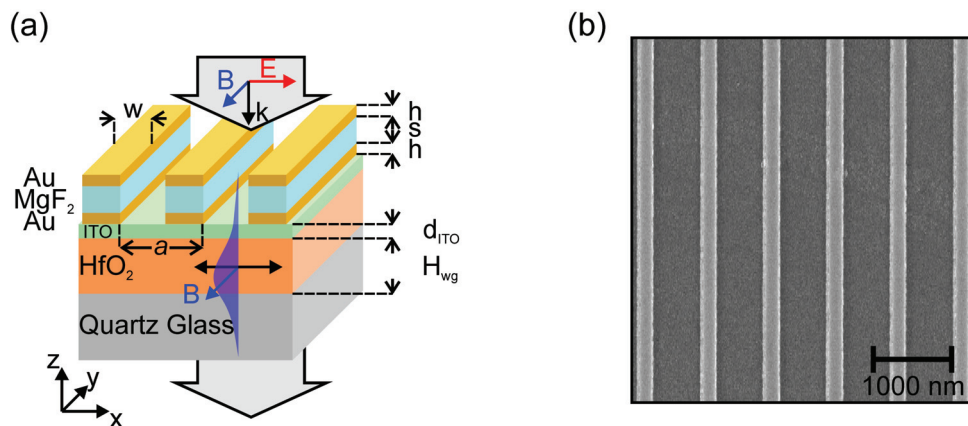


Figure 5.4: (a) Scheme of our coupled system composed of gold double-wire pairs on top of a dielectric waveguide. (b) Top-view electron micrograph of a typical sample with a lattice constant of  $a = 800$  nm.

The dielectric waveguide used in our experiments is formed by a quartz glass substrate covered with a 5-nm-thin layer of indium-tin-oxide (ITO) and a 200-nm-thick layer of

hafnium oxide ( $\text{HfO}_2$ ) which both are deposited by electron-beam evaporation. It supports guided transverse magnetic (TM) modes in the entire spectral region of interest. The lattice constant  $a$  of the wire pairs is varied within a set of samples from  $a = 400$  nm to  $a = 1050$  nm in steps of 25 nm. All other parameters are kept constant. The double-wire pairs have been fabricated by the standard EBL-process (Chapter 4.1.2) followed by a sequential evaporation of a sandwich of 20 nm gold, 50 nm  $\text{MgF}_2$  and 20 nm gold and a lift-off process. The individual arrays have a footprint of  $100 \mu\text{m} \times 100 \mu\text{m}$ . A top-view electron micrograph of the structure with a lattice constant  $a = 800$  nm is depicted in Fig. 5.4(b).

Owing to the structure's inherent periodicity in  $x$ -direction we can couple to the dielectric waveguide at normal-incidence and perform normal incidence spectroscopy. This approach has frequently been used for spectroscopy of leaky modes of dielectric photonic crystal slabs [86, 87], and is related to a usual grating coupler. For polarisation of the incident light perpendicular to the double-wire pairs (TM polarisation), two pronounced resonances result from coupling of the electric-dipole resonances of the two individual wires [66, 68, 85]. The long-wavelength antisymmetric oscillation mode is associated with the

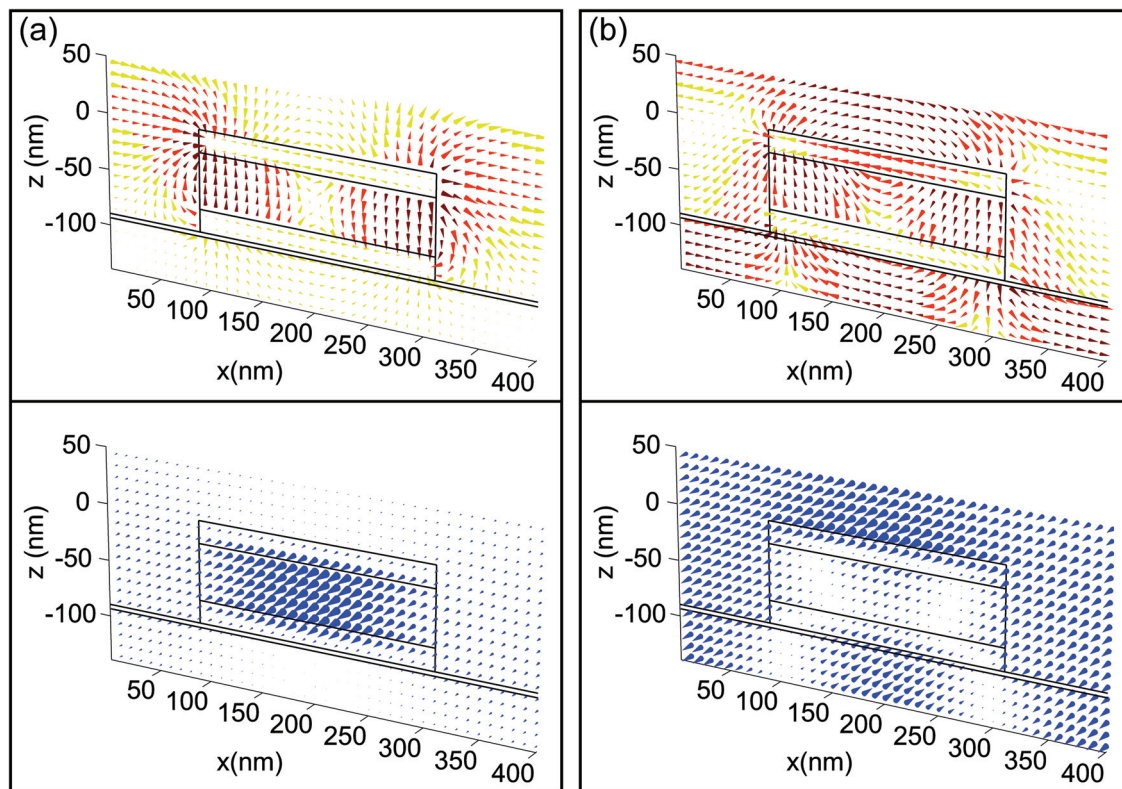


Figure 5.5: (a) Snapshot of the calculated electric (top) and magnetic (bottom) field distribution in the vicinity of a gold double-wire pair ( $a = 400$  nm) placed on a substrate without dielectric waveguide (reference sample). The wavelength  $\lambda = 1140$  nm of the incident light corresponds to the antisymmetric eigenmode exhibiting a magnetic-dipole response. The electric fields (hence the ohmic currents) in the two wires point in opposite directions. (b) Snapshot of the calculated electric (top) and magnetic (bottom) field distribution in the symmetric eigenmode of the double-wire pair. The wavelength  $\lambda = 675$  nm of the incident light corresponds to the electric resonance. Since the electric fields in the wires are almost in phase in this case, the electric resonance has mainly electric-dipole character.

magnetic resonance where the magnetic field is concentrated in the  $\text{MgF}_2$  spacer oriented along the wires (Fig. 5.5(a)). The short-wavelength symmetric eigenmode results in a purely electric response (Fig. 5.5(b)). For polarisation of the incident field parallel to the wires (TE polarisation), the array acts as a diluted metal [23] exhibiting no resonant behaviour. Since we are interested in the coupling of the magnetic-dipole moments to the (dielectric) waveguide we will focus on the magnetic resonance obtained in TM polarisation.

The transmittance properties of the coupled system are studied with the VIS-setup (Chapter 4.2.1) at normal incidence for TM polarisation. Normalisation of the spectra is accomplished with respect to the transmittance of the glass/ITO/waveguide substrate. Since the transmittance properties critically depend on the angle of incidence, great care has been taken to orient the surface of the samples normal to the incident light beam. Additionally, the effective full opening angle of the incident light beam has been reduced to less than  $1.5^\circ$ .

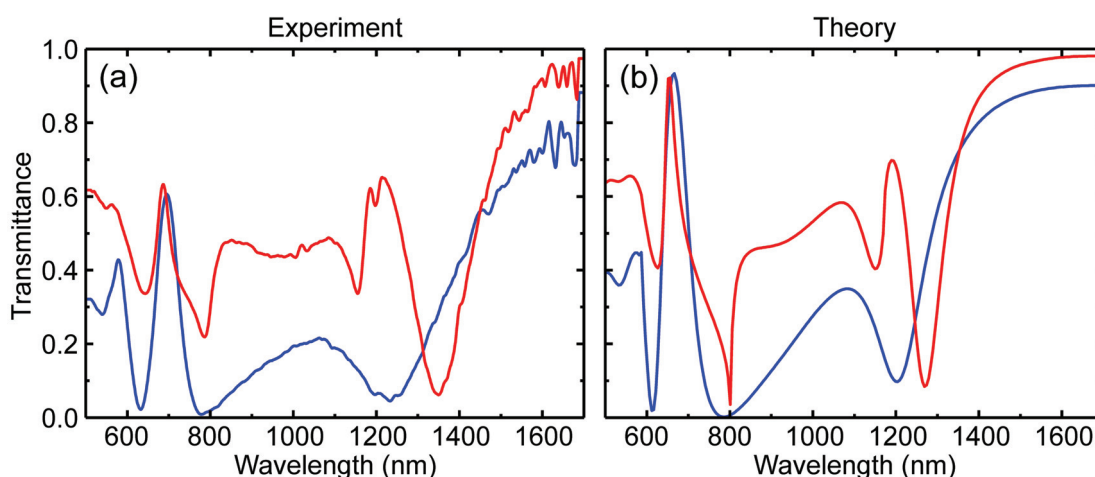


Figure 5.6: (a) Experimental transmittance spectra for selected lattice constants ( $a = 400$  nm in blue and  $a = 800$  nm in red) of the double-wire waveguide geometry depicted in Fig. 5.4(a). The corresponding calculated spectra obtained by a scattering matrix approach are plotted in (b).

Figure 5.6(a) shows measured transmittance spectra for two selected samples with a lattice constant of  $a = 400$  nm and  $a = 800$  nm. The magnetic resonance of the double-wire pairs corresponds to the dip in transmittance centered at  $\lambda = 1200$  nm.

- For  $a = 400$  nm, the Bragg resonance of the periodic arrangement of double-wire pairs coincides with the electric resonance of the double-wire pairs. An avoided crossing of the latter two modes [86] leads to two new resonances at  $\lambda = 630$  nm and  $\lambda = 780$  nm, respectively.
- By increasing the lattice constant from  $a = 400$  nm to  $a = 800$  nm, the Bragg resonance shifts to longer wavelengths (see red dashed curve in Fig. 5.7(a)) while the magnetic resonance keeps its spectral position for lattice constants smaller than 650 nm (yellow dashed curve). Small variations of the spectral position of the magnetic resonance can be attributed to variations of the wire width  $w$  for the different arrays due to fabrication tolerances.

- For lattice constants around  $a \approx 800$  nm, we observe an avoided crossing of the Bragg resonance and the magnetic resonance. It results from the strong coupling of the periodic arrangement of magnetic dipoles provided by the double-wire pairs to the quasi-guided waveguide mode. A further increase of the lattice constants beyond  $a \approx 900$  nm spectrally detunes the Bragg resonance and the magnetic resonance, which basically yields an uncoupled system again.

The other spectral features which shift to larger wavelengths with increasing lattice constant correspond to Rayleigh anomalies or to higher-order waveguide modes. Figure 5.7(a) gives an overview on the complete set of 27 samples with lattice constants from  $a = 400$ –1050 nm in steps of 25 nm depicted on an intuitive gray-scale plot.

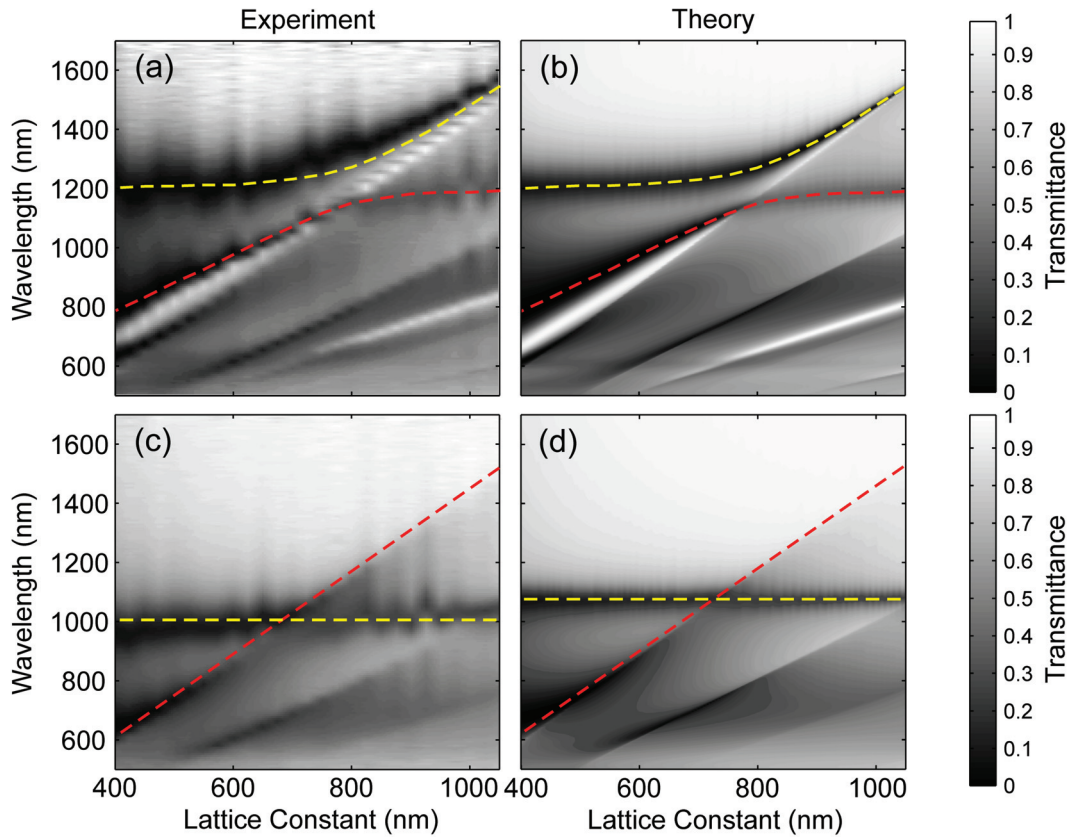


Figure 5.7: (a) Measured and (b) calculated transmittance on an intuitive gray scale *versus* lattice constant  $a$  and wavelength  $\lambda$  for the coupled system. In the experiment, the data from 27 samples of different lattice constants are summarised (two examples are shown in Fig. 5.6). A pronounced anticrossing can be observed at  $a \approx 800$  nm. (c) Measured and (d) calculated transmittance for the control samples without HfO<sub>2</sub> waveguide. In contrast to (a)+(b) no anticrossing behaviour can be observed for the double-wire pairs without waveguide (c)+(d). The dashed red and yellow curves are guides to the eye.

In order to support our experimental findings, we perform rigorous numerical calculations based on a scattering-matrix approach [88]. The calculations nicely reproduce the anticrossing of the magnetic and the waveguide mode (see Fig. 5.7(b)). For our calculation we use the permittivity of the ITO film  $\epsilon_{\text{ITO}} = 3.61$ , the permittivity of the HfO<sub>2</sub> waveguide

$\epsilon_{\text{HfO}_2} = 3.8$ , the permittivity of the glass substrate  $\epsilon_{\text{glass}} = 2.14$  and the permittivity of the  $\text{MgF}_2$  layer  $\epsilon_{\text{MgF}_2} = 1.9$ . The permittivity of gold is taken from Ref. [47]. The geometrical parameters correspond to Fig. 5.4(a). The calculated transmittance spectra for the two selected lattice constants of  $a = 400$  nm and  $a = 800$  nm are shown in Fig. 5.6(b). The calculated spectra of the overall set of samples is shown in Fig. 5.7(b). Here, the same graphical representation is chosen as for the experimental data. A direct comparison between experimental and calculated spectra reveals excellent agreement. In particular, the spectral position and the width of the avoided crossing are accurately reproduced by the numerical calculations.

As a control experiment, we also investigate a second set of arrays of double-wire pairs directly on top of a substrate (covered with 5-nm-thin ITO layer) without a  $\text{HfO}_2$  waveguide. The transmittance spectra shown in Fig. 5.7(c)+(d) are normalised with respect to the transmittance of the bare glass/ITO substrate. In the double-wire pairs without waveguide, no guided modes are supported and no avoided crossing can be observed (see Fig. 5.7(c)+(d)). Additionally, owing to the lack of the dielectric waveguide only a system of weakly coupled “magnetic atoms” remains. Now the magnetic resonance of the double-wire pairs and the Rayleigh anomalies [22] can be identified in the transmittance spectra. Rayleigh anomalies occur, whenever an integer multiple of the wavelength of the incident light in the substrate or vacuum becomes smaller than the actual lattice constant  $a$ . Then new grating orders appear and the energy is redistributed giving rise to a dip in the transmittance (of the 0th order). Rayleigh anomalies are found to have a strong influence on the lineshape of other resonances, *e.g.*, electric-dipole resonances [89]. However, an avoided crossing with the magnetic resonance is not expected because the damping is larger than the anticipated splitting energy of the weakly coupled system.

The measured transmittance spectra for the control samples are depicted in Fig. 5.7(c). Owing to the different dielectric environment (no  $\text{HfO}_2$  waveguide) and a slightly smaller width  $w = 200$  nm of the double-wire pairs, the magnetic resonance is shifted by approximately 200 nm to shorter wavelengths compared to the magnetic resonance of the coupled system (with waveguide) in Fig. 5.7(a). At  $\lambda = 600$  nm ( $a = 400$  nm) the first Rayleigh anomaly, which corresponds to the opening of a new diffraction order in the substrate, occurs. As expected for the situation of weak coupling, this Rayleigh anomaly simply crosses the magnetic resonance when the lattice constant  $a$  is increased (see red and yellow dotted curve in Fig. 5.7(c)). This observation is also reproduced by the numerical calculation (see Fig. 5.7(d)) and supports our interpretation that the “magnetic atoms” are only weakly coupled in our control samples without dielectric waveguide.

Comparing the optical properties for the coupled system and the uncoupled system of “magnetic atoms”, which obviously are rather different (see Fig. 5.7), we can classify the response of the two systems in the following way: on the one hand the strongly coupled system can be seen as a resonant magnetic photonic crystal while on the other hand the effective magnetic response of the uncoupled system is similar to a photonic metamaterial.

For the first case, *i.e.*, for the double-wire pairs on a dielectric waveguide one gets a pronounced avoided crossing (Fig. 5.7(a)+(b)) characteristic for strong coupling between the different building blocks (“magnetic atoms”). Hence, this structure reveals pronounced

signatures of Bloch waves (Bragg scattering), commonly ascribed to “photonic crystals”<sup>1</sup>. Hence the coupled system can be seen as a model system for a one-dimensional “magnetic photonic crystal” in analogy to a (resonant) dielectric photonic crystal (see Fig. 5.8).

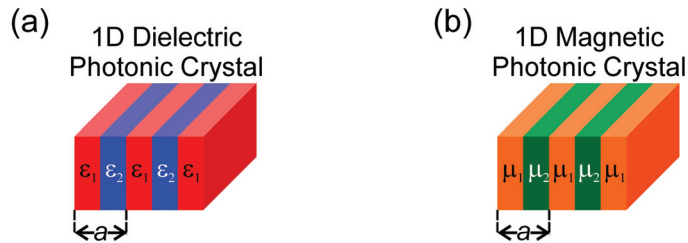


Figure 5.8: Illustration of dielectric (a) *versus* a magnetic (b) photonic crystal.

In the second case without the HfO<sub>2</sub> waveguide, the coupling between the fundamental magnetic building blocks is small. As a consequence the latter type of structure can well be seen as an effective magnetic medium in close analogy to a metamaterial. Nevertheless we have to be careful when using the term “metamaterial” for the control samples, as the characteristic ratio of the operation wavelength  $\lambda$  to the lattice constant  $a$  is around unity ( $\lambda/a \approx 1$ ) depending on the actual sample used. To avoid this ambiguity, we now move on to the metamaterial regime where  $\lambda/a > 2$ .

Our next goal therefore is to achieve direct coupling of the “artificial magnetic atoms” in a metamaterial which in turn requires an array of closely spaced functional building blocks.

## 5.2.2 Magnetic Coupling in Low-Symmetry Split-Ring-Resonator Supercells

For common magnetic metamaterial designs built from SRRs or cut-wire pairs [51, 57, 68, 83, 85] it is often assumed that the SRRs in a periodic array experience only little interaction with their neighbours. In particular, the resonant behaviour of the material’s permeability is often assumed to be equal to that of a single structural unit. However, previous theoretical work [90, 91] as well as experiments [29, 76, 78, 92] at optical frequencies have already shown that the mutual interaction by magneto-inductive coupling among SRRs can be a significant correction and results in phenomena like magnetisation waves, which are not covered by the effective-medium theory [90].

In the following section we investigate the influence mutual coupling between neighbouring SRRs on the optical response to an incident linearly polarised plane wave [73]. Figure 5.9(a) shows a periodic square lattice of equally oriented magnetic SRRs [57]. The unit cell containing a single SRR has no rotational symmetry but one vertical mirror plane.

<sup>1</sup>Photonic crystals are referred to as periodic (dielectric) structures with lattice periodicity  $a$  that is comparable to the wavelength of light. In photonic crystals, diffraction leads to the formation of a photonic bandstructure, *i.e.*, Bloch waves in the periodic dielectric structure. This behaviour can be seen in close analogy to electronic bandstructures in semiconductors resulting from the periodic modulation of the potential of the underlying crystal lattice.

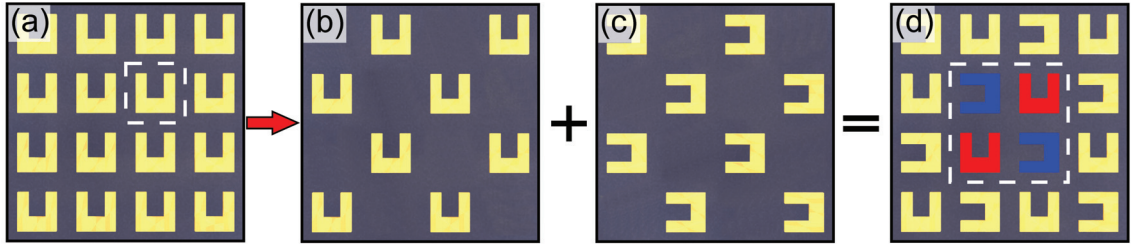


Figure 5.9: Scheme of (a) a usual split-ring-resonator array. The particular low-symmetry arrangement shown in (d) is a combination of two arrays of SRRs one oriented in vertical (b) and the other one oriented in horizontal (c) direction. The dashed white lines in (d) highlight one unit cell. The decomposition of (d) into the blue and red parts illustrates that by symmetry – without interactions – the array has identical optical properties for horizontal and vertical incident polarisations, respectively.

Hence, the corresponding point group is  $C_{1v}$ . The fundamental magnetic mode of the SRR can only be excited for horizontal polarisation of the incident light [57]. In this configuration electric and magnetic dipole-dipole coupling between the SRRs are on the same order of magnitude and compete with each other [76, 77, 93], the magnetic coupling being still weaker, though. In order to obtain a metamaterial, where coupling of magnetic dipoles is the prominent feature, we have designed a dedicated low-symmetry planar periodic arrangement of SRRs shown in Fig. 5.9(d). The arrangement consisting of four SRRs in a square unit cell has no rotational symmetry and no vertical mirror planes. The point group of the unit cell is  $C_1$ . In contrast to a conventional array of equally oriented SRRs [57] the split-ring resonators directly surrounding an arbitrary SRR are all oriented perpendicular. If we restrict ourselves to pure near-field dipole-dipole interactions, the effective electric dipoles of the neighbouring SRRs are perpendicular to each other and no electric dipole-dipole coupling is observed [76, 91, 92]. Hence, the leading order of nearest-neighbour interactions is given by magnetic dipole-dipole coupling. In the following, we show that the resulting polarisation behaviour of the low-symmetry metamaterial design specifically stems from in-plane (magnetic) interactions between the single SRRs in a unit cell. We want to restrict ourselves to nearest-neighbour interactions only as already next-nearest-neighbour interactions can be assumed to have only little influence (see [79, 80]).

All samples have been fabricated on a glass substrate coated with a 5-nm-thin film of ITO using standard EBL, electron-beam evaporation of the gold film, and a subsequent lift-off procedure. The thickness of the gold layer is 50 nm. The low-symmetry unit cells are arranged in a square lattice with a lattice constant of  $a = 480$  nm and the sample footprint is  $80 \mu\text{m} \times 80 \mu\text{m}$ . An electron micrograph of a representative part of one of the investigated samples is shown in Fig. 5.10(a).

If we assume zero coupling between the neighbouring SRRs in Fig. 5.9(d) in a first step, we can anticipate the corresponding optical response of the metamaterial. In this case, the square unit cell can be decomposed into two parts with equally oriented single SRRs aligned in the vertical (Fig. 5.9(b)) and in the horizontal (Fig. 5.9(c)) direction, respectively. By symmetry, the optical response of the array in Fig. 5.9(b) for horizontal (vertical) incident polarisation is identical to that of Fig. 5.9(c) for vertical (horizontal) polarisation. As a

consequence, for the combined structure (Fig. 5.9(d)) with four non-interacting SRRs in one unit cell, the optical response will be identical for horizontal and vertical polarisation. Additionally, the linear polarisation will be strictly maintained upon transmission for both polarisations in the absence of interactions between the SRRs.

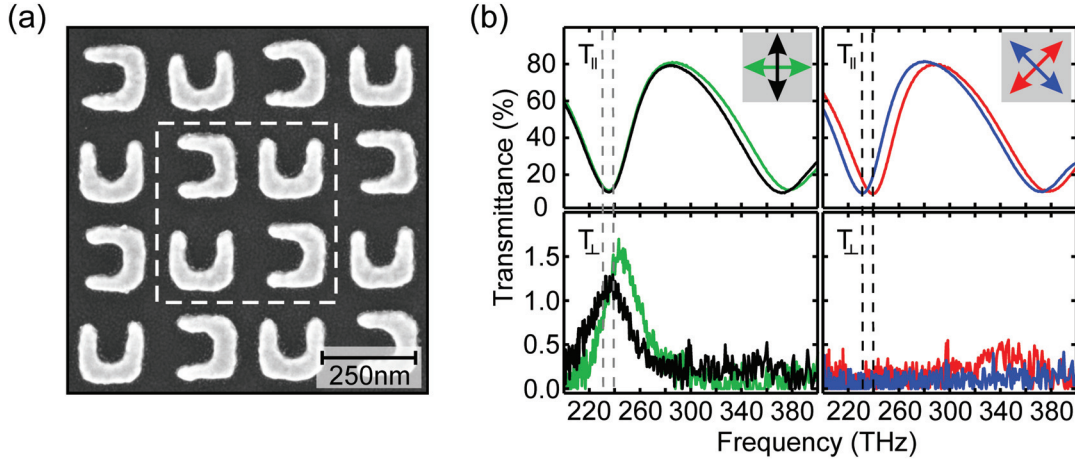


Figure 5.10: (a) Electron micrograph of a representative region of one of the samples under investigation. (b) Measured normal-incidence transmittance spectra.  $T_{\perp}$  (conversion) and  $T_{\parallel}$  refer to detecting the perpendicular and parallel component of the transmitted field with respect to the incident linear polarisation. Owing to SRR interactions the transmittance for horizontal (green) and vertical (black) incidence show non-zero conversion while for  $\pm 45^\circ$ -incidence no polarisation conversion can be detected.

In the next step, we take nearest-neighbour interactions into account. In this case, we can induce a circulating current, hence, a magnetic-dipole moment is induced in one SRR by exciting the neighbouring one. Owing to the specific orientation of the SRRs in the low-symmetry arrangement coupling of the  $90^\circ$ -rotated SRRs leads to substantial conversions of vertical (horizontal) linear incident polarisation into the perpendicular horizontal (vertical) polarisation state. The Jones matrix of the metamaterial design reads

$$\mathbf{J} = \begin{pmatrix} A & \pm B \\ \pm B & A \end{pmatrix}.$$

The polarisation eigenstates of this Jones matrix are given by the diagonal polarisations, *i.e.*,  $+45^\circ$ - and  $-45^\circ$ -linear polarisation. For the two eigenpolarisations, a symmetric and an antisymmetric magnetic mode are excited, respectively. Owing to transverse magnetic coupling the two eigenmodes show different resonance frequencies just like for the two coupled harmonic oscillators in Section 5.1.1: a high-frequency symmetric mode ( $+45^\circ$  incidence), where all four SRRs in the unit cell oscillate in phase, and a low-frequency antisymmetric mode ( $-45^\circ$  incidence), for which one pair of SRRs oscillates with  $180^\circ$  phase shift with respect to the other pair in the unit cell (see Fig. 5.11).

Figure 5.10(b) shows normal-incidence transmittance spectra for four different linear incident polarisations: along the horizontal, the vertical, and along the two diagonal directions. An additional polariser behind the sample allows for measuring the components parallel ( $T_{\parallel}$ ) and perpendicular ( $T_{\perp}$ ) to the incident linear polarisation, respectively. It

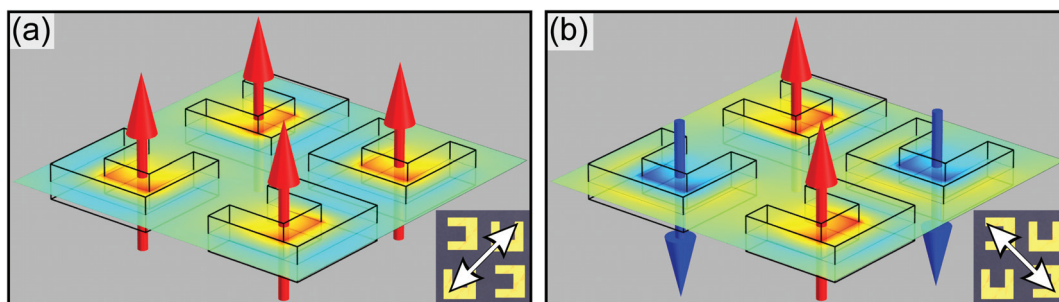


Figure 5.11: Snapshots of the axial magnetic component  $B_z$  in an  $xy$ -plane cutting through the middle of the split-ring resonators (red=positive, green=zero, blue=negative). Depending on the polarisation of the incident light (see white arrows) a symmetric (a) or an antisymmetric (b) configuration of the magnetic dipoles (red and blue arrows) can be observed. If coupling between the magnetic dipoles is present, a splitting of the otherwise degenerate plasmon resonance occurs. The resulting eigenfrequencies of (a) 240 THz and (b) 232 THz are highlighted by the two dashed black vertical lines in Fig. 5.10(b) and Fig. 5.12(b).

becomes obvious that horizontal or vertical linear incident polarisation lead to substantial polarisation conversions ( $T_{\perp} \neq 0$ ). In contrast, no significant conversion is found at all for incident polarisation along either one of the two diagonals which supports that the diagonal polarisations are indeed the eigenpolarisations of the low-symmetry SRR metamaterial. Additionally, we clearly observe two different resonance positions for the perpendicular diagonal polarisations (see two dashed black vertical lines in Fig 5.10(b), right-hand side) – the fingerprint of (magnetic) dipole-dipole coupling. The frequency splitting of about 8 THz between the antisymmetric and the symmetric magnetic modes is about 3.4% of the mean center frequency of 236 THz and indicates fairly strong coupling between the SRRs. Hence, this behaviour originates specifically from mutual interactions and is not expected for non-interacting SRRs. The experimental results suggest that the low-symmetry SRR metamaterial acts as effective waveplate with its two different principal axes along the two diagonals.

In order to support our above interpretation of the experimental results presented in Fig. 5.10(b), we have performed additional numerical calculations using COMSOL Multiphysics (see Fig. 5.12(b)). The geometrical parameters are chosen according to Fig. 5.12(a). The gold permittivity is described by the Drude model using a plasma frequency of  $\omega_{\text{pl}} = 2\pi \times 2108$  THz and a collision frequency  $\omega_{\text{coll}} = 2\pi \times 24$  THz plus a background dielectric constant of  $\epsilon_b = 9.07$ . The refractive index of the glass substrate is taken as  $n_{\text{SiO}_2} = 1.45$ , the thin ITO film is neglected. We use a square unit cell in a square lattice consisting of four SRRs. The calculated normal-incidence transmittance spectra depicted in Fig. 5.12(b) nicely reproduce the experiments shown in Fig. 5.10(b). In particular, both the spectral resonance positions as well as the conversion behaviour (for horizontal and vertical incidence) are reproduced. To further support our interpretation in terms of the eigenmodes of the metamaterial, Fig. 5.11(a)+(b) show snapshots of the calculated axial component of the magnetic field,  $B_z$ , in the plane cutting through the middle of the gold SRRs as false-colour plots. Clearly, the low-frequency resonance at 232 THz corresponds to the antisymmetric eigenmode of the low-symmetry arrangement while the high-frequency

resonance at 240 THz can be identified as the symmetric mode (see Fig. 5.11). Since we have omitted the influence of the glass substrate in our interpretation, we have performed additional calculations without any substrate and found a similar overall behaviour, yet shifted in frequency due to the different dielectric environment (not shown). This indicates that the overall behaviour is an intrinsic effect indeed.

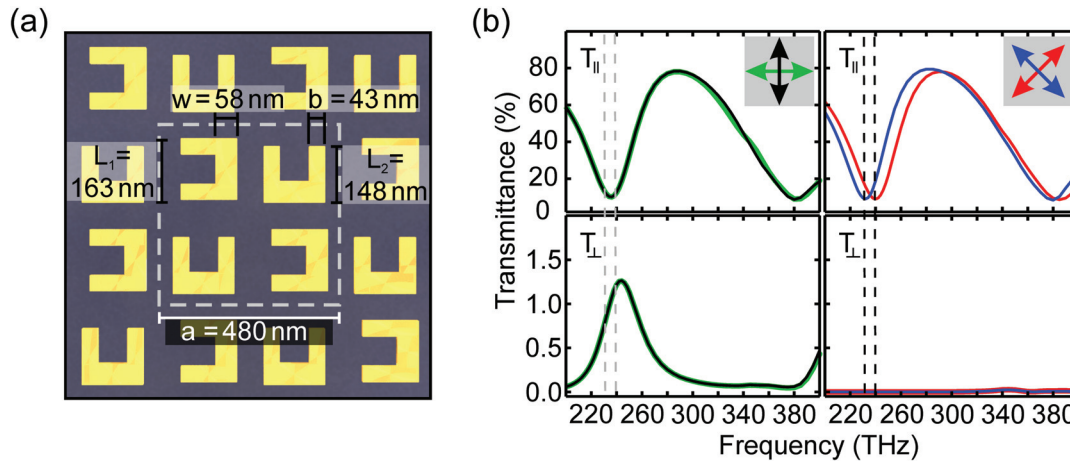


Figure 5.12: (a) Definition of the geometry assumed in our numerical calculations (compare with experiment in Fig. 5.10(a)). The gold thickness is 50 nm. (b) Calculated normal-incidence transmittance spectra that can directly be compared with the experiment in Fig. 5.10(b). The dashed vertical lines indicate the two eigenfrequencies of the symmetric and the antisymmetric mode for which Fig. 5.11 shows field distributions.

Thus, we find that (magnetic) interaction effects between the single functional elements within the unit cell of this metamaterial structure play a major role concerning the polarisation response of the structure. Since the parameters used for this metamaterial design are quite typical for photonic metamaterials (see, *e.g.*, [57, 94–96]) – in particular, the center-to-center SRR spacing in relation to the size – we can conclude that interaction effects between the functional building blocks are far more than a minor variation and have to be accounted for. Under these circumstances, the effective response of the metamaterial cannot be described by the averaged response of a single functional building block anymore.

### 5.2.3 Far-Field Retarded Magnetic-Dipole Interactions

Taking mutual interaction effects between isolated “magnetic atoms” into account, collective magnetic excitations [90], *i.e.*, magnetisation waves can occur for magnetic metamaterials. In particular, for magnetically coupled metamaterials like arrays of SRRs [90, 97–99] or negative-index “fishnet” structures [78] these magnetisation waves can have transversal or longitudinal characteristics depending on the relative arrangement of the “magnetic atoms” [90, 97–99]. However, it has been consistently assumed so far that interactions only take place in the near-fields and, hence, are inherently of short range. In contrast, recent work on pairs of spherical gold nanoparticles [100, 101] and gold/silver nanoparticle chains [102] shows that a quasi-static view on the problem of two or more coupled nanoparticles is not sufficient to describe the dispersive behaviour of the nanoparticle pairs or chains. Instead,

retardation effects have to be considered even for sub-wavelength particle spacings down to  $\lambda/5$  [102]. In the following section we investigate magnetisation waves in the low-symmetry SRR arrangement presented in Section 5.2.2. We demonstrate that (far-field) retardation effects have to be accounted for when modelling the dispersive behaviour of the magnetisation waves [74].

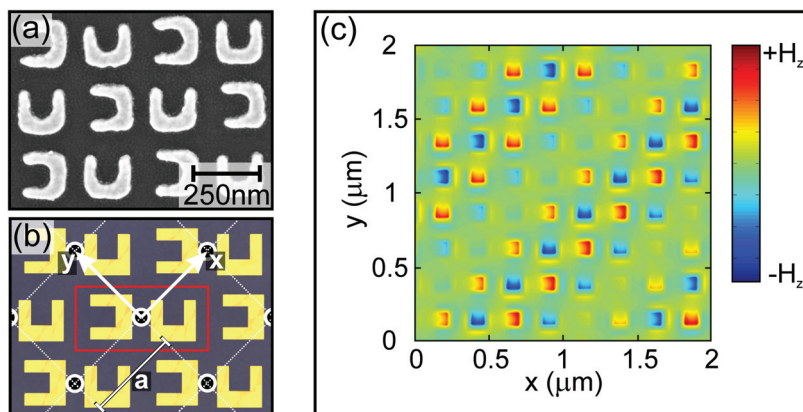


Figure 5.13: (a) Electron micrograph of the low-symmetry split-ring-resonator array under investigation [73, 74]. The primitive unit cell of the metamaterial structure in solid red and the underlying square lattice with lattice constant  $a$  (dashed white) are depicted in (b). Part (c) of the figure shows a snapshot of the axial component of the magnetic field for the “antiferromagnetic” mode at oblique incidence (p-polarisation) at an angle of  $\beta = 45^\circ$  where a magnetisation wave can clearly be observed.

Transverse coupling of the effective magnetic dipoles in the low-symmetry metamaterial design (see, *e.g.*, Fig. 5.13(a)) leads to an antisymmetric low-frequency and a symmetric high-frequency configuration of the magnetic dipoles closely resembling the configuration of quantummechanical orbital momenta or spins in antiferromagnetic and ferromagnetic materials. Despite this obvious analogy there are fundamental differences between magnetic-dipole and spin interactions:

- For one, the magnetic dipoles are inherently connected with the incident light field whereas the spins exist on their own. As a consequence, the magnetic moment of the metamaterial always oscillates in time while a spin-related magnetic moment can be static. Thus, for magnetic metamaterials, the terms “antiferromagnetic” and “ferromagnetic” mode refers to snapshots of the magnetic-dipole moments for a given time.
- Furthermore, the coupling mechanism of the “magnetic atoms” in metamaterials and of the quantum mechanical spins are quite different. For an SRR, interaction takes place *via* the electromagnetic field, which comprises magnetic and electric-dipole moments as well as higher-order magnetic- and electric-multipole moments. Thus, magnetic-dipole waves in metamaterials are always connected with electric-dipole waves. In contrast to that, interactions between spins are mediated by the (indirect) exchange interaction which is not connected with an electric response.

- Finally, the interaction of spins can be considered as instantaneous [103] while information transport *via* the electromagnetic field is limited by the speed of light and therefore subject to retardation.

Being aware of these points, we want to use the terms “antiferromagnetic” and “ferromagnetic” as an intuitive picture for the collective magnetic excitation modes of the metamaterial as illustrated in Fig. 5.13(c).

In the following we investigate the dispersion relation of the in-plane “antiferromagnetic” and “ferromagnetic” magnetisation waves in a low-symmetry planar SRR arrangement. We will show that not only the frequency but also the damping of the metamaterial’s magnetic excitation modes increases or decreases with the in-plane wavenumber depending on the propagation direction. This behaviour indicates direction-dependent retardation effects and shows that the damping of photonic-metamaterial modes is significantly influenced by the interactions among the SRRs and by their relative oscillation phase. This is not surprising since, in contrast to spin interactions, the information propagation over a typical lattice constant  $a$  of an SRR array takes on the order of  $1 - 2$  fs. This is comparable to the oscillation period of the magnetic dipoles in SRRs, resonant at about 200-THz-frequency ( $\approx 5$  fs). Hence, retardation effects can be expected to play a major role [101, 102].

We excite the “ferromagnetic” and the “antiferromagnetic” eigenmodes shown in Fig. 5.11 (a)+(b) by the two orthogonal diagonal linear eigenpolarisations of the low-symmetry SRR array. Having a closer look at the metamaterial’s unit cell in Fig. 5.9(d) these diagonals coincide with the primitive translation vectors of a second underlying square lattice, rotated by  $45^\circ$ . In the following we will refer to the primitive translation vectors as the  $x$ - and  $y$ -direction (see Fig. 5.13(b)). This square lattice has a lattice constant of  $a = \sqrt{2}a' = 339$  nm, where  $a'$  is the center-to-center spacing of the SRRs – in Section 5.2.2, on the contrary, we have used a unit cell with lattice constant  $a = 2a'$  which is different from the primitive unit cell used here and consists of four SRRs (this is owing to limitation of the COMSOL Multiphysics software package described in Chapter 4.3).

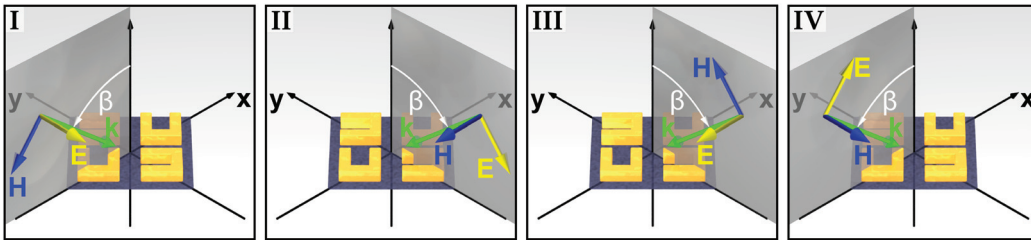


Figure 5.14: Scheme of the four different excitation geometries for oblique incidence of light. In each case, the in-plane wavevector  $\mathbf{k}_{\parallel}$  is parallel to the  $x$ - or the  $y$ -axis of the underlying lattice, hence, either the “antiferromagnetic” (I and II) or the “ferromagnetic” (III and IV) mode is excited. The configurations I and III represent s-polarised incidence while II and IV represent p-polarised incidence.

In order to measure the in-plane dispersion relation  $\omega(\mathbf{k}_{\parallel})$  of the magnetisation waves in the low-symmetry metamaterial directly in an optical experiment [104] we have to perform oblique incidence transmittance measurements [78]. The angle of incidence  $\beta$  together with

the free-space wavelength  $\lambda$  immediately allows for determination of the parallel component of the incident wave vector. It is conserved at the air-metamaterial interface and therefore identical with the in-plane wave vector  $\mathbf{k}_{\parallel}$ . The four different measurement scenarios are illustrated in Fig. 5.14. The corresponding angular eigenfrequency  $\omega = 2\pi \cdot f$  can be obtained by measuring the resonance position in the extinction spectrum (negative logarithm of the transmittance  $T$ ). Selected typical measured extinction spectra are depicted in Fig. 5.15(a).

To improve accuracy and reliability of the angular eigenfrequencies, we determine the resonance position and damping by fitting a Lorentzian to the raw data. Repeating this procedure for positive and negative angles from  $-45^\circ$  to  $+45^\circ$  in steps of  $5^\circ$  (with an opening angle of  $5^\circ$ ) as well as for the different polarisation configurations illustrated in Fig. 5.14 leads to the measured dispersion relation shown in Fig. 5.15(b). Here, we have plotted  $\mathbf{k}_{\parallel}$  in the first Brillouin zone of the primitive real-space unit cell. Angles  $\beta$  up to  $\pm 45^\circ$  with respect to the surface normal correspond to  $|\mathbf{k}_{\parallel}| \approx 0.4 \times \pi/a$ , hence, a substantial fraction of the first Brillouin zone can actually be accessed experimentally.

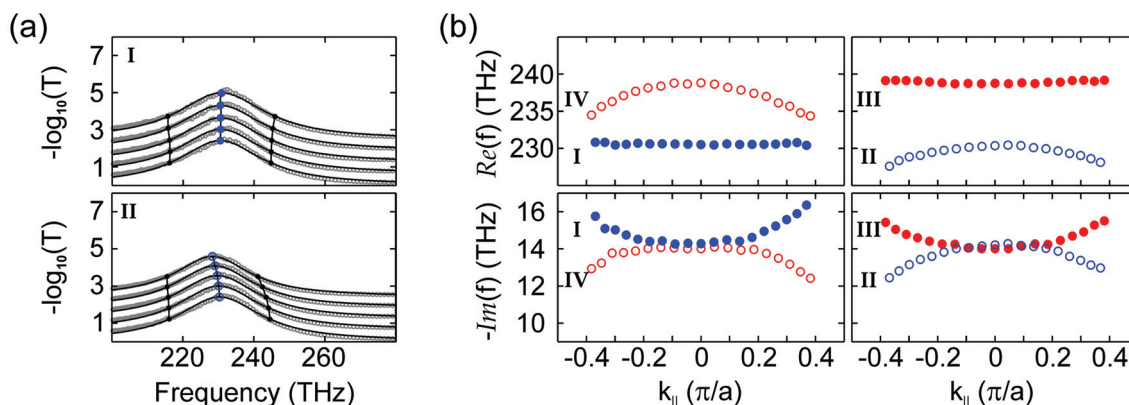


Figure 5.15: (a) Selected measured extinction spectra raw data (gray open circles) together with Lorentz fits in black for the oblique-incidence geometries depicted in Fig. 5.14 (I)-(II). The maximum and median values of the Lorentzians are indicated by the vertical black lines. The angle of incidence  $\beta$  varies from  $0^\circ$  to  $40^\circ$  in steps of  $10^\circ$  (from bottom to top). The spectra are vertically displaced for clarity. The measured extinction spectra for the configurations in Fig. 5.14 (III)-(IV) (not shown) have been evaluated in the same manner. In (b) the dispersion relations  $f(\mathbf{k}_{\parallel}) = \omega(\mathbf{k}_{\parallel})/(2\pi)$  resulting from the raw data for the configurations I-IV illustrated in Fig. 5.14 are presented. The transverse/longitudinal magnetic modes of the “antiferromagnetic” (blue) and the “ferromagnetic” (red) mode are represented by the solid/open circles. The configurations I and IV correspond to  $\mathbf{k}_{\parallel}$  along the  $x$ -direction, II and III to  $\mathbf{k}_{\parallel}$  along the  $y$ -direction.

The results shown in Fig. 5.15 are additionally confirmed by numerical calculations obtained in cooperation with S. Burger at the Zuse Institute in Berlin<sup>2</sup>. We solve Maxwell’s equations using JCMwave<sup>3</sup>, a frequency-domain finite-element solver, and Bloch-periodic boundary conditions in the  $x$ - and  $y$ -direction (see Ref. [78]). For achieving converged results we use higher-order, vectorial finite-elements and adaptive mesh refinement. This treatment clearly includes SRR interactions *via* higher-order multipole moments, interaction

<sup>2</sup>Zuse Institute Berlin, Takustraße 7, D-14195 Berlin, Germany and DFG Forschungszentrum Matheon, Straße des 17. Juni 136, D-10623 Berlin, Germany

<sup>3</sup>JCMSuite, JCMwave GmbH, Germany

effects beyond the nearest neighbours and retardation effects. The sample parameters are chosen identical to those used for our previous normal-incidence experiments presented in Section 5.2.2. Figure 5.16(a) shows selected numerically calculated raw data in analogy to Fig. 5.15(a). The calculated dispersion relation in Fig. 5.16(b) is derived by the same procedure as described above for the experiments. The numerical calculations nicely agree with the experiments shown in 5.15(a) and (b), respectively. Importantly, the behaviour of the four dispersion branches – real parts as well as imaginary parts – evolving out of the “antiferromagnetic” and “ferromagnetic” eigenmode at  $k_{\parallel} = 0$  qualitatively and almost quantitatively agrees with the experiments (compare Fig. 5.15 and 5.16).

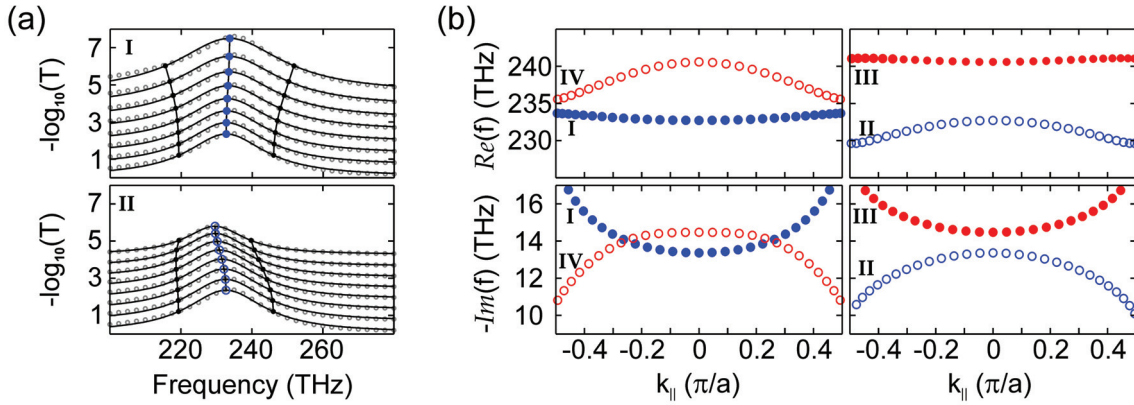


Figure 5.16: Selected calculated extinction spectra that can be compared directly with the experiment shown in Fig. 5.15(a). The angle of incidence  $\beta$  varies from  $0^\circ - 70^\circ$  degrees in steps of  $10^\circ$  (from bottom to top). (b) The resulting dispersion relation from the calculated raw data in (a).

Starting from the low-frequency “antiferromagnetic” and the high-frequency “ferromagnetic” mode at  $k_{\parallel} = 0$  in Fig. 5.15(b) and 5.16(b), four dispersion branches result. The branches are labelled with numbers that refer to the geometries depicted in Fig. 5.14. Although the planar SRR array in Fig. 5.13(b) has no center of inversion, no significant asymmetry of the four dispersion branches can be observed neither in the experiments nor in the calculations. For two of the four branches in Fig. 5.15(b) and 5.16(b), the resonance frequency, *i.e.*,  $Re(f)$  decreases with increasing modulus of the in-plane wavevector. Thus, the wave’s group velocity is antiparallel to its wavevector and therefore antiparallel to its phase velocity as well. This is the characteristic fingerprint of backward waves ( $\mathbf{v}_{\text{phase}} \cdot \mathbf{v}_{\text{group}} < 0$ ) and would lead to negative refraction at an interface in the plane of propagation. The other two dispersion branches exhibit parallel directions of phase and group velocity ( $\mathbf{v}_{\text{phase}} \cdot \mathbf{v}_{\text{group}} > 0$ ). More importantly, all four branches shown in Fig. 5.15(b) and 5.16(b) exhibit a dependence of the mode damping,  $Im(f)$ , on the in-plane wavenumber  $k_{\parallel}$ .

In order to model this specific dispersion behaviour of magnetisation waves in the present low-symmetry arrangement, we use a simple classical one-dimensional harmonic oscillator model. The equation of motion of a (magnetic-) dipole moment (or some higher-order moment)  $m_n(t)$  at time  $t$  and site  $n$  of the lattice reads (in analogy to Section 5.1.1)

$$\ddot{m}_n(t) + 2\gamma \dot{m}_n(t) + \tilde{\Omega}^2 m_n(t) = W\Omega (m_{n-1}(t - t_0) + m_{n+1}(t - t_0)) . \quad (5.4)$$

Here,  $\tilde{\Omega}$  is the eigenfrequency of the undamped system,  $\Omega = \sqrt{\tilde{\Omega}^2 - \gamma^2}$  is eigenfrequency of the damped system with the damping constant  $\gamma$  characteristic for the individual harmonic oscillators. Coupling between the nearest neighbours of the lattice is accounted for by the real coupling frequency  $W$ . The effect of retardation can be described by the time delay  $t_0$ . For time-harmonic behaviour  $\propto \exp(-i\omega t)$ , the time delay  $t_0$  ( $t_0 \geq 0$  due to causality) translates into a phase shift  $\varphi = \omega t_0 \approx \Omega t_0 = \text{const.}$ . The latter approximation is justified under the condition that the actual frequency  $\omega$  will turn out to differ from  $\Omega$  only by a few percent. This leads to the dispersion relation  $\omega(k)$  with complex  $\omega$  at real wavenumber  $k$  given by

$$\text{Re}[\omega] = +\Omega - W \cos(ka) \cos(\varphi), \quad (5.5)$$

$$\text{Im}[\omega] = -\gamma - W \cos(ka) \sin(\varphi). \quad (5.6)$$

Without retardation, *i.e.*, for  $\varphi = 0$ , the usual cosine-shaped magnon dispersion relation [90, 97, 103] is recovered and  $\text{Im}[\omega] = -\gamma$  is constant. In contrast, for finite phase delays,  $\varphi \neq 0$ , both the mode damping,  $\text{Im}[\omega]$ , and the resonance frequency,  $\text{Re}[\omega]$ , become dependent on the wavenumber  $k$ . For the special case of  $\varphi = \pi/2$  the resonance frequency is even independent of the wavenumber,  $\text{Re}[\omega] = \Omega = \text{const.}$ , while only the mode damping,  $\text{Im}[\omega]$ , is dispersive. A positive/negative sign of the real interaction frequency  $W$  indicates longitudinal/transversal coupling of the dipoles, respectively. Additionally the sign of the coupling frequency  $W$  determines whether the mode damping increases or decreases with increasing wavenumber  $k$ . As a consequence, the increase/decrease of the mode damping in the experimental and calculated dispersion curves (see Fig. 5.15(b) and 5.16(b)) clearly confirms the influence of retardation effects in our simple model. Having a closer look at all four dispersion branches, however, we find that the curvature of the dispersion branches cannot be explained by direct coupling of the transverse magnetic moments of the SRRs. Instead, the coupling of the individual magnetic moments is established by indirect interactions *via* the effective electric dipoles of the SRRs. This is roughly similar to the RKKY (Ruderman Kittel Kasuya Yosida) interaction where local magnetic moments couple *via* spin interactions of the conduction-band electrons in metals. Let us therefore assume that electric dipole-dipole interactions are the dominant effect between neighbouring primitive unit cells. In this case, the retardation effects depend on the direction of in-plane wave propagation and, furthermore, they are different for the ‘‘antiferromagnetic’’ and the ‘‘ferromagnetic’’ mode since the total electric-dipole moment of the two SRRs in each primitive unit cell is oriented parallel to the exciting electric-field vector and, hence, oriented along the  $y$ - ( $x$ -) direction (see Fig. 5.13(b)) for the ‘‘antiferromagnetic’’ (‘‘ferromagnetic’’) mode, for normal incidence. The ‘‘antiferromagnetic’’ mode propagating along the  $x$ -direction ( $y$ -direction) therefore turns out to be a transverse (longitudinal) electric-dipole wave. Without retardation ( $\varphi = 0$ ), it is well known that this leads to a decrease (increase) of the real part of the resonance frequency for increasing modulus of the in-plane wavenumber – exactly opposite to the experimental observation in Fig. 5.15(b). Including retardation effects in our reasoning, we find a retardation phase  $\varphi$  in the interval  $90^\circ < \varphi < 270^\circ$  which reverses the sign of the curvature of  $\text{Re}[\omega]$  versus wavenumber since  $\cos(\varphi)$  is negative for

these values. For the “ferromagnetic” mode, an analogous reasoning applies, but  $x$ - and  $y$ -direction have to be interchanged because of the orthogonal orientation of the total electric-dipole moment compared to that of the “antiferromagnetic” mode. This turns transverse into longitudinal waves and vice versa. This reasoning also correctly explains the curvature of the damping,  $-\text{Im}(\omega)$ , for all four dispersion branches, provided that the retardation phase is in the interval  $90^\circ < \varphi < 180^\circ$ . This finally results in an overall agreement of our simple model with the experimental observations in Fig. 5.15(b) and the numerical calculations in Fig. 5.16(b).

We now fit our model functions for the frequency-dispersion (Equation (5.5)) and the dispersion of the damping (Equation (5.6)) to the calculated data and determine both the frequency-coupling constant  $W$  and the retardation phase  $\varphi$  for the four different oblique-incidence configurations I-IV.

For transverse electric-dipole coupling (solid circles) of the “antiferromagnetic” (blue) and the “ferromagnetic” (red) excitation mode, we obtain coupling frequencies of  $W \approx -3.0$  THz and  $W \approx -2.3$  THz as well as retardation phases of  $\varphi \approx 110^\circ$  and  $\varphi \approx 109^\circ$ , respectively. For longitudinal electric-dipole coupling (open circles), values of  $W \approx +4.2$  THz and  $W \approx +6.2$  THz as well as retardation phases of  $\varphi \approx 146^\circ$  and  $\varphi \approx 156^\circ$  can be derived for the “antiferromagnetic” and the “ferromagnetic” excitation mode, respectively. The overall agreement of the calculated dispersion relations and our simple model is indeed

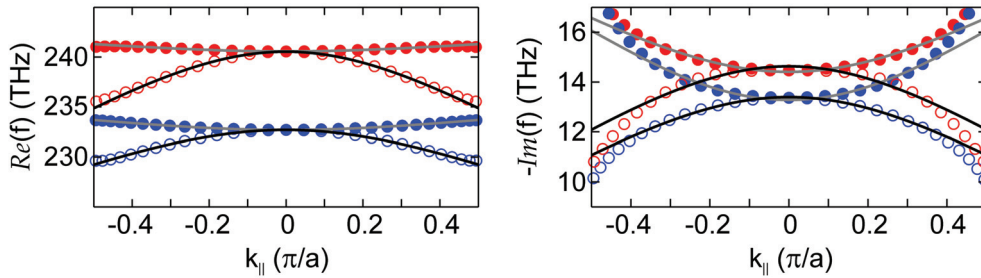


Figure 5.17: Comparison of the calculated dispersion relations shown in Fig. 5.16(b) with our simple model. Fitting of the model dispersion relations given by Equation (5.5) and (5.6) provides values for the coupling frequency  $W$  and the retardation phase  $\varphi$ . The overall behaviour of the four branches of the dispersion relations are nicely reproduced by our model.

quite convincing (see Fig. 5.17). Particularly, positive values of the coupling frequency  $W$  can be attributed to longitudinal electric-dipole coupling while transverse coupling of the electric dipoles indeed is characterised by negative values of  $W$ . Furthermore, the retardation phases  $\varphi$  turn out to be in the range of  $90^\circ < \varphi < 180^\circ$ , consistent with our previous expectations. We therefore conclude that electric dipole-dipole interactions are the dominant effect between neighbouring primitive unit cells. However, the frequency splitting of the “antiferromagnetic” and the “ferromagnetic” mode at zero in-plane momentum cannot be explained by electric dipole-dipole interactions. In this case, the frequency splitting of the “antiferromagnetic” and the “ferromagnetic” mode mainly originates from magnetic dipole-dipole interactions within each primitive unit cell although interaction via higher-order multipole moments are likely to play a role as well. Additionally, we can estimate

the retardation phase  $\varphi$  independently from the model fits presented in Fig. 5.17. Since the lattice constant of  $a = 339$  nm in Fig. 5.13(b) is larger than a quarter of the free-space resonance wavelength of about  $1.25$   $\mu\text{m}$  (equivalent to 240-THz-frequency) we can argue that this indeed leads to a retardation phase exceeding  $90^\circ$ , perfectly consistent with our above discussion. Although this estimate assumes wave propagation with the vacuum speed of light, slower propagation will further increase the estimated retardation phase.

Clearly retardation effects play a crucial role in our low-symmetry metamaterial design as well. We find a significant dispersion of the mode damping which can only be attributed to the influence of retardation between neighbouring metamaterial unit cells. Furthermore, retardation leads to frequency dispersion that cannot be described by the usual cosine-shaped dispersion curves anymore. Once again we conclude that for a common metamaterial designs the effective-medium description can only be seen as a merely good description for metamaterials since interaction and retardation effects between the metamaterial's unit cells result in significant contributions to the optical response.

### 5.3 3D-Coupling of Magnetic Dipoles

In Section 5.2.2 we have already investigated transverse magnetic coupling of the planar SRR arrangement shown in Fig. 5.9(d). If we now think of a metamaterial unit cell that consists of two SRRs aligned on top of each other, but separated by a dielectric spacer layer, as depicted in Fig. 5.18 we should be able to observe a similar frequency splitting or hybridisation to the one presented in Section 5.2.2 but for longitudinal coupling of the magnetic moments. With the help of the simple Lorentz-oscillator model introduced in Section 5.1 we conclude that the symmetric configuration of magnetic dipoles is the low-energy mode while the antisymmetric oscillation mode is the high-energy mode.

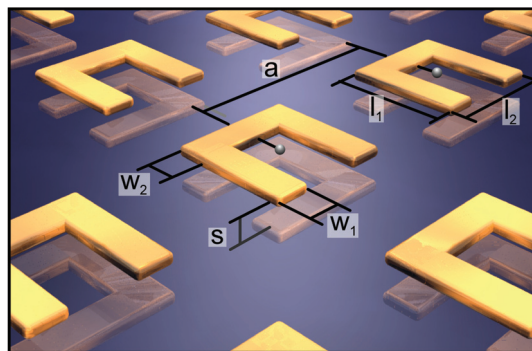


Figure 5.18: Illustration of the calculated design. The geometry dimensions of the split-ring resonators are  $l_1 = l_2 = 240$  nm,  $w_1 = 60$  nm and  $w_2 = 70$  nm. The lattice constant is  $a = 400$  nm. The thickness of the gold split-ring resonators is 25 nm.

Such metamaterials consisting of the same fundamental building block like, *e.g.*, an SRR but differing in the actual spacial arrangement of the constituents have recently been named “stereometamaterials” in analogy to stereoisomers in chemistry [76]. In the case of the “twisted” SRRs the relative in-plane rotation angle  $\alpha$  indeed determines the coupling

mechanism and therefore the optical response of the SRR dimers – for  $\alpha = 0^\circ$  and  $\alpha = 180^\circ$  the (transverse) dipole-dipole interactions of the effective electric-dipole moments of the single SRRs dominate, while for  $\alpha = \pm 90^\circ$  the longitudinal magnetic dipole-dipole coupling is of fundamental importance. Both arrangements give rise to a plasmon hybridisation, *i.e.*, to a symmetric and an antisymmetric arrangement of the effective dipoles [76] which is caused by electric or magnetic coupling mechanisms, respectively. In order to investigate longitudinal coupling of magnetic dipoles we therefore choose an SRR dimer characterised by a relative in-plane rotation angle of  $\alpha = 90^\circ$  (see Fig. 5.18).

We calculate the transmittance spectra for an ideal twisted-SRR structure embedded in vacuum and determine the eigenpolarisations of the twisted-SRR metamaterial design using COMSOL Multiphysics. The gold is modeled by a Drude model with plasma frequency  $\omega_{\text{pl}} = 2\pi \times 2155$  THz and collision frequency  $\omega_{\text{coll}} = 2\pi \times 30$  THz plus a background dielectric constant of  $\epsilon_b = 9.0685$ . The lateral geometrical parameters are shown in Fig. 5.18, the gold thickness is 25 nm. We varied the interparticle spacing from  $s = 100$  nm down to  $s = 25$  nm in steps of 25 nm. For the ideal case, we indeed observe a splitting of the magnetic resonance at an interparticle spacing below  $s = 50$  nm (see Fig. 5.19). The transmittance dip at lower/higher wavelengths corresponds to the antisymmetric/symmetric magnetic mode (see also Ref. [76]). Owing to the lack of rotational symmetry around the SRR-dimer axis, however, linear birefringence occurs even for the ideal structure, *i.e.*, linear-x/linear-y incident light shows significant intensity conversion into linear-y/linear-x polarisation. This results in elliptically polarised eigenstates (not shown).

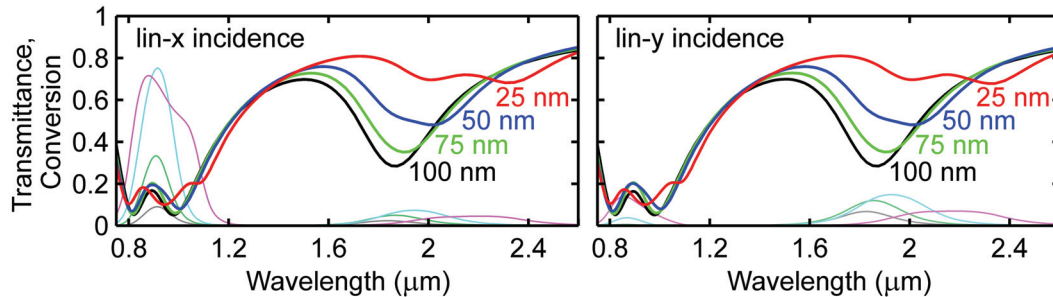


Figure 5.19: Calculated transmittance spectra of an ideal twisted split-ring-resonator structure embedded in vacuum are shown for linear-x (left-hand side) and linear-y (right-hand side) incident polarisation. The transmittance for four different interparticle spacings  $s$  between the split-ring resonators are plotted:  $s = 25$  nm (red),  $s = 50$  nm (blue),  $s = 75$  nm (green) and  $s = 100$  nm (black). The corresponding linear conversion spectra are shown in magenta, cyan, dark green and gray. They exhibit strong linear birefringence.

In principle the twisted-SRR design presented here is a blueprint for a so-called chiral metamaterial. For this material class the coupling of the electric and the magnetic field components is of fundamental importance. Owing to the strong linear birefringence, however, the twisted-SRR design has to be modified to obtain a truly chiral optical response. The resulting chiral twisted-SRR metamaterial design introduced in Chapter 8.2 shows indeed pronounced longitudinal magnetic coupling between the SRRs in the two layers, hence, large frequency splitting of the high-energy antisymmetric and the low-energy

symmetric mode (see Chapter 8.2). Furthermore, the modified design does not show any linear birefringence thus it exhibits a purely chiral optical response.



# Chapter 6

## An Introduction to Chirality

The principle motivation for investigating chiral metamaterials is their potential for manipulating the polarisation state of light. Historically, chirality is indeed inherently connected with optical activity, *i.e.*, the ability of a variety of substances to rotate the polarisation plane of incident linearly polarised light. Hence, it is not surprising that the investigation of optically active materials finally resulted in the discovery of the influence of a substance's handedness on the direction of polarisation rotation of light. Louis Pasteur was the first to attribute the sign of polarisation rotation to the different mirror symmetric forms of the substance under observation, namely tartaric acid, in 1849 [1]. Despite previous work on the

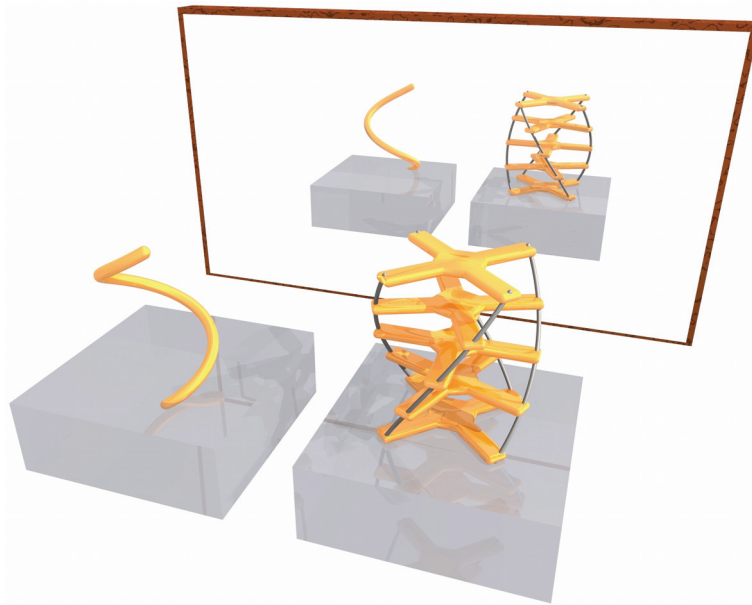


Figure 6.1: Artist's view of a right-handed helix (left) and a right-handed twisted-crosses design (right) and their mirror images. The five-layer twisted-crosses design is the one-pitch equivalent to the two-layer twisted-crosses metamaterial design introduced in Chapter 8.1.

optical rotatory power (optical activity) of, *e.g.*, quartz (by Arago in 1811) and turpentine (by Biot in 1812-15), Pasteur realised the importance of dissymmetry, *i.e.*, the relationship between the two forms of handedness of tartaric acid crystals (tartrate) and optical activity.

In particular, a solution of a purely right-handed (left-handed) tartrate led to a clockwise (anticlockwise) rotation of linear polarisation in contrast to a solution with equal amounts of both varieties (also known as racemic mixture) which left the initial polarisation state of light unchanged.

In general, optical activity is observed for two types of chiral media. For one, the effect of optical rotation in fluids can only result from the intrinsic chiral properties of the single molecules (molecular chirality). This is the case for a solution of sugar, for tartaric acid or in turpentine gas, for example. Secondly, chiral effects can also be produced by the crystalline structure of a material like a quartz crystal, for example (structural chirality). In this case, however, the effect of optical activity is restricted to the propagation parallel to the crystal's symmetry axis ( $c$ -axis). Consequently, for an isotropic optically active medium molecular chirality is a fundamental prerequisite.

The idea of combining the concepts of chirality and metamaterials gives us the opportunity to change the polarisation state of light. This chapter aims at giving the reader a basic understanding of how a chiral metamaterial should look like in terms of symmetry properties and how these properties transfer to the material parameters in the Maxwell's equations. We will have a look on the transmittance and reflectance spectra of a model system of a chiral material slab at normal incidence and introduce a procedure to derive the effective material parameters from the transmittance and reflectance spectra of a chiral medium. Then we will have a short look at the reflection and refraction behaviour of circularly polarised light at oblique incidence on an interface between a chiral and an achiral medium before we finally conclude with a detailed description of how circularly polarised light is generated and analysed in experiments.

## 6.1 A Geometrical View on Chirality

It was not before 1894 until the term “chirality” (from the greek word “ $\chi\epsilon\iota\rho$ ” meaning “hand”) was introduced by Lord Kelvin in a footnote of his lectures on “The Molecular Tactics of a Crystal” at the Oxford University Junior Science Club [105]. In the lectures Lord Kelvin stated:

*“I call any geometrical figure, or group of points, chiral, and say that it has chirality, if its image in a mirror, ideally realised, cannot be brought to coincide with itself”*

An object as described by Lord Kelvin has no mirror planes, no center of inversion and no rotation-reflection axes. Two representatives of chiral structures in the sense of Lord Kelvins definition are illustrated in Fig. 6.1. Following this recipe, the first artificial composite chiral medium was fabricated in 1898 by J. C. Bose [2] who literally twisted bundles of parallel jute fibres to measure the optical rotatory power of this chiral composite material in the radio-frequency spectral range.

Later, at the beginning of the 20th century, Paul Drude introduced a new concept to describe optical activity. Based on his previous model for the optical response of metals, he claimed, that “vibrations of charged particles” moving along a helix-shaped trajectory [3]

show optical rotatory power and deduced an analytical expression for the rotation angle of a linearly-polarised incident light beam which was verified by K. F. Lindman [4] in 1920. Presumably, Lindman fabricated the first chiral metamaterial at 13-cm-wavelength (1-MHz to 3-MHz-frequency) when he manually bent  $2 \times 500$  copper helices with a diameter of 1 cm and a height of about 2 cm and wrapped them in cotton balls to measure the optical rotatory power. His measurement revealed that the optical rotatory power of the helical composite structure reaches that of natural materials like in a sugar solution. Lindman verified Drudes prediction which can be summarised in the following four points:

- Optical activity can be described by a difference in the refractive indices for right-handed circularly polarised (RCP) light and left-handed circularly polarised (LCP) light for negligible differences in the absorption.
- The rotation angle is then given by  $\delta = z \cdot \frac{\pi}{\lambda_0} (n_{\text{RCP}} - n_{\text{LCP}})$ , where  $z$  is the propagation length in the chiral medium.
- The wavelength dependency of the rotation shows a resonant behaviour given by  $\delta(\lambda) \propto \frac{1}{\lambda^2 - \lambda_h^2}$ , where  $\lambda_h$  is the resonance wavelength of the “vibration”.
- A helix shaped “vibration of charged particles” is connected to a magnetic moment. Consequently there is a coupling of the electric and the magnetic field components (“magnetolectric coupling”).

Paul Drude suggested that optically active (chiral) media can be described by constitutive material relations accounting for magnetolectric coupling. He formulated a set of constitutive material equations equivalent to the equations presented in the next section. In the following, we will derive an explicit form of the constitutive material equations for chiral (and bianisotropic) media.

## 6.2 Effective Chiral Media

According to Drude, the main ingredient for obtaining a chiral response is the possibility to excite a magnetisation by an incident electric field and to excite an electric polarisation by an incident magnetic field. This magnetolectric coupling generally results in bianisotropic materials which can be described by modified effective material equations in which the coupling of the electric and the magnetic response is included.

$$\mathbf{D} = \epsilon_0 \bar{\epsilon} \mathbf{E} + \frac{\bar{\xi}}{c_0} \mathbf{H} \quad (6.1)$$

$$\mathbf{B} = \frac{\bar{\zeta}}{c_0} \mathbf{E} + \mu_0 \bar{\mu} \mathbf{H} \quad (6.2)$$

The material equations show the general linear effective parameter relations for bianisotropic media, where  $\bar{\epsilon}$ ,  $\bar{\mu}$ ,  $\bar{\xi}$  and  $\bar{\zeta}$  are tensors. For simplicity, we assume  $\epsilon$  and  $\mu$  being scalars in the following.

Due to the strong constraint of reciprocity of Maxwell's equations, the coupling coefficient of the electric field component to the magnetic field component  $\bar{\xi}$  and the coupling coefficient for the magnetic field component to the electric field component  $\bar{\zeta}$  have to be directly connected to each other. Hence, the relation  $\bar{\zeta} = -\bar{\xi}^t$  has to be fulfilled (see Ref. [42]), leading to

$$\mathbf{D} = \epsilon_0 \epsilon \mathbf{E} - \frac{\bar{\xi}}{c_0} \mathbf{H} \quad (6.3)$$

$$\mathbf{B} = \frac{\bar{\zeta}^t}{c_0} \mathbf{E} + \mu_0 \mu \mathbf{H}. \quad (6.4)$$

Now equations (6.3) and (6.4) describe a bianisotropic reciprocal effective material with scalar permittivity  $\epsilon$  and permeability  $\mu$ . If one further assumes that the magnetic/electric dipoles excited by the incident electric/magnetic field are oriented parallel to the incident electric/magnetic field vector, a diagonal form of  $\bar{\xi}$  results and one ends up with a reciprocal biisotropic material also referred to as isotropic chiral or Pasteur medium.

It is therefore of particular interest to compare chiral and bianisotropic media. This comparison is highlighted in the next section.

### 6.2.1 Symmetry Constraints

In this section we want to derive a set of constraints that have to be fulfilled for the effective material parameters of a medium exhibiting specific symmetry properties. In the course of this discussion, we neglect mutual interactions between different unit cells of the medium. Afterwards we will make use of these constraints when we derive and compare the effective material parameters for a chiral and a bianisotropic metamaterial design.

In order to make a statement on the effective material parameters of a given metamaterial it is essential to classify its electromagnetic response when illuminated by a plane wave. Assuming that the field response of the fundamental building blocks reflects the geometrical symmetry properties of the metal nanostructures we can derive specific selection rules for the tensor components of the effective parameter  $\bar{\xi}$  in the Maxwell's equations. However, this assumption has to be taken with great caution, as in practice (see Chapter 7.1 and 7.4) the apparent geometrical characteristics can be different from the actual field distributions excited by the incident plane wave – the latter being the relevant basis for the effective parameter evaluation. Keeping this in mind we derive the selection rules for the tensor components of  $\bar{\xi}$  for some basic symmetry properties, namely:

- Center of inversion
- Mirror planes
- Rotations.

As we assume the permittivity  $\bar{\epsilon}$  and permeability  $\bar{\mu}$  to be scalar, we are only interested in the magnetoelectric properties and restrict ourselves to the class of bianisotropic materials. From there we will go on to the subclass of biisotropic (chiral) materials.

The starting point of the following discussion is the general form of  $\bar{\xi}$  with initially nine independent entries:

$$\bar{\xi} = \begin{pmatrix} \xi_{xx} & \xi_{yx} & \xi_{zx} \\ \xi_{xy} & \xi_{yy} & \xi_{zy} \\ \xi_{xz} & \xi_{yz} & \xi_{zz} \end{pmatrix} \quad (6.5)$$

Taking into account that for each transformation the constitutive equations (6.3) and (6.4) have to be fulfilled, we finally end up with a distinct set of selection rules for this specific transformation. This provides the entries of  $\bar{\xi}$ . In the following we assume an electromagnetic wave propagating in the  $z$ -direction:

$$\mathbf{E} = \begin{pmatrix} E_x \\ E_y \\ 0 \end{pmatrix} e^{i(k_z z - \omega t)} \quad (6.6)$$

$$\mathbf{B} = \begin{pmatrix} B_x \\ B_y \\ 0 \end{pmatrix} e^{i(k_z z - \omega t)} = \frac{k_z}{\omega} \begin{pmatrix} -E_y \\ E_x \\ 0 \end{pmatrix} e^{i(k_z z - \omega t)} \quad (6.7)$$

Due to Faraday's induction law (2.3)  $\mathbf{k}$ ,  $\mathbf{E}$  and  $\mathbf{B}$  form a right-handed coordinate system.

### Center of Inversion

Applying the symmetry operation of space inversion to an electromagnetic wave and fulfilling Equation (2.3) gives us the transformations:

$$\mathbf{k} \rightarrow -\mathbf{k} \qquad \mathbf{E} \rightarrow -\mathbf{E} \qquad \mathbf{B} \rightarrow \mathbf{B} \quad (6.8)$$

After space inversion the material equations (6.3) and (6.4) still have to be valid:

$$\begin{aligned} B_x &= \frac{1}{c_0} (\xi_{xx} E_x + \xi_{yx} E_y) + \mu\mu_0 H_x \\ &\quad \downarrow \\ B_x &= \frac{1}{c_0} (-\xi_{xx} E_x - \xi_{yx} E_y) + \mu\mu_0 H_x \end{aligned}$$

and

$$\begin{aligned} B_y &= \frac{1}{c_0} (\xi_{xy} E_x + \xi_{yy} E_y) + \mu\mu_0 H_y \\ &\quad \downarrow \\ B_y &= \frac{1}{c_0} (-\xi_{xy} E_x - \xi_{yy} E_y) + \mu\mu_0 H_y \end{aligned}$$

This yields the conditions  $\xi_{xx} = -\xi_{xx}$ ,  $\xi_{xy} = -\xi_{xy}$ ,  $\xi_{yx} = -\xi_{yx}$  and  $\xi_{yy} = -\xi_{yy}$  which can only be fulfilled for  $\bar{\xi} = 0$ . Thus, neither chiral nor bianisotropic materials with inversion symmetry exist.

### Mirror Planes

For a plane wave with  $\mathbf{E} = (E_x, E_y, 0)$  and  $\mathbf{B} = k_z/\omega(-E_y, E_x, 0)$  we have to consider three possible mirror planes.

- The  $xz$ -plane as mirror plane transforms

$$k_z \rightarrow k_z \quad E_x \rightarrow E_x \quad B_x \rightarrow -B_x \quad E_y \rightarrow -E_y \quad B_y \rightarrow B_y \quad (6.9)$$

implying:

$$\begin{aligned} B_x &= \frac{1}{c_0} (\xi_{xx} E_x + \xi_{yx} E_y) + \mu\mu_0 H_x \\ &\quad \downarrow \\ B_x &= \frac{1}{c_0} (-\xi_{xx} E_x + \xi_{yx} E_y) + \mu\mu_0 H_x \end{aligned}$$

and

$$\begin{aligned} B_y &= \frac{1}{c_0} (\xi_{xy} E_x + \xi_{yy} E_y) + \mu\mu_0 H_y \\ &\quad \downarrow \\ B_y &= \frac{1}{c_0} (\xi_{xy} E_x - \xi_{yy} E_y) + \mu\mu_0 H_y \end{aligned}$$

Altogether we obtain  $\xi_{xx} = \xi_{yy} = 0$  while  $\xi_{xy}$  and  $\xi_{yx}$  can be nonzero.

- The  $yz$ -plane. Following the same reasoning as above for the  $xz$ -plane we get the same results for the entries of  $\bar{\xi}$  namely  $\xi_{xx} = \xi_{yy} = 0$ ,  $\xi_{xy}$  and  $\xi_{yx}$  can be nonzero – as expected from symmetry.
- The  $xy$ -plane is different from the  $xz$ - and the  $yz$ -plane as it is oriented perpendicular to the wave vector of the incident wave. We obtain the following transformations:

$$k_z \rightarrow -k_z \quad E_x \rightarrow E_x \quad B_x \rightarrow -B_x \quad E_y \rightarrow E_y \quad B_y \rightarrow -B_y \quad (6.10)$$

Consequently:

$$\begin{aligned} B_x &= \frac{1}{c_0} (\xi_{xx} E_x + \xi_{yx} E_y) + \mu\mu_0 H_x \\ &\quad \downarrow \\ B_x &= -\frac{1}{c_0} (\xi_{xx} E_x + \xi_{yx} E_y) + \mu\mu_0 H_x \end{aligned}$$

and

$$\begin{aligned} B_y &= \frac{1}{c_0} (\xi_{xy} E_x + \xi_{yy} E_y) + \mu\mu_0 H_y \\ &\quad \downarrow \\ B_y &= -\frac{1}{c_0} (\xi_{xy} E_x + \xi_{yy} E_y) + \mu\mu_0 H_y \end{aligned}$$

This can only be fulfilled provided that  $\xi_{xx} = \xi_{yy} = \xi_{xy} = \xi_{yx} = 0$ . Once again neither chirality nor bianisotropy are observable for propagation in  $z$ -direction.

### Rotations

Rotations around one axis leave the orientation of an object unchanged. They can be described by a specific unitary rotation matrix  $\overline{U}_i$  for each of the rotation axes ( $x$ -,  $y$ -, and  $z$ -axis). Again we assume that the geometrical symmetry of a structure is reflected in the optical response. Consequently, if an object is invariant under a specific rotation  $\overline{U}$ , the electric and magnetic fields have to be invariant as well. Applying this condition to the general material equation (6.4) leads us to the condition

$$\begin{aligned} \mathbf{B} &= \frac{1}{c_0} \overline{\xi} \mathbf{E} + \mu_0 \mu \mathbf{H} \\ &\downarrow \\ \mathbf{B}' &= \frac{1}{c_0} \overline{\xi}' \mathbf{E}' + \mu_0 \mu \mathbf{H}' \\ &\downarrow \\ \overline{U} \mathbf{B} &= \frac{1}{c_0} \overline{U} \overline{\xi} \overline{U}^{-1} \overline{U} \mathbf{E} + \mu_0 \mu \overline{U} \mathbf{H} \end{aligned}$$

where  $\mathbf{B}' = \overline{U} \mathbf{B}$ ,  $\mathbf{E}' = \overline{U} \mathbf{E}$  and  $\overline{\xi}' = \overline{U} \overline{\xi} \overline{U}^{-1}$  are the respective quantities  $\mathbf{B}$ ,  $\mathbf{E}$  and  $\overline{\xi}$  after rotation. Hence an object's property of invariance under the rotation  $\overline{U}$  is expressed by the constraint

$$\overline{\xi}' = \overline{U} \overline{\xi} \overline{U}^{-1} = \overline{\xi} \quad (6.11)$$

For a three-dimensional isotropic medium Equation (6.11) has to be fulfilled for all rotations around the  $x$ -,  $y$ - and  $z$ -axis. This finally results in:

(a) **purely bianisotropic materials** characterised by:

$$\overline{\xi} = \xi' \begin{pmatrix} 0 & 1 & -1 \\ -1 & 0 & 1 \\ 1 & -1 & 0 \end{pmatrix} \quad (6.12)$$

(b) **purely biisotropic chiral materials** characterised by:

$$\overline{\xi} = \xi \begin{pmatrix} 1 & 0 & 0 \\ 0 & 1 & 0 \\ 0 & 0 & 1 \end{pmatrix} \quad (6.13)$$

As a final result we obtain two scalar values  $\xi'$  and  $\xi$  specific for bianisotropic and biisotropic chiral media, respectively. In contrast to bianisotropic media, which are characterised by the off-diagonal elements of  $\overline{\xi}$ , chiral media can be distinguished by the diagonal (in 2D) or even scalar form (in 3D) of  $\overline{\xi}$ . It is important to notice that the effective material parameters  $\epsilon$ ,  $\mu$  and  $\xi$  ( $\epsilon$ ,  $\mu$  and  $\xi'$ ) for chiral (bianisotropic) media are not independent of each other but connected *via* energy conservation required for passive media (see Chapter 2.2).

### 6.2.2 Bianisotropy vs. Chirality

After the preceding general treatment of symmetry properties and their influence on the effective material parameters, we now want to discuss two examples of metamaterial designs

that have already been published – a chiral twisted-crosses design from Ref. [43] and a bianisotropic design similar to Ref. [106]. Starting from the symmetry properties of the two structure designs, we want to derive an explicit form for the material parameter  $\bar{\xi}$  for both cases. Both structures are assumed to be arranged in a periodic lattice in the  $xy$ -plane.

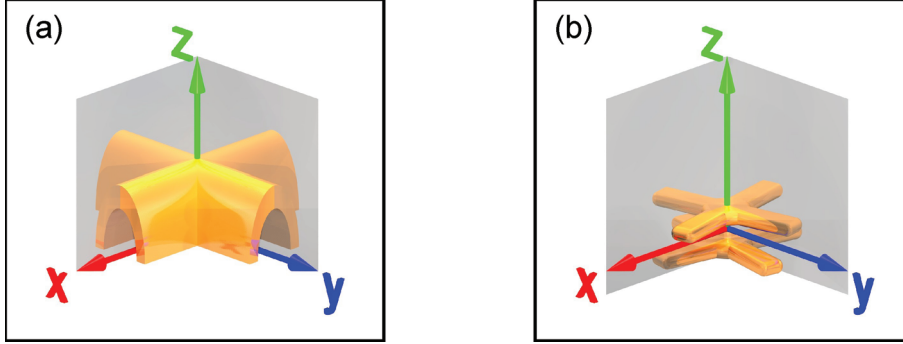


Figure 6.2: (a) Bianisotropic split-ring-resonator design with  $C_{4v}$ -symmetry [106]. (b) Chiral twisted-crosses design with  $C_4$ -symmetry [43].

The incident plane wave propagates in the  $z$ -direction. It is therefore sufficient to analyse the coupling of the electric and magnetic field components in the  $xy$ -plane. Consequently  $\bar{\xi}$  reduces to

$$\bar{\xi} = \begin{pmatrix} \xi_{xx} & \xi_{yx} \\ \xi_{xy} & \xi_{yy} \end{pmatrix} \quad (6.14)$$

For an arbitrary rotation ( $\phi_z$ ) around the  $z$ -axis we use

$$\bar{U}_z = \begin{pmatrix} \cos(\phi_z) & -\sin(\phi_z) \\ \sin(\phi_z) & \cos(\phi_z) \end{pmatrix} \quad (6.15)$$

Following our reasoning of the last section we derive the effective material parameters  $\bar{\xi}$  for a bianisotropic (a) and a biisotropic chiral (b) metamaterial.

## Symmetry

First, the symmetry properties of the two designs (a) and (b) shown in Fig. 6.2 have to be identified.

- (a) **bianisotropic SRR design:**
- 4-fold rotational symmetry in the  $xy$ -plane
  - 2 mirror planes ( $xz$ - and  $yz$ -plane)
  - no rotational symmetry in the  $xz$ - and  $yz$ -plane
  - Symmetry group  $C_{4v}$ ,  $D_4$

- (b) **chiral twisted-crosses design:**
- 4-fold rotational symmetry in the  $xy$ -plane
  - no mirror planes
  - 2-fold rotational symmetry in the  $xz$ - and  $yz$ -plane
  - Symmetry group  $C_4$

Applying Equation (6.11) to a structure with 4-fold rotational symmetry in the  $xy$ -plane yields

$$\bar{\xi} = \begin{pmatrix} \xi_{xx} & \xi_{yx} \\ \xi_{xy} & \xi_{yy} \end{pmatrix} \rightarrow \bar{\xi} = \begin{pmatrix} \xi_{xx} & \xi_{yx} \\ -\xi_{yx} & \xi_{xx} \end{pmatrix} = \bar{\xi}'. \quad (6.16)$$

This result is valid for both, the bianisotropic (a) and the chiral (b) design. Differences occur when having a closer look at the out-of-plane rotation axes (like, *e.g.*, the  $x$ -axis) and the mirror planes.

- (a) **bianisotropic SRR design:**

The two mirror planes ( $xz$ - and  $yz$ -plane) result in the additional requirement that  $\xi_{xx} = \xi_{yy} = 0$ , hence,

$$\bar{\xi} = \xi' \begin{pmatrix} 0 & 1 \\ -1 & 0 \end{pmatrix}. \quad (6.17)$$

- (b) **chiral twisted-crosses design:**

The two-fold rotational symmetry in the  $xz$ - and  $yz$ -plane results in the additional condition  $\xi_{yx} = \xi_{xy} = 0$ , hence,

$$\bar{\xi} = \xi \begin{pmatrix} 1 & 0 \\ 0 & 1 \end{pmatrix}. \quad (6.18)$$

Obviously, the 2D-uniaxial variants of the material parameters for the bianisotropic (a) and the biisotropic chiral design (b) are consistent with the three-dimensional counterparts given by Equation (6.12) and (6.13) for normal incidence.

## 6.3 Wave Propagation in Chiral Media

Having found the general form of the effective material equations for a chiral medium,

$$\mathbf{D} = \epsilon\epsilon_0\mathbf{E} - \frac{\xi}{c_0}\mathbf{H} \quad (6.19)$$

$$\mathbf{B} = \frac{\xi}{c_0}\mathbf{E} + \mu\mu_0\mathbf{H}, \quad (6.20)$$

we can further investigate the properties of a plane wave propagating in this medium. The basic equation for this process is the chiral wave equation, that can be derived directly from Maxwell's equations (2.1)-(2.4) (see Appendix A.1).

$$\nabla^2\mathbf{E} + 2i\frac{\omega\xi}{c_0}\nabla \times \mathbf{E} + \frac{\omega^2}{c_0^2}(\mu\epsilon + \xi^2)\mathbf{E} = 0 \quad (6.21)$$

Obviously in a chiral medium there is a coupling of the  $x$ -,  $y$ -, and  $z$ -components of the electric/magnetic field vector. Thus, linearly polarised light cannot be a polarisation eigenstate of the wave equation anymore. As Equation (6.21) is an eigenvalue problem for the electric/magnetic field vector, we can determine the eigenvalues of Equation (6.21) to calculate the polarisation eigenstates and to find an expression for the refractive index in a chiral medium. For a plane wave propagating in  $z$ -direction

$$\mathbf{E} = \begin{pmatrix} E_x \\ E_y \\ 0 \end{pmatrix} \cdot e^{i(k_z z - \omega t)} \quad (6.22)$$

the solution of the eigenvalue problem yields two eigenvalues, *i.e.*, two dispersion relations  $k_z(\omega)$  for a chiral medium.

$$k_z^2 = k_{1,2}^2 = \frac{\omega^2}{c_0^2} (\sqrt{\mu\epsilon} \mp i\xi)^2 = \frac{\omega^2}{c_0^2} \cdot n_{1,2}^2 \quad (6.23)$$

Hence the two refractive indices are

$$n_{1,2} = \sqrt{\mu\epsilon} \mp i\xi. \quad (6.24)$$

For the field components  $E_x$  and  $E_y$  we obtain two solutions

$$E_y = \mp i E_x \quad (6.25)$$

corresponding to right-handed circular polarisation (RCP) and left-handed circular polarisation (LCP). For a detailed derivation of the preceding results, we refer to Appendix A.1.

If we further substitute  $\xi = i\kappa$ , we can summarise the results for the propagation properties of a plane wave in a chiral medium as we can find it in many textbooks, *e.g.*, Ref. [42].

### Plane Wave Properties in Chiral Media

- The constitutive material equations for a chiral medium are:

$$\mathbf{D} = \epsilon\epsilon_0 \mathbf{E} - i \frac{\kappa}{c_0} \mathbf{H} \quad (6.26)$$

$$\mathbf{B} = i \frac{\kappa}{c_0} \mathbf{E} + \mu\mu_0 \mathbf{H} \quad (6.27)$$

where  $\kappa$  is the so-called chirality parameter.

- The polarisation eigenstates of plane wave propagation are circular polarisations,

$$\mathbf{E}_+ = \mathbf{E}_{\text{RCP}} = \frac{1}{\sqrt{2}} \begin{pmatrix} 1 \\ -i \\ 0 \end{pmatrix} \cdot e^{i(k_+ z - \omega t)} \quad (6.28)$$

and

$$\mathbf{E}_- = \mathbf{E}_{\text{LCP}} = \frac{1}{\sqrt{2}} \begin{pmatrix} 1 \\ i \\ 0 \end{pmatrix} \cdot e^{i(k_- z - \omega t)} \quad (6.29)$$

namely right-handed circular polarisation (RCP, “+”) and left-handed circular polarisation (LCP, “-”).

- The impedance of circularly polarised light in a chiral medium is given by (see Appendix A.1)

$$Z_+ = Z_- = \sqrt{\frac{\mu}{\epsilon}} \cdot Z_0 \quad (6.30)$$

Remarkably, the impedances ( $Z_+$  and  $Z_-$ ) for RCP and LCP light are identical and do not depend on the chirality parameter.

- The refractive index for circularly polarised incident light is then given by:

$$n_{1,2} = n_{\text{RCP,LCP}} = n_{\pm} = \sqrt{\mu\epsilon} \pm \kappa \quad (6.31)$$

Apparently, chiral media open up an alternative route to a negative refractive index. In particular, by varying only  $\kappa$ , we can obtain a negative refractive index for one circular polarisation even if  $\epsilon$  and  $\mu$  are both positive.

## 6.4 Reflection and Transmission of Chiral Media

In the preceding sections we found that circularly polarised light is the eigenpolarisation of the wave equation for chiral media. Thus, we can describe the transmission and reflection properties for RCP and LCP incidence in a circular polarisation basis using the corresponding refractive index ( $n_+$  and  $n_-$ ) and impedance ( $Z_+$  and  $Z_-$ ) of the polarisation state under consideration. Only in this basis, the use of a refractive index for chiral media is justified. In the first part of this section, we deal with normal incidence of circular polarisation onto a chiral slab. Here, the handedness of the incident circularly polarised light is conserved for the transmitted wave and flipped for the reflected light beam<sup>1</sup>. Hence, intensity conversion from RCP to LCP light and *vice versa* is absent in transmission. For oblique incidence, the situation is more complicated. In the second part of this section we therefore investigate the influence of a chiral interface on the polarisation state of an incident circularly polarised light beam impinging at an arbitrary angle.

<sup>1</sup>Although in reflection RCP/LCP incident light emerges as LCP/RCP light this must not be confused with polarisation conversion. To understand this point, let us decompose circularly polarised light into s-polarised field components and p-polarised field components. Upon reflection there is a change of sign for the s-polarised field component while the p-polarised component remains unaffected. This phaseshift of one linear component of the circular polarisation leads to a change of handedness – circularly polarised light therefore changes its handedness when reflected from an interface.

### 6.4.1 Normal Incidence on a Chiral slab

In order to obtain the normal incidence transmittance and reflectance spectra we use an analytical model of an SRR [61] to account for the magnetoelectric coupling and calculate the reflectance and transmittance spectra through such a chiral slab by inserting the complex effective material parameters, namely the refractive indices into a plane wave *ansatz*. The chiral material parameter values  $\epsilon$ ,  $\mu$  and  $\kappa$  (see Fig. 6.3) are given as:

$$\epsilon(\omega) = 1 + \left( \frac{dc_0}{l^2} \right)^2 \frac{F}{\omega_{LC}^2 - \omega^2 - i\gamma\omega} \quad (6.32)$$

$$\mu(\omega) = 1 + \frac{F\omega^2}{\omega_{LC}^2 - \omega^2 - i\gamma\omega} \quad (6.33)$$

$$\kappa(\omega) = - \left( \frac{dc_0}{l^2} \right) \frac{F\omega}{\omega_{LC}^2 - \omega^2 - i\gamma\omega} \quad (6.34)$$

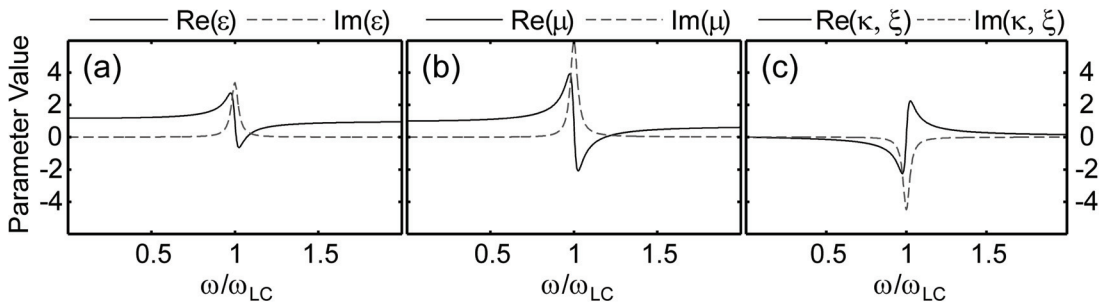


Figure 6.3: The parameters of the analytical model are given by the slab thickness  $d = c_0\pi/\omega_{LC}$ ,  $dc_0/l^2 = 0.75 \cdot \omega_{LC}$ ,  $F = 0.3$  and  $\gamma/\omega_{LC} = 0.05$ . The calculated effective material parameters  $\epsilon$ ,  $\mu$ ,  $\kappa$  (for a chiral medium) and  $\xi$  (for a bianisotropic medium) are shown in (a)-(c). The material slab is situated on a glass substrate ( $\epsilon = 2.25$ ).

This results in the refractive index curves and in the transmittance/reflectance spectra shown in Fig. 6.4. Indeed the spectra reflect the chiral properties of the medium:

- RCP and LCP are indeed eigenpolarisations in a chiral medium. Hence, incident RCP/LCP light emerges as RCP/LCP light in transmittance – no polarisation conversion from RCP to LCP and *vice versa* is present (not shown).
- The two refractive indices  $n_{\pm} = \sqrt{\mu\epsilon} \pm \kappa$  result in different transmittance spectra for RCP and LCP, respectively. This difference is due to the chirality parameter  $\kappa$  only.
- As for a purely chiral medium the impedances for RCP and LCP are identical, the reflectance spectra are identical as well.
- Due to symmetry (a right-handed helix remains right-handed when observed from the backside), the spectra for forward and backward propagation are the same for a chiral medium (not shown).

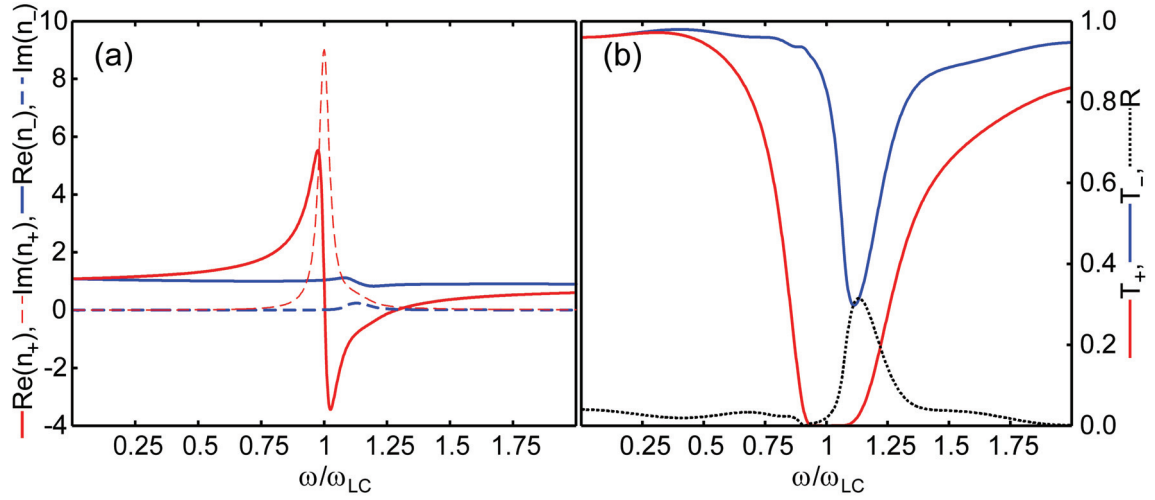


Figure 6.4: Model calculation of a chiral design with the model parameters shown in Fig. 6.3(a)-(c). The transmittance spectra (b) show a polarisation dependence owing to different refractive indices (a) for RCP (“+”, red) and LCP (“-”, blue) light. As a result, strong circular dichroism ( $\Delta T = T_+ - T_-$ ) occurs. The reflectance spectra (b) for RCP and LCP are identical as the impedances for the two circular polarisations are identical ( $Z_+ = Z_- = Z$ ).

Using the equivalent material parameters as for the chiral medium, we can also calculate the spectra for a purely bianisotropic material and compare them with the spectra for the chiral medium. This is indeed of particular interest as for a bianisotropic material linear polarisation is conserved on transmission despite magnetoelectric coupling. From Equation (2.49) and (2.50) we obtain (see also Fig. 6.5) [61]:

- Two values for the impedance of a bianisotropic medium, one for propagation in forward direction  $Z_f$  and one for propagation in backward direction  $Z_b$ . We consequently obtain two different reflectance spectra  $R_f \neq R_b$ .
- The refractive index  $n = \sqrt{\epsilon\mu - \xi^2}$  of a bianisotropic medium is identical in forward and backward direction. Therefore the transmittances  $T_f = T_b = T$  are identical.

Obviously, the optical properties of chiral and bianisotropic materials strongly differ from each other although the material equations seem to be very similar at first sight.

### Chiral Parameter Retrieval

To determine the effective material parameters of chiral metamaterials from experiments, we have to follow the same approach as for normal isotropic metamaterials (see Chapter 2.2.2). As one often has access to the transmittance spectra only, the complex-valued transmission has to be obtained from numerical calculations in order to retrieve the effective material parameters. However, in contrast to the retrieval procedure for isotropic media introduced in Chapter 2.2.2 we are now dealing with a different class of materials. In the case of chiral media, we have to determine the additional material parameter  $\kappa$ . It is therefore necessary to take both RCP and LCP transmission and reflection spectra into account (see Fig. 6.6).

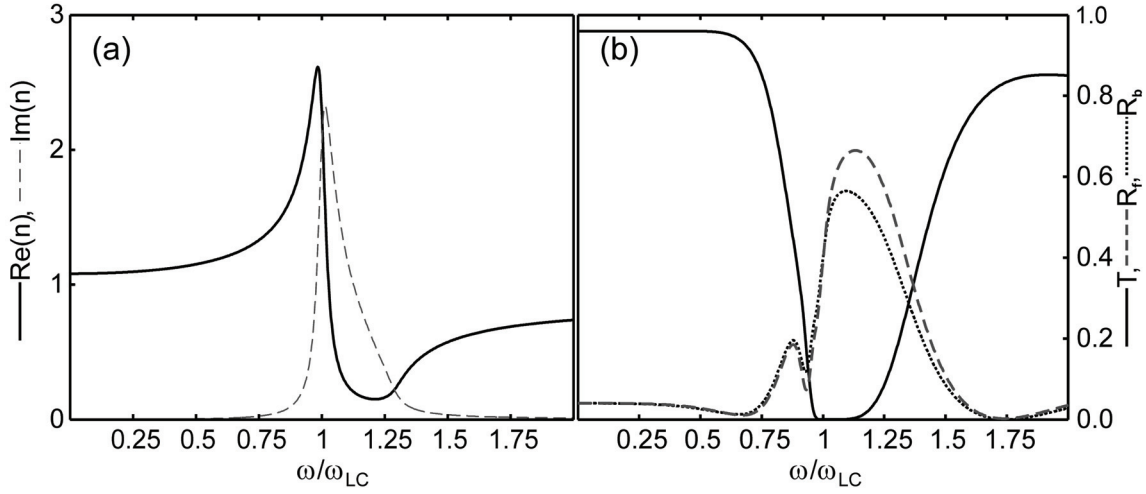


Figure 6.5: Model calculation of a bianisotropic design with the model parameters depicted in Fig. 6.3(a)-(c). The real (solid) and imaginary (dashed) parts of the refractive index for bianisotropic media (a) is independent of the propagation direction. Hence, the transmittances in forward-  $T_f$  and backward  $T_b$  direction are equal ( $T_f = T_b = T$ ) while the reflectances  $R_f$  and  $R_b$  differ owing to the different impedances  $Z_f \neq Z_b$  (not shown).

As a result we obtain different expressions for the impedance  $Z$  and the refractive indices  $n_{\pm}$  [107] (for details we refer to Appendix A.2). For reciprocal chiral media we deduce (see Appendix A.2):

$$0 = [(1+r)^2 - t_+ t_-] \left( \frac{1}{Z} \right)^2 + \frac{t_+ t_-}{Z_t^2} - \frac{(1-r)^2}{Z_i^2} \quad (6.35)$$

and

$$\cos(n_{\pm} k_0 d) = \frac{1}{2} \left[ \frac{(1+r)/Z + (1-r)/Z_i}{t_{\pm} \left( \frac{1}{Z_t} + \frac{1}{Z} \right)} + \frac{(1-r)/Z_i - (1+r)/Z}{t_{\mp} \left( \frac{1}{Z_t} - \frac{1}{Z} \right)} \right], \quad (6.36)$$

where  $r = r_+ = r_-$  is the complex-valued reflection coefficient,  $t_{\pm}$  are the transmission coefficients for RCP/LCP light and  $Z_i$  ( $Z_t$ ) is the impedance of the front (back) side dielectric medium. Once again, energy conservation and the demand of a passive material resolves the ambiguities for  $Re[Z]$ ,  $Im[Z]$ ,  $Im[n]$  and  $Re[n]$ . Then the effective parameter values can be calculated by:

$$n = \frac{1}{2} (n_+ + n_-), \quad \kappa = \frac{1}{2} (n_+ - n_-), \quad \mu = Zn, \quad \epsilon = \frac{n}{Z}. \quad (6.37)$$

However, the effective parameter retrieval for chiral media is subject to the same physical restrictions as the isotropic retrieval in Chapter 2.2.2. Particularly, for resonant structures, effective parameters gained from the retrieval procedure have to be taken with caution.

## 6.4.2 Oblique Incidence on Chiral Interfaces

In contrast to normal incidence of circularly polarised light onto a chiral slab, the situation for oblique incidence is more subtle since the interface “mixes” circular polarisations. In

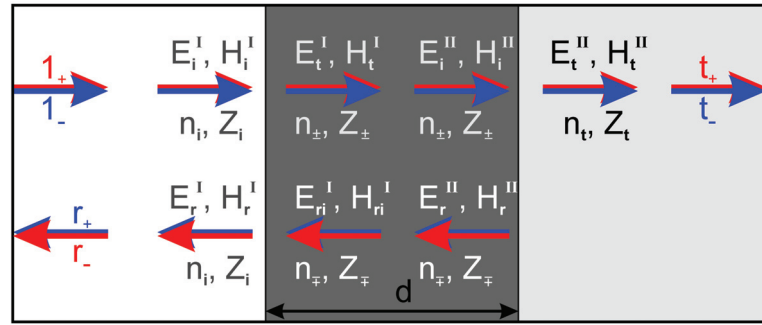


Figure 6.6: Schematic illustration of the field components for the generalised version of the Fresnel equations for the retrieval of the effective material parameters of a chiral material slab of thickness  $d$  from the complex reflection and transmission coefficients. For the chiral retrieval procedure, the different polarisation states have to be taken into account for the determination of the refractive indices  $n_{\pm}$ , impedances  $Z_{\pm}$ , permeability  $\mu$ , permittivity  $\epsilon$  and chirality parameter  $\kappa$ . Note that the backward propagating light changes handedness.

the following we want to put our focus on the behaviour of circularly polarised light when it passes an interface from an achiral to a chiral halfspace and *vice versa*.

In general, we will observe two refracted or reflected circularly polarised light beams emerging from the interface. Hence, the transmitted and reflected light is a superposition of RCP and LCP partial waves [108, 109] and will generally be elliptically polarised. The different refractive indices for RCP and LCP light result in different angles of refraction or reflection [109]. Thus the emerging (refracted or reflected) light splits up again into two circularly polarised beams. Keeping this in mind we can now have a look at the angles of the reflected and transmitted light beams for two basic configurations:

### Birefracton

When a circularly polarised plane wave impinges at an angle  $\theta_i$  from an isotropic dielectric halfspace onto a chiral halfspace, we get two partial waves for the refracted beam and two partial waves for the reflected beam. The reflected RCP and LCP partial wave both are reflected at the same angle ( $\theta_{r\pm} = \theta_i$ ) as the refractive index of the dielectric is independent of the polarisation state of light. The transmitted RCP and LCP partial waves in the chiral medium on the contrary are refracted differently as  $n_+ \neq n_-$ . We therefore get two angles of refraction (birefracton),  $\theta_{t+}$  for the RCP and  $\theta_{t-}$  for the LCP partial wave. This configuration is illustrated in Fig. 6.7(a).

### Bireflection

If we now send RCP (LCP) light from the opposite direction onto the interface (from the chiral medium into the achiral medium) we obtain once again two partial waves for the reflected and for the refracted beam. The RCP and LCP partial waves now are reflected at different angles  $\theta_{r+} \neq \theta_{r-}$  as  $n_+ \neq n_-$ . For the two transmitted partial waves we obtain the same angle of refraction ( $\theta_{t+} = \theta_{t-} = \theta_t$ ) as the refractive index of the dielectric medium is insensitive to the polarisation state of the partial waves. We therefore obtain bireflection

(see Fig. 6.7(b)). In both cases total internal reflection can be observed when one (or both) circularly polarised partial wave becomes evanescent [108, 110].

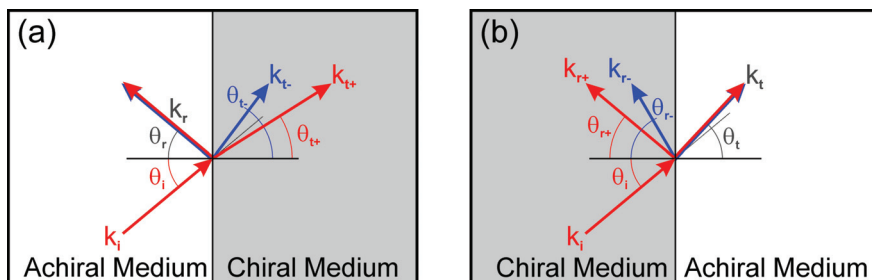


Figure 6.7: The effect of birefractive (a) and bireflection (b) for an RCP (red) light beam has its origin in the different behaviour of the two reflected and refracted partial waves. Due to the different refractive indices for the RCP (red) and the LCP (blue) partial wave in the chiral medium two different angles of refraction (a) and reflection (b) result, respectively.

Another remarkable special case is the reflection of circularly polarised light at the interface of a strongly chiral medium and a perfectly conducting plane. In this configuration, when the refractive index of one circular polarisation becomes negative, even negative reflection occurs which allows for focussing one circular polarisation (see Fig. 6.8) [109] just like a flat reflecting lens.

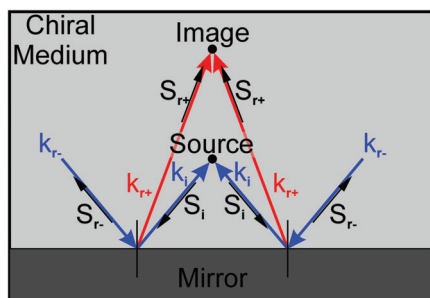


Figure 6.8: Negative reflection can occur if circularly polarised light is reflected at the interface of a strongly chiral medium and a mirror. This effect can be used to focus one circular polarisation on an image plane in front of the mirror.

## 6.5 Polarisation Spectroscopy

For experiments at normal incidence, chiral metamaterials are characterised by circular polarisation eigenstates of the chiral wave equation 6.21. As a consequence, any change in the phase delay, resulting from  $Re[n_+] \neq Re[n_-]$  of one circular polarisation with respect to the other, leads to a rotation of the polarisation axis, *i.e.*, to optical activity (see Fig. 6.9(a)). Additionally,  $Im[n_+] \neq Im[n_-]$  causes circular dichroism (see Fig. 6.9(b)) that corresponds to different absorption coefficients for the two circular polarisations. Hence, the different dispersive behaviour of RCP and LCP light in chiral media always translates into a change of the polarisation state of non-circularly polarised incident light.

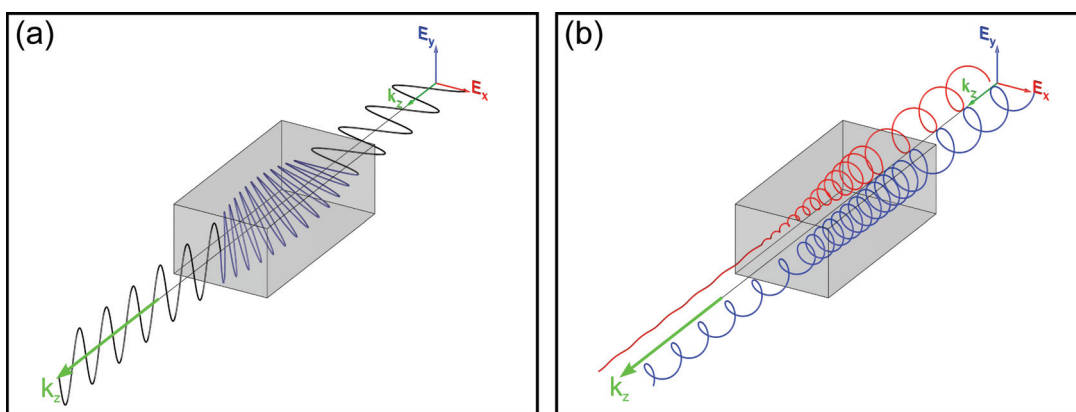


Figure 6.9: (a) Optical activity caused by propagation through an optically active medium. Owing to  $Re[n_+] \neq Re[n_-]$  the polarisation plane of the incident light is rotated by an angle  $\varphi$  ( $\varphi = 90^\circ$  in this case). The emerging plane wave is still linearly polarised. (b) Circular dichroism ( $Im[n_+] \neq Im[n_-]$ ) causes higher absorption losses for one circular polarisation (RCP in red) with respect to the perpendicular circular polarisation (LCP in blue). The emerging polarisation state of light is elliptical polarisation, in general.

In the following, we want to give a short introduction to the different polarisation states that can be obtained for a plane wave emerging from a chiral material slab. We want to provide some simple tools used in this Thesis to transform from a linear to a circular basis and to determine the actual polarisation state of light from numerical calculations. We also want to give a short summary of the different conventions used for plane-wave propagation, the polarisation state of circularly polarised light and the observer's point of view on the handedness of the field vectors (in space and time).

Having introduced these tools, we will finally put our focus on the manifestation of optical activity and circular dichroism in optical transmittance spectra.

### 6.5.1 Calculation of the Polarisation State of Light

A transverse electromagnetic wave is always characterised by a polarisation vector for the electric field component and the corresponding perpendicular polarisation vector for the magnetic field component. For linear polarisation the orientation of the polarisation vector does not depend on time, hence the direction of the E-field vector and the B-field vector

is conserved. Owing to the superposition principle, we can obtain linear polarisation with an arbitrary angle  $\varphi$  with respect to the  $x$ -axis by a superposition of two linearly polarised waves with the same frequency  $\omega$  and wavevector  $\mathbf{k}$ :

$$\mathbf{E}_x(z, t) = E_{0x}e^{i(k_z z - \omega t)} \cdot \hat{e}_x \quad (6.38)$$

$$\mathbf{E}_y(z, t) = E_{0y}e^{i(k_z z - \omega t)} \cdot \hat{e}_y \quad (6.39)$$

When the ratio of the field amplitudes is changed (see Fig. 6.10(a)), *e.g.*, by introducing different absorption coefficients, an inclination angle of the E-field vector results. This angle is given by

$$\tan(\varphi) = \frac{E_{0y}}{E_{0x}}. \quad (6.40)$$

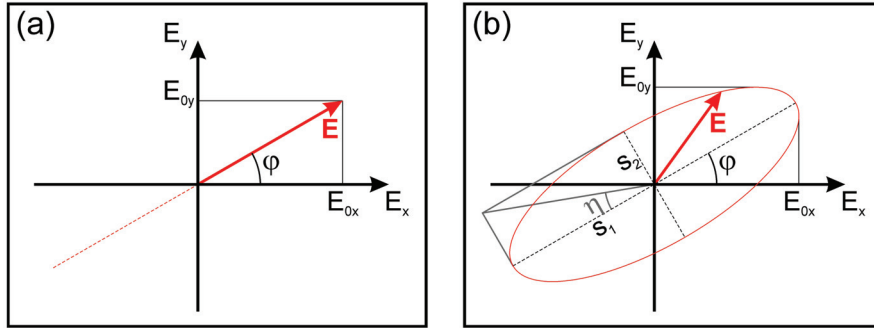


Figure 6.10: (a) By in-phase superposition of two linear polarisations  $\mathbf{E}_x$ ,  $\mathbf{E}_y$  an arbitrary angle  $\varphi$  of the polarisation plane with respect to the coordinate axes can be obtained. (b) After transmission through an arbitrary medium an emerging plane wave is elliptically polarised, in general. The resulting polarisation ellipse is given by the inclination  $\varphi$  between the major axis and the  $x$ -axis and the ellipticity  $e = \tan(\eta) = s_2/s_1$  ( $-1 \leq e \leq +1$ ) which is the ratio of the minor to the major axis of the polarisation ellipse.

Such a change of polarisation *via* selective absorption is obtained in dichroic crystals like tourmaline and even in a simple linear polariser. Note that this is not an isotropic effect since the rotation angle  $\varphi$  depends on the orientation of the field components with respect to the crystal axis.

If we now introduce a relative phase difference  $\theta = \theta_y - \theta_x$  between the two (perpendicular) linear polarisations

$$\mathbf{E}_x(z, t) = E_{0x}e^{i(kz - \omega t + \theta_x)} \cdot \hat{e}_x = E_{0x}e^{i(kz - \omega t)} \cdot \hat{e}_x \quad (6.41)$$

$$\mathbf{E}_y(z, t) = E_{0y}e^{i(kz - \omega t + \theta_y)} \cdot \hat{e}_y = E_{0y}e^{i(kz - \omega t + \theta_y - \theta_x)} \cdot \hat{e}_y \quad (6.42)$$

the resulting polarisation state of light turns out to be elliptical, in general. The orientation of the polarisation plane therefore varies in time and, for a fixed position in space, the tip of the electric (magnetic) field component moves on an elliptical trajectory (see Fig. 6.10(b)) that can be described by [17]

$$\left(\frac{E_x}{E_{x0}}\right)^2 + \left(\frac{E_y}{E_{y0}}\right)^2 - 2\left(\frac{E_x}{E_{x0}}\right)\left(\frac{E_y}{E_{y0}}\right)\cos(\theta) = \sin^2(\theta). \quad (6.43)$$

The actual polarisation state of light can be derived from the complex (electric) field components in the  $x$ - and the  $y$ -direction (see Appendix A.3 and [111]) given by

$$\mathbf{E}(t) \stackrel{z=0}{\equiv} \mathbf{E}_0 e^{-i\omega t}. \quad (6.44)$$

We therefore define the real-valued quantities:

$$\mathbf{p} \equiv \text{Re}[\mathbf{E}_0] \quad (6.45)$$

$$\mathbf{q} \equiv \text{Im}[\mathbf{E}_0] \quad (6.46)$$

For a snapshot of the electric field component at a fixed position see Fig. 6.11.

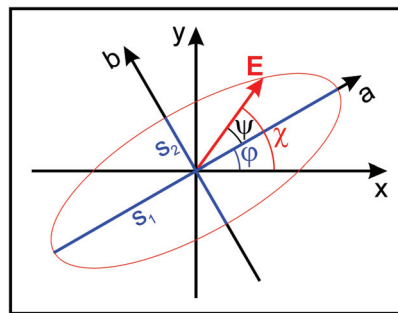


Figure 6.11: The polarisation ellipse is characterised by the major axis  $s_1$  and the minor axis  $s_2$  as well as by the inclination  $\varphi$  of the major axis with respect to the  $x$ -axis. To calculate the ratio of the axes  $e$  and the inclination  $\varphi$  a transformation into a coordinate system parallel to the axes of the ellipse ( $a$  and  $b$ ) is necessary.

### Ellipticity

Following Appendix A.3 we derive an expression for the length of the minor and the major axis of the polarisation ellipse:

$$s_1^2 = \frac{1}{2} \left( p^2 - q^2 + \sqrt{(p^2 - q^2)^2 + 4(\mathbf{p} \cdot \mathbf{q})^2} \right) \quad (6.47)$$

and

$$s_2^2 = \frac{1}{2} \left( p^2 - q^2 - \sqrt{(p^2 - q^2)^2 + 4(\mathbf{p} \cdot \mathbf{q})^2} \right) \quad (6.48)$$

The ellipticity is given by the ratio of the minor to the major axis

$$e = s_2/s_1. \quad (6.49)$$

The sign of the relative phase difference  $\theta = \theta_y - \theta_x$  of the  $x$ - and the  $y$ -component of the electric field determines the sense of rotation ( $\theta < 0$  for RCP and  $\theta > 0$  for LCP). As a consequence,  $e = +1$  corresponds to RCP light and  $e = -1$  corresponds to LCP light ( $-1 \leq e \leq +1$ ).

### Rotation Angle

The inclination  $\varphi$  can be calculated (see Appendix A.3) with the help of the angle  $\chi$  between the  $x$ -axis and the complex E-field vector at a given time ( $t = 0$ )

$$\cos \chi = \frac{p_x}{|\mathbf{p}|} \quad (6.50)$$

and the angle  $\psi$  between the major axis and the E-field vector at the same point in time

$$\tan \psi = -\frac{s_2}{s_1} \tan \theta, \quad (6.51)$$

where

$$\tan(2\theta) = \frac{2\mathbf{p} \cdot \mathbf{q}}{\mathbf{p}^2 + \mathbf{q}^2}. \quad (6.52)$$

With the help of Fig. 6.11 we find the inclination of the major axis with respect to the  $x$ -axis to be

$$\varphi = \chi - \psi. \quad (6.53)$$

The calculation of the polarisation state of light from the complex field vector according to Appendix A.3 was implemented in MATLAB and used to evaluate the numerical calculations of the transmission data of the structures fabricated in this Thesis.

### 6.5.2 Circular Polarisation

If in Equation (6.43) we set  $E_{x0} = E_{y0} = E_0$  and choose the relative phase difference to be  $\varphi = \pi/2$  we obtain

$$E_x^2 + E_y^2 = E_0^2. \quad (6.54)$$

Obviously, the tip of the electric field moves on a circle (for a fixed position in space) resulting in a circular polarisation state. We can find two circular polarisations:

- for right-handed circular polarisation (RCP) the  $y$ -component of the E-field is delayed by  $\theta = -\pi/2$  with respect to the  $x$ -component.
- for left-handed circular polarisation (RCP) the  $y$ -component of the E-field is delayed by  $\theta = +\pi/2$  with respect to the  $x$ -component.

Hence for a circularly polarised plane wave propagating in  $z$ -direction this results in:

$$\mathbf{E}_+ = \mathbf{E}_{\text{RCP}} = \frac{1}{\sqrt{2}} \begin{pmatrix} 1 \\ -i \end{pmatrix} \cdot e^{i(k_+z - \omega t)} \quad (6.55)$$

and

$$\mathbf{E}_- = \mathbf{E}_{\text{LCP}} = \frac{1}{\sqrt{2}} \begin{pmatrix} 1 \\ i \end{pmatrix} \cdot e^{i(k_-z - \omega t)} \quad (6.56)$$

In order to determine the spatial behaviour of the E-field vector for a given time ( $t = 0$ ) and to compare it with the time dependent behaviour at a fixed position ( $z = 0$ ) we have to look at the real parts of the field components

$$\begin{aligned} \text{Re} [\mathbf{E}_{\pm}] &= \text{Re} \left[ \frac{1}{\sqrt{2}} \begin{pmatrix} 1 \\ \mp i \end{pmatrix} \cdot e^{i(k_{\pm}z - \omega t)} \right] \\ &= \frac{1}{\sqrt{2}} \begin{pmatrix} \cos(k_{\pm}z - \omega t) \\ \cos(k_{\pm}z - \omega t \mp \pi/2) \end{pmatrix}. \end{aligned} \quad (6.57)$$

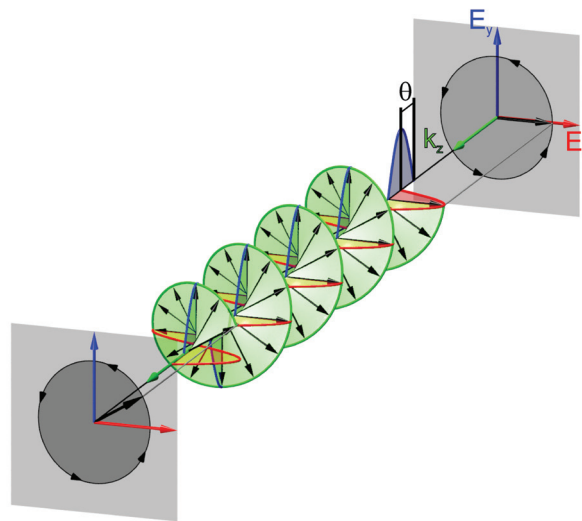


Figure 6.12: Left-handed circular polarisation (LCP) is a superposition of a linear-x polarised wave with a linear-y polarised wave of the same amplitude which is delayed by a relative phase factor of  $\theta = +\pi/2$ . From a detector's point of view the electric field vector rotates counterclockwise at a fixed position. For a given time, the field vector describes a left-handed helix in space.

Now we can investigate the time dependency ( $z = 0$ ) and the space dependency ( $t = 0$ ) separately (see Table 6.1). As a result we find that the field vectors of an RCP wave move on a right-handed helix (in space) for a given time and rotate clockwise (in time) in a plane at a fixed position in space while an LCP wave moves on a left-handed helix in space and rotates counterclockwise in time when propagating in positive  $z$ -direction.

### Circular Polarisation in Physics and Engineering

So far when we talked about circular polarisation we tacitly made some assumptions concerning the observer's point of view and the definition of a plane wave, namely:

- The plane wave is given by  $\mathbf{E}(z, t) = \text{Re} [\mathbf{E}_0 \exp(i(k_z z - \omega t))]$  and
- The observer sees the plane wave from a detectors point of view. Hence, the plane wave propagates towards the observer.

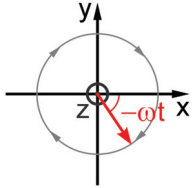
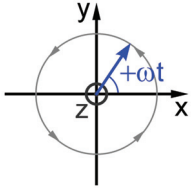
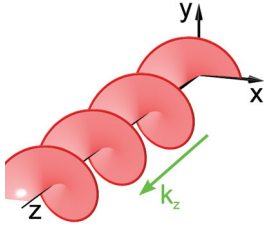
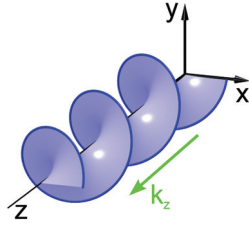
$z = 0$		$t = 0$	
+/RCP	-/LCP	+/RCP	-/LCP
$Re [\mathbf{E}_+ (z = 0)]$ $\propto \begin{pmatrix} \cos(\omega t) \\ -\sin(\omega t) \end{pmatrix}$	$Re [\mathbf{E}_- (z = 0)]$ $\propto \begin{pmatrix} \cos(\omega t) \\ \sin(\omega t) \end{pmatrix}$	$Re [\mathbf{E}_+ (t = 0)]$ $\propto \begin{pmatrix} \cos(k_+ z) \\ \sin(k_+ z) \end{pmatrix}$	$Re [\mathbf{E}_- (t = 0)]$ $\propto \begin{pmatrix} \cos(k_- z) \\ -\sin(k_- z) \end{pmatrix}$
			

Table 6.1: Time-dependent and spatial behaviour of the E-field vector of an RCP and an LCP plane wave.

This is the convention used in many physics textbooks as in Ref. [17], for example. However, there is a second way of defining a plane wave from the observer’s point of view that is equivalent to the latter one and often used in an engineering context:

- The plane wave is given by  $\mathbf{E}(z, t) = Re [\mathbf{E}_0 exp(j(\omega t - k_z z))]$  and
- The observer looks in propagation direction of the plane wave (source view).

For the time varying behaviour ( $z = 0$ ) and the spatial behaviour ( $t = 0$ ) of circular polarisation, we obtain from this second point of view (see Table 6.2):

$$Re [\mathbf{E}_\pm(z, t)] = \frac{1}{\sqrt{2}} \begin{pmatrix} \cos(\omega t - k_\pm z) \\ \cos(\omega t - k_\pm z \mp \pi/2) \end{pmatrix} \tag{6.58}$$

Obviously, “for an engineer” the E-field vector of RCP (LCP) light moves clockwise (counterclockwise) on a circle at fixed position in space (in source view) while for a given time the E-field vector describes a left-handed (right-handed) helix in space, in contrast to the “physicist’s point of view”.

If the wave additionally propagates in the opposite  $z$ -direction ( $k_z \rightarrow -k_z$ ) the handedness of the helix changes once again. It is therefore important to pay attention when dealing with numerical tools like COMSOL Multiphysics and CST Microwave Studio, which follow the “engineering conventions”. We use the “physics convention” in the following.

### 6.5.3 Jones Calculus

If we now send a linear-x polarised plane wave onto a metamaterial slab or an optical device, the polarisation state of the incident plane wave is generally not conserved after transmission. Generally, a linear-x polarised plane wave is composed of two partial waves after propagation through the metamaterial slab/optical device (see Fig. 6.13). The first partial wave is the

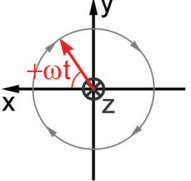
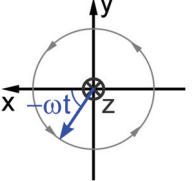
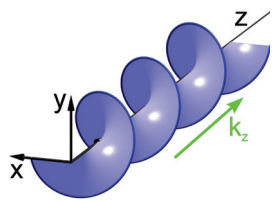
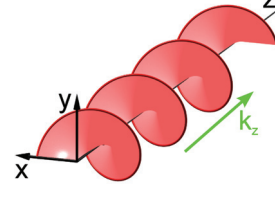
$z = 0$		$t = 0$	
+/RCP	-/LCP	+/RCP	-/LCP
$Re[\mathbf{E}_+(z=0)]$ $\propto \begin{pmatrix} \cos(\omega t) \\ \sin(\omega t) \end{pmatrix}$	$Re[\mathbf{E}_-(z=0)]$ $\propto \begin{pmatrix} \cos(\omega t) \\ -\sin(\omega t) \end{pmatrix}$	$Re[\mathbf{E}_+(t=0)]$ $\propto \begin{pmatrix} \cos(k_+z) \\ -\sin(k_+z) \end{pmatrix}$	$Re[\mathbf{E}_-(t=0)]$ $\propto \begin{pmatrix} \cos(k_-z) \\ \sin(k_-z) \end{pmatrix}$
			

Table 6.2: Time-dependent and spatial behaviour of the E-field vector of an RCP and an LCP plane wave from an “engineer’s point of view”.

linear-x polarised transmitted wave characterised by its complex transmission coefficient  $t_{xx}$  – the polarisation state of the incident and the transmitted wave is the same in this case. The second partial wave is a linear-y polarised wave – here, a conversion of the linear-x polarised incident wave into the perpendicular polarisation state takes place. This polarisation conversion is characterised by the complex coefficient  $t_{xy}$ . In analogy, we can define the transmission  $t_{yy}$  and the conversion  $t_{yx}$  for a linear-y polarised incident plane wave. Using the superposition principle, we can now determine the transmission characteristics of our metamaterial slab/optical device for arbitrarily polarised incident light.

The transmission characteristics of an arbitrary (non-depolarising) material can therefore be described by four complex transmission coefficients ( $t_{xx}, t_{xy}, t_{yx}, t_{yy}$ ) in form of the so-called Jones matrix of the system.

$$\bar{\mathbf{J}} = \begin{pmatrix} t_{xx} & t_{yx} \\ t_{xy} & t_{yy} \end{pmatrix} \quad (6.59)$$

For optical components introducing only a phase shift, the Jones matrix is unitary, *i.e.*,  $\bar{\mathbf{J}} = \bar{\mathbf{J}}^\dagger$ . One intuitive example is a conventional (non-absorbing) wave plate (quarter-wave plate or half-wave plate). For absorbing devices like a linear polariser, for example, the Jones matrix is not unitary. In the Jones calculus, introduced by Robert Clark Jones, an arbitrary state of polarisation is represented by a  $2 \times 1$  vector and each optical component is represented by a  $2 \times 2$  matrix [112]. By simply multiplying the Jones matrices for different optical components one can calculate the Jones matrix of the resulting system. Hence the output polarisation vector is connected *via* the Jones matrix of the system with the input polarisation state.

$$\begin{pmatrix} x' \\ y' \end{pmatrix}_{out} = \prod_{i=1}^j \bar{\mathbf{J}}_i \cdot \begin{pmatrix} x \\ y \end{pmatrix}_{in} \quad (6.60)$$

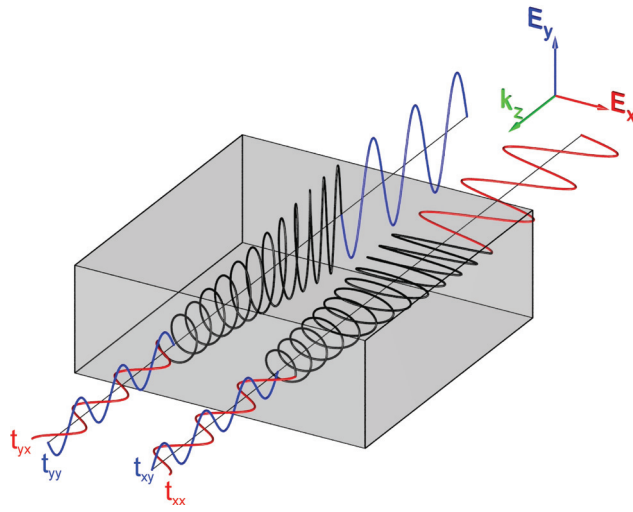


Figure 6.13: After propagation through an arbitrary material, linear-x (linear-y) polarised light in red (blue) emerges with an additional linear-y (linear-x) polarised component, in general. The transformation of the incident field components into the emerging field components is described by the coefficients  $t_{xx}$ ,  $t_{xy}$ ,  $t_{yx}$  and  $t_{yy}$  of the Jones matrix  $\bar{J}$ .

Although the Jones calculus fails for partially polarised light and doesn't account for multiple reflections it is a very straightforward tool to describe the transformation of polarised light by an optical system. Some basic Jones vectors and matrices are given in Table 6.3. In the following the method for obtaining the eigenvectors and the circular transmission coefficients from the Jones matrix used in this Thesis are presented. They are applied to evaluate the complex field-transmission spectra gained from numerical calculations by COMSOL Multiphysics and were implemented in MATLAB.

Polarisation State	Jones Vector	Optical Component	Jones Matrix
Linear-x	$\begin{pmatrix} 1 \\ 0 \end{pmatrix}$	Linear-x Polariser	$\begin{pmatrix} 1 & 0 \\ 0 & 0 \end{pmatrix}$
Linear-y	$\begin{pmatrix} 0 \\ 1 \end{pmatrix}$	Linear-y Polariser	$\begin{pmatrix} 0 & 0 \\ 0 & 1 \end{pmatrix}$
RCP	$\frac{1}{\sqrt{2}} \begin{pmatrix} 1 \\ -i \end{pmatrix}$	Retarder $C(\theta)$ (fast axis in $x$ -direction)	$\begin{pmatrix} e^{-i\frac{\theta}{2}} & 0 \\ 0 & e^{i\frac{\theta}{2}} \end{pmatrix}$
LCP	$\frac{1}{\sqrt{2}} \begin{pmatrix} 1 \\ i \end{pmatrix}$	Rotator $R(\phi)$	$\begin{pmatrix} \cos \phi & -\sin \phi \\ \sin \phi & \cos \phi \end{pmatrix}$

Table 6.3: The basic polarisation states of light and a selection of optical devices are presented in form of Jones vectors on the left-hand side and Jones matrices on the right-hand side.

### Eigenvectors of the Jones Matrix

The Jones matrix can not only be used to determine the emerging polarisation state of light but also to calculate the polarisation eigenvectors of an optical system. We can write the eigenvalue problem of an E-field vector passing an optical system as follows:

$$\bar{\mathbf{J}}_s \cdot \begin{pmatrix} x \\ y \end{pmatrix} = j_{ev} \begin{pmatrix} x \\ y \end{pmatrix} \quad (6.61)$$

Where  $\bar{\mathbf{J}}_s$  is the Jones matrix of the optical system. From here, we deduce the polarisation eigenvectors of the Jones matrix, *i.e.*, the complex field vectors for which the polarisation state of light is conserved. The eigenvalues  $j_{ev}$  represent the absorption and phase delay of the eigenpolarisation induced by the optical system.

### Transformation from Linear to Circular Basis

In the case of chiral media, the eigenpolarisations of the Jones matrix turn out to be RCP and LCP light. We therefore transform the Jones vector from a linear polarisation basis to a circular polarisation basis:

$$\begin{pmatrix} E_- \\ E_+ \end{pmatrix}_{out} = \bar{\mathbf{M}}_{lin2circ} \cdot \begin{pmatrix} E_x \\ E_y \end{pmatrix}_{in} \quad (6.62)$$

$$\bar{\mathbf{M}}_{lin2circ} = \frac{1}{\sqrt{2}} \begin{pmatrix} 1 & -i \\ 1 & i \end{pmatrix} \quad (6.63)$$

RCP and LCP consequently transform to

$$\text{RCP:} \quad \bar{\mathbf{M}}_{lin2circ} \cdot \frac{1}{\sqrt{2}} \begin{pmatrix} 1 \\ -i \end{pmatrix}_{in} = \begin{pmatrix} 0 \\ 1 \end{pmatrix}_{out} \quad (6.64)$$

$$\text{LCP:} \quad \bar{\mathbf{M}}_{lin2circ} \cdot \frac{1}{\sqrt{2}} \begin{pmatrix} 1 \\ i \end{pmatrix}_{in} = \begin{pmatrix} 1 \\ 0 \end{pmatrix}_{out} \quad (6.65)$$

The transmittance Jones matrix in the circular basis  $\bar{\mathbf{J}}_{circ}$  is obtained from the Jones matrix in the linear basis  $\bar{\mathbf{J}}_{lin}$  by:

$$\bar{\mathbf{J}}_{circ} = \bar{\mathbf{M}}_{lin2circ}^\dagger \bar{\mathbf{J}}_{lin} \bar{\mathbf{M}}_{lin2circ} \quad (6.66)$$

Hence, for the special case of a chiral component at normal incidence, we are now able to calculate the change of the polarisation state for linearly polarised incident light (Section 6.5.1) and the transmittance spectra of RCP and LCP incident light in a circular basis (Section 6.5.3) from the complex-valued Jones matrix obtained by numerical calculations.

### 6.5.4 Generation of Circular Polarisation

Let us now have a closer look at the part of the polarisation-spectroscopy setups for the visible/near-infrared (VIS-setup) and the infrared (FTIR-setup) that generates the circular

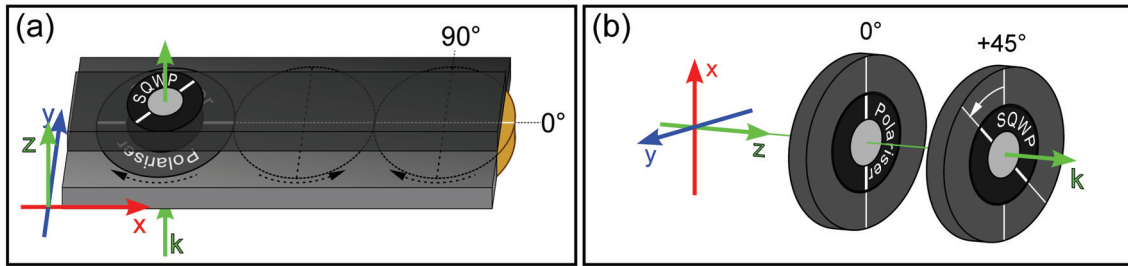


Figure 6.14: Illustration of the polarising part of the optical system of the FTIR-setup (a) and the VIS-setup (b). In contrast to (a) where the linear polariser is rotated by 0° (90°) to produce RCP (LCP) light, the SQWP in (b) is rotated by +45° (−45°) to produce RCP (LCP) light. Propagation direction of light is in +z-direction (green arrows).

polarisation. In particular the relative orientation of the linear polariser and the superachromatic quarter-wave plate (SQWP) has to be chosen appropriately to end up with the desired circular polarisation – either RCP or LCP. The optical components under consideration have the following specifications with regard to their polarisation properties.

- Polariser: The orientation of the polarisation plane of the emerging light is indicated by a mark (white line on the mount)
- SQWP: The orientation of the fast axis is indicated by a white line on the mount.

The polarisation devices in the VIS-setup and the FTIR-setup are mounted as illustrated in Fig. 6.14.

- FTIR-setup: Here, the polariser is rotated by 0°/90° with respect to the horizontally aligned  $x$ -direction to produce RCP/LCP light after the SQWP (fixed) which is mounted at +45° with respect to the  $x$ -direction (see Fig. 6.14(a)). In this setup the total intensity is measured without an analysing optical system between sample and detector. Thus, the polarisation state of the emerging light is not analysed.
- VIS-setup: The polariser is fixed in vertical direction at 0° ( $x$ -direction), thus, the emerging light is vertically polarised. The following SQWP is oriented with the fast axis in  $x$ -direction (0°). To produce RCP/LCP light the SQWP is rotated by +45°/−45° (see Fig. 6.14(b)). The light transmitted through the sample passes a second SQWP rotated by −45°/+45° with respect to the  $x$ -direction and finally an analyser at 0° (90°) selects the circular transmittance (conversion) of the metamaterial structure for detection (see Fig. 6.16).

Note that we use the detector view for our reasoning, hence, light propagates towards the observer. In order to check the relative orientation of the polariser and the SQWP to obtain RCP and LCP light, respectively, we assume a plane wave given by:

$$\mathbf{E}(z, t) = E_0 \cos(k_z z - \omega t) \cdot \hat{e}_x. \quad (6.67)$$

If linearly polarised light is oriented perpendicular to the fast axis of the SQWP it is delayed by  $\theta = +\pi/2 = \lambda/4$  with respect to light polarised parallel to the fast axis. Consequently,

$$E_{fast} = E_0 \cos(k_z z - \omega t) \quad (6.68)$$

$$E_{slow} = E_0 \cos\left(k_z z - \omega t + \frac{\pi}{2}\right) \quad (6.69)$$

If the SQWP is rotated by  $+45^\circ$  with respect to the polarisation plane of light (see lhs of Fig. 6.15(a)) the light field is decomposed into field components parallel to the fast axis and parallel to the slow axis (middle parts of Fig. 6.15(a)). In this configuration the emerging light is RCP as:

$$E_{fast} = \frac{1}{\sqrt{2}} E_0 \cos(k_z z - \omega t) \quad \xrightarrow{z=0} \quad E_{fast} \propto \cos(\omega t) \quad (6.70)$$

$$E_{slow} = -\frac{1}{\sqrt{2}} E_0 \cos\left(k_z z - \omega t + \frac{\pi}{2}\right) \quad \xrightarrow{z=0} \quad E_{slow} \propto -\sin(\omega t) \quad (6.71)$$

For the configuration presented in Fig. 6.15(b) we obtain LCP emerging light. Finally, we

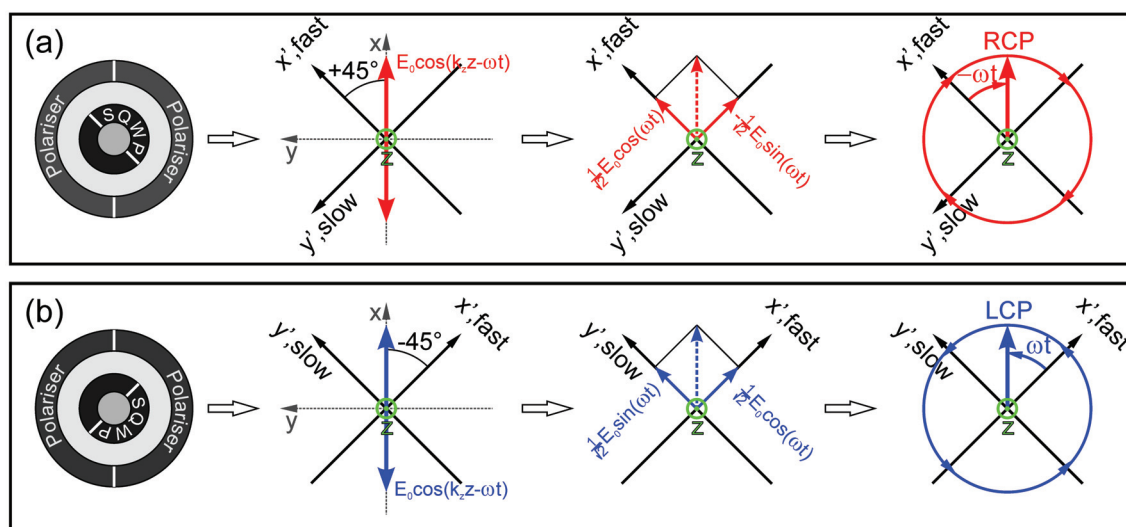


Figure 6.15: The relative orientation of a polariser in  $x$ -direction and a rotated SQWP (first part of (a) and (b)) determines the polarisation state of light. The incident light is decomposed into components parallel and perpendicular to the fast ( $x'$ , fast) and the slow ( $y'$ , slow) axis of the SQWP (second part of (a) and (b)). Due to retardation of the  $y'$ -component of the incident light field by  $\lambda/4$  (third part of (a) and (b)), the emerging wave is (a) RCP and (b) LCP if the SQWP is rotated by  $+45^\circ$  and  $-45^\circ$ , respectively (part four (a) and (b)).

want to do a last check of the overall polarisation part of the optical system of the VIS-setup (see Fig.6.16) using the Jones matrices in Table 6.3. The equation system for the

conversion of linear-x polarisation to RCP and the analysis of the back-converted RCP to linear polarisation therefore reads:

$$\begin{pmatrix} 1 \\ 0 \end{pmatrix}_{out} = \underbrace{\frac{1}{\sqrt{2}} \begin{pmatrix} 1 & 1 \\ -1 & 1 \end{pmatrix}}_{R(-45^\circ)} \underbrace{e^{-i\frac{\pi}{4}} \begin{pmatrix} 1 & 0 \\ 0 & i \end{pmatrix}}_{\text{SQWP } 2=C(\frac{\pi}{2})} \underbrace{\frac{1}{\sqrt{2}} \begin{pmatrix} 1 & -1 \\ 1 & 1 \end{pmatrix}}_{R(+45^\circ)} \cdot \underbrace{\frac{1}{\sqrt{2}} \begin{pmatrix} 1 & -1 \\ 1 & 1 \end{pmatrix}}_{R(+45^\circ)} \underbrace{e^{-i\frac{\pi}{4}} \begin{pmatrix} 1 & 0 \\ 0 & i \end{pmatrix}}_{\text{SQWP } 1=C(\frac{\pi}{2})} \underbrace{\frac{1}{\sqrt{2}} \begin{pmatrix} 1 & 1 \\ -1 & 1 \end{pmatrix}}_{R(-45^\circ)} \begin{pmatrix} 1 \\ 0 \end{pmatrix}_{in} \quad (6.72)$$

-45° rotated SQWP 2  
+45° rotated SQWP 1

Consequently, for measurements of the pure polarisation transmittance (RCP→RCP) the polarisers at the beginning and the end of the VIS-setup have to be aligned parallel to each other if we rotate the SQWPs by +45° in opposite directions (see Fig. 6.16). The pure polarisation conversion (RCP→LCP) is then measured in a crossed-polariser configuration. The corresponding reasoning is also valid for the detection of LCP light if the SQWPs are rotated by -45° in opposite directions.

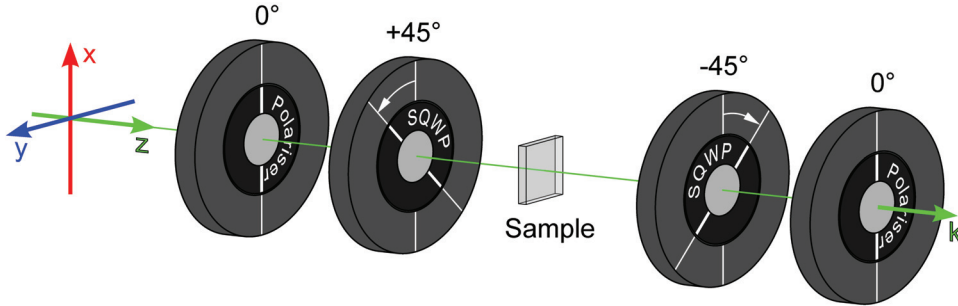


Figure 6.16: Illustration of the polarising part of the VIS-setup. The first polariser/SQWP-pair (lhs) produces RCP light from unpolarised incident light. The second SQWP/polariser-pair acts as analyser. For parallel orientation of the polarisers the circular transmittance RCP→RCP is detected, for crossed polarisers the circular conversion RCP→LCP is detected.

## 6.6 Optical Activity and Circular Dichroism

With the use of the circular-polarisation setups for visible/near-infrared (VIS-setup) and infrared (FTIR-setup) frequencies we can measure the circular transmittance for the metamaterial structures presented in Chapter 7 and 8, respectively. Owing to the circular eigenstates of the chiral material, no circular polarisation conversion occurs and it is sufficient to detect the circular-polarisation transmittance only, *i.e.*, the RCP→RCP and LCP→LCP transmittances, respectively. Typical circular-transmittance spectra of a chiral material are shown in Fig. 6.17(a) [43]. They show two resonances (see Fig. 6.17(a) dashed blue/red

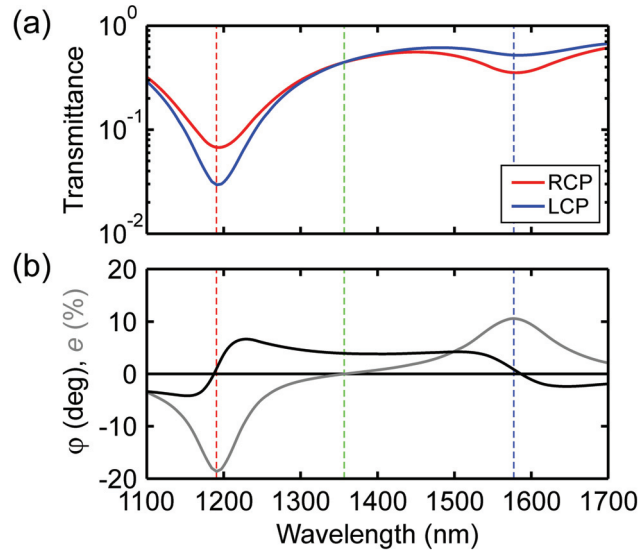


Figure 6.17: (a) The calculated circular transmittance spectra for RCP (red) and LCP (blue) incident light of a twisted-crosses chiral metamaterial (see Chapter 8.1) show two pronounced resonances (dashed red and blue lines) where strong circular dichroism occurs. (b) The deduced curves for the rotation angle  $\varphi$  (in black) and the ellipticity  $e$  (in gray) also exhibit a resonant behaviour. Maximum absolute values for the ellipticity are achieved in the resonance where  $\varphi$  changes sign. Only between the two absorption bands pure optical activity ( $e = 0$ ) can be observed (green dashed line). Here, the RCP and the LCP transmittances are identical.

line) with strong circular dichroism, *i.e.*, the resonance of one circular polarisation is more pronounced than the resonance of the complementary circular polarisation. Furthermore, the rotation angle of the polarisation plane  $\varphi$  of linearly polarised incident light shows a resonant behaviour and the emerging wave nearly becomes circularly polarised ( $e \rightarrow \pm 1$ , see Fig. 6.17(b) dashed blue/red line) at the same time. In the spectral region between the two resonances the ellipticity becomes nearly zero leading to pure optical activity ( $e = 0$ , see Fig. 6.17(b) dashed green line). The combination of circular dichroism and optical rotatory dispersion in the absorption region are known as the Cotton effect and can be explained by the Kuhn-Kirkwood mechanism which states that coupling of two (identical) non-parallel oscillators gives rise to the optical activity and the circular dichroism of chiral molecules [113].

As chiral materials can be described by an effective index of refraction  $n_{\pm}$  for either of the two circular polarisations we can now calculate the angle of rotation  $\varphi$  and the ellipticity  $e$  of a linear-x polarised plane wave after transmission through a chiral slab of thickness  $d$ .

$$\begin{aligned} \mathbf{E}_{out} &= \frac{1}{2} \left( \begin{pmatrix} 1 \\ -i \end{pmatrix} e^{in_+k_0d} + \begin{pmatrix} 1 \\ i \end{pmatrix} e^{in_-k_0d} \right) e^{-i\omega t} \\ &= e^{i\frac{n_++n_-}{2}k_0d} \begin{pmatrix} \cos\left(\frac{n_+-n_-}{2}k_0d\right) \\ \sin\left(\frac{n_+-n_-}{2}k_0d\right) \end{pmatrix} e^{-i\omega t} \end{aligned} \quad (6.73)$$

As a consequence we find

$$\tan(\varphi) = \frac{E_y}{E_x} = \tan\left(\frac{n_+ - n_-}{2}k_0d\right) \quad (6.74)$$

which is equivalent to

$$\varphi = \frac{\pi d}{\lambda}(n_+ - n_-) \quad (6.75)$$

for real-valued refractive indices  $n_+$  and  $n_-$ . Thus, the rotation angle is a function of the real parts of the refractive indices of the chiral medium. If  $n_+$  and  $n_-$  are purely imaginary, we can calculate the ellipticity  $e$  from

$$\mathbf{E}_{out} = \begin{pmatrix} \cosh\left(\frac{n_+ - n_-}{2}k_0d\right) \\ i \sinh\left(\frac{n_+ - n_-}{2}k_0d\right) \end{pmatrix} e^{i(-\omega t)} \quad (6.76)$$

Now we can deduce the ellipticity

$$e = \tan(\eta) = \tanh\left(\frac{n_+ - n_-}{2}k_0d\right) \quad (6.77)$$

For small arguments of the hyperbolic tangent we can conclude

$$e \approx \frac{\pi d}{\lambda}(n_+ - n_-). \quad (6.78)$$

The ellipticity  $e$  therefore is a function of the circular dichroism of the chiral medium.

Since the real and the imaginary parts of the refractive indices of the chiral medium are closely related *via* the Kramers-Kronig relations, an optically active medium always exhibits circular dichroism as well. Therefore it is in principle possible to measure the circular dichroism spectrum only and deduce the optical rotatory dispersion spectrum if all spectral features of the structure are within the measurement range.

### 6.6.1 Derivation of the Polarisation State of Light from Experiments

In experiments we obtain the transmitted intensity spectra for incident RCP and LCP light. As a consequence, we have to do some post-processing in order to calculate the rotation angle  $\varphi$  and the ellipticity  $e$ . The main goal is to obtain the complex transmission spectra which can be used to deduce the rotation angle and ellipticity according to Section 6.5.1. This can be achieved in two different ways:

1. Calculation of the complex transmission spectra *via* numerical calculations.
2. Calculation of the transmission phases  $\theta(\omega)$  of circular dichroism spectra  $T(\omega)$  using the Kramers-Kronig relations (KKR) [114].

For the latter approach we first have to rewrite the complex field transmission:

$$\begin{aligned} t(\omega) &= \sqrt{T(\omega)}e^{i\theta(\omega)} \\ &\Downarrow \\ \log(t(\omega)) &= \log\left(\sqrt{T(\omega)}\right) + i\theta(\omega). \end{aligned}$$

Due to causality, the real part and the imaginary part have to be related to each other *via* the Kramers-Kronig relations (Equation (2.36)) and the phases  $\theta(\omega)$  of the circular dichroism spectra can be derived from [114]

$$\theta(\omega) = -\frac{2\omega}{\pi}PV \int_0^\infty \frac{\log(t(\omega'))}{\omega'^2 - \omega^2} d\omega' \approx -\frac{2\omega}{\pi}PV \int_{\omega_1}^{\omega_2} \frac{\log(t(\omega'))}{\omega'^2 - \omega^2} d\omega'.$$

Fig. 6.18 shows a comparison of the calculated rotation angle  $\varphi$  and ellipticity  $e$  (Fig. 6.17(b)) obtained from numerical calculations shown in Fig. 6.17(a) in contrast to the derived values *via* the Kramers-Kronig relations from the transmittance amplitudes shown in Fig. 6.17(a). Although the curves in Fig. 6.18 calculated from the KKR-method fit very well to the

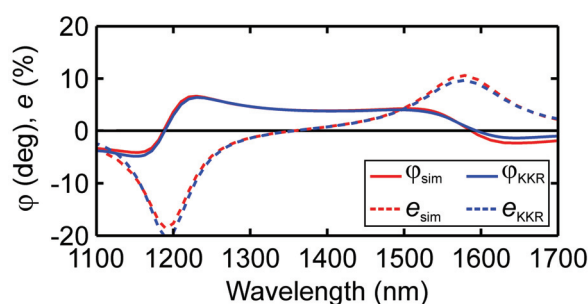


Figure 6.18: Comparison of the rotation angle  $\varphi$  (solid) and ellipticity  $e$  (dashed) deduced from numerical calculations plotted in red in contrast to the method using the Kramers-Kronig relations plotted in blue.

curves obtained from numerical calculations, one has to be careful when calculating the transmission phases with the Kramers-Kronig relations since we can only integrate over the finite frequency interval given by the measured or calculated spectra, in practice. As a consequence,  $\log(\sqrt{T(\omega)})$  has to be negligible above and below the boundaries of the (measured) frequency interval. In the case of the spectra shown in Fig. 6.17(a) this is fulfilled to a great extent owing to the resonance behaviour of the transmittance spectra.

In this Thesis, however, we use numerical calculations with COMSOL Multiphysics and calculate the rotation angle  $\varphi$  and the ellipticity  $e$  from the complex-valued transmission Jones matrix of a chiral metamaterial slab (see Section 6.5.1).



## Chapter 7

# “Planar” Chiral Photonic Metamaterials

In order to obtain a metamaterial structure exhibiting optical activity and circular dichroism, we want to design a chiral unit cell, *i.e.*, a unit cell made of metallic nanostructures whose “...image in a mirror, ideally realised, cannot be brought to coincide with itself.”, speaking with the words of Lord Kelvin [105]. This simple definition, however, is not the only condition that a “chiral atom” has to fulfill if we want to obtain a “purely” chiral optical response in the sense that, as described in Chapter 6, circular polarisations are the polarisation eigenstates of the chiral metamaterial. In order to achieve this goal, we first have to eliminate linear birefringence as otherwise the polarisation eigenstates of such structures are generally elliptical polarisations (see, *e.g.*, Refs. [115, 116]). As a result, the chiral unit cell requires a four-fold rotational symmetry – the twisted-crosses metamaterial design, presented in Chapter 8.1 is one example that exhibits circularly polarised eigenstates, the main ingredient for pure optical activity.

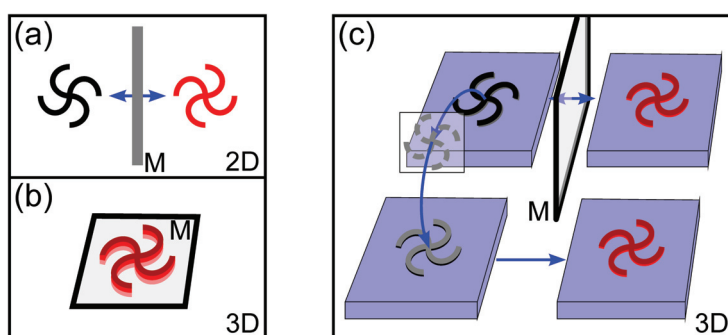


Figure 7.1: (a) The mirror image of an *S*-shaped cross cannot be mapped onto the original structure in a two-dimensional world. As a result the planar *S*-shaped cross is chiral in two dimensions. (b) In three dimensions a mirror can always be placed in the plane of any planar structure design mapping the structure onto itself. In this sense no planar chirality can exist in three dimensions. (c) If the planar structure is placed on a substrate, however, the mirror symmetry is broken and the structure can only be mapped onto its mirror image when it is lifted off the substrate.

Fabrication of this particular metamaterial design using a standard EBL-process (see Chapter 4.1.2), however, is experimentally challenging since EBL is inherently connected with planar or stacked structure designs. As a consequence, the question arises if “planar

chiral” metamaterial designs have the capability to exhibit optical activity and circular dichroism.

## 7.1 Chiral Symmetry in Two Dimensions

To address this question, we investigate the properties of the planar  $S$ -shaped cross design shown in Fig. 7.1. If we have a look at the symmetry properties of the structure in a purely two-dimensional world we realise that it is indeed impossible to superimpose its mirror image onto the original (see Fig. 7.1(a)). In two dimensions this design is therefore characterised by a four-fold rotation axis and the absence of mirror-symmetry. Thus, it is “truly chiral”.

In optical experiments, however, the term “planar chirality” loses its meaning, since in three dimensions the plane in which any “planar chiral” structure is positioned always maps the two-dimensional structure onto itself (see Fig. 7.1(b)). As a consequence, no chiral response, *i.e.*, no optical activity and no circular dichroism is observable for an ideal planar structure embedded in a homogeneous medium at normal incidence. Only structural asymmetry or the presence of a substrate break this mirror symmetry (Fig. 7.1(c)) and therefore can lead to a significant chiral optical response of the planar metamaterial.

Remarkably, the handedness of a “planar chiral” structure positioned in the  $xy$ -plane changes when the sample is illuminated from the negative  $z$ -direction in contrast to illumination from the positive  $z$ -direction. This behaviour is in sharp contrast to a three-dimensional helix which keeps its handedness when looked at from the other side. If this change of handedness of the “planar chiral” structure also translated into the optical response of the metamaterial slab this would lead to an overall non-reciprocal response of the planar “chiral” metamaterial, *i.e.*, the transmittance spectra measured in forward direction would be different from the spectra measured in backward direction. Recent work, however, [11, 117] has shown that the polarisation behaviour of planar “chiral” metamaterials neither violates reciprocity nor time-reversal symmetry. A more detailed analysis of this aspect is provided in Section 7.4 using the double-layer gammadion metamaterial design presented in the following section.

## 7.2 Chiral Double-Layer Gammadions

In order to investigate the polarisation properties of quasi-planar chiral metamaterials, we use the double-layer gammadion<sup>1</sup>-shaped structure design illustrated in Fig. 7.2 which closely resembles the  $S$ -shaped cross depicted in Fig. 7.1 [118]. Two-dimensional arrays of single-layer gammadion-shaped nanostructures have been investigated by several groups, so far:

---

<sup>1</sup>The name gammadion reflects that the structure itself consists of four greek “gamma”- ( $\Gamma$ -) letters. Using this term, we refrain from attributing any symbolic meaning to the actual shape of the structure or its mirror structure.

- On the one hand Refs. [10, 119–121] have mainly investigated the dependence of the optical rotation on the handedness of the gammadions in the first diffraction order. Owing to the asymmetry in the measurement setup, the observed polarisation change can be attributed both to the molecular “chirality” of the single-layer gammadion structures and to structural chirality introduced by the oblique angle detection configuration. For the detection of the polarisation change in the diffraction orders, however, the two different contributions to the polarisation change cannot be distinguished, in general [122]. In this context, it is therefore not clear if the polarisation change stems from the “planar chiral” gammadions or their “chiral arrangement” in the measurement setup. In particular, no polarisation effects were observed in the 0th diffraction order [120, 123].
- Refs. [11, 124–126] on the other hand have focussed on single-layer gammadion-shaped metamaterials exhibiting no Bragg scattering in the relevant spectral region and measured the emerging polarisation state of linearly polarised incident light. The polarisation properties of the gammadion-shaped metamaterials were found to originate from symmetry breaking, *i.e.*, from the missing of the in-plane mirror symmetry of the planar gammadions. This symmetry breach originates from plasmon coupling between the non-identical top and bottom surface of the metal nanoparticles [11, 124] and leads to a chiral response in the (0th order) transmittance spectra. Thus, changes of the polarisation state of light is a purely three-dimensional effect [11, 124, 126]. In this case, the term “planar chiral” metamaterial cannot be used for the metamaterial structures under investigation.

In order to demonstrate optical activity and circular dichroism that arise from the chiral symmetry of gammadion-shaped unit cells, we discuss a quasi three-dimensional metamaterial design consisting of two functional layers of metal gammadions which are separated by a dielectric spacer (see Fig. 7.2(a)+(c) and Fig. 7.4(a)) [118]. As a result, strong magnetic-dipole moments in analogy to the magnetic moments in cut-wire pairs (see Chapter 3.5) are expected in the double-layer gammadion structure. We show that the resulting polarisation effects, *i.e.*, circular dichroism and optical activity are stronger than for the corresponding planar single-layer gammadion metamaterial and specifically arise from the structural asymmetry introduced by the different sizes of the two stacked metal gammadions.

In our samples, the chiral “photonic atoms” are arranged in a square lattice with lattice constant  $a = 340$  nm (Fig. 7.2). We emphasise that in contrast to previous work [10, 11, 119] the operation wavelength  $\lambda$  for our metamaterial structure is large with respect to the lattice constant  $a$  such that our structures can be described as effective materials in the same spirit as, *e.g.*, magnetic [64, 68] or negative-index photonic metamaterials [85, 127, 128]. Precisely, we have  $\lambda/a > 2$  ( $\lambda/a = 2$  is the fundamental Bragg condition), whereas previous work had  $\lambda/a \approx 0.16$  [10, 119] and  $\lambda/a \approx 1$  [11], respectively.

Our stacked gammadion metamaterial structures are fabricated by standard single-layer EBL followed by a three-step electron-beam evaporation process. The photonic atoms (see Fig. 7.2(a)+(c) and Fig. 7.4(a)) consist of a sandwich of 25 nm gold, 25 nm magnesium

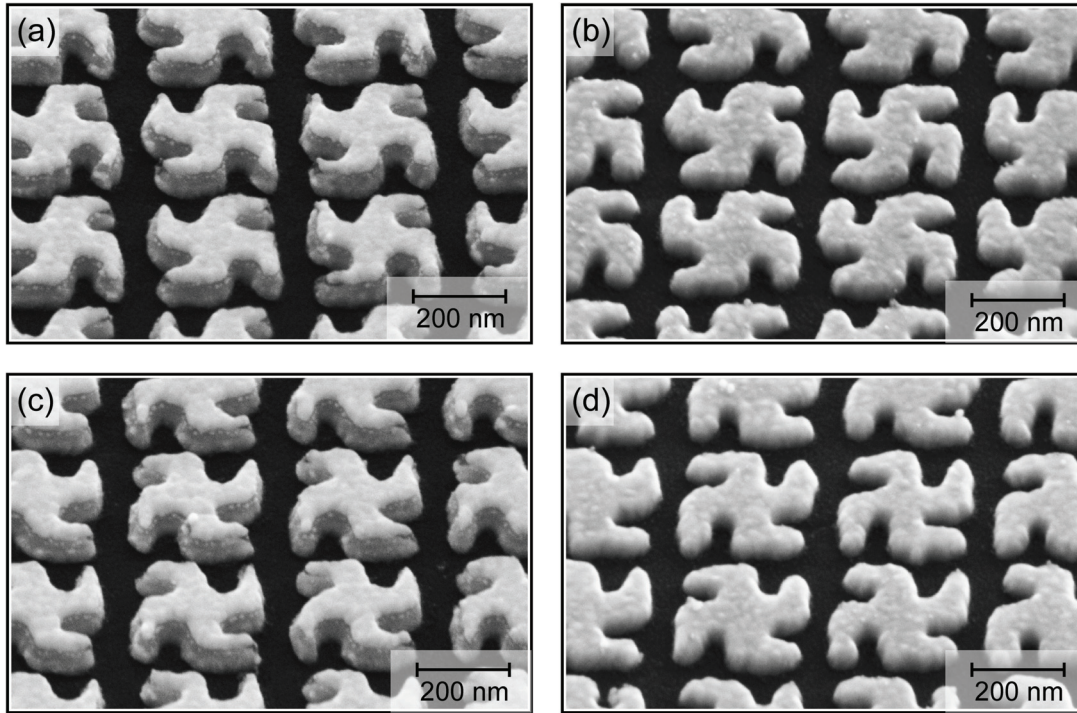


Figure 7.2: SEM-images of the right-handed (rh) and left-handed (lh) double-layer gammadion metamaterial are shown in (a) and (c), respectively. The corresponding single-layer structures are presented in (b) for the rh- and in (d) for the lh-structure. The lattice constant of  $a = 340$  nm is significantly smaller than the wavelength of the incident light ( $\lambda/a > 2$ ).

fluoride ( $\text{MgF}_2$ ) and 25 nm gold on a glass substrate, which is coated with a 5-nm-thin film of ITO. The footprint of all samples is  $100\ \mu\text{m} \times 100\ \mu\text{m}$ . Typical SEM images of a right-handed (lh) and a left-handed (rh) metamaterial are shown in Fig. 7.2(a)+(c). The minimum feature sizes of the gammadions are on the order of 50 nm. Owing to the three-step evaporation process, the upper gammadion in a unit cell is slightly smaller than the lower one (see Fig. 7.4(a),  $t_{\text{Diff}} = 15$  nm). This introduces an obvious structural asymmetry of the double-layer gammadions in the  $z$ -direction, thus breaking in-plane mirror symmetry.

The optical characterisation of the double-layer gammadions is performed with the VIS-setup described in Chapter 4.2.1. For detection we use the optical-spectrum analyser for the spectral region from 500-nm to 1.7- $\mu\text{m}$ -wavelength and the home-built Fourier-transform spectrometer for the spectral region from 1.7- $\mu\text{m}$  to 2.3- $\mu\text{m}$ -wavelength. We then perform circular polarisation spectroscopy on the rh- and the lh-gammadion structures. In this fashion, we essentially measure the circular dichroism of the samples, *i.e.*, effects resulting from the imaginary parts of the refractive indices for the two circular polarisation eigenstates, while previous work has focussed on differences in the real part of the refractive index by measuring the rotation angle  $\varphi$  and/or ellipticity angle  $\eta$  [10, 11, 119]. The circular transmittance spectra of the double-layer structures are shown in the left column of Fig. 7.3. The transmittances  $T_+$  and  $T_-$  are different for RCP and LCP incident light. Notably, the measurement of the circular conversion spectra reveals no detectable conversion from RCP

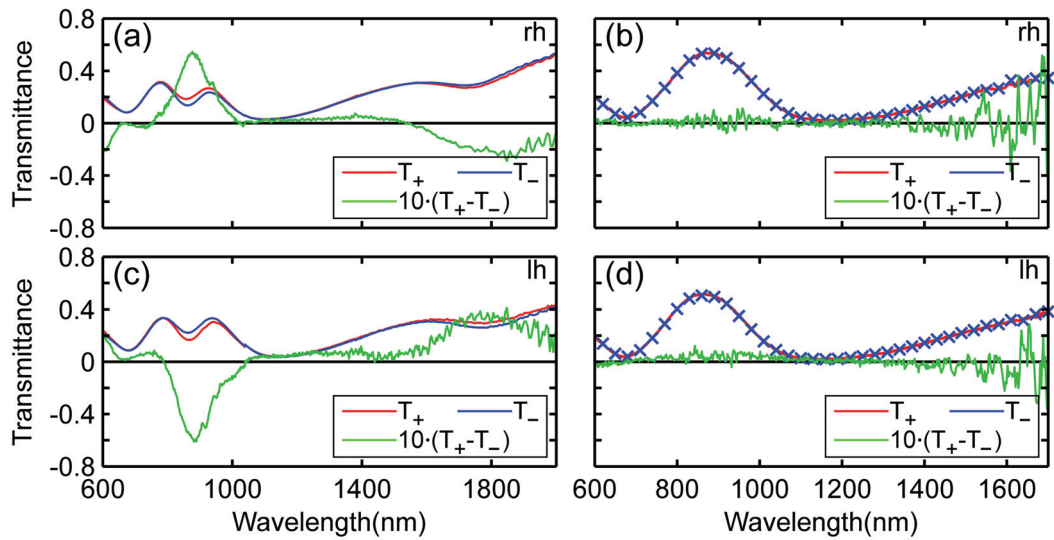


Figure 7.3: The measured circular transmittances of rh and lh double-layer gammadions are presented in (a)+(c), respectively. Transmittance spectra are shown for RCP (red) as well as for LCP (blue). Both structures exhibit significant circular dichroism  $\Delta T = T_+ - T_-$  (green curve). In contrast, the corresponding single-layer structures exhibit no circular dichroism at all, neither for the rh (b) nor for the lh (d) structures. The circular dichroism spectra are multiplied by a factor of ten, for clarity.

to LCP and vice versa (not shown). Hence, RCP and LCP are polarisation eigenstates of the double-layer gammadion metamaterial. The differences in transmittances  $\Delta T = T_+ - T_-$  of the double-layer structures, multiplied by a factor of ten, are shown as green curves in Fig. 7.3(a)+(c). Remarkably, the spectra for the rh structures and the lh structures reveal a reversed sign of the transmittance difference – as expected from symmetry. This observation rules out a major influence of unintentional linear birefringence.

The physical origin of the circular dichroism observed in Fig. 7.3(a)+(c) lies in the fact that the coupling in the double-layer structure allows for symmetric and antisymmetric charge-oscillation eigenmodes equivalent to the modes occurring in the cut-wire pairs introduced in Chapter 3.5. Thus, the low-energy antisymmetric mode can be interpreted as part of a ring current, leading to a local magnetic-dipole moment (see Fig. 7.4(b)). This aspect has also been the key for realising magnetic [68] and negative-index metamaterials [85, 127, 128].

The magnetic-dipole oscillation mode provides coupling of the electric field component with the magnetic field component, a basic requirement for chiral structures (see Chapter 6). Furthermore, the structural asymmetry of the two gammadion layers gives the combined plasmon mode a certain “twist” into the propagation direction of light which makes the metamaterial structure a quasi three-dimensional chiral metamaterial, hence a chiral optical response, *i.e.*, circular dichroism is observable. The long and short arms of the gammadions give rise to two pairs of resonances. These four resonances are visible as transmittance minima in Fig. 7.3(a)+(c). Qualitatively, the experimental results can be understood using the Kuhn-Kirkwood mechanism [11] which ascribes the optical activity to the coupling of two non-parallel dipole oscillators [113] and results in a resonance behaviour of the optical

rotation  $\varphi$  and the ellipticity  $e$  described by the Cotton effect (see Chapter 6.6). To allow for a direct comparison we have also fabricated corresponding single-layer structures with identical lateral dimensions but with a single 50-nm-thin gold layer. Obviously, the circular dichroism spectra in Fig. 7.3(b)+(d), which are arranged just as in (a)+(c), show strongly reduced effects, if any. Also, owing to the missing plasmon coupling, only two plasmon resonances occur for the single-layer structures. This comparison between double-layer (Fig. 7.3(a)+(c)) and single-layer (Fig. 7.3(b)+(d)) samples shows that the differences are due to design rather than the amount of metal. Finally, we have also fabricated gammadion structures with angles other than  $90^\circ$  between the long and the short arms (*e.g.*,  $45^\circ$ ). These structures show smaller polarisation effects and are not discussed here. Indeed, from symmetry it is obvious that structures with  $0^\circ$  and  $180^\circ$  angles would not exhibit any circular dichroism at all.

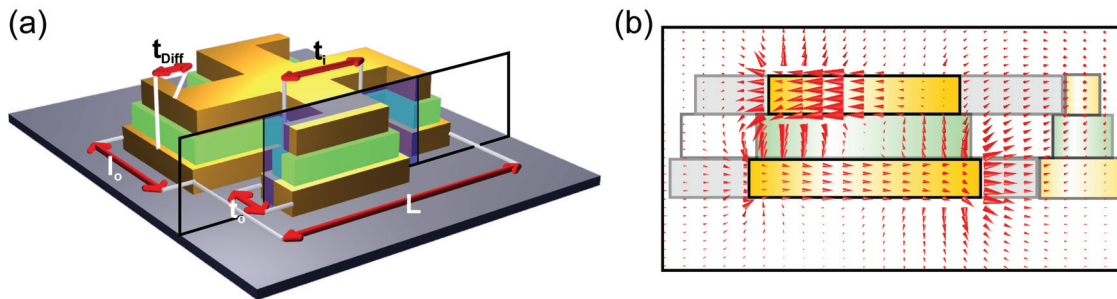


Figure 7.4: (a) Scheme of the double-layer magnetic metamaterial. The geometrical parameters are indicated and given by  $L = 274$  nm,  $t_i = 90$  nm,  $l_o = 135$  nm,  $t_o = 50$  nm, and  $t_{\text{Diff}} = 15$  nm. (b) Snapshot of the E-field at  $0.86\text{-}\mu\text{m}$ -wavelength for LCP incident light. The cutting plane is indicated in (a).

To support our interpretation, we have additionally performed numerical calculations with the COMSOL Multiphysics software package. The geometrical parameters are taken from the experiment and given in Fig. 7.4, the refractive index of the glass substrate is taken as 1.5, that of magnesium fluoride as 1.38, the gold is described as a Drude metal with plasma frequency  $\omega_{pl} = 2\pi \times 2081$  THz and collision frequency  $\omega_{coll} = 2\pi \times 35$  THz. The calculated spectra are shown in Fig. 7.5 for the double-layer (Fig. 7.5(a)+(c)) and the single-layer (Fig. 7.5(b)+(d)) gammadion samples, respectively. A snapshot of the electric-field distribution of the antisymmetric mode of the short arms of the double-layer structures is shown in Fig. 7.4(b). The overall qualitative agreement is very good. In particular, four resonances occur for the double-layer structures, whereas only two resonances occur for the single-layer structures. Furthermore, the spectral positions of all resonances agree very well with experiment and finally, the magnitude of the circular dichroism is nicely reproduced and supports our reasoning. Specifically, we find no circular dichroism for the single-layer gammadion metamaterial. Hence, we verified that planar “chiral” behaviour indeed cannot be observed for single-layer gammadion metamaterials at normal incidence. Only for double-layer chiral metamaterials, the antisymmetric magnetic plasmon mode shows significant circular dichroism of up to  $\pm 6\%$ . Hence, the magnetic oscillation mode gives

the double-layer gammadion metamaterial a certain “twist” into the propagation direction - very similar to three-dimensional chirality.

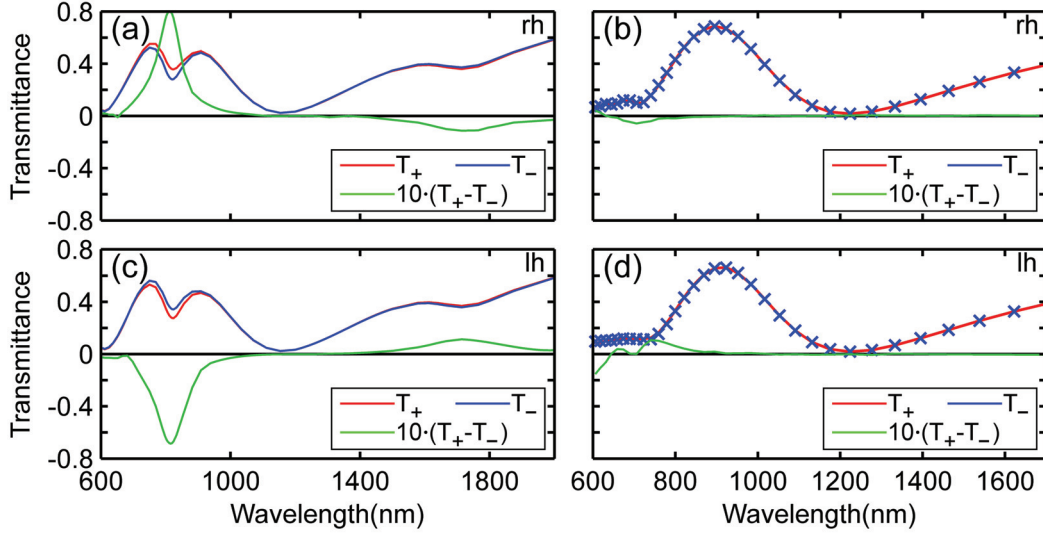


Figure 7.5: Calculated circular transmittance and circular dichroism spectra for the rh (a) and the lh (c) double-layer gammadion design as well as for the rh (b) and lh (d) single-layer design. The sample dimensions are given in Fig. 7.4(a).

### 7.3 Influence of Symmetry Breaking

Since the presence of the substrate and the structural asymmetry of the double-layer gammadions in  $z$ -direction is responsible for the symmetry breaking in the otherwise two-dimensional metamaterial design (see Section 7.1) we now want to clarify, to what extent the polarisation response of the metamaterial is influenced by these two aspects. We therefore performed numerical calculations, using COMSOL Multiphysics, for a symmetric double-layer gammadion design, *i.e.*,  $t_{\text{Diff}} = 0$ . The comparison of the circular dichroism spectra (multiplied by a factor of 10) of the asymmetric double-layer structure and the symmetric double-layer is presented in Fig. 7.6(a)+(b) for an rh and Fig. 7.6(c)+(d) for an lh structure design. Obviously the circular dichroism of the symmetric structure design is nearly zero. As a result, we can identify the structural asymmetry introduced by the different sizes of the upper and the lower gammadions in each metamaterial unit cell as main origin for the chiral response of the double-layer gammadion metamaterial presented in this chapter.

### 7.4 Forward and Backward Propagation

At the beginning of this chapter (Section 7.1), we stated that a planar chiral structure changes handedness when observed from the back side meaning that rh gammadions become lh gammadions when we flip the sample upside-down. It is therefore of particular

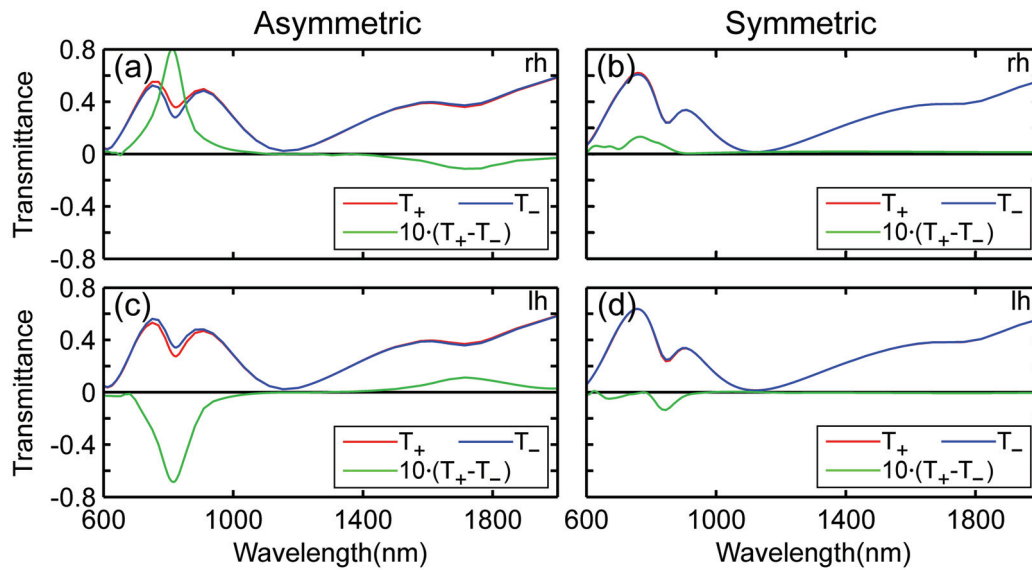


Figure 7.6: Comparison of the calculated circular transmittance spectra of the asymmetric rh (a) and lh (c) design and the symmetric rh (b) and lh (d) design. The RCP and LCP transmittances are plotted in red and blue, respectively. The circular dichroism spectra (in green) are multiplied by a factor of 10.

interest, if the optical response, *i.e.*, the circular dichroism and the optical activity of the double-layer asymmetric gammadion metamaterial also switches sign if we illuminate the structure from the back side. We consequently calculated the circular transmittance spectra of the asymmetric double-layer gammadions using the geometry parameters in Fig. 7.4. The substrate has been neglected in order to exclusively investigate the response of the chiral gammadion design. The circular dichroism spectra are presented in Fig. 7.7 for circularly polarised incident light, propagating in the forward and in the backward direction. Remarkably, the RCP and LCP transmittance spectra do not change for backward propagation with respect to the RCP and LCP spectra for forward propagation although the handedness of the geometrical shape changes. In order to investigate optical activity we have additionally deduced the angle of rotation  $\varphi$  and the ellipticity  $e$  of the emerging polarisation state of a linear-x polarised incident plane wave from the calculated Jones matrix obtained from COMSOL Multiphysics. The optical rotatory dispersion spectra for the calculated spectra of the asymmetric double-layer gammadions are presented in Fig. 7.8. We clearly observe pronounced resonances of both the rotation angle  $\varphi$  and the ellipticity  $e$  which closely resemble the Cotton effect. The results presented in Fig. 7.8 confirm our above finding that the change of the polarisation state of the incident linear polarisation is (nearly) identical for forward and backward propagation (see also [11]).

This overall behaviour is also consistent with reciprocity [11, 117], which means, simply speaking, that the optical response of a (reciprocal) scatterer illuminated by a plane wave is identical if we switch the position of the source and the detector (see Ref. [111]).

Hence, the optical response of the quasi-planar chiral gammadion metamaterial under investigation is rather similar to the optical response of a three-dimensional chiral structure like a helix.

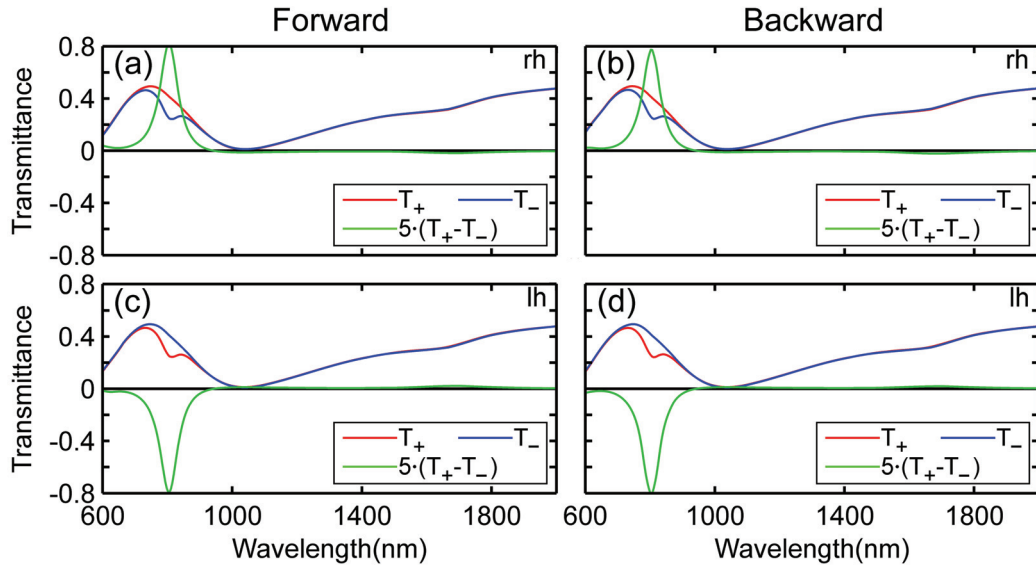


Figure 7.7: Calculated circular transmittances for the asymmetric rh-double-layer gammadions in forward (a) and backward (b) direction. The corresponding spectra for the lh gammadions are plotted in (c) and (d), respectively. The circular dichroism spectra are multiplied by a factor of 5, the substrate is neglected.

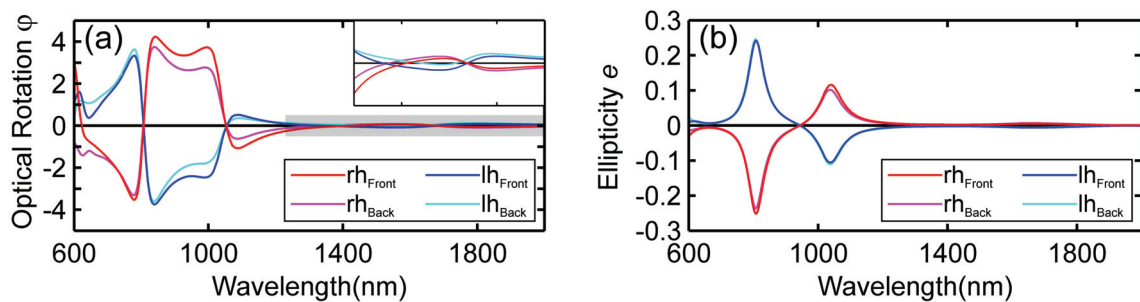


Figure 7.8: (a) The calculated optical rotation  $\varphi$  and (b) the ellipticity  $e$  of the rh/lh double-layer gammadions are qualitatively the same for illumination from the frontside (in red/blue) and from the backside (in magenta/cyan) of the sample. The inset shows a close-up of the gray shaded area.



# Chapter 8

## 3D-Chiral Photonic Metamaterials

Having investigated the optical properties of double-layer and single-layer gammadion-shaped metamaterials in Chapter 7, we can state that chiral optical effects are only present for structures with a structural asymmetry in the  $z$ -direction. As a consequence, the polarisation response can rather be compared with that of a three-dimensional helix, for instance. We therefore want to investigate the polarisation response of metamaterials with a unit cell consisting of two identical nanostructures where one structure is translated in  $z$ -direction and rotated by a twist angle  $\alpha$  with respect to the lower one (see Fig. 8.1). In Chapter 5.3 we have already investigated the twisted-SRR metamaterial as a blueprint of such a 3D-chiral structure design that indeed exhibits a chiral response. The lack of four-fold rotational symmetry and the resulting linear birefringence, however, clearly distinguishes this design from the “purely” chiral structures presented in this section. Multi-layered chiral

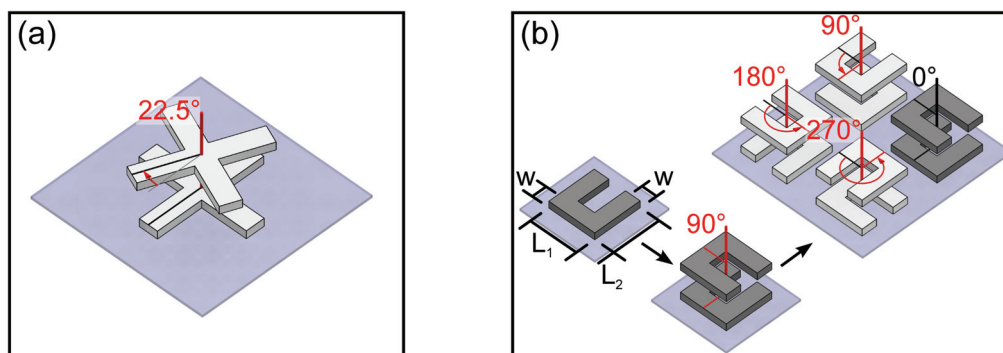


Figure 8.1: (a) Illustration of the bi-layer twisted-crosses chiral unit cell presented in Section 8.1. The upper cross is rotated by  $22.5^\circ$  with respect to the lower one. (b) Construction scheme of the chiral twisted-SRR unit cell presented in Section 8.2. The unit cell consists of four SRR dimers rotated by  $0^\circ$ ,  $90^\circ$ ,  $180^\circ$  and  $270^\circ$  with respect to the stacking axis. Both structures exhibit four-fold rotational symmetry and no mirror symmetry.

structures with four-fold rotational symmetry have already been published [125, 129, 130]. Those structures, consisting of multiple layers of twisted gammadions, exhibit pronounced optical activity [129] or even a negative refractive index for circular polarisations at 5-GHz-frequency [130]. Since the chirality of multi-layer twisted structures is rather based on the “twist into the third dimension” (structural chirality) than to the “planar” chirality of

the structured metal layers (molecular chirality) even achiral planar structure designs can be used as a starting point. This allows much simpler designs than gammadion-shaped nanostructures, for instance.

In the following we want to discuss the polarisation properties of chiral twisted-crosses in Section 8.1 [43] and of chiral twisted-SRR metamaterials in Section 8.2 [44] (see Fig. 8.1). For fabrication of the two-layer metamaterial structures a specific two-step EBL process with an intermediate planarisation step has been developed (see Chapter 4.1.3). Great care has been taken during the alignment of the second functional layer above the first one in order to minimise alignment shifts, since these structural asymmetries lead to the excitation of unwanted higher-order plasmon modes in nanostructures as stated by Refs. [131, 132].

## 8.1 Twisted-Crosses Photonic Metamaterial

Optical activity and circular dichroism in natural molecules can be attributed to the interaction of magnetic and electric dipole moments within a molecule [113]. This interaction can be explained by coupling of two (identical) non-parallel electric/magnetic dipoles and is commonly known as Kuhn-Kirkwood mechanism [113]. Translating this mechanism to plasmonics, we find that a cut-wire pair [68, 85] where the upper wire is rotated with respect to the lower one is the plasmonic analogue of the non-parallel coupled electric dipoles in molecules. Here, magnetoelectric coupling, *i.e.*, the interplay between the electric/magnetic dipoles present in twisted cut-wires and the magnetic/electric component of the incident light field [95] leads to large chiral optical effects [133] even exceeding that of natural substances. We therefore choose this design to demonstrate optical activity in three-dimensional chiral metamaterials. In order to avoid undesired linear birefringence we use twisted crosses instead of cut-wire pairs and obtain four-fold rotational symmetry (see Fig. 8.1(a)).

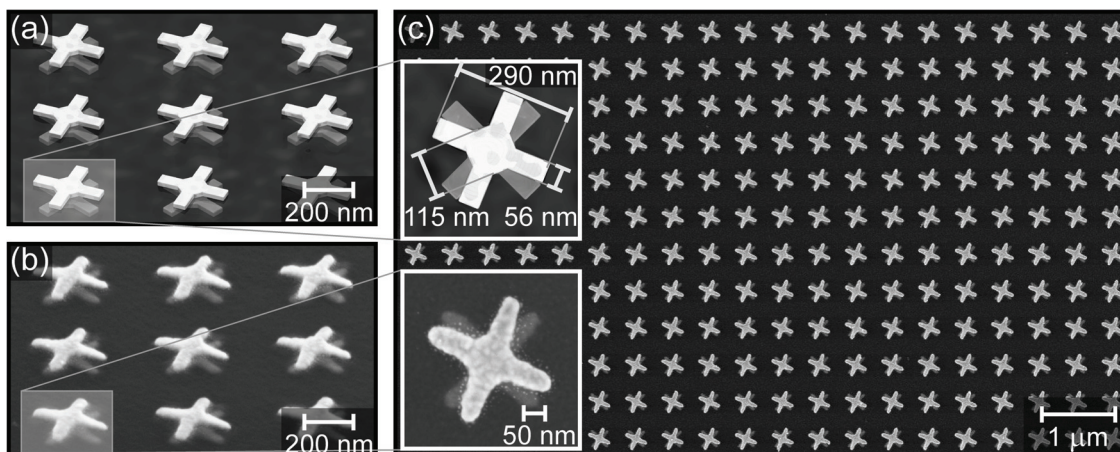


Figure 8.2: (a) Scheme of a chiral twisted-crosses metamaterial composed of right-handed (rh) twisted gold crosses at oblique view. (b) SEM image of the fabricated rh structure and (c) top-view large-area SEM image of an rh structure. The insets in (c) show top-view close-ups of the chiral unit cell.

Here, we investigate a chiral double-layer design at optical frequencies consisting of individual layers of twisted gold crosses [43, 134] arranged on a simple square lattice with a lattice constant of 500 nm. Electron micrographs of structures we have fabricated are shown in Fig. 8.2. The arms of the gold double crosses have a thickness of 25 nm, a full width of 56 nm, and a length of 315 nm. The center of the crosses is slightly overexposed owing to the proximity effect. The two gold layers are separated by an approximately 37.5-nm-thin spacer layer of SOD. From Fig. 8.2(c) and the insets therein, it becomes obvious that the sample quality is very high. Particularly, the alignment mismatch between the two crosses in each pair is smaller than 10 nm over the entire sample footprint of  $100\ \mu\text{m} \times 100\ \mu\text{m}$  (see inset in Fig. 8.2). Both, left-handed (lh) and right-handed (rh) twisted-crosses structures have been fabricated and characterised optically. We used a twist angle of  $22.5^\circ$  between the crosses shown in Fig. 8.2 as neither  $0^\circ$  [135] nor  $45^\circ$  lead to a chiral unit cell and consequently no optical activity or circular dichroism can be expected.

For optical characterisation, we have used the VIS-setup described in Chapter 4.2.1. In order to provide circular polarisation we use Glan-Thompson polarisers in combination with superachromatic quarter-wave plates (SQWPs, see Chapter 6.5.4). This additionally allows for analysing the emerging polarisation state of light, especially the conversion of circular as well as of linear incident polarisation into the corresponding orthogonal polarisation state. The experimental spectra for lh and rh twisted-crosses reveal two distinct resonances as presented in Fig. 8.3. In close analogy to the cut-wire pairs [68, 85], these two resonances correspond to the two effective (electric and magnetic) modes of the otherwise degenerate fundamental electric-dipole Mie resonances of the two coupled crosses. Furthermore, we have verified that RCP and LCP are polarisation eigenstates of the twisted-crosses chiral metamaterial by measuring the circular conversion spectra (RCP $\rightarrow$ LCP, LCP $\rightarrow$ RCP). If we now compare the two resonances of the rh-twisted-crosses structure (see Fig. 8.3(b)), for example, we observe strong coupling of RCP light to the short-wavelength resonance and strong coupling of LCP light to the long wavelength resonance at the same time. Hence, the twisted-crosses chiral metamaterial exhibits ambichiral [136] behaviour meaning that the twisted-crosses chiral metamaterial responds like a left-handed structure for the short-wavelength resonance and like a right-handed structure for the long-wavelength resonance. Further comparison of the results for incident LCP and RCP light on lh and rh structures in Fig. 8.3(a)+(b), reveals that reproducibility is excellent and that fundamental symmetries are obeyed since the spectra for the rh structures and the lh structures show a complementary behaviour of the RCP and LCP transmittances. Indeed, intensity conversion of incident LCP and RCP light is smaller than  $10^{-3}$ , a value corresponding to our experimental measurement limit. Hence, LCP and RCP are the eigenpolarisations of our structures throughout the entire spectral range shown, in contrast to other recently presented 3D-chiral metamaterials [76] which exhibited wavelength-dependent elliptical eigenpolarisations. Furthermore, the measured circular transmittance spectra are identical for forward and backward propagation, as expected from symmetry. As a result, the optical response of the twisted-crosses fulfills reciprocity. Finally, as desired for a chiral material, coupling to the two effective resonances is strongly dependent on the handedness of the incident light resulting in huge circular dichroism. Note that, in between the two resonances (see gray areas in Figs. 8.3-8.5), the

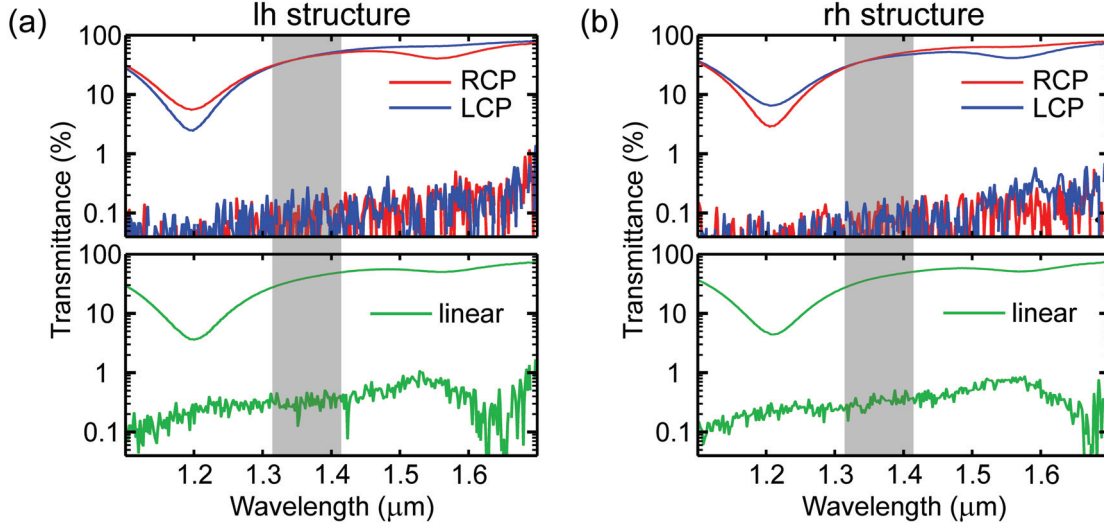


Figure 8.3: Measured normal-incidence transmittance and conversion spectra (on a logarithmic scale) of the twisted-crosses metamaterial shown in Fig. 8.2. Transmittance of an lh (a) and an rh (b) structure for LCP and RCP light (top row) is plotted in blue and red, respectively. The conversion from LCP to RCP and *vice versa* is extremely small and plotted in the same colour. In contrast to circularly polarised incident light, we do find significant conversion for linearly polarised incident light (bottom row) in between the two resonances, where the intensity transmittances for the two incident circular polarisations are almost identical. This regime (highlighted in gray) delivers pure, large optical activity.

amplitudes of the two circular transmittances are very nearly identical. Thus, incident linearly polarised light is expected to remain linearly polarised, but rotated due to the different refractive indices  $n_+$  and  $n_-$  for circular polarisation. This is the fingerprint of pure optical activity. Indeed, as a result of optical activity, the spectra for linear polarisation of the incident light in Fig. 8.3 (bottom row) show significant conversion in this regime. From the values for the linear-x polarised transmittance and the linear-y polarised conversion the optical rotatory power can be calculated. The measured conversion of  $3 \times 10^{-3}$  at 1.36- $\mu\text{m}$ -wavelength results in a rotation of the linear polarisation axis of  $\varphi \approx 4.3^\circ$  that is compatible with the rotation angle of  $\varphi = 4.0^\circ$  obtained from Fig. 8.5. This value is achieved for a total thickness of the metamaterial of only  $l = 87.5 \text{ nm}$ . The polarisation rotation angle  $\varphi$  after propagation over length  $l$  at free-space wavelength  $\lambda$  is connected with the difference of the refractive indices by

$$\varphi = (n_+ - n_-) \frac{\pi}{\lambda} l, \quad (8.1)$$

and provides an estimate of  $|n_+ - n_-| \approx 0.35$ .

To support our experimental findings, we compare the experimental spectra with numerical calculations using COMSOL Multiphysics. As before, the gold dispersion is described by the free-electron Drude model with plasma frequency  $\omega_{\text{pl}} = 2\pi \times 2159 \text{ THz}$  and collision frequency  $\omega_{\text{coll}} = 2\pi \times 25 \text{ THz}$  plus a background dielectric constant of  $\epsilon_b = 9.07$ . The refractive indices of the glass substrate and the spin-on dielectric are taken as 1.45 and 1.41, respectively, the thin ITO film is neglected. The lateral geometrical parameters are shown in the insets of Fig. 8.2(c), the gold thickness is 25 nm, that of the spacer layer

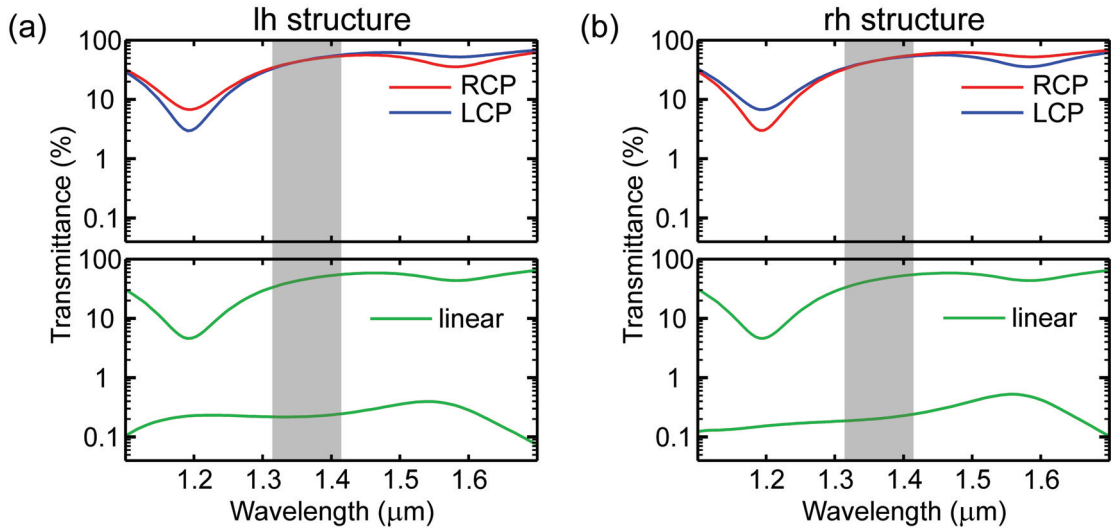


Figure 8.4: Calculated normal-incidence transmittance and conversion spectra of the lh (a) and rh (b) twisted-crosses structure on a logarithmic scale. The conversions for LCP and RCP are below  $5 \cdot 10^{-5}$  (not shown).

37.5 nm. The calculated results in Fig. 8.4 are presented like the experiments shown in Fig. 8.3. Obviously, the overall agreement is very good in all aspects discussed above. In particular, we find very little conversion of circular polarisation and significant conversion of linear polarisation corresponding to optical activity. From the calculations we deduce a maximum rotation angle  $\varphi = 4.0^\circ$  at  $\lambda = 1.36\text{-}\mu\text{m}$ -wavelength (see Fig. 8.5) as described in Chapter 6.5.1. The ellipticity [112],  $e$ , is smaller than 1% in this spectral region.

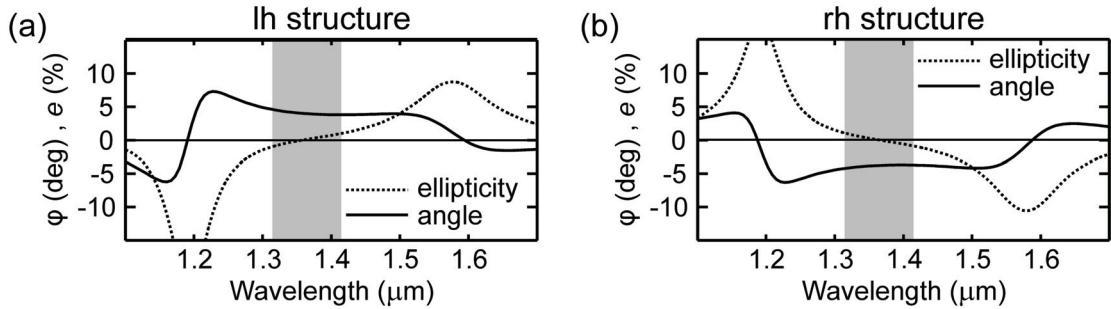


Figure 8.5: Calculated rotation angle  $\varphi$  (solid) and ellipticity,  $e = \tan \eta$ , (dashed) of the lh (a) and rh (b) structures for linearly polarised incident light.

A chiral effective-parameter retrieval as discussed in Appendix A.2 and in Ref. [107] leads to a refractive index difference of  $|n_+ - n_-| = 0.34$  for our twisted-crosses metamaterial structures. This is consistent with our above estimates. Note that the (real parts of the) refractive indices stay positive throughout the entire spectral range, unlike their microwave counterparts [134]. However, the effective-parameter retrieval for metamaterial structures with less than one lattice constant in  $z$ -direction should be taken with caution (see Chapter 2.2.2).

In summary, the three-dimensional twisted-crosses metamaterial presented in this section exhibits circular polarisation eigenstates and, hence, pure, large optical activity of up to  $4^\circ$  at  $1.36\text{-}\mu\text{m}$ -wavelength. This rotation for a total metamaterial thickness of only  $87.5\text{ nm}$  corresponds to an angle of  $45,714^\circ/\text{mm}$  and clearly exceeds values for natural chiral substances. The optical rotation can be translated into a difference of the refractive indices for the two circular polarisations as large as  $|n_+ - n_-| \approx 0.35$  in a spectral region around  $1.36\text{-}\mu\text{m}$ -wavelength.

## 8.2 Chiral Twisted-Split-Ring-Resonator Metamaterial

Optical activity of the twisted gold crosses presented in the last section arises specifically from interactions of the Mie-like electric-dipole resonances which result in a coupling of the electric and the magnetic field components of the incident light [9, 130, 137]. For pairs of twisted SRRs even stronger coupling effects have been reported [76]. However, they do not only exhibit strong optical activity but also strong linear birefringence owing to the obvious asymmetry between the  $x$  and the  $y$ -direction (see Chapter 5.3). In order to avoid linear birefringence, we design a square unit cell which is formed by four of these SRR pairs or dimers [44], whereby the pairs are rotated by  $0^\circ$ ,  $90^\circ$ ,  $180^\circ$ , and  $270^\circ$  with respect to the stacking axis (see Fig. 8.1(b)). The resulting overall crystal structure has four-fold rotational symmetry, no center of inversion, and no mirror planes. Hence, it is truly chiral.

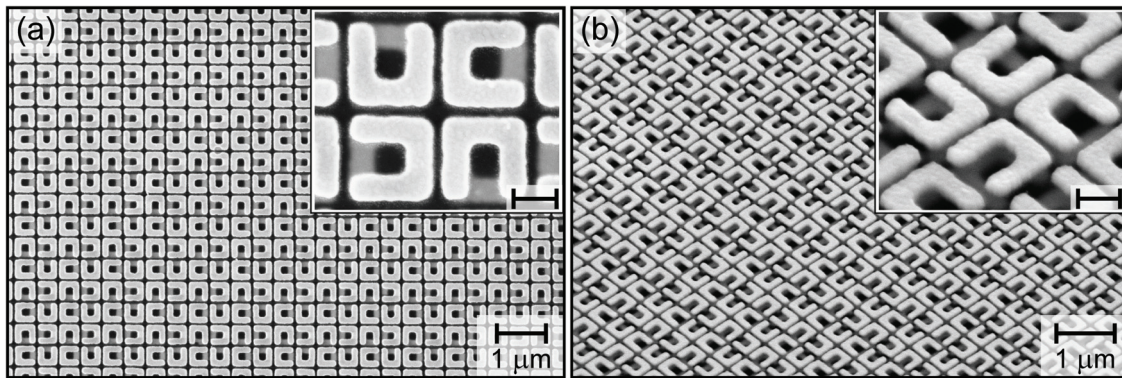


Figure 8.6: Top- (a) and oblique- (b) view SEM-images of a typical fabricated structure. The insets show zoom-ins, the scale bars are  $200\text{ nm}$ .

We emphasise that the detailed arrangement of the SRR dimers within the unit cell does matter. For example, Ref. [138] uses a different arrangement of SRRs in order to eliminate circular dichroism and focusses on investigating the polarisation-dependent magnetic/electric optical response of the achiral arrangement of twisted SRRs. This highlights that the relative arrangement (symmetry) of the SRR pairs is of fundamental importance for the effective optical response of the metamaterial structure.

In contrast to Ref. [138] we investigate the polarisation response of a chiral lateral arrangement of twisted SRRs that, by symmetry, exhibits vanishing linear optical birefringence. This structure has been mentioned theoretically by Ref. [91] and is discussed in another paper

[139] at much larger wavelengths. In contrast to Ref. [139], however, we characterise our chiral twisted-SRR metamaterial using the “natural” optical polarisations, namely LCP and RCP light, the eigenpolarisations of the chiral structure. This allows us to unambiguously identify the eigenmodes from the experiment.

Fabrication of the two-layer chiral medium shown in Fig. 8.6 requires a two-step EBL process with intermediate planarisation as introduced in Chapter 4.1.3. The SRR dimensions are given by  $L_1 = 380$  nm,  $L_2 = 350$  nm, and  $w = 115$  nm (see Fig. 8.1(b)). The gold thickness in each layer is 60 nm, that of the spacer layer roughly 85 nm. The unit cell is arranged in a square lattice with an in-plane lattice constant of  $a = 885$  nm. In order to obtain large coupling effects between the two SRR layers we performed numerical calculations beforehand. The optimum separation of the two SRR layers results from a trade-off: for too large SRR layer separation, the SRR coupling in each pair vanishes and no optical activity can be expected. If, on the contrary, the two SRR layers lie in the same plane, the structure itself is clearly not chiral and optical activity vanishes once again. We have found the optimum SRR separation to be at about 85 nm leading to maximum optical activity. Figure 8.6 shows SEM-images of the fabricated sample. Obviously, the sample quality is very high. In particular, no misalignment between the two SRRs in each pair is detectable (see inset in Fig. 8.6(a)). The in-plane lattice constant of the set of four SRR pairs of  $a = 885$  nm is significantly smaller than the resonance wavelength at about  $3 \mu\text{m}$ . Thus, the structure can safely be regarded as metamaterial ( $\lambda/a > 3$ ).

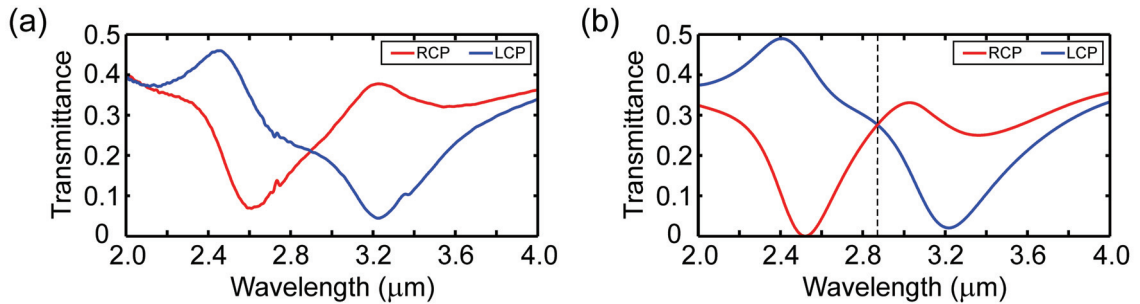


Figure 8.7: Measured (a) and calculated (b) normal-incidence intensity transmittance spectra for LCP and RCP light incident onto the sample shown in Fig. 8.6. The calculated intensity conversion (not shown) is below  $10^{-5}$  for the entire spectral range.

For optical characterisation, we use the FTIR-setup presented in Chapter 4.2.2 [140]. Normalisation of the transmittance spectra is with respect to the transmittance of the glass substrate, the ITO- and the spacer layer. The measured transmittance spectra in Fig. 8.7(a) for LCP and RCP light indeed show much stronger circular dichroism compared to those of our “planar chiral” metamaterial structure [118] presented in Chapter 7 as well as compared to those of our twisted-crosses metamaterial structure [43] presented in the previous section (Section 8.1). Precisely, the circular dichroism reaches values as large as 33 % for the present two-layer chiral twisted-SRR metamaterial. Here, once again, an ambichiral [136] optical response can be observed. Remarkably, the measured circular transmittance spectra are identical for forward and backward propagation (not shown), as expected from symmetry. Hence the twisted-SRR metamaterial shows an overall reciprocal behaviour.

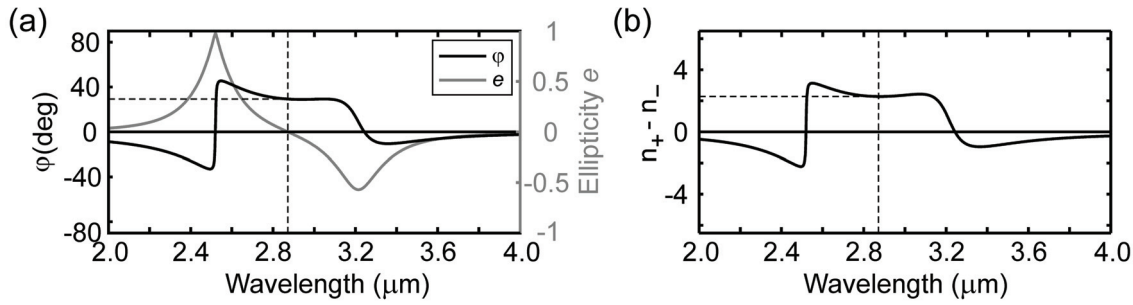


Figure 8.8: (a) Calculated rotation angle  $\varphi$  and ellipticity  $e$  of the transmitted light for linearly polarised incident light. (b) Difference of refractive indices  $\Delta n = n_+ - n_-$  retrieved from the complex transmittance (and reflectance) spectra shown in Fig. 8.7(b).

To investigate the nature of the observed resonances, we perform additional numerical modelling using COMSOL Multiphysics in cooperation with R. Zhao<sup>1</sup> and C. M. Soukoulis<sup>2</sup> using CST Microwave Studio. The lateral geometrical parameters of the SRRs are taken as  $L_1 = 380$  nm,  $L_2 = 350$  nm,  $w = 115$  nm and  $a = 885$  nm. The gold thickness is 60 nm and that of the spacer layer is 85 nm. The gold optical properties are modelled by the Drude model with plasma frequency  $\omega_{\text{pl}} = 2\pi \times 2133$  THz and collision frequency  $\omega_{\text{coll}} = 2\pi \times 33$  THz. The refractive indices of the glass substrate and the spin-on dielectric are 1.45 and 1.41, respectively. The calculated results in Fig. 8.7(b) nicely agree with our experimental findings in Fig. 8.7(a). Remarkably, the intensity conversion of circular polarisation is below  $10^{-5}$  throughout the entire spectral range, which means that LCP and RCP are the eigenpolarisations of the Jones matrix of this chiral twisted-SRR metamaterial. Fig. 8.8 shows the corresponding calculated rotation angle  $\varphi$  of linearly polarised incident light as well as the calculated ellipticity,  $e = \tan(\eta)$ . We find that the rotation angle and the ellipticity  $e$  exhibit a resonance behaviour as described by the Cotton effect. In order to obtain pure optical activity,  $e = 0$  is required. At this zero crossing, marked by the dashed line in Fig. 8.8(a), we find a rotation angle of about  $30^\circ$  for a metamaterial thickness of only 205 nm. Employing the usual parameter retrieval [107] accounting for the glass substrate leads to the difference between RCP and LCP refractive indices  $|\Delta n| = |n_+ - n_-| \approx 2$  at around 3- $\mu\text{m}$ -wavelength, as shown in Fig. 8.8(b). As expected, the spectral shape of the retrieved index difference  $\Delta n$  (Fig. 8.8(b)) closely resembles the rotation angle (Fig. 8.8(a)) directly obtained from the calculated transmission phases. Finally, we calculated the axial component of the local magnetic field in the resonance positions of the spectra shown in Fig. 8.7. The corresponding field and current distributions in the cutting plane through the two SRR layers at resonance wavelengths of 3.2  $\mu\text{m}$  and 2.5  $\mu\text{m}$  are shown in Fig. 8.9. For the long-wavelength LCP resonance, the longitudinally coupled magnetic moments within each SRR dimer are obviously parallel in contrast to the short-wavelength RCP resonance, where the magnetic moments are antiparallel. This is in perfect agreement with our reasoning that

<sup>1</sup>Ames Laboratory and Department of Physics and Astronomy, Iowa State University, USA and Applied Optics Beijing Area Major Laboratory, Department of Physics, Beijing Normal University, China.

<sup>2</sup>Ames Laboratory and Department of Physics and Astronomy, Iowa State University, USA and IESL-FORTH and Department of Materials Science and Technology, University of Crete, Greece.

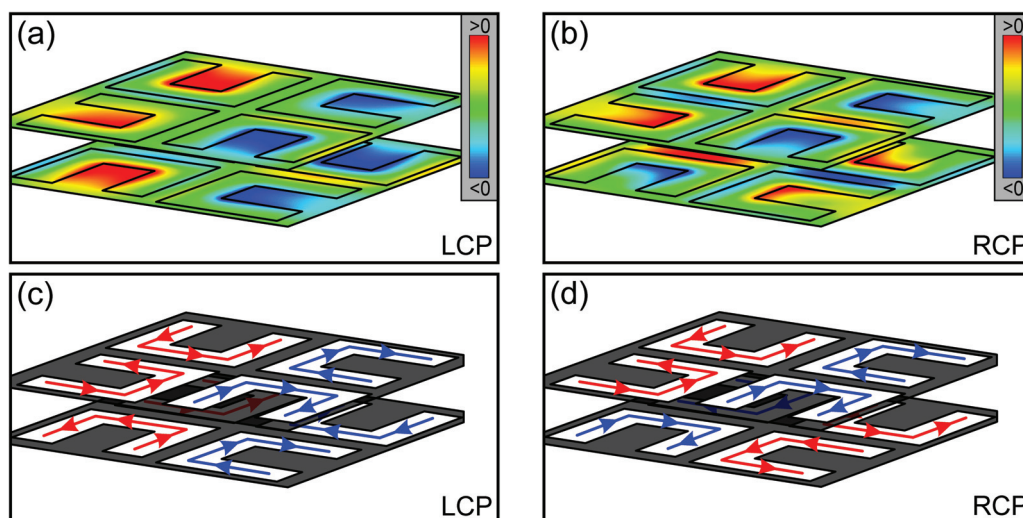


Figure 8.9: False-colour plots of the axial component of the local magnetic field in two planes cutting through the SRR layers for (a) LCP incidence at 3.2- $\mu\text{m}$ -wavelength and (b) for RCP incidence at 2.5- $\mu\text{m}$ -wavelength. Schemes of the corresponding underlying electric currents within the SRRs are shown in (c) and (d), respectively.

interaction effects in ( $90^\circ$ -) twisted-SRR dimers are based on the coupling of longitudinally arranged magnetic dipoles, as introduced in Chapter 5.3.

As a result, we obtain rotation angles (optical activity) as large as  $30^\circ$  and circular dichroism of about 33% at around 3- $\mu\text{m}$ -wavelength that translates to values of  $|\Delta n| \approx 2$  that outperform our previous best results on twisted crosses (see Section 8.1) by about a factor of six.

### 8.3 Three-Dimensional Metallic Helices

In the last two sections, we have investigated two-layer 3D-chiral metamaterials that exhibit three-dimensional chirality. Now the question arises how magnetoelectric coupling takes place in the most evident three-dimensional chiral structure – a circular metal helix. Consequently, we theoretically investigate the polarisation behaviour of the gold helices [140] shown in Fig. 8.10(b)+(c) using CST MicroWave Studio and calculate the circular transmittance spectra of the helical structure. Indeed we observe pronounced circular dichroism for one-pitch and two-pitch gold helices as illustrated on the right-hand side of Fig. 8.10(b)+(c). In order to explain the remarkable polarisation behaviour of the gold helices, we take a step back to a single SRR on a plane substrate (see Fig. 8.10(a)). This structure already provides magnetoelectric coupling, a fundamental prerequisite for chiral metamaterials. The circular transmittance spectra for the single SRR on the substrate exhibits two pronounced sharp resonances corresponding to the plasmonic modes of the SRR (right-hand side of Fig. 8.10(a)). Owing to the presence of mirror symmetry (no chirality), the transmittance spectra for both LCP and RCP light are identical. If we now “pull” one end of the SRR (positioned in the  $xy$ -plane) in the  $z$ -direction we elongate the SRR and

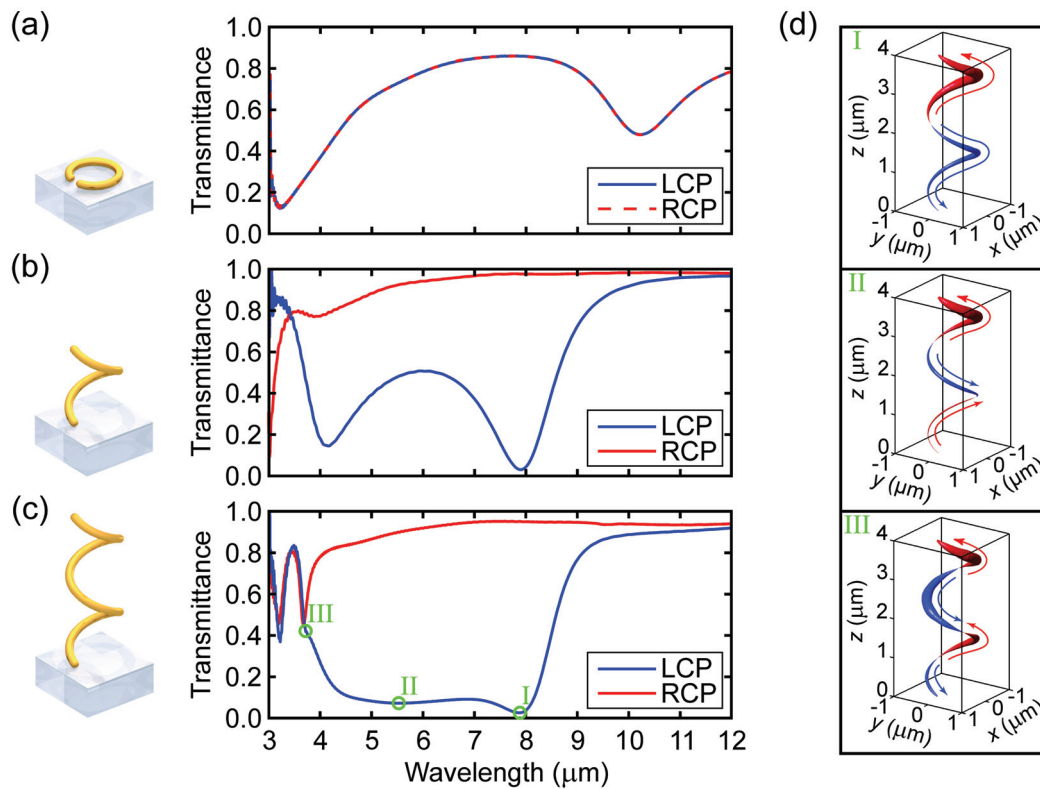


Figure 8.10: (a) Calculated circular transmittance spectra of the achiral split-ring resonator illustrated on the left. RCP and LCP transmittance are identical exhibiting two pronounced resonances. The gold is modelled by the standard Drude model with  $\omega_{pl} = 2\pi \times 2181$  THz and  $\omega_{pl} = 2\pi \times 19.1$  THz. The dimensions of the unit cell is given by  $2\mu\text{m} \times 2\mu\text{m}$ . (b) 'Pulling' one arm of the SRR in (a) in  $z$ -direction results in the left-handed one-pitch helix with a pitch height of  $2\mu\text{m}$  (illustrated on the left). The circular transmittance spectra show a strong chiral response of the helix. (c) For a left-handed two-pitch helix a broad stopband is formed for LCP light while RCP is nearly completely transmitted. The broad stop band can be seen as superposition of three (coupled) plasmonic modes indicated by the (green) roman numbers. The current distributions of these three modes are depicted in (d).

a one-pitch helix is formed (Fig. 8.10(b)). In this case, the circular transmittance spectra still exhibit two pronounced resonances just like it is the case for the single SRR but for one circular polarisation (LCP) only (right-hand side of Fig. 8.10(b)). Hence, the one-pitch helix already shows a chiral optical response. The intensity conversion of the incident RCP light is slightly below 5% in the spectral range from  $3.75 - 7.5\mu\text{m}$ . This value is actually larger than that for our previous chiral structures and can be attributed to linear birefringence that is introduced by the symmetry breaking (no rotational symmetry is present in the axial direction) introduced by the termination of the helix at the top and the bottom end of the helix. As a consequence the polarisation eigenstates of helices with a finite number of pitches are expected to be elliptical polarisations, in general [141]. Note that even an infinite helix "only" exhibits rotational symmetry in a wider sense, namely direct isometry. Hence a rotation in combination with a translation along the helix' axis, or a translation alone, maps an infinite helix onto itself. However, this helix will show an isotropic response at normal

incidence and circular polarisation eigenstates result. Hence, it is favourable to increase the number of pitches.

We have therefore calculated the circular transmittance spectra for two-pitch helices and obtained a broad stop band consisting of three plasmonic excitation modes (Fig. 8.10(c)). The current distributions within the two-pitch helix are depicted in Fig. 8.10(d) for each of the three plasmonic modes. Owing to the coupling of the two helix pitches (two elongated SRRs) the single sharp resonances form a broad stop band for one circular polarisation (LCP in this case) very similar to the formation of electronic bands in natural crystal lattices. The broadband polarisation behaviour consequently has its origins in the coupling of the helix pitches, *i.e.*, the single “split-ring-resonator modes” within the helix. A detailed investigation of the influence of the helix dimensions on the polarisation response is performed in Ref. [141].

In order to fabricate three-dimensional metal helices, however, EBL is not applicable and new fabrication techniques have to be developed. The approach chosen by Gansel *et al* [140] uses direct laser writing to fabricate three-dimensional polymer templates which are finally filled with gold by electrochemical deposition (for details see Ref. [140]). The experimental results are in very good qualitative agreement with the theoretical predictions [140]. In fact, a two-pitch gold helix metamaterial as depicted in Fig. 8.10(c) can be regarded as prototype for a broadband circular polariser at infrared wavelengths and is a promising candidate for future applications.



# Chapter 9

## Conclusions

In this Thesis we have designed, fabricated and characterised three-dimensional chiral metamaterials exhibiting pure, large optical activity and circular dichroism at optical frequencies. In order to provide magnetoelectric coupling – a fundamental prerequisite for a chiral optical response – we have also investigated magnetic coupling phenomena in periodic nanostructured arrays in the optical spectral range using standard electron-beam lithography (EBL) techniques for fabrication of these planar structures. However, since a chiral response requires metallic nanostructures exhibiting chiral symmetry (molecular chirality) which cannot be achieved by planar structure designs, EBL is not applicable without modifications in this case. We have therefore developed a dedicated fabrication procedure combining standard electron-beam lithography and a planarisation step in order to fabricate bi-layered chiral metamaterial structures where the second functional layer within a unit cell is rotated with respect to the first one. Using a special alignment technique to position the two functional layers above each other during the second EBL step we have achieved an alignment accuracy better than 10 nm over the whole extend of a  $100\ \mu\text{m} \times 100\ \mu\text{m}$ -large chiral metamaterial field. The resulting “twisted” chiral metamaterial structures with four-fold rotational symmetry exhibit circular polarisation eigenstates and, thus, pure, large optical activity and circular dichroism at optical frequencies exceeding that of natural materials by orders of magnitude.

In order to make use of magnetoelectric coupling for chiral metamaterial designs we have investigated coupling effects of magnetic photonic nanostructures in the first part of this Thesis. One possibility to couple magnetic moments in the optical regime has been realised by positioning a periodic array of gold double-wire pairs on top of a dielectric waveguide (Chapter 5.2.1). The magnetic plasmon resonance of the double-wire pairs is then coupled to a photonic Bragg resonance *via* the underlying dielectric waveguide. The periodic lattice of the double-wire pairs works as a grating coupler and only allows light of specific wavelengths to propagate in the dielectric waveguide. When finally the field distributions of the two resonances overlap, a frequency splitting or avoided crossing is observed. Hence, strong coupling of the magnetic plasmonic resonance and the Bragg or waveguide resonance is present in our coupled system when the lattice constant of the array of double-wire pairs

is on the order of the magnetic resonance wavelength. This structure design can therefore be regarded as a model of a “magnetic photonic crystal” in analogy to (resonant) dielectric photonic crystals.

Furthermore, when proceeding to metamaterials, *i.e.*, to arrays of magnetic nanostructures with sub-wavelength lattice constant, we have observed direct coupling of effective magnetic-dipole moments in a low-symmetry arrangement of gold split-ring resonators, where the neighbouring SRRs are oriented perpendicular to the centered one (Chapter 5.2.2). In this configuration, the neighbouring effective electric dipoles of the SRRs are all perpendicular to each other and, thus, no electric-dipole coupling takes place. The optical response of the metamaterial is then dominated by transverse magnetic coupling effects leading to linear polarisation eigenstates oriented in the  $\pm 45^\circ$ -direction with respect to horizontal polarisation. This is similar to the behaviour of a wave plate with its principle axes in  $\pm 45^\circ$ -direction. For the two eigenpolarisations we have observed a frequency splitting of the magnetic plasmon mode into a symmetric and an antisymmetric mode. Thus, direct near-field coupling of in-plane magnetic dipoles within a metamaterial’s unit cell already allows for manipulation of the polarisation state of light.

In practice, however, metamaterial unit cells are separated by a finite distance. We should therefore also ask if near-field interactions between metamaterial unit cells are sufficient to explain the optical response of metamaterials. Indeed, when having a closer look, we leave the regime of near-field interactions and observe (far-field) retardation effects. For oblique incidence of light on the above mentioned low-symmetry structure, for instance, we have measured the dispersion relation of magnetisation waves which are a direct consequence of the coupling of neighbouring magnetic dipoles (Chapter 5.2.3). Applying a simple Lorentz-oscillator model including retardation effects to the experimental data, we have demonstrated that this model describes the dispersion curves for  $\pm 45^\circ$  incidence at s- and p-polarisation in contrast to a corresponding model without retardation. Specifically, we have found a significant dispersion in the mode damping of this planar low-symmetry metamaterial that is beyond the quasistatic picture commonly used in literature to describe the optical response of metamaterials.

Apart from transverse coupling of effective magnetic dipoles in planar metamaterials, also longitudinal coupling can be expected using a three-dimensional structure design. In a 3D-SRR dimer which consists of two stacked SRRs oriented perpendicular to the stacking axis and rotated by  $90^\circ$  with respect to each other (Chapter 5.3), the effective electric dipoles of the single SRRs are, once again, perpendicular to each other and magnetic-dipole coupling dominates. For a layer separation below 50 nm significant coupling of the two SRRs is obtained, leading to a low-energy symmetric and a high-energy antisymmetric magnetic mode, as expected for longitudinal coupling. The twisted-SRR metamaterial additionally exhibits chiral symmetry which, in combination with magnetoelectric coupling, leads to a chiral response. Owing to the missing four-fold rotational symmetry and the resulting linear birefringence, however, we obtain elliptical eigenpolarisations and no pure optical activity is observable. Hence, in order to obtain pure optical activity both chiral symmetry and four-fold rotational symmetry have to be present for a chiral structure design. Only then right-handed circular polarisation (RCP) and left-handed circular polarisation (LCP)

are polarisation eigenstates of the metamaterial leading to pure optical activity. Such chiral metamaterials have been investigated in the second part of this Thesis.

While four-fold structural symmetry is a very defined property, which is clearly visible in the structure design, the requirement of chiral symmetry is somewhat more tricky when dealing with planar structures. Specifically, “planar chirality” does not exist in three dimensions as there is always a mirror plane that maps an ideal “planar chiral” structure like gammadion-shaped nanostructures onto itself. Only by introducing structural asymmetry in the axial direction or by introducing a substrate this mirror symmetry vanishes and a chiral structure is obtained.

In practice, we have identified the structural asymmetry to be the key ingredient for obtaining a chiral response of “planar” gammadion metamaterials and we have found that the influence of the substrate is negligible. Specifically, we have observed coupling of the particle plasmons in a bi-layer gammadion sandwich which results in optical activity and circular dichroism, only if the dimensions of the top layer are different from the dimensions of the bottom layer (Chapter 7). A corresponding symmetric structure design or a single-layer gammadion structure has not shown any chiral response at all. Here again, magnetoelectric coupling comes into play since the coupled top-layer and bottom-layer particle plasmons give rise to a magnetic moment equivalent to that in a cut-wire pair. Additional peculiarities arise when we illuminate a gammadion metamaterial from the back side. When we change our transmittance setup from front-side illumination to back-side illumination, the handedness of a gammadion changes, while the circular transmittances and, thus, the optical activity remain unchanged. This implies that, for such “planar” structures, chirality can rather be compared to three-dimensional chirality like in metallic helices, for instance. As a result, we have found that the chiral response of multi-layer sandwiches of gammadions is compatible with reciprocity, *i.e.*, the circular transmittance spectra are identical for forward and backward illumination, and that optical activity originates from “twisting” the planar gammadion into the third dimension. Consequently, the chiral response is not necessarily connected to a “planar chiral” structure design like the gammadions.

We can therefore also start with simpler achiral two-dimensional structure designs with four-fold rotational symmetry and introduce a second functional layer that is rotated with respect to the first one. We have fabricated such twisted-chiral metamaterial structures by positioning two gold crosses, only separated by a dielectric spacer, above each other and rotating the top cross by a specific angle  $\alpha$  with respect to the bottom cross. This twisted-crosses metamaterial structure provides a “purely” chiral response, namely circular polarisation eigenstates leading to optical activity without exhibiting linear birefringence (Chapter 8.1). Naturally, optical activity in chiral (meta-)materials is always connected to circular dichroism *via* the Kramers-Kronig relations – optical activity is based on a difference in the real parts of the refractive indices for RCP and LCP light while circular dichroism results from different imaginary parts of the RCP and LCP refractive indices. Hence, we have observed a specific resonance behaviour of the chiral twisted-crosses metamaterials both in the optical rotatory dispersion spectrum (optical activity) and in the circular dichroism spectrum. This is commonly known as Cotton effect. The observed Cotton effect can

be explained by the Kuhn-Kirkwood mechanism used in molecular biology to describe the optical response of chiral molecules. This means, in our case, that two coupled non-parallel gold wires (cut-wire pairs) give rise to an antisymmetric magnetic mode and a symmetric electric excitation mode which results in two resonances both in the optical rotatory dispersion spectrum and the circular dichroism spectrum. Since the optical rotatory dispersion spectrum and the difference of the real parts of the refractive indices for circular polarisations are directly connected with each other, the measured rotation angle of  $\varphi \approx 4^\circ$  for a total thickness of 87.5 nm of our twisted-crosses chiral metamaterial corresponds to a refractive index difference of  $|n_+ - n_-| \approx 0.35$  in the spectral regime where pure optical activity occurs. The polarisation properties of right-handed and left-handed twisted-crosses have shown a complementary behaviour, as expected from symmetry, and are compatible with reciprocity.

In order to obtain even stronger optical activity from bi-layer chiral metamaterials one has to increase magnetoelectric coupling within the chiral unit cell. We have achieved this by coupling the effective magnetic dipoles of split-ring resonators (SRRs) in a chiral twisted-SRR arrangement (Chapter 8.2). Now, the chiral symmetry of the unit cell is not so obvious anymore, even if all requirements to obtain a “purely” chiral response are fulfilled: four-fold rotational symmetry on the one hand and the absence of mirror planes on the other hand. As a result we have achieved rotation angles of up to  $30^\circ$  and circular dichroism of about 33% that outperform our previous results on twisted-crosses and double-layer gammadions by a factor of six for a metamaterial thickness of only 205 nm. Equivalent to our previous findings in Chapter 5.3, the chiral optical response arises from the symmetric and the antisymmetric magnetic modes. In the case of the chiral twisted-SRR arrangement (Chapter 8.2), however, we found that circular polarisations are eigenpolarisations of the structure, as expected. Indeed, the intensity conversion of circular polarisation has been well below  $10^{-5}$ .

This is not quite the case for gold helices with two windings (itches), the intuitive representative of 3D-chiral structures (Chapter 8.3). Owing to the surface termination of the helix linear birefringence occurs and, as a result, circular polarisation conversion of up to 5% has been observed for the two-pitch gold helices. Nevertheless, the circular transmittance spectra have shown a pronounced stop band for one circular polarisation with a spectral width of up to one octave. We have attributed the broadband behaviour of the gold helices to strong coupling between the excitation modes of the two individual windings within the two-pitch helix. This is very similar to the formation of electronic bands in natural crystal lattices.

Chiral metamaterials allow for large chiral optical effects, namely large optical activity that is orders of magnitude larger than in tartaric acid or in a solution of chiral sugar molecules, for instance. The pronounced circular dichroism also opens new possibilities for using chiral metamaterials as compact broadband circular polarisers – a promising candidate for future applications. But there is even more to explore – chiral metamaterials with a negative refractive index, for example. In principle, we can obtain a negative index of refraction for circular polarisations even without requiring negative values for the permittivity  $\epsilon$  and permeability  $\mu$ . As a result, we can also achieve, *e.g.*, negative refraction and super-resolution imaging by using chiral metamaterials, instead. Another fascinating

effect predicted for chiral metamaterials is bireflection and birefracton that occurs at an interface between a chiral and an achiral halfspace. If we replace the achiral halfspace by a metallic mirror, negative reflection can result for a selected circular polarisation. Using this effect, one can think of building a flat reflecting “lens” that is capable of producing an image of an object that is placed in the chiral medium in front of the mirror. Since the latter effects are normally related to bulk material properties it is desirable to fabricate isotropic three-dimensional chiral metamaterials. This is one of the major challenges in the field of metamaterials and subject to current research. One possible fabrication scheme employs a combination of 3D-direct-laser writing and a subsequent metallisation procedure. Alternatively, the synthesis of solutions composed of chiral metal nanoparticles may be another way to obtain isotropic 3D-chiral metamaterial.



# Appendix A

## Plane Wave Properties in Chiral Media

### A.1 Wave Propagation in Chiral Media

Starting from Maxwell's equations (2.1)-(2.4) we can derive the wave equation for an electromagnetic wave propagating in an effective medium described by the scalar material parameters  $\epsilon$ ,  $\mu$  and  $\xi$ . With Faraday's law (2.3) we can further calculate

$$\begin{aligned}
 \nabla \times (\nabla \times \mathbf{E}) &= \nabla \times \left( -\frac{\partial}{\partial t} \mathbf{B} \right) \\
 -\nabla^2 \mathbf{E} + \nabla (\nabla \cdot \mathbf{E}) &= -\frac{\xi}{c_0} \cdot \nabla \times \frac{\partial}{\partial t} \mathbf{E} - \mu \mu_0 \frac{\partial}{\partial t} \nabla \times \mathbf{H} \\
 -\nabla^2 \mathbf{E} &= \frac{i\omega\xi}{c_0} \cdot \nabla \times \mathbf{E} - \mu \mu_0 \frac{\partial}{\partial t} \left( \frac{\partial}{\partial t} \mathbf{D} \right) \\
 &= \frac{i\omega\xi}{c_0} \cdot \nabla \times \mathbf{E} - \mu \mu_0 \epsilon \epsilon_0 \frac{\partial^2}{\partial t^2} \mathbf{E} + \frac{\xi}{c_0} \cdot \frac{\partial^2}{\partial t^2} (\mu \mu_0 \mathbf{H}) \\
 &= \frac{i\omega\xi}{c_0} \cdot \nabla \times \mathbf{E} + \frac{\omega^2}{c_0^2} \mu \epsilon \mathbf{E} + \frac{\xi}{c_0} \cdot \frac{\partial^2}{\partial t^2} \left( \mathbf{B} - \frac{\xi}{c_0} \cdot \mathbf{E} \right) \\
 &= \frac{i\omega\xi}{c_0} \cdot \nabla \times \mathbf{E} + \frac{\omega^2}{c_0^2} \mu \epsilon \mathbf{E} - \frac{\xi}{c_0} \cdot \frac{\partial}{\partial t} \underbrace{\left( -\frac{\partial}{\partial t} \mathbf{B} \right)}_{=\nabla \times \mathbf{E}} + \frac{\omega^2}{c_0^2} \xi^2 \mathbf{E} \\
 &= 2 \frac{i\omega\xi}{c_0} \cdot \nabla \times \mathbf{E} + \frac{\omega^2}{c_0^2} (\mu \epsilon + \xi^2) \mathbf{E}.
 \end{aligned}$$

This leads us to the wave equation for chiral media given by:

$$\nabla^2 \mathbf{E} + 2i \frac{\omega\xi}{c_0} \cdot \nabla \times \mathbf{E} + \frac{\omega^2}{c_0^2} (\mu \epsilon + \xi^2) \mathbf{E} = 0 \quad (\text{A.1})$$

Now we have to solve the wave equation and calculate the polarisation eigenstates to find an expression for the refractive index in a chiral medium. For a plane wave  $\mathbf{E} = \mathbf{E}_0 \cdot e^{ik_z z}$ , *i.e.*, propagating in  $z$ -direction, we get for the  $x$ -component

$$-k_z^2 E_x + 2 \frac{\omega\xi}{c_0} k_z E_y + \frac{\omega^2}{c_0^2} (\mu \epsilon + \xi^2) E_x = 0 \quad (\text{A.2})$$

and for the  $y$ -component

$$-k_z^2 E_y - 2 \frac{\omega \xi}{c_0} k_z E_x + \frac{\omega^2}{c_0^2} (\mu \epsilon + \xi^2) E_y = 0. \quad (\text{A.3})$$

Solving this two dimensional eigenvalue problem

$$\begin{pmatrix} \frac{\omega^2}{c_0^2} (\mu \epsilon + \xi^2) + \left( 2 \frac{\omega \xi}{c_0} k_z \right) \\ \left( -2 \frac{\omega \xi}{c_0} k_z \right) + \frac{\omega^2}{c_0^2} (\mu \epsilon + \xi^2) \end{pmatrix} \begin{pmatrix} E_x \\ E_y \end{pmatrix} = k_z^2 \begin{pmatrix} E_x \\ E_y \end{pmatrix} \quad (\text{A.4})$$

finally provides us two eigenvalues, *i.e.*, two dispersion relations  $k_z(\omega)$  for a chiral medium:

$$k_z^2 = k_{RCP,LCP}^2 = k_{\pm}^2 = \frac{\omega^2}{c_0^2} (\sqrt{\mu \epsilon} \mp i \xi)^2 = \frac{\omega^2}{c_0^2} \cdot n_{\pm}^2 \quad (\text{A.5})$$

Inserting Equation (A.5) into (A.4) we end up with the two eigenpolarisation states of the system described by Equation (A.4):

$$\begin{aligned} \left[ \frac{\omega^2}{c_0^2} (\mu \epsilon + \xi^2) - k_z^2 \right] \cdot E_x &= - \left( 2 \frac{\omega \xi}{c_0} k_z \right) \cdot E_y \\ \left[ \frac{\omega^2}{c_0^2} (\mu \epsilon + \xi^2) - \frac{\omega^2}{c_0^2} (\sqrt{\mu \epsilon} \mp i \xi)^2 \right] \cdot E_x &= - \left( 2 \frac{\omega \xi}{c_0} \cdot \frac{\omega}{c_0} (\sqrt{\mu \epsilon} \mp i \xi) \right) \cdot E_y \\ \frac{\omega^2}{c_0^2} (\mu \epsilon + \xi^2 - \mu \epsilon + \xi^2 \pm 2i \sqrt{\mu \epsilon} \xi) \cdot E_x &= -2 \frac{\omega^2}{c_0^2} \xi (\sqrt{\mu \epsilon} \mp i \xi) \cdot E_y \\ 2 \frac{\omega^2}{c_0^2} \xi (\sqrt{\mu \epsilon} \mp i \xi) \cdot E_x &= \pm 2i \frac{\omega^2}{c_0^2} \xi (\sqrt{\mu \epsilon} \mp i \xi) \cdot E_y \\ E_y &= \mp i E_x \end{aligned} \quad (\text{A.6})$$

This corresponds to right-handed circular polarisation (RCP, “+”) and left-handed circular polarisation (LCP, “-”)

$$E_+ = \mathbf{E}_{RCP} = \frac{1}{\sqrt{2}} \begin{pmatrix} 1 \\ -i \end{pmatrix} \cdot e^{i(k_+ z - \omega t)} \quad \text{and} \quad E_- = \mathbf{E}_{LCP} = \frac{1}{\sqrt{2}} \begin{pmatrix} 1 \\ i \end{pmatrix} \cdot e^{i(k_- z - \omega t)} .$$

### Impedance of Circularly Polarised Light in Chiral Media

To complete the set of material equations of a chiral medium, we have to find an expression for the impedance of the two circular polarisations. If we consider the chiral medium to be an isotropic medium [42] with the respective material parameters  $\epsilon_{\pm}$  and  $\mu_{\pm}$ , we can write

$$\begin{aligned} \mathbf{D}_{\pm} &= \underbrace{\epsilon \epsilon_0}_{\epsilon_m} \mathbf{E}_{\pm} - \underbrace{\frac{i \kappa}{c_0}}_{\eta} \mathbf{H}_{\pm} \\ &= \epsilon_{\pm} \mathbf{E}_{\pm} \end{aligned} \quad (\text{A.7})$$

$$\begin{aligned} \mathbf{B}_{\pm} &= \underbrace{\frac{i \kappa}{c_0}}_{\eta} \mathbf{E}_{\pm} + \underbrace{\mu \mu_0}_{\mu_m} \mathbf{H}_{\pm} \\ &= \mu_{\pm} \mathbf{H}_{\pm} \end{aligned} \quad (\text{A.8})$$

resulting in

$$\mathbf{E}_{\pm} = \frac{\eta}{\epsilon_m - \epsilon_{\pm}} \mathbf{H}_{\pm} \quad (\text{A.9})$$

$$\mathbf{E}_{\pm} = \frac{\mu_{\pm} - \mu_m}{\eta} \mathbf{H}_{\pm}. \quad (\text{A.10})$$

As both equations have to be fulfilled, we can eliminate the field vectors. This yields the condition

$$(\epsilon_m - \epsilon_{\pm})(\mu_m - \mu_{\pm}) + \eta^2 = 0. \quad (\text{A.11})$$

Reformulating Maxwell's equations (2.3) and (2.4) for a chiral isotropic medium with the above isotropic parameters yields

$$\nabla \times \mathbf{E}_{\pm} - i\omega\mu_{\pm}\mathbf{H}_{\pm} = 0 \quad (\text{A.12})$$

$$\nabla \times \mathbf{H}_{\pm} + i\omega\epsilon_{\pm}\mathbf{E}_{\pm} = 0. \quad (\text{A.13})$$

Now we can solve Equation (A.12) for the two circular polarisations RCP and LCP:

$$\begin{pmatrix} \nabla_x \\ \nabla_y \\ \nabla_z \end{pmatrix} \times E_{\pm} \begin{pmatrix} 1 \\ \mp i \\ 0 \end{pmatrix} e^{i(k_{\pm}z - \omega t)} = i\omega\mu_{\pm}H_{\pm} \begin{pmatrix} 1 \\ \mp i \\ 0 \end{pmatrix} e^{i(k_{\pm}z - \omega t)} \quad (\text{A.14})$$

$$E_{\pm} = \mp i \frac{\omega}{k_{\pm}} \mu_{\pm} H_{\pm} = \mp i Z_{\pm} H_{\pm} \quad (\text{A.15})$$

$Z_{\pm}$  is the (isotropic chiral) impedance for RCP and LCP. Comparing equation (A.15) with (A.10) provides the impedances dependent on the actual material parameters  $\epsilon_m$ ,  $\mu_m$  and  $\eta$  as well as on the isotropic parameters  $\epsilon_{\pm}$  and  $\mu_{\pm}$ .

$$Z_{\pm} = \pm i \frac{\eta}{\epsilon_m - \epsilon_{\pm}} = \pm i \frac{\mu_{\pm} - \mu_m}{\eta} \quad (\text{A.16})$$

Furthermore (A.12) and (A.13) both have to be fulfilled for the field components (A.15) of the two circular polarisations, hence

$$\nabla \times \mathbf{H}_{\pm} + i\omega\epsilon_{\pm}\mathbf{E}_{\pm} = \mp \frac{1}{iZ_{\pm}} (\nabla \times \mathbf{E}_{\pm} - i\omega\epsilon_{\pm}Z_{\pm}^2\mathbf{H}_{\pm}) = 0 \quad (\text{A.17})$$

implies that

$$Z_{\pm} = \sqrt{\frac{\mu_{\pm}}{\epsilon_{\pm}}} \quad (\text{A.18})$$

The isotropic chiral parameters  $\mu_{\pm}$  and  $\epsilon_{\pm}$  can be derived from the original material parameters  $\mu$ ,  $\epsilon$  and  $\kappa$  using (A.11), (A.16) and (A.18):

$$Z_{\pm}^2 = -\frac{(\mu_{\pm} - \mu_m)^2}{\eta^2} = \frac{\mu_{\pm}}{\epsilon_{\pm}} = \frac{\mu_{\pm}}{\epsilon_m - \frac{\eta^2}{\mu_{\pm} - \mu_m}} \quad (\text{A.19})$$

resulting in

$$\mu_{\pm} = \mu_m \mp i\eta \sqrt{\frac{\mu_m}{\epsilon_m}} \quad (\text{A.20})$$

and likewise

$$\epsilon_{\pm} = \epsilon_m \mp i\eta \sqrt{\frac{\epsilon_m}{\mu_m}}. \quad (\text{A.21})$$

Importantly, the refractive index calculated from (A.20) and (A.21) is consistent with (6.31):

$$\begin{aligned} n_{\pm} &= c_0 \sqrt{\epsilon_{\pm} \mu_{\pm}} \\ &= c_0 \sqrt{\left( \epsilon_m \mp i\eta \sqrt{\frac{\epsilon_m}{\mu_m}} \right) \left( \mu_m \mp i\eta \sqrt{\frac{\mu_m}{\epsilon_m}} \right)} \\ &= c_0 \sqrt{\epsilon_m \mu_m \mp 2i\eta \sqrt{\epsilon_m \mu_m} - \eta^2} \\ &= c_0 (\sqrt{\epsilon_m \mu_m} \mp i\eta) \\ &= \sqrt{\epsilon \mu} \pm \kappa \end{aligned} \quad (\text{A.22})$$

Finally we insert (A.20) and (A.21) in (A.16) and obtain the isotropic chiral impedance  $Z_{\pm}$  for RCP and LCP.

$$Z_{\pm} = \pm i \frac{\mu_m \mp i\eta \sqrt{\frac{\mu_m}{\epsilon_m}} - \mu_m}{\eta} = \pm i \frac{\eta}{\epsilon_m - \epsilon_m \pm i\eta \sqrt{\frac{\epsilon_m}{\mu_m}}} = \sqrt{\frac{\mu_m}{\epsilon_m}} = \sqrt{\frac{\mu \mu_0}{\epsilon \epsilon_0}} \quad (\text{A.23})$$

Hence, the impedance of circularly polarised light in a chiral medium is given by

$$Z_+ = Z_- = \sqrt{\frac{\mu}{\epsilon}} \cdot Z_0. \quad (\text{A.24})$$

## A.2 Chiral Retrieval Procedure

In order to derive the effective material parameters for chiral media, we have define the scattering matrix problem as scetched in Fig.A.1. Starting with the normal incidence of a circularly polarised plane wave given by  $\mathbf{E} = E_{\pm} \exp(i(k_{\pm}z - \omega t))$  and  $\mathbf{H} = H_{\pm} \exp(i(k_{\pm}z - \omega t))$ , we now have to take account for the boundary conditions at the interfaces. Generally, the transmission/reflection coefficients between incident and transmitted/reflected field components<sup>1</sup> are given by:

$$E_r^I = r_{\pm} E_i^I \quad (\text{A.25})$$

$$E_t^II = t_{\pm} E_i^I \quad (\text{A.26})$$

$$H_r^I = r_{\pm} H_i^I \quad (\text{A.27})$$

$$H_t^II = t_{\pm} H_i^I \quad (\text{A.28})$$

<sup>1</sup>Note that  $r_+$  ( $r_-$ ) is associated with the reflection coefficient for RCP (LCP) incident light that is reflected as LCP (RCP) light.

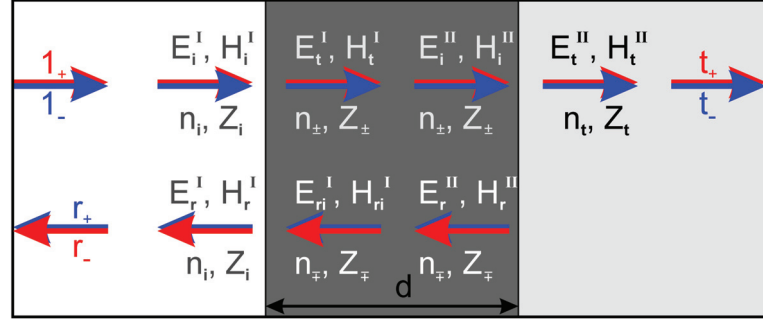


Figure A.1: Schematic illustration of the field components for the generalised version of the Fresnel equations for the retrieval of the effective material parameters from the complex reflection and transmission coefficients of a chiral material slab of thickness  $d$ . For the chiral retrieval procedure, the different polarisation states have to be taken into account for the determination of the refractive indices  $n_{\pm}$ , impedances  $Z_{\pm}$ , permeability  $\mu$ , permittivity  $\epsilon$  and chirality parameter  $\kappa$ . Note that the backward propagating light changes handedness.

The field components of the first and the second surface inside the chiral slab are related *via* the propagation relations:

$$E_i^{\text{II}} = e^{ik_{\pm}d} E_t^{\text{I}} \quad (\text{A.29})$$

$$E_{ri}^{\text{I}} = e^{i(-k_{\mp})(-d)} E_r^{\text{II}} \quad (\text{A.30})$$

$$H_i^{\text{II}} = e^{ik_{\pm}d} H_t^{\text{I}} \quad (\text{A.31})$$

$$H_{ri}^{\text{I}} = e^{i(-k_{\mp})(-d)} H_r^{\text{II}} \quad (\text{A.32})$$

Now, we apply the boundary conditions for the (tangential) field components of  $\mathbf{E}$  and  $\mathbf{H}$  at the two interfaces “I” and “II”.

$$E_i^{\text{I}} + E_r^{\text{I}} = E_t^{\text{I}} + E_{ri}^{\text{I}} \quad (\text{A.33})$$

$$E_i^{\text{II}} + E_r^{\text{II}} = E_t^{\text{II}} \quad (\text{A.34})$$

$$H_i^{\text{I}} + H_r^{\text{I}} = H_t^{\text{I}} + H_{ri}^{\text{I}} \quad (\text{A.35})$$

$$H_i^{\text{II}} + H_r^{\text{II}} = H_t^{\text{II}} \quad (\text{A.36})$$

The impedances in the corresponding media for waves propagating in the forward direction (“ $f$ ”) and in the backward direction (“ $b$ ”)

$$Z_i = + \left( \frac{E_i^{\text{I}}}{H_i^{\text{I}}} \right)_f = - \left( \frac{E_r^{\text{I}}}{H_r^{\text{I}}} \right)_b \quad (\text{A.37})$$

$$Z_t = + \left( \frac{E_t^{\text{II}}}{H_t^{\text{II}}} \right)_f \quad (\text{A.38})$$

$$Z_{\pm} = + \left( \frac{E_t^{\text{I}}}{H_t^{\text{I}}} \right)_f = + \left( \frac{E_i^{\text{II}}}{H_i^{\text{II}}} \right)_f \quad (\text{A.39})$$

$$Z_{\mp} = - \left( \frac{E_{ri}^{\text{I}}}{H_{ri}^{\text{I}}} \right)_b = - \left( \frac{E_r^{\text{II}}}{H_r^{\text{II}}} \right)_b \quad (\text{A.40})$$

can then be inserted into the boundary conditions for the H-fields and we obtain:

$$\left( \frac{E_i^I}{Z_i} - \frac{E_r^I}{Z_i} \right) = \left( \frac{E_t^I}{Z_{\pm}} - \frac{E_{ri}^I}{Z_{\mp}} \right) \quad (\text{A.41})$$

$$\left( \frac{E_i^{II}}{Z_{\pm}} - \frac{E_r^{II}}{Z_{\mp}} \right) = \frac{E_t^{II}}{Z_t} \quad (\text{A.42})$$

If we further include the transmission/reflection coefficients and the boundary conditions for the E-fields we get:

$$\left( \frac{1}{Z_i} + \frac{1}{Z_{\mp}} \right) E_i^I + \left( \frac{1}{Z_{\mp}} - \frac{1}{Z_i} \right) r_{\pm} E_i^I = \left( \frac{1}{Z_{\pm}} + \frac{1}{Z_{\mp}} \right) E_t^I \quad (\text{A.43})$$

$$\left( \frac{1}{Z_i} - \frac{1}{Z_{\pm}} \right) E_i^I - \left( \frac{1}{Z_i} + \frac{1}{Z_{\pm}} \right) r_{\pm} E_i^I = - \left( \frac{1}{Z_{\mp}} + \frac{1}{Z_{\pm}} \right) E_{ri}^I \quad (\text{A.44})$$

$$- \left( \frac{1}{Z_{\mp}} + \frac{1}{Z_{\pm}} \right) E_r^{II} = \left( \frac{1}{Z_t} - \frac{1}{Z_{\pm}} \right) t_{\pm} E_i^I \quad (\text{A.45})$$

$$\left( \frac{1}{Z_{\pm}} + \frac{1}{Z_{\mp}} \right) E_i^{II} = \left( \frac{1}{Z_t} + \frac{1}{Z_{\pm}} \right) t_{\pm} E_i^I \quad (\text{A.46})$$

The use of the propagation relations leads us to:

$$E_{ri}^I = e^{ik_{\mp}d} \frac{\frac{1}{Z_{\pm}} - \frac{1}{Z_t}}{\frac{1}{Z_{\pm}} + \frac{1}{Z_{\mp}}} t_{\pm} E_i^I \quad (\text{A.47})$$

$$E_t^I = e^{-ik_{\pm}d} \frac{\frac{1}{Z_t} + \frac{1}{Z_{\mp}}}{\frac{1}{Z_{\pm}} + \frac{1}{Z_{\mp}}} t_{\pm} E_i^I \quad (\text{A.48})$$

Now we are able to eliminate the unknown field components and finally obtain

$$e^{ik_{\mp}d} = \frac{(1 - r_{\pm})/Z_i - (1 + r_{\pm})/Z_{\pm}}{t_{\pm} \left( \frac{1}{Z_t} - \frac{1}{Z_{\pm}} \right)} \quad (\text{A.49})$$

$$e^{-ik_{\pm}d} = \frac{(1 - r_{\pm})/Z_i + (1 + r_{\pm})/Z_{\mp}}{t_{\pm} \left( \frac{1}{Z_t} - \frac{1}{Z_{\mp}} \right)} \quad (\text{A.50})$$

From these two expressions we can derive in a last step a transcendental equation for the impedances  $Z_{\pm}$  and an inverse cosine expression for the refractive indices  $n_{\pm}$

$$0 = [(1 + r_+) (1 + r_-) - t_+ t_-] \left( \frac{1}{Z_{\mp}} \right)^2 + \frac{2(r_{\mp} - r_{\pm})}{Z_i} \left( \frac{1}{Z_{\mp}} \right) + \frac{t_+ t_-}{Z_t^2} - \frac{(1 - r_+) (1 - r_-)}{Z_i^2}. \quad (\text{A.51})$$

$$n_{\pm} k_0 d = \arccos \left( \frac{1}{2} \left[ \frac{(1 + r_{\pm})/Z_{\mp} + (1 - r_{\pm})/Z_i}{t_{\pm} \left( \frac{1}{Z_i} + \frac{1}{Z_{\mp}} \right)} + \frac{(1 - r_{\mp})/Z_i - (1 + r_{\mp})/Z_{\mp}}{t_{\mp} \left( \frac{1}{Z_i} - \frac{1}{Z_{\mp}} \right)} \right] \right) + 2\pi m \quad (\text{A.52})$$

Equations (A.51) and (A.52) (see also [107]) are used in our own retrieval code adapted from [61]. As the impedances (and consequently the reflection coefficients) for RCP and LCP are identical,  $Z_+ = Z_- = Z$  and  $r_+ = r_- = r$  (see Equation (A.24)), one can further simplify Equation (A.51) and (A.52) and we finally end with.

$$0 = [(1+r)^2 - t_+t_-] \left(\frac{1}{Z}\right)^2 + \frac{t_+t_-}{Z_t^2} - \frac{(1-r)^2}{Z_i^2} \quad (\text{A.53})$$

$$n_{\pm}k_0d = \arccos \left( \frac{1}{2} \left[ \frac{(1+r)/Z + (1-r)/Z_i}{t_{\pm} \left(\frac{1}{Z_t} + \frac{1}{Z}\right)} + \frac{(1-r)/Z_i - (1+r)/Z}{t_{\mp} \left(\frac{1}{Z_t} - \frac{1}{Z}\right)} \right] \right) + 2\pi m \quad (\text{A.54})$$

### A.3 Polarisation State of Complex-Valued Fields

The following method is adapted from [111] and used to calculate the polarisation state of light of the complex-valued E-field transmission coefficients obtained from numerical calculations by COMSOL Multiphysics. The polarisation ellipse and the underlying variables are illustrated in Fig. 6.11. To investigate the time-varying behaviour of the E-field vector at a fixed position ( $z = 0$ ) we derive the actual polarisation state of light *via* the complex (electric) field components in the  $x$ - and the  $y$ -direction for a plane wave propagating in  $z$ -direction

$$\mathbf{E}(t) = \text{Re} [\mathbf{E}_0 e^{-i\omega t}] \quad (\text{A.55})$$

and introduce

$$\mathbf{E}_0 = \mathbf{p} + i\mathbf{q}, \quad (\text{A.56})$$

the (two-component, real valued) real part and imaginary part of the complex E-field  $\mathbf{p}$  and  $\mathbf{q}$ , respectively. As

$$\mathbf{E}(t) = \mathbf{p} \cos(\omega t) + \mathbf{q} \sin(\omega t) \quad (\text{A.57})$$

the resulting E-field vector is an addition of  $\mathbf{p}$  and  $\mathbf{q}$  which in general are not perpendicular to each other. We therefore transform into a coordinate system with perpendicular base vectors  $\mathbf{a}$  and  $\mathbf{b}$  *via*

$$\mathbf{p} + i\mathbf{q} = (\mathbf{a} + i\mathbf{b}) e^{i\theta}. \quad (\text{A.58})$$

The scalar product of  $\mathbf{a}$  and  $\mathbf{b}$  has to vanish, thus,

$$\mathbf{a} \cdot \mathbf{b} = (\mathbf{p} \cos \theta + \mathbf{q} \sin \theta) \cdot (-\mathbf{p} \sin \theta + \mathbf{q} \cos \theta) = 0. \quad (\text{A.59})$$

This leads us to a condition for  $\theta$ :

$$\tan(2\theta) = \frac{2\mathbf{p} \cdot \mathbf{q}}{\mathbf{p}^2 + \mathbf{q}^2} \quad (\text{A.60})$$

Now the E-field is given by

$$\begin{aligned}\mathbf{E}(t) &= \text{Re} \left( (\mathbf{a} + i\mathbf{b}) e^{-i(\omega t - \theta)} \right) \\ &= \mathbf{a} \cos(\omega t - \theta) + \mathbf{b} \sin(\omega t - \theta).\end{aligned}\quad (\text{A.61})$$

If we place the coordinate axes  $a$  and  $b$  (axes of the polarisation ellipse) in the directions of  $\mathbf{a}$  and  $\mathbf{b}$  respectively the E-field vector transforms to

$$\begin{aligned}\begin{pmatrix} E_a \\ E_b \end{pmatrix} &= \begin{pmatrix} s_1 \cos(\omega t - \theta) \\ s_2 \sin(\omega t - \theta) \end{pmatrix} \\ s_1 &= |\mathbf{a}| \quad \text{and} \quad s_2 = |\mathbf{b}|\end{aligned}\quad (\text{A.62})$$

As

$$\frac{E_a^2}{s_1^2} + \frac{E_b^2}{s_2^2} = 1 \quad (\text{A.63})$$

The field moves on an ellipse with the axes  $\mathbf{a}$  and  $\mathbf{b}$ . From (A.58) follows that

$$\mathbf{a} = \mathbf{p} \cos \theta + \mathbf{q} \sin \theta \quad (\text{A.64})$$

$$\mathbf{b} = -\mathbf{p} \sin \theta + \mathbf{q} \cos \theta \quad (\text{A.65})$$

and subsequently

$$\begin{aligned}s_1^2 &= p^2 \cos^2 \theta + q^2 \sin^2 \theta + 2\mathbf{p} \cdot \mathbf{q} \sin \theta \cos \theta \\ &= \frac{1}{2} (p^2 + q^2) + \frac{1}{2} (p^2 - q^2) \cos (2\theta) + \mathbf{p} \cdot \mathbf{q} \sin (2\theta)\end{aligned}\quad (\text{A.66})$$

From (A.60) we get

$$\sin (2\theta) = \frac{2\mathbf{p} \cdot \mathbf{q}}{\sqrt{(p^2 - q^2)^2 + 4(\mathbf{p} \cdot \mathbf{q})^2}} \quad (\text{A.67})$$

$$\cos (2\theta) = \frac{p^2 - q^2}{\sqrt{(p^2 - q^2)^2 + 4(\mathbf{p} \cdot \mathbf{q})^2}} \quad (\text{A.68})$$

which leads us to an expression for the length of the axis  $\mathbf{a}$

$$s_1^2 = \frac{1}{2} \left( p^2 - q^2 + \sqrt{(p^2 - q^2)^2 + 4(\mathbf{p} \cdot \mathbf{q})^2} \right) \quad (\text{A.69})$$

and similar for the length of  $\mathbf{b}$

$$s_2^2 = \frac{1}{2} \left( p^2 - q^2 - \sqrt{(p^2 - q^2)^2 + 4(\mathbf{p} \cdot \mathbf{q})^2} \right). \quad (\text{A.70})$$

The ellipticity is then given by the ratio of the two axes of the polarisation ellipse  $e = s_2/s_1$  ( $-1 \leq e \leq +1$ ). The sense of rotation of the electric field vector  $\mathbf{E}_0$  on the polarisation

ellipse (clockwise or counterclockwise) can be derived from the relative phase difference of its  $x$ - and  $y$ -components:

$$\mathbf{E}_0 = \begin{pmatrix} p_x + iq_x \\ p_y + iq_y \end{pmatrix} = \begin{pmatrix} E_{0x}e^{i\theta_x} \\ E_{0y}e^{i\theta_y} \end{pmatrix} \quad (\text{A.71})$$

$$= E_{0x}e^{i\theta_x} \begin{pmatrix} 1 \\ \frac{E_{0y}}{E_{0x}}e^{i(\theta_y-\theta_x)} \end{pmatrix} \quad (\text{A.72})$$

$$\propto \begin{pmatrix} 1 \\ Ce^{i\theta} \end{pmatrix} \quad (\text{A.73})$$

The sign of the relative phase difference  $\theta = \theta_y - \theta_x$  therefore determines the sense of rotation ( $\theta < 0$  for RCP and  $\theta > 0$  for LCP).

From equation (A.61) we can deduce the angle  $\psi$  between the E-field vector for  $t = 0$  and the axis  $\mathbf{a}$  by

$$\tan \psi = -\frac{s_2}{s_1} \tan \theta \quad (\text{A.74})$$

The angle  $\chi$  between the E-field vector  $E_0$  for  $t = 0$  and the original  $x$ -axis can be obtained by Equation (A.57)

$$\cos \chi = \frac{p_x}{|\mathbf{p}|} \quad (\text{A.75})$$

Finally the inclination of the polarisation ellipse  $\varphi$  results from Equation (A.74) and (A.75):

$$\varphi = \chi - \psi \quad (\text{A.76})$$



# Bibliography

- [1] L. Pasteur, *Mémoire sur la relation qui peut exister entre la forme cristalline et la composition chimique, et sur la cause de la polarisation rotatoire*, Comp. Rend. Paris **26**, 535 (1848).
- [2] J. C. Bose, *On the Rotation of Plane of Polarisation of Electric Waves by a Twisted Structure*, Proc. R. Soc. Lond. **63**, 146 (1898).
- [3] P. Drude, *Lehrbuch der Optik* (Hirzel, S., 1912).
- [4] K. F. Lindman, *Über eine durch ein isotropes System von spiralförmigen Resonatoren erzeugte Rotationspolarisation der elektromagnetischen Wellen*, Ann. Phys. **368**, 621 (1920).
- [5] J. B. Pendry, A. J. Holden, D. J. Robbins, and W. J. Stewart, *Magnetism from Conductors and Enhanced Nonlinear Phenomena*, IEEE Trans. Microw. Theory Tech. **47**, 2075 (1999).
- [6] V. A. Podolskiy, A. K. Sarychev, and V. M. Shalaev, *Plasmon Modes in Metal Nanowires and Left-Handed Materials*, J. Nonlin. Opt. Phys. Mat. **11**, 65 (2002).
- [7] R. A. Shelby, D. R. Smith, S. C. Nemat-Nasser, and S. Schultz, *Microwave transmission through a two-dimensional, isotropic, left-handed metamaterial*, Appl. Phys. Lett. **78**, 489 (2001).
- [8] R. A. Shelby, D. R. Smith, and S. Schultz, *Experimental Verification of a Negative Index of Refraction*, Science **292**, 77 (2001).
- [9] M. Wegener and S. Linden, *Giving light yet another new twist*, Physics **2**, 3 (2009).
- [10] A. Papakostas, A. Potts, D. M. Bagnall, S. L. Prosvirnin, H. J. Coles, and N. I. Zheludev, *Optical Manifestations of Planar Chirality*, Phys. Rev. Lett. **90**, 107404 (2003).
- [11] M. Kuwata-Gonokami, N. Saito, Y. Ino, M. Kauranen, K. Jefimovs, T. Vallius, J. Turunen, and Y. Svirko, *Giant Optical Activity in Quasi-Two-Dimensional Planar Nanostructures*, Phys. Rev. Lett. **95**, 227401 (2005).
- [12] D. R. Smith, W. J. Padilla, D. C. Vier, S. C. Nemat-Nasser, and S. Schultz, *Composite Medium with Simultaneously Negative Permeability and Permittivity*, Phys. Rev. Lett. **84**, 4184 (2000).
- [13] G. Dolling, C. Enkrich, M. Wegener, C. M. Soukoulis, and S. Linden, *Low-loss negative-index metamaterial at telecommunication wavelengths*, Opt. Lett. **31**, 1800 (2006).

- [14] U. K. Chettiar, A. V. Kildishev, H. Yuan, W. Cai, S. Xiao, V. P. Drachev, and V. M. Shalaev, *Dual-band negative index metamaterial: double negative at 813 nm and single negative at 772 nm*, *Opt. Lett.* **32**, 1671 (2007).
- [15] J. C. Maxwell Garnett, *Colours in Metal Glasses and in Metallic Films*, *Phil. Trans. R. Soc. Lond. A* **203**, 385 (1904).
- [16] J. D. Jackson, *Klassische Elektrodynamik* (deGruyter, 1999).
- [17] E. Hecht, *Optics* (Addison Wesley, 2002).
- [18] J. Kästel and M. Fleischhauer, *Quantum Electrodynamics in Media with Negative Refraction*, *Laser Phys.* **15**, 1 (2005).
- [19] J. B. Pendry, *Negative Refraction Makes a Perfect Lens*, *Phys. Rev. Lett.* **85**, 3966 (2000).
- [20] S. Linden, *Kontrolle der Wechselwirkung zwischen Licht und Partikelplasmonen durch selektive Unterdrückung der Extinktion*, Ph.D. thesis, Philipps-Universität Marburg (2001).
- [21] Lord Rayleigh, *On the Dynamical Theory of Gratings*, *Proc. R. Soc. Lond. A* **79**, 399 (1907).
- [22] A. Hessel and A. A. Oliner, *A New Theory of Wood's Anomalies on Optical Gratings*, *Appl. Opt.* **4**, 1275 (1965).
- [23] J. B. Pendry, A. J. Holden, W. J. Stewart, and I. Youngs, *Extremely Low Frequency Plasmons in Metallic Mesostructures*, *Phys. Rev. Lett.* **76**, 4773 (1996).
- [24] M. Bayindir, K. Aydin, E. Ozbay, P. Markos, and C. M. Soukoulis, *Transmission properties of composite metamaterials in free space*, *Appl. Phys. Lett.* **81**, 120 (2002).
- [25] J. Valentine, S. Zhang, T. Zentgraf, E. Ulin-Avila, D. A. Genov, G. Bartal, and X. Zhang, *Three-dimensional optical metamaterial with a negative refractive index*, *Nature* **455**, 376 (2008).
- [26] D. R. Smith, S. Schultz, P. Markos, and C. M. Soukoulis, *Determination of effective permittivity and permeability of metamaterials from reflection and transmission coefficients*, *Phys. Rev. B.* **65**, 195104 (2002).
- [27] G Dolling, *Design, Fabrication, and Characterization of Double-Negative Metamaterials for Photonics*, Ph.D. thesis, Universität Karlsruhe (TH) (2007).
- [28] S. Zhang, W. Fan, N. C. Panoiu, K. J. Malloy, R. M. Osgood, and S. R. J. Brueck, *Optical negative-index bulk metamaterials consisting of 2D perforated metal-dielectric stacks*, *Opt. Express* **14**, 6778 (2006).
- [29] N. Liu, H. Guo, L. Fu, S. Kaiser, H. Schweizer, and H. Giessen, *Three-dimensional photonic metamaterials at optical frequencies*, *Nat. Mater.* **7**, 31 (2007).
- [30] G. Dolling, M. Wegener, and S. Linden, *Realization of a three-functional-layer negative-index photonic metamaterial*, *Opt. Lett.* **32**, 551 (2007).

- [31] Y. Zhang, B. Fluegel, and A. Mascarenhas, *Total Negative Refraction in Real Crystals for Ballistic Electrons and Light*, Phys. Rev. Lett. **91**, 157404 (2003).
- [32] X. L. Chen, M. He, Y. X. Du, W. Y. Wang, and D. F. Zhang, *Negative refraction: An intrinsic property of uniaxial crystals*, Phys. Rev. B **72**, 113111 (2005).
- [33] H. Luo, W. Hu, X. Yi, H. Liu, and J. Zhu, *Amphoteric refraction at the interface between isotropic and anisotropic media*, Opt. Commun. **254**, 353 (2005).
- [34] P. S. J. Russell, *Interference of integrated Floquet-Bloch waves*, Phys. Rev. A **33**, 3232 (1986).
- [35] R. Zengerle, *Light propagation in singly and doubly periodic planar waveguides*, J. Mod. Opt. **34**, 1589 (1987).
- [36] H. Shin and S. Fan, *All-Angle Negative Refraction for Surface Plasmon Waves Using a Metal-Dielectric-Metal Structure*, Phys. Rev. Lett. **96**, 73907 (2006).
- [37] H. J. Lezec, J. A. Dionne, and H. A. Atwater, *Negative Refraction at Visible Frequencies*, Science **316**, 430 (2007).
- [38] V. A. Podolskiy and E. E. Narimanov, *Near-Sighted Superlens*, Opt. Lett. **30**, 75 (2005).
- [39] Z. Liu, S. Durant, H. Lee, Y. Pikus, N. Fang, Y. Xiong, C. Sun, and X. Zhang, *Far-Field Optical Superlens*, Nano Lett. **7**, 403 (2007).
- [40] E. E. Narimanov and V. M. Shalaev, *Optics: Beyond diffraction*, Nature **447**, 266 (2007).
- [41] Z. Liu, H. Lee, Y. Xiong, C. Sun, and X. Zhang, *Far-Field Optical Hyperlens Magnifying Sub-Diffraction-Limited Objects*, Science **315**, 1686 (2007).
- [42] I. V. Lindell, A. H. Sihvola, S. A. Tretyakov, and A. J. Viitanen, *Electromagnetic Waves in Chiral and Bi-Isotropic Media* (Artech House, 2004).
- [43] M. Decker, M. Ruther, C. E. Kriegler, J. Zhou, C. M. Soukoulis, S. Linden, and M. Wegener, *Strong optical activity from twisted-cross photonic metamaterials*, Opt. Lett. **34**, 2501 (2009).
- [44] M. Decker, R. Zhao, C. M. Soukoulis, S. Linden, and M. Wegener, *Twisted split-ring-resonator photonic metamaterial with huge optical activity*, Opt. Lett. **35**, 1593 (2010).
- [45] L. Novotny and B. Hecht, *Principles of Nano-Optics* (Cambridge University Press, 2007).
- [46] U. Kreibig and M. Vollmer, *Optical Properties of Metal Clusters* (Springer-Verlag Berlin Heidelberg, 1995).
- [47] P. B. Johnson and R. W. Christy, *Optical Constants of the Noble Metals*, Phys. Rev. B **6**, 4370 (1972).
- [48] H. E. Bennett and J. M. Bennett, *Optical Properties and Electronic Structure of Metals and Alloys* (North-Holland Publishing Corporation, 1966).
- [49] G. Mie, *Beiträge zur Optik trüber Medien, speziell kolloidaler Metallösungen*, Ann. Phys. **330**, 377 (1908).

- [50] C. F. Bohren and D. R. Huffman, *Absorption and scattering of light by small particles* (Wiley, 1983).
- [51] S. Linden, C. Enkrich, M. Wegener, J. Zhou, T. Koschny, and C. M. Soukoulis, *Magnetic Response of Metamaterials at 100 Terahertz*, *Science* **306**, 1351 (2004).
- [52] M. W. Klein, C. Enkrich, M. Wegener, C. M. Soukoulis, and S. Linden, *Single-slit split-ring resonators at optical frequencies: limits of size scaling*, *Opt. Lett.* **31**, 1259 (2006).
- [53] N. Katsarakis, T. Koschny, M. Kafesaki, E. N. Economou, and C. M. Soukoulis, *Electric coupling to the magnetic resonance of split ring resonators*, *Appl. Phys. Lett.* **84**, 2943 (2004).
- [54] T. J. Yen, W. J. Padilla, N. Fang, D. C. Vier, D. R. Smith, J. B. Pendry, D. N. Basov, and X. Zhang, *Terahertz Magnetic Response from Artificial Materials*, *Science* **303**, 1494 (2004).
- [55] N. Katsarakis, G. Konstantinidis, A. Kostopoulos, R. S. Penciu, T. F. Gundogdu, M. Kafesaki, E. N. Economou, T. Koschny, and C. M. Soukoulis, *Magnetic response of split-ring resonators in the far-infrared frequency regime*, *Opt. Lett.* **30**, 1348 (2005).
- [56] C. Enkrich, F. Pérez-Willard, D. Gerthsen, J. Zhou, T. Koschny, C. M. Soukoulis, M. Wegener, and S. Linden, *Focused-Ion-Beam Nanofabrication of Near-Infrared Magnetic Metamaterials*, *Adv. Mater.* **17**, 2547 (2005).
- [57] C. Enkrich, M. Wegener, S. Linden, S. Burger, L. Zschiedrich, F. Schmidt, J. F. Zhou, T. Koschny, and C. M. Soukoulis, *Magnetic Metamaterials at Telecommunication and Visible Frequencies*, *Phys. Rev. Lett.* **95**, 203901 (2005).
- [58] B. Lahiri, S. G. McMeekin, A. Z. Khokhar, R. M. De La Rue, and N. P. Johnson, *Magnetic response of split ring resonators (SRRs) at visible frequencies*, *Opt. Express* **18**, 3210 (2010).
- [59] J. Zhou, T. Koschny, M. Kafesaki, E. N. Economou, J. B. Pendry, and C. M. Soukoulis, *Saturation of the Magnetic Response of Split-Ring Resonators at Optical Frequencies*, *Phys. Rev. Lett.* **95**, 223902 (2005).
- [60] S. Linden, C. Enkrich, G. Dolling, M. W. Klein, J. Zhou, T. Koschny, C. M. Soukoulis, S. Burger, F. Schmidt, and M. Wegener, *Photonic Metamaterials: Magnetism at Optical Frequencies*, *IEEE J. Sel. Top. Quantum Electron.* **12**, 1097 (2006).
- [61] C. E. Kriegler, M. S. Rill, S. Linden, and M. Wegener, *Bianisotropic Photonic Metamaterials*, *IEEE J. Sel. Top. Quantum Electron.* **16**, 367 (2010).
- [62] R. Marqués, F. Medina, and R. Rafii-El-Idrissi, *Role of bianisotropy in negative permeability and left-handed metamaterials*, *Phys. Rev. B* **65**, 144440 (2002).
- [63] D. R. Smith, J. Gollub, J. J. Mock, W. J. Padilla, and D. Schurig, *Calculation and measurement of bianisotropy in a split ring resonator metamaterial*, *J. Appl. Phys.* **100**, 24507 (2006).
- [64] C. Rockstuhl, F. Lederer, C. Etrich, T. Zentgraf, J. Kuhl, and H. Giessen, *On the reinterpretation of resonances in split-ring-resonators at normal incidence*, *Opt. Express* **14**, 8827 (2006).

- [65] A. Ishikawa, T. Tanaka, and S. Kawata, *Negative Magnetic Permeability in the Visible Light Region*, Phys. Rev. Lett. **95**, 237401 (2005).
- [66] A. N. Lagarkov and A. K. Sarychev, *Electromagnetic properties of composites containing elongated conducting inclusions*, Phys. Rev. B **53**, 6318 (1996).
- [67] V. A. Podolskiy, A. K. Sarychev, and V. M. Shalaev, *Plasmon modes and negative refraction in metal nanowire composites*, Opt. Express **11**, 735 (2003).
- [68] G. Dolling, C. Enkrich, M. Wegener, J. F. Zhou, C. M. Soukoulis, and S. Linden, *Cut-wire pairs and plate pairs as magnetic atoms for optical metamaterials*, Opt. Lett. **30**, 3198 (2005).
- [69] A. Boltasseva and V. M. Shalaev, *Fabrication of optical negative-index metamaterials: Recent advances and outlook*, Metamaterials **2**, 1 (2008).
- [70] G. Subramania and S. Y. Lin, *Fabrication of three-dimensional photonic crystal with alignment based on electron beam lithography*, Appl. Phys. Lett. **85**, 5037 (2004).
- [71] M. W. Klein, *Nonlinear Optics of Metallic Photonic Crystal Slabs and Planar Metamaterials*, Ph.D. thesis, Universität Karlsruhe (TH) (2007).
- [72] S. Linden, M. Decker, and M. Wegener, *Model System for a One-Dimensional Magnetic Photonic Crystal*, Phys. Rev. Lett. **97**, 83902 (2006).
- [73] M. Decker, S. Linden, and M. Wegener, *Coupling effects in low-symmetry planar split-ring-resonator arrays*, Opt. Lett. **34**, 1579 (2009).
- [74] M. Decker, S. Burger, S. Linden, and M. Wegener, *Magnetization waves in split-ring-resonator arrays: Evidence for retardation effects*, Phys. Rev. B **80**, 193102 (2009).
- [75] W. Rechberger, A. Hohenau, A. Leitner, J. R. Krenn, B. Lamprecht, and F. R. Aussenegg, *Optical properties of two interacting gold nanoparticles*, Opt. Commun. **220**, 137 (2003).
- [76] N. Liu, H. Liu, S. Zhu, and H. Giessen, *Stereometamaterials*, Nat. Photonics **3**, 157 (2009).
- [77] I. Sersic, M. Frimmer, E. Verhagen, and A. F. Koenderink, *Electric and Magnetic Dipole Coupling in Near-Infrared Split-Ring Metamaterial Arrays*, Phys. Rev. Lett. **103**, 213902 (2009).
- [78] G. Dolling, M. Wegener, A. Schädle, S. Burger, and S. Linden, *Observation of magnetization waves in negative-index photonic metamaterials*, Appl. Phys. Lett. **89**, 231118 (2006).
- [79] M. L. Brongersma, J. W. Hartman, and H. A. Atwater, *Electromagnetic energy transfer and switching in nanoparticle chain arrays below the diffraction limit*, Phys. Rev. B **62**, R16356 (2000).
- [80] S. A. Maier, M. L. Brongersma, P. G. Kik, S. Meltzer, A. A. G. Requicha, and H. A. Atwater, *Plasmonics - A Route to Nanoscale Optical Devices*, Adv. Mater. **13**, 1501 (2001).

- [81] S. A. Maier, M. L. Brongersma, P. G. Kik, and H. A. Atwater, *Observation of near-field coupling in metal nanoparticle chains using far-field polarization spectroscopy*, Phys. Rev. B **65**, 193408 (2002).
- [82] K. H. Su, Q. H. Wei, X. Zhang, J. J. Mock, D. R. Smith, and S. Schultz, *Interparticle Coupling Effects on Plasmon Resonances of Nanogold Particles*, Nano Lett. **3**, 1087 (2003).
- [83] S. Zhang, W. Fan, N. C. Panoiu, K. J. Malloy, R. M. Osgood, and S. R. J. Brueck, *Experimental Demonstration of Near-Infrared Negative-Index Metamaterials*, Phys. Rev. Lett. **95**, 137404 (2005).
- [84] A. N. Grigorenko, A. K. Geim, H. F. Gleeson, Y. Zhang, A. A. Firsov, I. Y. Khrushchev, and J. Petrovic, *Nanofabricated media with negative permeability at visible frequencies*, Nature **438**, 335 (2005).
- [85] V. A. Shalaev, W. Cai, U. K. Chettiar, H. Yuan, A. K. Sarychev, V. P. Drachev, and A. V. Kildishev, *Negative index of refraction in optical metamaterials*, Opt. Lett. **30**, 3356 (2005).
- [86] A. Christ, S. G. Tikhodeev, N. A. Gippius, J. Kuhl, and H. Giessen, *Waveguide-Plasmon Polaritons: Strong Coupling of Photonic and Electronic Resonances in a Metallic Photonic Crystal Slab*, Phys. Rev. Lett. **91**, 183901 (2003).
- [87] V. N. Astratov, D. M. Whittaker, I. S. Culshaw, R. M. Stevenson, M. S. Skolnick, T. F. Krauss, and R. M. De La Rue, *Photonic band-structure effects in the reflectivity of periodically patterned waveguides*, Phys. Rev. B **60**, R16255 (1999).
- [88] D. M. Whittaker and I. S. Culshaw, *Scattering-matrix treatment of patterned multilayer photonic structures*, Phys. Rev. B **60**, 2610 (1999).
- [89] B. Lamprecht, G. Schider, R. T. Lechner, H. Ditlbacher, J. R. Krenn, A. Leitner, and F. R. Aussenegg, *Metal Nanoparticle Gratings: Influence of Dipolar Particle Interaction on the Plasmon Resonance*, Phys. Rev. Lett. **84**, 4721 (2000).
- [90] E. Shamonina and L. Solymar, *Properties of magnetically coupled metamaterial elements*, J. Magn. Magn. Mater. **300**, 38 (2006).
- [91] N. Liu and H. Giessen, *Three-dimensional optical metamaterials as model systems for longitudinal and transverse magnetic coupling*, Opt. Express **16**, 21233 (2008).
- [92] N. Liu, S. Kaiser, and H. Giessen, *Magnetoinductive and Electroinductive Coupling in Plasmonic Metamaterial Molecules*, Adv. Mater. **20**, 4521 (2008).
- [93] F. Hesmer, E. Tatartschuk, O. Zhuromskyy, A. A. Radkovskaya, M. Shamonin, T. Hao, C. J. Stevens, G. Faulkner, D. J. Edwards, and E. Shamonina, *Coupling mechanisms for split ring resonators: Theory and experiment*, Phys. Status Solidi B **244**, 1170 (2007).
- [94] V. M. Shalaev, *Optical negative-index metamaterials*, Nat. Photonics **1**, 41 (2007).
- [95] C. M. Soukoulis, S. Linden, and M. Wegener, *Negative Refractive Index at Optical Wavelengths*, Science **315**, 47 (2007).

- [96] K. Busch, G. von Freymann, S. Linden, S. F. Mingaleev, L. Tkeshelashvili, and M. Wegener, *Periodic nanostructures for photonics*, Phys. Rep. **444**, 101 (2007).
- [97] O. Sydoruk, O. Zhuromskyy, E. Shamonina, and L. Solymar, *Phonon-like dispersion curves of magnetoinductive waves*, Appl. Phys. Lett. **87**, 72501 (2005).
- [98] I. V. Shadrivov, A. N. Reznik, and Y. S. Kivshar, *Magnetoinductive waves in arrays of splitting resonators*, Physica B **394**, 180 (2007).
- [99] T. Li, R. X. Ye, C. Li, H. Liu, S. M. Wang, J. X. Cao, S. N. Zhu, and X. Zhang, *Structural-configured magnetic plasmon bands in connected ring chains*, Opt. Express **17**, 11486 (2009).
- [100] C. Dahmen, B. Schmidt, and G. von Plessen, *Radiation Damping in Metal Nanoparticle Pairs*, Nano Lett. **7**, 318 (2007).
- [101] P. Olk, J. Renger, M. T. Wenzel, and L. M. Eng, *Distance Dependent Spectral Tuning of Two Coupled Metal Nanoparticles*, Nano Lett. **8**, 1174 (2008).
- [102] A. F. Koenderink, R. de Waele, J. C. Prangma, and A. Polman, *Experimental evidence for large dynamic effects on the plasmon dispersion of subwavelength metal nanoparticle waveguides*, Phys. Rev. B **76**, 201403(R) (2007).
- [103] N. W. Ashcroft and N. D. Mermin, *Solid State Physics* (Saunders College Publishing, 1976).
- [104] M. C. K. Wiltshire, E. Shamonina, I. R. Young, and L. Solymar, *Dispersion characteristics of magneto-inductive waves: comparison between theory and experiment*, Electron. Lett. **39**, 215 (2003).
- [105] Lord Kelvin, *The Molecular Tactics of a Crystal*, in *Oxford University Junior Science Club Lectures* (1894).
- [106] M. S. Rill, C. E. Kriegler, M. Thiel, G. von Freymann, S. Linden, and M. Wegener, *Negative-index bianisotropic photonic metamaterial fabricated by direct laser writing and silver shadow evaporation*, Opt. Lett. **34**, 19 (2009).
- [107] D. Kwon, D. H. Werner, A. V. Kildishev, and V. M. Shalaev, *Material parameter retrieval procedure for general bi-isotropic metamaterials and its application to optical chiral negative-index metamaterial design*, Opt. Express **16**, 11822 (2008).
- [108] A. Lakhtakia, V. V. Varadan, and V. K. Varadan, *A Parametric Study of Microwave Reflection Characteristics of a Planar Achiral-Chiral Interface*, IEEE Trans. Electromag. Compat. **28**, 90 (1986).
- [109] C. Zhang and T. J. Cui, *Negative reflections of electromagnetic waves in a strong chiral medium*, Appl. Phys. Lett. **91**, 194101 (2007).
- [110] S. Bassiri, *Electromagnetic Wave Propagation and Radiation in Chiral Media*, Ph.D. thesis, California Institute of Technology (1987).
- [111] M. Born and E. Wolf, *Principles of Optics* (Cambridge University Press, 1999).

- [112] C. Brosseau, *Fundamentals of Polarized Light* (John Wiley & Sons, Inc., 1998).
- [113] J. A. Schellmann, *Symmetry Rules for Optical Rotation*, *Acc. Chem. Res.* **1**, 144 (1968).
- [114] C. F. Klingshirn, *Semiconductor Optics* (Springer, 2007).
- [115] V. A. Fedotov, P. L. Mladyonov, S. L. Prosvirnin, A. V. Rogacheva, Y. Chen, and N. I. Zheludev, *Asymmetric Propagation of Electromagnetic Waves through a Planar Chiral Structure*, *Phys. Rev. Lett.* **97**, 167401 (2006).
- [116] B. K. Canfield, S. Kujala, M. Kauranen, K. Jefimovs, T. Vallius, and J. Turunen, *Remarkable polarization sensitivity of gold nanoparticle arrays*, *Appl. Phys. Lett.* **86**, 183109 (2005).
- [117] M. Reichelt, S. W. Koch, A. V. Krasavin, J. V. Moloney, A. S. Schwanecke, T. Stroucken, E. M. Wright, and N. I. Zheludev, *Broken enantiomeric symmetry for electromagnetic waves interacting with planar chiral nanostructures*, *Appl. Phys. B* **84**, 97 (2006).
- [118] M. Decker, M. W. Klein, M. Wegener, and S. Linden, *Circular dichroism of planar chiral magnetic metamaterials*, *Opt. Lett.* **32**, 856 (2007).
- [119] A. S. Schwanecke, A. Krasavin, D. M. Bagnall, A. Potts, A. V. Zayats, and N. I. Zheludev, *Broken Time Reversal of Light Interaction with Planar Chiral Nanostructures*, *Phys. Rev. Lett.* **91**, 247404 (2003).
- [120] A. Potts, A. Papakostas, D. M. Bagnall, and N. I. Zheludev, *Planar chiral meta-materials for optical applications*, *Microelectron. Eng.* **73-74**, 367 (2004).
- [121] Y. Chen, J. Tao, X. Zhao, Z. Cui, A. S. Schwanecke, and N. I. Zheludev, *Nanoimprint lithography for planar chiral photonic meta-materials*, *Microelectron. Eng.* **78-79**, 612 (2005).
- [122] S. N. Volkov, K. Dolgaleva, R. W. Boyd, K. Jefimovs, J. Turunen, Y. Svirko, B. K. Canfield, and M. Kauranen, *Optical activity in diffraction from a planar array of achiral nanoparticles*, *Phys. Rev. A* **79**, 43819 (2009).
- [123] S. L. Prosvirnin and N. I. Zheludev, *Polarization effects in the diffraction of light by a planar chiral structure*, *Phys. Rev. E* **71**, 37603 (2005).
- [124] K. Konishi, T. Sugimoto, B. Bai, Y. Svirko, and M. Kuwata-Gonokami, *Effect of surface plasmon resonance on the optical activity of chiral metal nanogratings*, *Opt. Express* **15**, 9575 (2007).
- [125] A. V. Rogacheva, V. A. Fedotov, A. S. Schwanecke, and N. I. Zheludev, *Giant Gyrotropy due to Electromagnetic-Field Coupling in a Bilayered Chiral Structure*, *Phys. Rev. Lett.* **97**, 177401 (2006).
- [126] T. Vallius, K. Jefimovs, J. Turunen, P. Vahimaa, and Y. Svirko, *Optical activity in subwavelength-period arrays of chiral metallic particles*, *Appl. Phys. Lett.* **83**, 234 (2003).
- [127] S. Zhang, W. Fan, B. K. Minhas, A. Frauenglass, K. J. Malloy, and S. R. J. Brueck, *Midinfrared Resonant Magnetic Nanostructures Exhibiting a Negative Permeability*, *Phys. Rev. Lett.* **94**, 37402 (2005).

- [128] G. Dolling, C. Enkrich, M. Wegener, C. M. Soukoulis, and S. Linden, *Simultaneous Negative Phase and Group Velocity of Light in a Metamaterial*, *Science* **312**, 892 (2006).
- [129] E. Plum, V. A. Fedotov, A. S. Schwanecke, N. I. Zheludev, and Y. Chen, *Giant optical gyrotropy due to electromagnetic coupling*, *Appl. Phys. Lett.* **90**, 223113 (2007).
- [130] E. Plum, J. Zhou, J. Dong, V. A. Fedotov, T. Koschny, C. M. Soukoulis, and N. I. Zheludev, *Metamaterial with negative index due to chirality*, *Phys. Rev. B.* **79**, 35407 (2009).
- [131] A. Christ, O. J. F. Martin, Y. Ekinici, N. A. Gippius, and S. G. Tikhodeev, *Symmetry Breaking in a Plasmonic Metamaterial at Optical Wavelength*, *Nano Lett.* **8**, 2171 (2008).
- [132] D. A. Powell, M. Lapine, M. V. Gorkunov, I. V. Shadrivov, and Y. S. Kivshar, *Metamaterial tuning by manipulation of near-field interaction*, arXiv , 0912.1152v2 (2010).
- [133] J. B. Pendry, *A Chiral Route to Negative Refraction*, *Science* **306**, 1353 (2004).
- [134] J. Zhou, J. Dong, B. Wang, T. Koschny, M. Kafesaki, and C. M. Soukoulis, *Negative refractive index due to chirality*, *Phys. Rev. B* **79**, 121104(R) (2009).
- [135] C. Helgert, C. Menzel, C. Rockstuhl, E. Pshenay-Severin, E. B. Kley, A. Chipouline, A. Tünnermann, F. Lederer, and T. Pertsch, *Polarization-independent negative-index metamaterial in the near infrared*, *Opt. Lett.* **34**, 704 (2009).
- [136] I. J. Hodgkinson, A. Lakhtakia, Q. H. Wu, L. De Silva, and M. W. McCall, *Ambichiral, equichiral and finely chiral layered structures*, *Opt. Commun.* **239**, 353 (2004).
- [137] S. Zhang, Y. Park, J. Li, X. Lu, W. Zhang, and X. Zhang, *Negative Refractive Index in Chiral Metamaterials*, *Phys. Rev. Lett.* **102**, 23901 (2009).
- [138] X. Xiong, W. H. Sun, Y. J. Bao, R. W. Peng, M. Wang, C. Sun, X. Lu, J. Shao, Z. F. Li, and N. B. Ming, *Switching the electric and magnetic responses in a metamaterial*, *Phys. Rev. B.* **80**, 201105(R) (2009).
- [139] X. Xiong, W. H. Sun, Y. J. Bao, M. Wang, R. W. Peng, C. Sun, X. Lu, J. Shao, Z. F. Li, and N. B. Ming, *Construction of a chiral metamaterial with a U-shaped resonator assembly*, *Phys. Rev. B.* **81**, 75119 (2010).
- [140] J. K. Gansel, M. Thiel, M. S. Rill, M. Decker, K. Bade, V. Saile, G. von Freymann, S. Linden, and M. Wegener, *Gold Helix Photonic Metamaterial as Broadband Circular Polarizer*, *Science* **325**, 1513 (2009).
- [141] J. K. Gansel, M. Wegener, S. Burger, and S. Linden, *Gold helix photonic metamaterials: A numerical parameter study*, *Opt. Express* **18**, 1059 (2010).



# Acknowledgements

Success of a PhD thesis is not only based on hard work, but it is also, to a significant part, result of the experimental conditions and a stimulating environment that allow us to develop and realise our ideas. In this sense, I would like thank all the people who have contributed to the success of this Thesis and supported me throughout the past couple of years.

First of all, I like to show my appreciation to my advisor Prof. Dr. Martin Wegener for giving me the opportunity to work on this exciting topic. It was a great pleasure for me to contribute to the emerging field of chiral photonic metamaterials from its early days on. My work has largely benefited from his profound knowledge, stimulating discussions and from the extraordinary equipment available in his work group.

Second, I want to express my gratitude to Prof. Dr. Kurt Busch for kindly agreeing to co-referee this Thesis and for the theoretical support he and his work group granted me during my time as PhD student. In particular, I would like thank Julia Budde and Sabine Essig for their enduring efforts spent on a theoretical description of the gammadions (Chapter 7) and the twisted-SRR dimers (Chapter 5.3), respectively.

Third, I would like to thank Prof. Dr. Stefan Linden for mentoring and supporting me in many questions in the course of this work and nonetheless for his encouragement to create an extraordinary team spirit within his metamaterialists' subgroup. In this sense, I am also very grateful to every colleague in the Wegener group for many inspiring discussions and the delightful atmosphere in the group. Specifically, I want to mention Nils Feth, Nina Meinzer, Christine Kriegler and Jörg Wissler for their support in and out of office. Furthermore, I am indebted to Isabelle Staude, Nina Meinzer and Stefan Linden for the critical proofreading of this Thesis. Thank you for helping me to reduce all the typing errors and to improve its readability.

I also want to say thank you to the following persons:

- Thorsten Kuhn who knew every screw of the e-beam evaporation chamber and took care of all the smaller and bigger technical problems and needs of the group.
- Matthias Klein who programmed the COMSOL library functions that I used for nearly all my calculations.
- Renate Helfen, Christa Weißenburger, Monika Brenkmann and Gisela Habitzreither in the secretariat of the Institute for Applied Physics for helping me with all the bureaucracy I had to face during my PhD thesis.
- The members of the electronic workshop, namely, Heinz Hoffmann, Helmut Lay and Werner Gilde for taking care of all computers and electronic problems.
- Johann Westhauser, the technician of our group.

- The members of the mechanical workshop around Werner Wagner.

Furthermore, I acknowledge the financial support of the DFG-Center for Functional Nanostructures (CFN), the Karlsruhe School of Optics and Photonics (KSOP) and the project PHOME supported by the Future and Emerging Technologies (FET) programme.

My last words in this Thesis are dedicated to my precious family and all my friends for sharing the good times and helping me through the hard times. In particular, my special thanks go to Isabelle Staude for her patience and support in the final months of my PhD thesis.